EVENT-BY-EVENT MULTIPLICITY FLUCTUATIONS IN HIGH ENERGY HEAVY ION COLLISIONS AT THE LHC ENERGIES IN THE ALICE EXPERIMENT

By

Maitreyee Mukherjee

Enrolment No. PHYS04201004004

Variable Energy Cyclotron Centre, Kolkata, India

A thesis submitted to

The Board of Studies in Physical Sciences

In partial fulfillment of requirements for the Degree of

DOCTOR OF PHILOSOPHY

of

HOMI BHABHA NATIONAL INSTITUTE

July, 2016

Homi Bhabha National Institute[1]

Recommendations of the Viva Voce Committee

As members of the Viva Voce Committee, we certify that we have read the dissertation prepared by Ms. Maitreyee Mukherjee entitled "Event-by-Event Multiplicity Fluctuations in High Energy Heavy Ion Collisions at the LHC energies in the ALICE Experiment" and recommend that it may be accepted as fulfilling the thesis requirement for the award of Degree of Doctor of Philosophy.

Chairman – Prof. Jane Alam Jane Alam **Date: 30/11/2016**

Guide / Convener – Prof. Tapan K. Nayak **Date: 30/11/2016**

Tapan Nayak

Co-guide - NA **Date: 30/11/2016**

Examiner – Prof. Anju Bhasin Anju Bhasin **Date: 30/11/2016**

Member 1- Prof. Subhasish Chattopadhyay **Date: 30/11/2016**

Member 2- Prof. Basanta Nandi **Date: 30/11/2016**

B Nandi

Final approval and acceptance of this thesis is contingent upon the candidate's submission of the final copies of the thesis to HBNI.

I/We hereby certify that I/we have read this thesis prepared under my/our direction and recommend that it may be accepted as fulfilling the thesis requirement.

Date: 30/11/2016

Place: Kolkata

Tapan Nayak

<Signature> **<Signature>**

Co-guide (if applicable) **Guide**

---

[1] Version approved during the meeting of Standing Committee of Deans held during 29-30 Nov 2013

STATEMENT BY AUTHOR

This dissertation has been submitted in partial fulfilment of requirements for an advanced degree at Homi Bhabha National Institute (HBNI) and is deposited in the Library to be made available to borrowers under rules of the HBNI.

Brief quotations from this dissertation are allowable without special permission, provided that accurate acknowledgement of source is made. Requests for permission for extended quotation from or reproduction of this manuscript in whole or in part may be granted by the Competent Authority of HBNI when in his or her judgement the proposed use of the material is in the interests of scholarship. In all other instances, however, permission must be obtained from the author.

Maitreyee Mukherjee

Maitreyee Mukherjee

DECLARATION

I, hereby declare that the investigation presented in the thesis has been carried out by me. The work is original and has not been submitted earlier as a whole or in part for a degree/diploma at this or any other Institution/University.

Maitreyee Mukherjee

Maitreyee Mukherjee

Homi Bhabha National Institute

Ph. D. PROGRAMME

SYNOPSIS

1. **Name of the Student:** Ms. MAITREYEE MUKHERJEE
2. **Name of the Constituent Institution:** Variable Energy Cyclotron Centre
3. **Enrolment No.:** PHYS04201004004
4. **Title of the Thesis:** *Event-by-Event multiplicity fluctuations in high energy heavy-ion collisions at the LHC energies in the ALICE experiment*
5. **Board of Studies:** Physical Sciences

Based on the research work performed by the candidate, the Doctoral committee recommends for the submission of the synopsis.

SYNOPSIS

Quark-Gluon-Plasma (QGP) is a state of matter, described by Quantum Chromo Dynamics (QCD), which may exist in extremely high temperature and energy-density. By colliding nuclei at ultra-relativistic energies, it is possible to create such an extreme environment, where this QGP-state of matter may exist. This is similar to the state of matter that might have existed in the early universe within few microseconds after the Big Bang. The QCD-phase diagram describes the different states of matters at different temperatures (T) and different baryon-densities (μ_{B}). Specified particle detectors have been built with specialized techniques to detect and to measure the properties associated with the state of matter. A Large Ion Collider Experiment (ALICE) [1] at the Large Hadron Collider (LHC) [2] of CERN is designed to study the properties of the strongly interacting matter.

One of the basic advantages of the heavy-ion collisions at relativistic energies is the production of large number of particles in each event, which facilitates the event-by-event study of several observables. Event-by-event fluctuations of thermodynamic quantities have been proposed as the basic tools for understanding the particle production mechanisms and to probe the QCD phase transition. The fluctuations of experimentally accessible quantities, such as particle multiplicities, mean transverse momenta, temperature, particle ratios, and other global observables are related to the thermodynamic properties of the system, such as the entropy, specific heat, chemical potential and matter compressibility. These studies help to understand the nature of the phase transition and the critical fluctuations at the QCD phase boundary [3]. A non-monotonic behaviour of multiplicity fluctuations may signal the onset of deconfinement, and can be used to probe the critical point in the QCD phase diagram.

Multiplicity of produced particles is an important quantity, which characterizes the system produced in heavy-ion collisions. Multiplicity distributions are very important to study. The charged-particle multiplicity is one of the simplest observables in collisions of hadrons, yet it imposes important constraints on the mechanisms of particle production. Experiments have been performed with cosmic rays, fixed target setups, and particle colliders. These measurements have been used to improve, or reject, models of particle production, which are often available as Monte Carlo event generators. The multiplicity distribution contains information about particle correlations. The charged-particle multiplicity is a key observable for the understanding of multi-particle production in collisions of hadrons at high energy. The probability P(n) for producing n charged particles in the final state is related to the production mechanism of the particles. The multiplicity distribution follows a Poisson distribution if the final-state particles are produced independently. Observation of a deviation from Poisson distribution indicates presence of correlation [4].

The multiplicity fluctuations may affect the other measurements. Extracted multiplicity fluctuations have contributions from statistical components as well as those, which have dynamical origin. The statistical components of the multiplicity fluctuations have direct impact on the fluctuations in other measured quantities. The statistical components have contributions from the choice of centrality, fluctuation in impact parameter or number of participants, finite particle multiplicity, effect of limited acceptance of the detectors, fluctuations in the number of primary collisions, effect of rescattering, etc [3]. In order to extract the dynamical part of the fluctuations, the contribution to multiplicity from statistical part has to be well understood [5].

Multiplicity fluctuations are normally characterized by the scaled variances of the multiplicity distributions, defined as,

$$\omega_n = \frac{\sigma_n^2}{\langle n \rangle}, \tag{1}$$

where $\langle n \rangle$ and σ_n^2 are the mean and variance of the multiplicity distribution, respectively [3]. Multiplicity fluctuations have been reported by E802 experiment at BNL, Alternate Gradient Synchrotron (AGS), WA98, NA49 and CERES experiments at the CERN Super Proton Synchrotron (SPS), as well as the PHENIX experiment at RHIC [5]. The nature of the multiplicity distributions as a function of centrality and beam energy has been extracted and compared to statistical and different model calculations. These results have generated a great deal of theoretical interests.

Recently, the source of the multiplicity fluctuation has been extensively studied theoretically in the microscopic level. Within framework of the relativistic fluctuating hydrodynamics, entropy and in turn, event-by-event multiplicity fluctuation has been studied as the outcome of noises during hydrodynamic evolution of the quark-gluon fluid created in high-energy nuclear collisions [6].

The LHC delivers colliding pp beams at maximum center-of-mass energies of 14 TeV and PbPb beams at 5.5 A TeV. LHC is also capable to provide light ion collisions such as ArAr and as well as asymmetric collisions like pPb. Pb-Pb collisions at LHC energies produces a system of high temperature and low baryon-density, where we expect a smooth crossover in the phase diagram. The local multiplicity fluctuations have been predicted as a signature of critical hadronization in Pb-Pb collisions at the Large Hadron Collider (LHC) energies at CERN. Measurements at the vanishing $\mu_{\rm B}$ at LHC energies set the scale of theoretical calculations, and one can accurately calculate several quantities and their fluctuations. Thus the fluctuation measurements are of high importance at the LHC.

The ALICE detector [1] systems allow tracking down to very low transverse momentum, where the particle production are much much higher than the region for higher transverse momentum. The ALICE setup can be broadly described by three groups of detectors, i.e, the central barrel, the forward detectors and the forward muon spectrometer. From India, Variable Energy Cyclotron Centre (VECC) is involved in the construction and operation of the Photon Multiplicity Detector (PMD), which is a forward detector in ALICE.

The ALICE experiment probes a continuous range of Bjorken-x below 10^{-4} with the central detectors. Thus, ALICE experiment will be able to access a novel regime where initial state effects can be studied very well [7]. The parameters characterizing the multiplicity distributions can be connected to the early stages of collision and it is important to investigate how these parameters change for different systems.

In this work, ALICE data analysis on the event-by-event multiplicity fluctuations is presented for charged particle multiplicity distributions produced in Pb-Pb collisions at $\sqrt{s}_{\mathrm{NN}}$= 2.76 TeV. For the present work, detectors used are - Inner Tracking System (ITS) for vertex-selection and tracking, Time Projection Chamber (TPC) for tracking and V0 for centrality selection. In course of the analysis, volume fluctuations have also been estimated. After selection of the minimum-bias events, proper vertex-selection has been done for the analysis. Extensive studies have been performed for centrality selection, track selection, centrality bin width correction for non-uniformity in charged particle multiplicity distribution, correction of the results for the detector inefficiency (including the phase-space dependence of the efficiency factor), correction for contamination, error estimation for limited statistics and error estimation for the systematics arising from the experiment. The systematic studies mainly include the effect of magnetic field, effect of changing track-cuts and vertex-cuts, effect of cleanup of the uncorrelated events from the data-set, etc. A universal scaling in the multiplicity fluctuation observable has been presented. The results have been compared with HIJING and AMPT event generators. The observable has been studied for different transverse momentum range and different acceptance range too. Multiplicity fluctuations are related to the isothermal compressibility (k_{T}) of the system produced in the high energy collisions [8]. An estimation for the values of k_{T} has been done for Pb-Pb collisions at $\sqrt{s_{\mathrm{NN}}} = 2.76$ TeV.

Similar analysis for the multiplicity fluctuations has been performed for p-Pb collisions at $\sqrt{s_{\mathrm{NN}}} = 5.02$ TeV. These results are presented and discussed.

Additionally, multiplicity distributions of produced particles and their event-by-event fluctuations are presented in the thesis using the AMPT model in the default and string melting modes. In addition to being sensitive to the QCD phase transitign, these fluctuations provide baselines for other event-by-event measurements. The collision energy and centrality dependence of fluctuations are estimated for heavy-ion collisions from $\sqrt{s_{\mathrm{NN}}}$= 7.7 GeV to 2.76 TeV. The choice of narrow centrality bins and the corrections of centrality bin width effect helps to avoid inherent volume fluctuations within a given centrality window. The multiplicity fluctuations expressed in terms of scaled variances, decrease from peripheral to central collisions for all energies, except for that of the Pb-Pb collisions at $\sqrt{s_{\mathrm{NN}}}$= 2.76 TeV. The beam energy dependence shows an increase of multiplicity fluctuations with increasing beam energy [5].

Bibliography

[1] The ALICE experiment at the CERN LHC, 2008 JINST 3 S08002.

[2] T. S. Pettersson (ed.), P. Lefevre (ed.), The Large Hadron Collider : conceptual design, CERN-AC-95-05 LHC (1995).

[3] M. M. Aggarwal *et al.* (WA98 Collaboration) Phys. Rev. **C 65**, 054912 (2002).

[4] Jan Fiete Grosse-Oetringhaus, K. Reygers, J. Phys. **G37** 083001(2010).

[5] Maitreyee Mukherjee *et al.* 2016 J. Phys. G: Nucl. Part. Phys. **43** 085102.

[6] T.Hirano, QM 2014, Nuclear Physics **A 931** (2014) c831.

[7] E. Iancu, CERN-2014-003, pp. 197-266, arxiv:1205.0579 [hep-ph] (2012).

[8] A. Adare *et al.* (PHENIX Collaboration) Phys. Rev. **C 78**, 044902 (2008), arXiv: 0805.1521[nucl-ex] (2008).

LIST OF PUBLICATIONS

JOURNALS:

a. Published

1. Fluctuations in Charged Particle Multiplicities in Relativistic Heavy-Ion Collisions.
   Maitreyee Mukherjee, S. Basu, S. Choudhury and T.K. Nayak; J. Phys. G: Nucl. Part. Phys. 43 085102 (2016), arXiv:1603.02083 [nucl-ex]

2. Centrality determination of Pb-Pb collisions at $\sqrt{s}_{\mathrm{NN}}$= 2.76 TeV with ALICE.
   Maitreyee Mukherjee (for the ALICE Collaboration), Phys.Rev. C88 (2013) 4, 044909. arXiv: 1301.4361 [nucl-ex].

b. Communicated

1. Charged-particle multiplicities in proton-proton collisions at $\sqrt{s} = 0.9\, to\, 8$ TeV.
   Maitreyee Mukherjee (for the ALICE Collaboration), Sept 24, 2015;
   arXiv: 1509.07541 [nucl-ex].

2. Charged Particle Multiplicity Fluctuations in PbPb collisions at $\sqrt{s}_{\mathrm{NN}} =$ 2.76 TeV in ALICE.
   Maitreyee Mukherjee (for the ALICE Collaboration), under Collaboration review.

c. Other ALICE Collaboration Papers

1. Pseudorapidity and transverse-momentum distributions of charged particles in proton-proton collisions at $\sqrt{s}$= 13 TeV.

   ALICE Collaboration, Phys. Lett. B 753 (2016) 319-329; arXiv: 1509.08734 [nucl-ex].

2. Centrality evolution of the charged-particle pseudorapidity density over a broad pseuodorapidity range in Pb-Pb collisions at $\sqrt{s_{\rm NN}}$= 2.76 TeV.

   ALICE Collaboration, Phys. Lett. B 754 (2016) 373-385; arXiv: 1509.07299 [nucl-ex].

3. Centrality dependence of pion freeze-out radii in Pb-Pb collisions at $\sqrt{s_{\rm NN}}$= 2.76 TeV.

   ALICE Collaboration, Phys. Rev. C 93 (2016) 024905; arXiv: 1507.06842 [nucl-ex].

4. Forward-central two-particle correlations in p-Pb collisions at $\sqrt{s_{\rm NN}}$= 5.02 TeV.

   ALICE Collaboration, Phys. Lett. B 753 (2016) 126-139; arXiv: 1506.08032 [nucl-ex].

5. Centrality dependence of the nuclear modification factor of charged pions, kaons, and protons in Pb-Pb collisions at $\sqrt{s_{\rm NN}}$= 2.76 TeV.

   ALICE Collaboration, Phys. Rev. C 93, 034913 (2016); arXiv: 1506.07287 [nucl-ex].

6. Measurement of pion, kaon and proton production in proton-proton collisions at $\sqrt{s}$= 7 TeV.

   ALICE Collaboration, Eur.Phys.J. C75 (2015) 5, 226. arXiv: 1504.00024 [nucl-ex].

7. Forward-backward multiplicity correlations in pp collisions at $\sqrt{s}$= 0.9, 2.76 and 7 TeV.
   ALICE Collaboration, JHEP 1505 (2015) 097. arXiv: 1502.00230 [nucl-ex].

8. Centrality dependence of particle production in p-Pb collisions at $\sqrt{s_{\rm NN}}$= 5.02 TeV.
   ALICE Collaboration, Phys.Rev. C91 (2015) 6, 064905. arXiv: 1412.6828 [nucl-ex].

9. Inclusive photon production at forward rapidities in proton-proton collisions at $\sqrt{s}$= 0.9, 2.76 and 7 TeV.
   ALICE Collaboration, Eur.Phys.J. C75 (2015) 4, 146. arXiv: 1411.4981 [nucl-ex].

10. Event-by-event mean p_T fluctuations in pp and Pb-Pb collisions at the LHC.
    ALICE Collaboration, Eur.Phys.J. C74 (2014) 10, 3077. arXiv: 1407.5530 [nucl-ex].

11. Performance of the ALICE Experiment at the CERN LHC.
    ALICE Collaboration, Int.J.Mod.Phys. A29 (2014) 1430044. arXiv: 1402.4476 [nucl-ex].

12. Multiplicity dependence of Pion, Kaon, Proton and Lambda Production in p-Pb Collisions at $\sqrt{s_{\rm NN}}$= 5.02 TeV.
    ALICE Collaboration, Phys.Lett. B728 (2014) 25-38. arXiv: 1307.6796 [nucl-ex].

13. Multiplicity dependence of the average transverse momentum in pp, p-Pb and Pb-Pb collisions at the LHC.

ALICE Collaboration, Phys.Lett. B727 (2013) 371-380. arXiv: 1307.1094 [nucl-ex].

14. Performance of the ALICE VZERO system.

    ALICE Collaboration, JINST 8 (2013) P10016. arXiv: 1306.3130 [nucl-ex].

15. Mid-rapidity anti-baryon to baryon ratios in pp collisions at $\sqrt{s}$= 0.9, 2.76 and 7 TeV measured by ALICE.

    ALICE Collaboration, Eur.Phys.J. C73 (2013) 2496. arXiv: 1305.1562 [nucl-ex].

16. Centrality dependence of the pseudorapidity density distribution for charged particles in Pb-Pb collisions at $\sqrt{s_{\rm NN}}$= 2.76 TeV.

    ALICE Collaboration, Phys.Lett. B726 (2013) 610-622. arXiv: 1304.0347 [nucl-ex].

17. Centrality dependence of π, K, p production in Pb-Pb collisions at $\sqrt{s_{\rm NN}}$= 2.76 TeV.

    ALICE Collaboration, Phys.Rev. C88 (2013) 4, 044910. arXiv: 1303.0737 [nucl-ex].

18. Charge correlations using the balance function in Pb-Pb collisions at $\sqrt{s_{\rm NN}}$= 2.76 TeV.

    ALICE Collaboration, Phys.Lett. B723 (2013) 267-279. arXiv: 1301.3756 [nucl-ex].

19. Transverse momentum distribution and nuclear modification factor of charged particles in p-Pb collisions at $\sqrt{s_{\rm NN}}$= 5.02 TeV.

ALICE Collaboration, Phys.Rev.Lett. 110 (2013) 8, 082302. arXiv: 1210.4520 [nucl-ex].

20. Pseudorapidity density of charged particles in p-Pb collisions at $\sqrt{s}_{\rm NN}$= 5.02 TeV.
    ALICE Collaboration, Phys.Rev.Lett. 110 (2013) 3, 032301. arXiv: 1210.3615 [nucl-ex].

21. Centrality Dependence of Charged Particle Production at Large Transverse Momentum in Pb-Pb Collisions at $\sqrt{s}_{\rm NN}$= 2.76 TeV.
    ALICE Collaboration, Phys.Lett. B720 (2013) 52-62. arXiv: 1208.2711 [nucl-ex].

22. Net-Charge Fluctuations in Pb-Pb collisions at $\sqrt{s}_{\rm NN}$= 2.76 TeV.
    ALICE Collaboration, Phys.Rev.Lett 110 (2013)15, 152301. arXiv: 1207.6068 [nucl-ex].

CONFERENCE PROCEEDINGS:

1. Beam energy and centrality dependence of multiplicity fluctuations in heavy ion collisions.
   Maitreyee Mukherjee, S. Basu, S. Choudhury and T.K.Nayak;
   Strangeness in Quark Matter (6-11 July 2015, Dubna, Russia)
   http://iopscience.iop.org/article/10.1088/1742-6596/668/1/012118/pdf

2. Multiplicity Distributions and Fluctuations in Heavy Ion Collisions.
   Maitreyee Mukherjee;
   6th International Conference on Physics Opportunities at an Electron-Ion Collider (7-11 September 2015, Ecole Polytechnique, Palaiseau, France)

http://www.epj-conferences.org/articles/epjconf/pdf/2016/07/epjconf_poetic2016_04004.pdf

3. Beam energy and centrality dependence of multiplicity fluctuations in heavy ion collisions.

   Maitreyee Mukherjee, S. Basu, S. Choudhury and T.K.Nayak;

   e-Proceedings of 60th DAE-BRNS Symposium on Nuclear Physics (snp2015)

4. Event-by-event multiplicity fluctuations in Pb-Pb collisions in ALICE.

   Maitreyee Mukherjee (on behalf of the ALICE collaboration)

   XI Workshop on Particle Correlations and Femtoscopy (3- 7 Nov, 2015, Warsaw, Poland),arXiv:1603.06824 [hep-ex] (Published in Acta Physica Polonica B, DOI:10.5506/APhysPolBSupp.9.283)

5. Event-by-event multiplicity fluctuations in heavy-ion collisions.

   Maitreyee Mukherjee, S. Basu, S. Choudhury and T.K.Nayak;

   7th International Conference on Physics and Astrophysics of Quark Gluon Plasma (2-6 February 2015, VECC, Kolkata)

   (to be published in Proceedings of Science)

Doctoral Committee Report for Maitreyee Mukherjee

On the basis of the work done by Maitreyee Mukherjee, the doctoral committee recommends the submission of thesis to HBNI for Ph. D.

Signature of Student: Maitreyee Mukherjee
(Maitreyee Mukherjee)

Date: 15/10/2015

Doctoral Committee:

S. No.	Name	Designation	Signature	Date
1.	Prof. Jane Alam	Chairman	Jane Alam	15/10/2015
2.	Prof. Tapan K. Nayak	Convener	T. K. Nayak	15/10/2015
3.	Prof. Subhasish Chattopadhyay	Member	[illegible]	15/10/2015
4.	Prof. Basanta Nandi	Member	B. Nandi	15/10/2015

Dedicated to my parents

ACKNOWLEDGMENTS

I would like to express my gratitude to my supervisor, Prof. Tapan Kumar Nayak for his continuous support, encouragement, enthusiasm, and guidance during my PhD work. I would like to thank my doctoral committee members Prof. Jane Alam, Prof. Subhasish Chattopadhyay, and Prof. Basanta K. Nandi for their valuable advices. I would like to thank Dr. Y.P. Viyogi, Dr. Premomoy Ghosh, Dr. Zubayer Ahmed and Dr. Anand Dubey of Experimental High Energy Physics and Application Group, VECC, for inspiring me. I am thankful to the staffs of the Photon Multiplicity Detector (PMD) laboratory in VECC to help me to understand the functions of the detectors as well as to help in detector testing, etc. I sincerely thank Mr. Vikas Singhal for constant help in matters related to computing and grid at VECC. I am thankful to my seniors Sidharth Prashad, Sudipan De, Nihar Ranjan Sahoo, Partha Pratim Bhaduri, Sukanya Mitra and Surasree Mazumder for helping me with advices and suggestions. I convey my gratitude to Dr. Prithwish Tribedy for his support and help. I would like to thank all my friends Sumit, Subikash, Arindam, Rajesh, Balaram, Vishal and Rihan for making my journey enjoyable.

I am fortunate to have discussions on several topics, especially on my analysis work, with Dr. Jurgen Schukraft (Former Spokesperson of ALICE), Dr. Federico Antinori (Physics Coordinator), Dr. Andreas Morsch, Dr. Leonardo Milano and Dr. Alice Ohlson (Convenors of the Physics Analysis Group (PAG) in ALICE), Dr. Michael Weber and Dr. Panos Christakoglou (Convenors of Physics Working Group (Correlations and Fluctuations) in ALICE) and Dr. Satyajit Jena during my stay in CERN. I would like to thank the ALICE-India Collaboration members and all my friends from ALICE-India.

I express my gratitude to my parents for their unconditional support throughout my PhD work. I thank my husband, Sayan Sadhu, for his encouragement in the completion of my thesis.

Maitreyee Mukherjee

Maitreyee Mukherjee

Contents

List of Figures

List of Tables

1 Introduction

This chapter provides a brief introduction on the fundamental particles, Quantum Chromodynamics (QCD), etc. The deconfined state of quarks and gluons, known as Quark Gluon Plasma, and its signatures have been discussed with some observed results from the high energy experiments. The event-by-event fluctuation measures have been discussed in brief. At the end, the organization of the thesis work has been presented.

1.1 The fundamental particles

Over the last several decades, scientists have been searching for the fundamental constituents of matter. In 1909, Rutherford found that most of the mass of an atom is concentrated in a nucleus [1]. By 1932, the electrons, protons, photons and the neutrons [2] were known as the elementary particles. However, the binding between the neutrons and the protons inside the nucleus could not be explained by the electromagnetism.

In 1968, Stanford Linear Accelerator Centre (SLAC) found neutrons and protons to contain more fundamental particles, known as the *quarks* (named by Murray

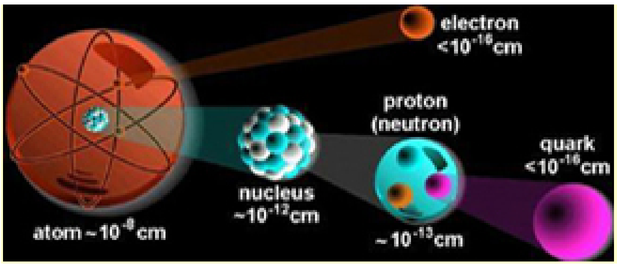

Figure 1.1: Journey from the atom to the quarks

Gell-Mann). Previously, the quark model was independently proposed by physicists Murray Gell-Mann and George Zweig in 1964. Therfore, neutrons and protons are basically the hadrons made of the quarks, as shown in Fig. 1.1. Quarks are not found as free particles in nature. Hadrons are classified into two categories : *baryons* are the stable matters made of three quarks and *mesons* are short-lived, made of the quark-antiquark pair. Besides the nucleus, the leptons are also found within the atoms. Many particles were found within a short period of time, from the scattering experiments and using the particle accelerators, in 1950's.

Since 1970's, the fundamental constituents of matter were described within the framework of the *Standard Model*. Quarks can be classified as, up (u), down (d), charm (c). strange (s), top (t) and bottom (b). The leptons are classified as, the electorn (e^-), electron neutino (ν_e), muon (μ^-), muon neutino (ν_μ), tau (τ) and tau neutrino (ν_τ). Protons and neutrons are made up of up and down quarks, *uud* and *udd*, respectively. These are the *fermions*. They can be grouped into three generations as shown in Fig. 1.2. The Generation I consists of the lightest and the stable particles. Generation II and Generation III consist of the heavier and short-lived particles.

Four fundamental forces govern the interactions between the particles. These

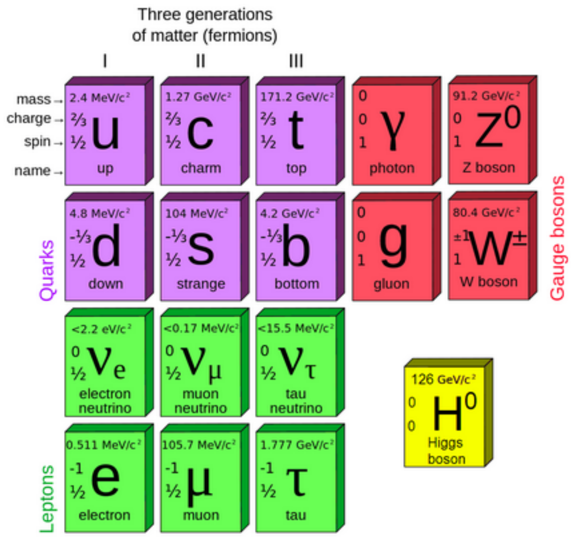

Figure 1.2: The elementary particles within the Standard Model

are the strong force, the electromagnetic force, the weak force and the gravitational force. Particles acting as the carriers of three of the fundamental forces are called *bosons*. The strong force, the electromagnetic force and the weak force are carried by the mediators called the *gluons*, *photons*, and, *W and Z bosons*, respectively. The carriers are shown in Fig. 1.3.

The Higgs boson has been discovered by the ATLAS and CMS experiments at the largest accelerator in the world, i.e, the Large Hadron Collider (LHC) [3, 4] in CERN, Geneva in 2012. The source of the mass of the other particles are expected to be explained by the Higgs mechanism that gives the masses to the particles by breaking the electroweak symmetry, without any explicit mass-term introduced into the Lagrangian. However, the understanding of how the Higgs decays etc., are still ongoing.

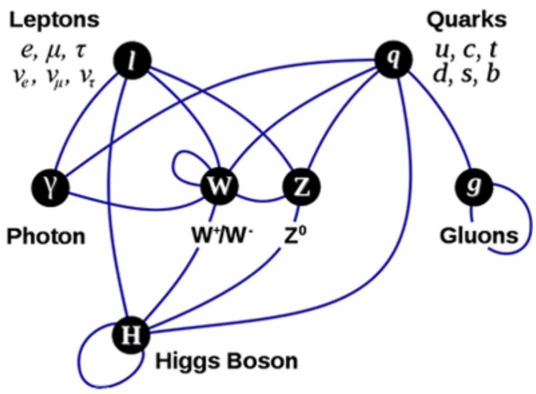

Figure 1.3: Interactions between the fundamental particles through the carriers of the fundamental forces

1.2 QCD : The Theory of the Strong Interactions

In 1972, Gell-Mann introduced Quantum Chromodynamics (QCD), the theory of the strong interactions between the quarks and the gluons [5]. QCD and the electroweak theory are the important parts of the Standard Model. QCD is basically a renormalizable non-abelian gauge theory based on the symmetry group $SU(3)_{\text{color}}$. A new quantum number, called the *color quantum number*, is introduced in QCD. There are three different color charges red, green and blue, whereas one electric charge is observed in Quantum Electrodynamics (QED). Gluon self-interactions are required in QCD, unlike QED. Eight different colors of gluons are there in QCD. The color of the quarks can be changed by the gluon exchange, but the flavors (u,d,s,c,t,b, etc) of the quarks are not changed.

The two most important properties of QCD are the *asymptotic freedom* and the *confinement*. The asymptotic freedom was discovered in 1973 by Gross, Politzer and Wilczek [6]. Nobel prize was awarded to them in 2004 for this work. The static

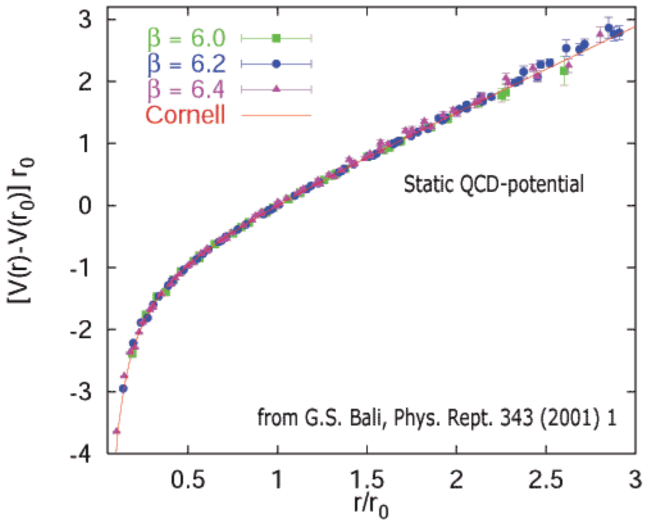

Figure 1.4: The qq-potential calculated from lattice QCD with $r_0 = 0.5\ fm$ and $V(r_0) = 0$.

QCD potential is described as,

$$V_{\rm s} = -\frac{4}{3} \times \frac{\alpha_{\rm s}}{r} + k \times r, \tag{1.1}$$

where, $\alpha_{\rm s}$ is the strong coupling constant. Here, the first term is important in small distances. As the distance between the quarks decrease, the quark-quark potential decreases as shown in Fig. 1.4 [7]. QCD generates a negative β-function, which explains the SLAC data [6]. The running coupling strength [8] has been defined as,

$$\alpha_{\rm s}(Q^2) = \frac{12\pi}{(33 - 2N_{\rm f})log(Q^2/\Lambda_{\rm QCD})}. \tag{1.2}$$

where, Q^2 is the momentum transfer scale and $\Lambda_{\rm QCD}$ is called the QCD scale$\sim$200 MeV, $N_{\rm f}$ is the number of quark flavors. The values of $\alpha_{\rm s}$ as a function of energy scale for different experiments and theoretical calculations from the reference [9]

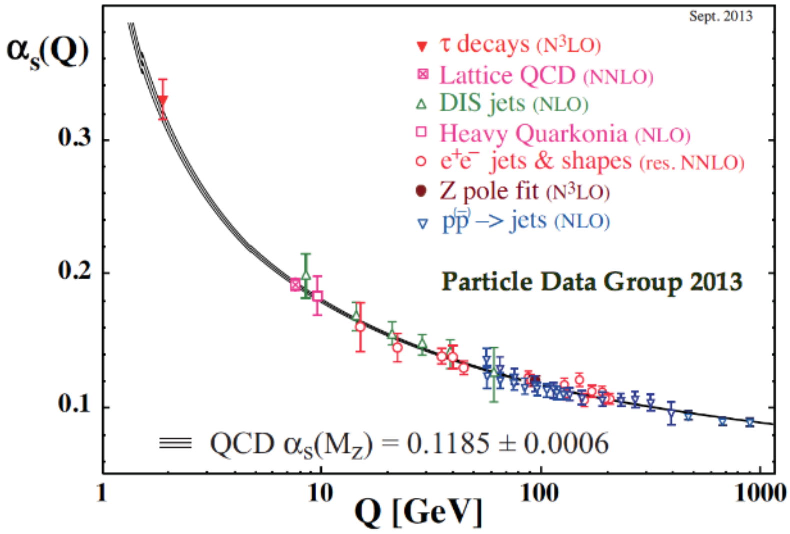

Figure 1.5: α_s as a function of energy scale for different experiments and theoretical calculations.

have been presented in Fig. 1.5. For large values of Q, we have very small values of α_s. Therefore, with the increase in the momentum transfer, the coupling between the quarks and gluons decreases, which is the *asymptotic freedom*. The behavior of the quarks has been described in the bag model of quarks. In this model, the quarks are confined in an elastic bag, which allows quarks to move freely around within the bag. The colour force has almost no effect at short distances. Thus, inside the hadrons, the quarks behave like free particles. [10].

From the Fig. 1.4, it is also evident that with increasing distance, the qq-potential increases. As a result, to isolate the quarks, an infinite energy is required. The colour force become stronger with increasing distance at a rate of 1GeV per fm. According to bag model, if two quarks are pulled apart, at some point, the connecting colour field breaks and q-$\bar{q}$ pair is produced [10]. Thus, quarks can not be observed as free particles, rather they are confined within the hadrons. This is called the *confinement*.

For the study of QCD, different approaches are adapted. *Perturbative QCD* allows to use the perturbation theory accurately and this is based on the asymptotic freedom. In very short distance or for large momentum transfer, this approach gives reliable results. For large $\alpha_{\rm s}$, perturbation theory can not work. *Lattice QCD* is the most widely used non-perturbative approach, which uses lattice (discrete set of space-time points) to help reducing the path integrals of the continuum theory (difficult to deal with) to numerical computations (computable with the help of the supercomputers). Effective theories are also used to describe certain aspects of QCD.

1.3 The Big Bang and Early Universe

According to Georges Lemaitres the Big Bang theory of the universe, proposed in 1927, the universe was created in a huge explosion, the Big Bang, approximately 13.7 billion years ago. Thus, the universe expanded explosively from an extremely dense and hot state, and continues to expand today [11]. According to General relativity, a gravitational singularity existed at the beginning of time. In the Planck epoch, (from zero to $\sim 10^{-43}$ seconds, i.e, the earliest stage after the Big Bang), the universe was very tiny ($\sim 10^{-35}$ m), the energy density and temperature was very very high ($\rho \sim$ 1094 g/cm^3, T$\sim 10^{32}$ K) and the known physics laws can not be applied at this condition. The four fundamental forces, discussed in the previous section, were unified at this time, according to the Grand Unification Theory.

Within a very short time after the creation of the Universe, the temperature started dropping fast. First, it was the separation of gravitational force (during the

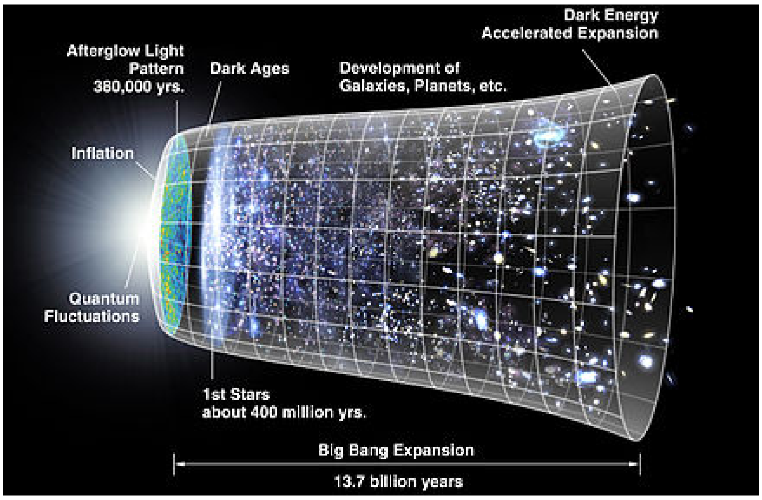

Figure 1.6: The Big Bang and the creation of the Universe [12]

Grand Unification Epoch) and the earliest elementary particles are created [10, 13]. The strong force decoupled next (during the Inflationary Epoch, when the cosmic inflation happens), then the electromagnetic and finally the weak force got separated at about 10^{-11} seconds after the Big Bang. After these short time sequences, the Universe was still too hot to allow quarks to bind together to form composite particles (hadrons). This stage, called the Quark Epoch began $\sim 10^{-12}$ seconds after the Big Bang. During this time (10^{-12} to 10^{-6} seconds), the Universe was filled with dense, hot quark-gluon plasma (described in the next section), containing quarks and gluons within it. Collisions between particles were too energetic to allow quarks to combine into mesons or baryons. The Quark Epoch ended when the Universe was about 10^{-6} second old. At this time, the average energy of particle interactions had fallen below the binding energy of hadrons. The period following this, when the quarks became confined within hadrons, is known as the Hadron Epoch. At this time, the protons and the neutrons were formed. This is beautifully described in the Ref. [10]. Then, the nuclei formed gradually, at the time of tens of minutes. Star and Galaxy formation happened later, 300 to 500 million years after the Big Bang (The time of the Galaxy formation is known from the Cosmic Microwave Background Radiation (CMBR) experiments [10]). Solar system forms after 8.5 to 9 billion years [13] after the Big Bang. According to the astronomical predictions, only 4% of the whole universe is visible. About 26% is made with the unknown dark matter [11].

1.4 QCD Phase diagram

At the time of Quark epoch, the matter existed in very high temperature and density, consisting of asymptotically free quarks and gluons. This state is known as the Quark-Gluon Plasma [14]. Thermodynamics can be used to describe the system as the system achieves thermodynamic equilibrium after the thermalization process. Here, the partonic degrees of freedom describes the system.

The QCD phase diagram (shown in Fig. 1.7) describes the transition from hadronic state to QGP state and vice versa, where the diagram presents the dependence between the net baryon number density μ_{B} in the x-axis (representing the energy needed for the addition or removal of a baryon to or from the system) to the temperature T in the y-axis (in MeV, where 1eV$\simeq$11605K) [10]. The early universe is represented by zero μ_{B} and at very high T, gradually expands and cools down. The boundary between the QGP and hadronic phase is represented by the QCD-critical point. At larger μ_{B} and lower T than the critical point, first order phase transition (i.e, finite discontinuity in the first derivative of thermodymaic potential (internal energy, entropy etc.) in the infinite volume limit) has been predicted by the lattice QCD calculations [15]. Therefore, the end-point of the first order phase transition is the critical point (T_c) [16]. T_c from hadronic to QGP phase is predicted to be ∼170-190 MeV [17]. At lower μ_B and larger T than the expected critical

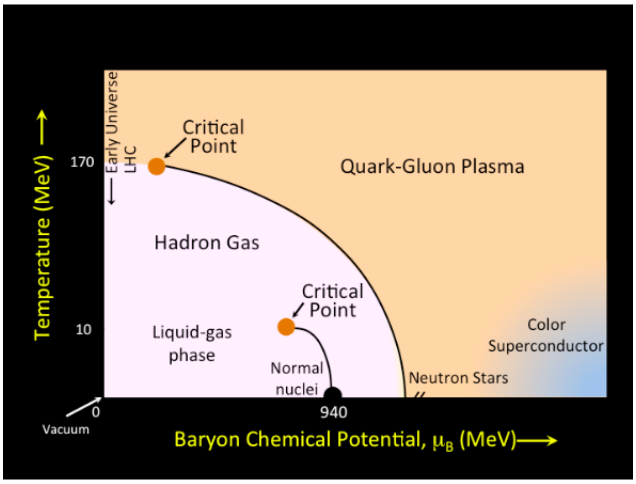

Figure 1.7: Schematic phase diagram of strongly interacting matter [10]

point, a smooth crossover (with no discontinuous change in the energy-density) from hadronic to QGP phase is expected. In terms of chirality, QGP phase is a chiral symmetric phase, where the chiral condensate $\langle q\bar{q}\rangle \neq 0$. In hadronic phase, the chiral symmetry is broken and $\langle q\bar{q}\rangle = 0$.

At low T and extreme high density, the matters expected are similar to what may exist in neutron starts. At larger densities and lower temperatures, existence of color superconductirs, Color Flavour locked (CFL) phases are predicted.

1.5 Relativistic Collisions

It is possible to create the state of Quark Gluon Plasma in the laboratory by colliding nuclei at ultra-relativistic energies. The aim is to achieve very high temperature and energy-density.

1.5.1 Space-time evolution and Bjorken Prediction

The space-time evolution of the hadronic matter produced in the central rapidity region in extreme relativistic nucleus-nucleus collisions was first described by Bjorken in 1983 [18]. According to Bjorken prediction, the initial energy-density and the rapidity density of the produced particles are connected.

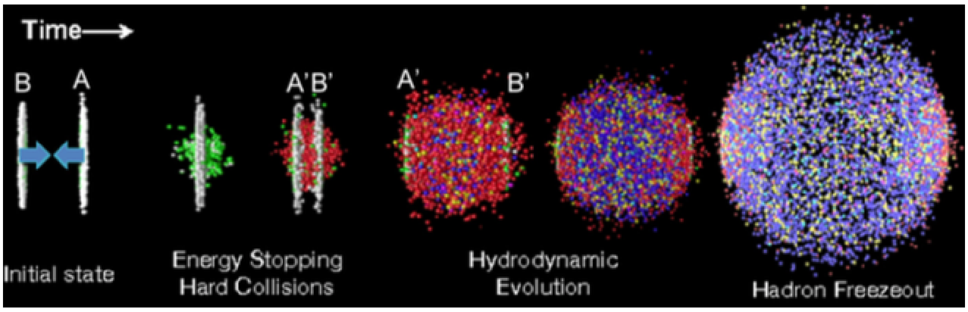

Figure 1.8: Relativistic heavy ion collisions

In this context, head-on collision of two equal Lorentz contracted nuclei coming with the speed of light along the z-axis, is considered. They collide at $(z, t) = (0, 0)$. The projectile and target nucleus B and A are denoted as B' and A' after the collision in Fig. 1.8. The baryons collide at very high energies and move away from the collision zone, with a deposition of the energy lost by the baryons in the collision region. Thus, a large amount of energy is deposited within a short duration of time in a very region of space, having very high energy-density and small net baryon content in the collision region.

In the central rapidity region, because of this very high energy-density, a system of QGP may be formed. The initial energy-density predicted by Bjorken may be

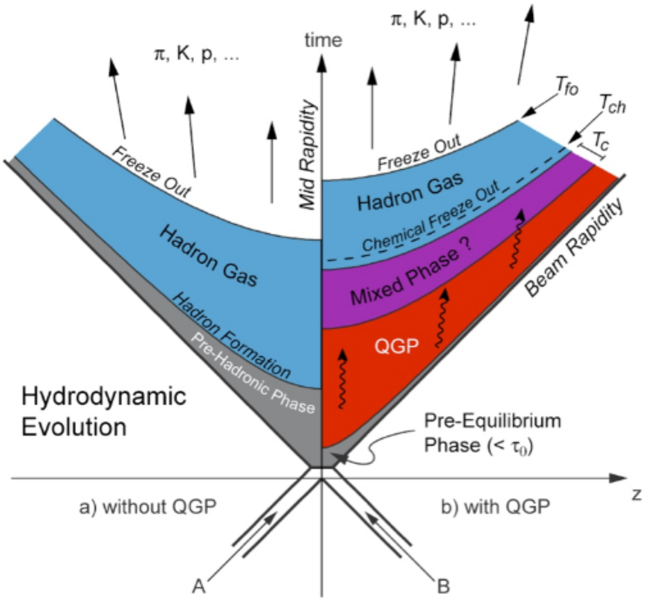

Figure 1.9: Space-time evolution in the nucleus-nucleus collisions.

expressed as,

$$\epsilon_0 = \frac{\langle m_{\mathrm{T}} \rangle}{\tau_0 A} \frac{dN}{dy}|_{y=0}, \tag{1.3}$$

where, according to Bjorken estimation, the proper time $\tau_0 = 1$ fm/c, y represents the rapidity, $\langle m_{\mathrm{T}} \rangle$ represents the mean transverse mass of the particle, and A represents the transverse overlap area.

Laws of hydrodynamics can be applied to this system after it achieves local thermal equilibrium at proper time τ_0 by means of subsequent equilibration of the plasma created initially. With the expansion of the plasma, it cools down and gradually hadronizes at a later proper time. These hadrons stream out of the collision region as the temperature drops down below the chemical freeze-out temperature, as shown in Fig. 1.9, where all the inelastic scatterings between the hadrons cease to occur. At a later time, with the mean free path of the hadrons exceeding the size of the system created, the elastic scatterings also stop, thus kinetic freeze-out occurs and after this, free streaming of the hadrons is possible, which then are detected by the detectors in the laboratory.

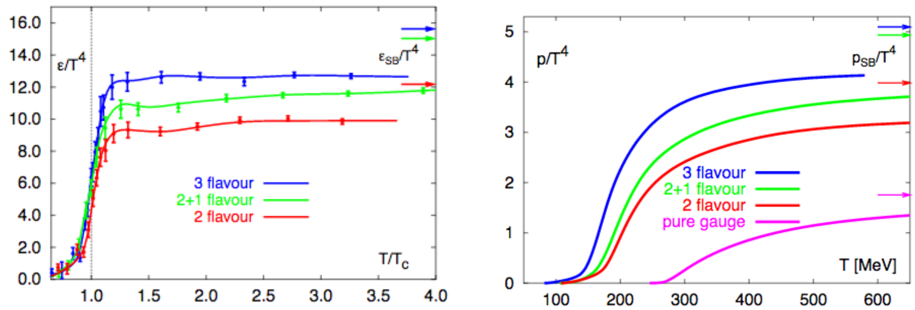

Figure 1.10: Left panel : The energy-density in QCD with different number of degrees of freedom as a function of temperature. Right panel : The pressure in QCD with different number of degrees of freedom as a function of temperature. [19]

One interesting thing should be mentioned about the created QGP state. In this state, the degrees of freedom increases as a result of the strong increase in pressure and the energy density. In addition to the isospin degrees of freedom (plays important role in hadrons), the color and flavor degrees of freedom dominate in the QGP state. With the help of the simulation in lattice QCD, the sudden increase of pressure and the energy density of QCD matter at certain temperature has been observed, as presented in Fig. 1.10. T_c is predicted to be 173 ± 15 MeV, and ϵ_c is around 0.7 GeV/fm^3 [19].

1.5.2 Experimental programs

In the year 1974, Prof. T.D. Lee (received Nobel Prize in Physics in 1957) had predicted that it might be possible to create QGP like conditions in the laboratory by distributing very high energy, thus liberating quarks for a short time, over a relatively large volume [10]. Then, the search for QGP (exists for a very short time) started with the collision of two nuclei at ultra-relativistic energies.

Over last three decades, probing the hot and dense matter produced in high-energy heavy-ion collisions is one of the major tasks of the nuclear and high-energy physics experiments. The quest started with the first experiment at Bevalac in Lawrence Berkeley Laboratory, where Au beam at 1 GeV/nucleon was bombarded on fixed Au target. The early success of the experiments in terms of bringing out the collective nature of the produced matter prompted the scientists at Brookhaven National Laboratory (BNL) and CERN to make concrete programs for the future accelerator developments for heavy ions. After this, the experiments with Au beam at 11.7 GeV/nucleon at BNL and Pb beam at 158 GeV/nucleon at CERN Super Proton Synchotron (SPS) took place [10].

From 2000, a detailed study on the phase diagram with a beam energy scan program was performed in Relativistic Heavy Ion Collider (RHIC) at BNL. In RHIC, (including four experiments) pp, d-Au and heavy ion collisions at energies $\sqrt{s}$ = 7.7 to 200 GeV help to make a deeper understanding of the nature of the QCD matter at high temperature and energy densities.

Later, from 2009, the Large Hadron Collider (LHC) experiment (consisting of ALICE, ATLAS, CMS and LHCb experiments) in CERN, Geneva, having a very strong program for QGP studies, collides pp, p-Pb and Pb-Pb at much higher energies. For heavy ions and for p-Pb collisions, energies of 2.76 TeV/nucleon and 5.02 TeV/nucleon have been achieved, respectively. Recently, in 2015, $\sqrt{s} = 13$ TeV is achievable for pp collisions. These are the highest colliding energies possible to reach through the relativistic high energy collisions in laboratory till now.

First hints of the formation of the new QGP state of matter were obtained from the CERN data by combining results from three experiments, in the year 2000. Strong evidence for the production of extreme hot and dense matter had been reported by RHIC experiments in the year 2005. The results from the data collected by ALICE already indicate that the matter created at LHC is an ideal fluid which is extremely dense and hot and the quarks and gluons are not confined within this fluid [10].

1.6 Signatures of QGP

In the nucleus-nucleus collisions at ultra-relativistic energies, the QGP phase exists for very short time, followed by the hadronization of the QGP system. However, as the energy of the collision increases, the initial energy densities, system size etc. increase, as well as the lifetime becomes longer. Occurance of the QGP phase is expected in RHIC and LHC energies. The initial energy density found at LHC energies is about 15 GeV/fm^3, which is almost 3 times higher than that found in RHIC energies [20].

In this section, the proposed signatures of the QGP phase have been briefly discussed.

1.6.1 High p_{T} Suppression

In heavy ion collisions, the hard scattered partons move through a dense and hot medium resulting in a large energy loss in the medium. This basically distorts the back-to-back jets, which are expected in pp collisions, where the partons are fragmented into hadrons in vacuum. Thus, the particle production is suppressed in high p_{T} in heavy ion collisions compared to pp collisions, and the dijet asymmetry provides the signature of QGP. This effect is called **jet quenching** and the effect is quantified by **nuclear modification factor** (R_{AA}), defined as the heavy ion yields compared to that of pp collisions, scaled by the number of binary collisions, i.e,

$$R_{\mathrm{AA}} = \frac{d^2N^{\mathrm{AA}}/dp_{\mathrm{T}}dy_{\mathrm{AA}}}{\langle N_{\mathrm{coll}}\rangle d^2N_{\mathrm{pp}}/dp_{\mathrm{T}}dy_{\mathrm{pp}}} \tag{1.4}$$

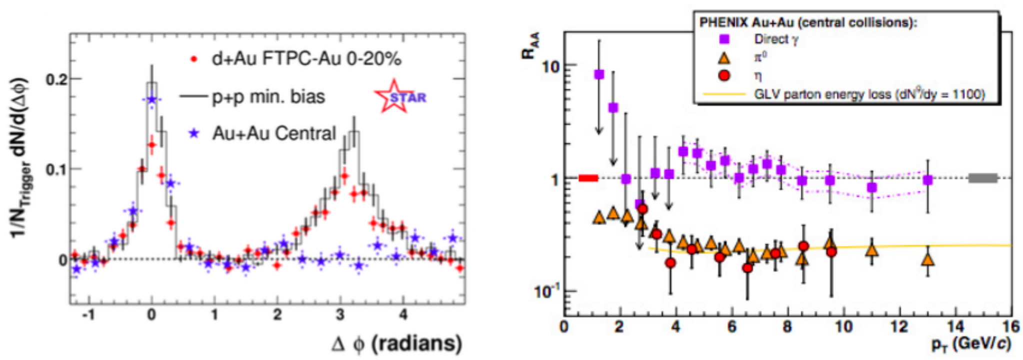

Figure 1.11: Left : Comparison of the hadron yield at $\phi = \pi$ for pp, central d-Au and central Au-Au collisions, while triggering on a jet at $\phi = 0$ [21]. Right : Suppression of π^0,η particles compared to direct photon [22].

The study of jets in pp, d-Au and Au-Au collisions from STAR experiment have been presented in the left panel of Fig. 1.11. The suppression of hadrons in Au-Au collisions is more than pp and d-Au collisions. From the right panel of Fig. 1.11, the result of R_{AA} from PHENIX experiment shows that the strongly interacting particles are suppressed more compared to the direct photons, which interact through the electromagnetic interaction.

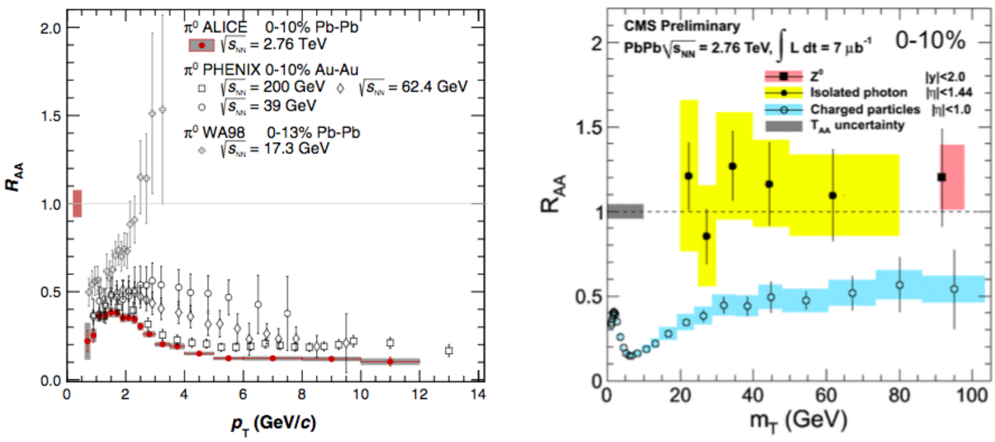

Figure 1.12: Left : Neutral-pion production at midrapidity from WA98 to ALICE. Right : R_{AA} from charged particles, photons and Z_0 from CMS.

The result for the invariant yields of neutral pions at midrapidity for $0.6 < p_{\mathrm{T}} < 12$ GeV/c for Pb-Pb collisions at $\sqrt{s_{\mathrm{NN}}} = 2.76$ TeV in ALICE have been shown in the left panel of Fig. 1.12. R_{AA} is suppressed by a factor of 8 to 10 for $5 < p_{\mathrm{T}} < 7$ GeV/c [23]. The results from PHENIX and WA98 have been also shown. Due to the harder initial parton p_{T}-spectra, R_{AA} is less for LHC for $p_{\mathrm{T}} > 2$ GeV/c. In the right panel of Fig. 1.12, the results from CMS have been shown [24]. No suppression is observed in R_{AA} of direct photons. As expected, the suppression of the light hadrons have been observed, which indicates the presence of a strongly interacting medium.

1.6.2 J/Ψ suppression

Another signature of QGP is the suppression of J/Ψ-particles (bound state of charm quark (c) and charm antiquark ($\bar{c}$)) in heavy ion collisions compared to proton-proton collisions [25, 26].

J/Ψ-particles are produced by hard scattering processes in the initial stage of collisions. In the presence of QGP, a kind of screening, called Debye Screening has been observed, which basically screens the color charge of a quark, modifying the long-range Coulomb type interaction between c and $\bar{c}$, to short-range Yukawa type interaction within the Debye screening length. This length becomes very small at very high energies, leading to the dissociation of $c\bar{c}$ into c,$\bar{c}$ and hadronizes as D-mesons ($c\bar{u}$,$c\bar{d}$), etc.

In the QGP, deconfinement between quarks and gluons occur. The string tension between $c\bar{c}$ vanishes. Thus, J/Ψ-particle production is suppressed in QGP. A part of suppression also arises because of the interaction of the produced J/Ψ with hadrons and breaking up of J/Ψ.

J/Ψ suppression has been observed with the results from PHENIX experiment earlier for rapidities $-2.2 < y < 2.2$ in Au-Au collisions at $\sqrt{s_{\mathrm{NN}}} = 200$ GeV [27]. The prediction from the models describing the CERN SPS data was contradicted by the results from PHENIX.

In ALICE experiment, the measurement of inclusive J/Ψ production in the rapidity $2.5 < y < 4$ for Pb-Pb collisions at $\sqrt{s_{\mathrm{NN}}} = 2.76$ TeV, down to zero transverse momentum shows a suppression of J/Ψ yield compared to that in pp collisions scaled by the number of binary nucleon-nucleon collisions. Models including J/Ψ production from charm quarks in a deconfined QGP phase can describe the data [28]. The

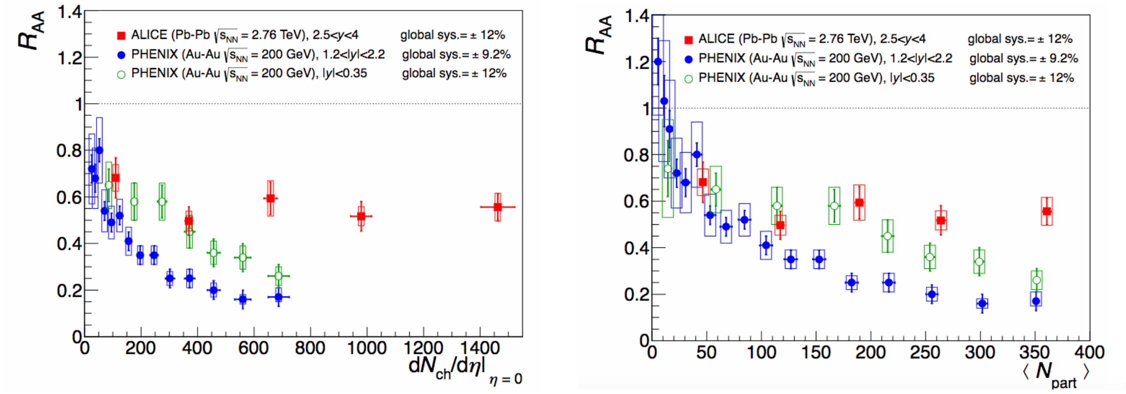

Figure 1.13: Left : J/Ψ $R_{\rm AA}$ as a fuction of midrapidity charged particle density for Pb-Pb collisions at $\sqrt{s_{\rm NN}} = 2.76$ TeV [28]. Right : Same, as a fuction of $\langle N_{\rm part}\rangle$ [28]. Results are compared with that of PHENIX.

results are shown in Fig. 1.13. The charged particle density is related to the energy density of the medium and $\langle N_{\rm part}\rangle$ is related to the collision geometry. Results show J/Ψ suppression, with no significant centrality dependence.

In ALICE, J/Ψ suppression has been also observed in p-Pb collisions at $\sqrt{s_{\rm NN}} = 5.02$ TeV for the rapidity range $2.03 < y_{\rm cms} < 3.53$ in $\mu^+\mu^-$ decay channel [29].

1.6.3 Identified hadron spectra

The main aim to study the identified primary hadron spectra is to know about the properties of the medium at chemical and kinetic freeze-out temperatures. The results from ALICE experiment have been shown in Fig. 1.14. ALICE spectra are harder than RHIC ones and protons are flatter probably due to stronger radial flow [30]. To determine integrated yields and average transverse momentum, fits on individual particles with a blast-wave function have been performed. Results for K^-/π^- (left) and $\bar{p}/\pi^-$ (right) ratios as a function of $\frac{dN_{\rm ch}}{d\eta}$ have been presented in Fig. 1.15. K^-/π^- ratios increase with centrality as well as from pp to Pb-Pb,

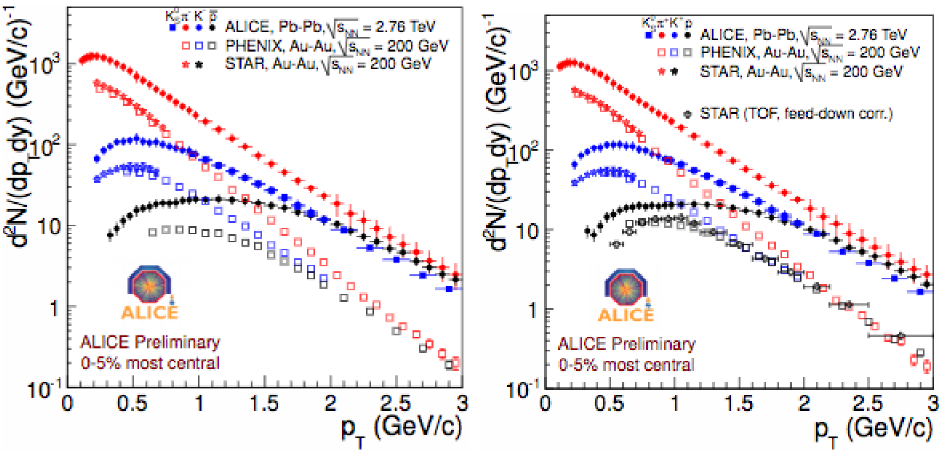

Figure 1.14: Transverse momentum spectra for π, K, p negative (left) and positive (right) in the most central bin. A comparison between results obtained by ALICE, STAR and PHENIX collaborations is shown [30].

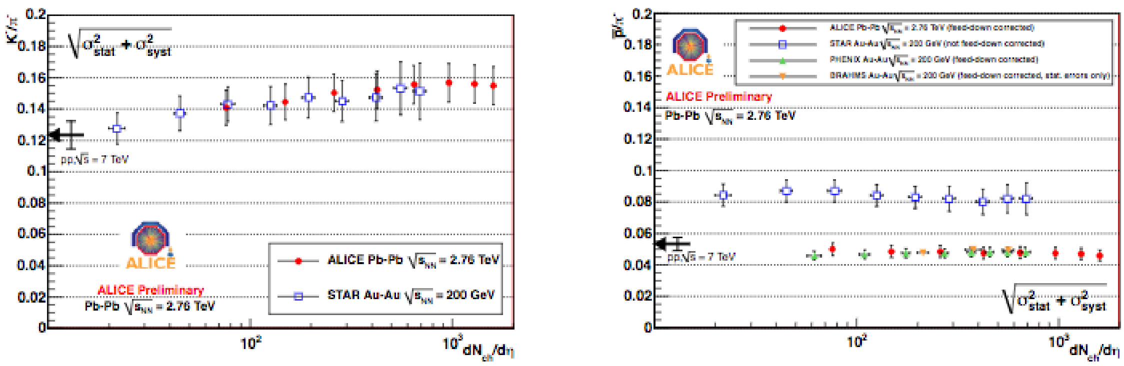

Figure 1.15: K^-/π^- (left) and $\bar{p}/\pi^-$ (right) ratios as a function of $\frac{dN_{\rm ch}}{d\eta}$ [31].

whereas $\bar{p}/\pi^-$ have been found to be almost constant. Results are compatible except STAR, probably due to $\bar{p}$, not being feed-down corrected. At same value of $\frac{dN_{\rm ch}}{d\eta}$, mean transverse momentum is observed to be higher in ALICE than STAR [31].

In order to obtain information on the thermal properties of the medium at the kinetic freeze-out, a global fit of the spectra with a blast-wave function in which the kinetic freezeout temperature ($T_{\rm fo}$) and the radial flow ($\langle\beta\rangle$) are free parameters, is used. In Fig. 1.16, the fit parameters for ALICE and STAR in different centrality

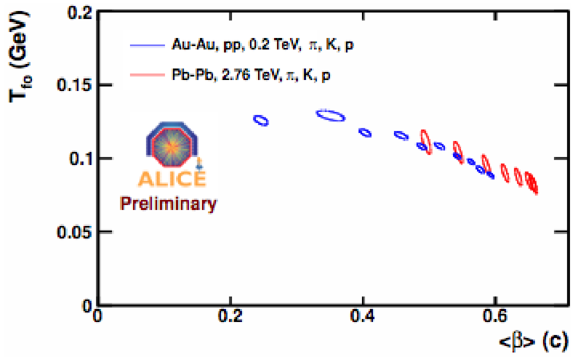

Figure 1.16: Kinetic freezeout temperature and radial flow parameter as obtained from a global fit of the spectra with a blast-wave function for increasing centrality [30].

bins are shown. It can be noticed that the radial flow is $\sim 10\%$ higher in ALICE than STAR [30].

1.6.4 Strangeness Enhancement

The enhancement of the strange particles in the QGP was predicted to be another signature of the presence of QGP [32]. The energy required for the production of strange quark in QGP is less. In QGP, sufficient amount of gluons (that can produce $s\bar{s}$) are present. In comparison to hadron gas, strangeness in QGP is expected to equilibrate faster because of the lower mass of the strangeness carriers in QGP [33]. This phenomena has been observed in many experiments till now [34]. The results from ALICE experiment have been already shown in Fig. 1.15. The ratio of p/π of pp to Pb-Pb collisions is almost unity, whereas the K/π ratio has been found to increase with $\frac{dN_{\rm ch}}{d\eta}$.

Recent result from ALICE experiment has shown that the hyperon-to-pion ratio increases from pp to A-A, showing strangeness enhancement [35].

1.6.5 Flow

The collective evolution of the system formed in high energy heavy ion collisions is observed as a pattern, correlating the momenta of the final state particles. This is the anisotropic flow which arises due to the initial asymmetry of the collision. In

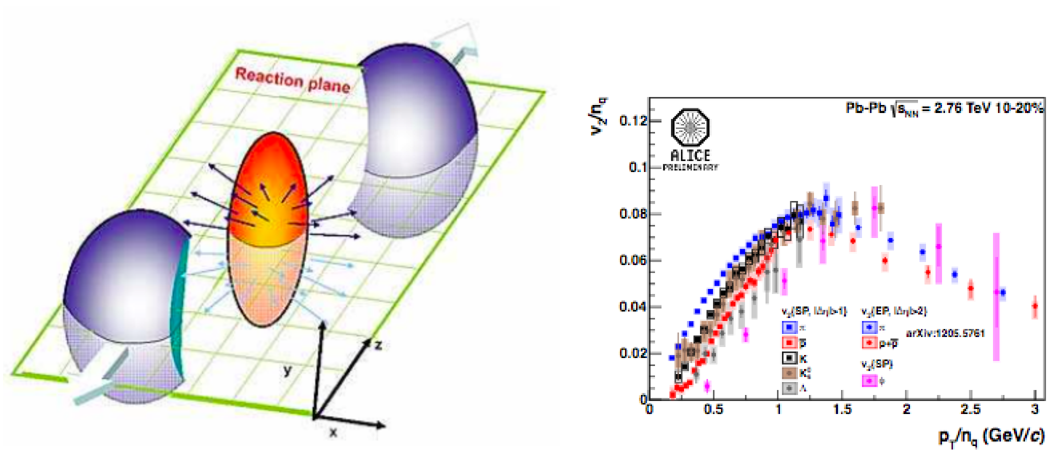

Figure 1.17: Left panel : The reaction plane. Right panel : Identified particle elliptic flow scaled with the number of constituent quarks.

a non central heavy ion collision, the reaction plane is defined as the plane formed with the impact parameter b together with the z axis (the beam-line), as shown in

Fig. 1.17 (left panel). the reaction plane is spatially asymmetric. The initial spatial asymmetry is transferred into momentum anisotropy by the pressure gradient, and the anisotropic momentum distribution of the produced particles represents the collective behaviour of the system. The azimuthal anisotropy may be characterized by the decomposition into Fourier components [36] as,

$$E\frac{d^3N}{dp^3} = \frac{d^2N}{2\pi p_{\mathrm{T}} dp_{\mathrm{T}} dy}(1 + \sum_{n=1}^{\infty} 2v_{\mathrm{n}} cos(n(\phi - \psi_{\mathrm{R}}))), \tag{1.5}$$

where, ϕ and ψ_{R} represent the azimuthal angle and the reaction plane angle, respectively. The first and second Fourier components, i.e, v_1 and v_2 are the directed and transverse elliptic flow, respectively.

The dependence of the elliptic flow on the transverse momentum of charged and identified particles in Pb-Pb collisions at $\sqrt{s}_{\mathrm{NN}} = 2.76$ TeV has been presented in Fig. 1.17 (right panel) [36]. The size indicates collective behaviour. The results are in good agreement with the hydrodynamical calculations, including viscous corrections. In the Fig., p_{T} and v_2 are scaled by the number of constituent quarks. Compared to RHIC (Au-Au collisions at $\sqrt{s}_{NN} = 200$ GeV), the elliptic flow increases by about 30% [37]. The triangular flow can be described in terms of the initial spatial anisotropy and its fluctuations, which provides strong constraints on its origin. In the most central events, where the elliptic flow v_2 and v_3 have similar magnitude, a double peaked structure in the two-particle azimuthal correlations is observed, which is often interpreted as a Mach cone response to fast partons. This structure can be naturally explained from the measured anisotropic flow Fourier coefficients [38].

1.7 Fluctuation measures

Fluctuations in several observables are very important to measure to characterize the properties of the bulk description of the system. The study of fluctuations may reveal information even beyond the thermodynamic properties of a system, i.e, the fluctuations in the cosmic microwave background radiation, as first observed by COBE.

In the event-by-event fluctuation studies, an observable is measured on an event-by-event basis and the fluctuations are studied over the ensemble of the events [39]. An observable may be conserved in a global basis, but it will have fluctuations when studied on event-by-event basis, thus describing the properties of the system minutely. Some observables may vary dramatically from event to event, especially, near the critical point. Thus, It is possible to study the QGP phase transition and nature of the QGP matter. The event-by-event fluctuation studies provide informations on the dynamics of the system as well as address to the information on the correlations in different collision systems. In high energy heavy ion collisions, such as, in STAR and LHC experiments, etc., the production of the large number of particles in each event make the event-by-event fluctuation studies possible with accuracy.

The event-by-event fluctuation studies in ALICE experiment include studies on the net charge fluctuations, balance functions, mean p_{T} fluctuations, multiplicity fluctuations, long range correlations, particle ratio fluctuations, temperature fluctuations, etc. In this section, the recent results from the event-by-event fluctuation studies have been briefly discussed.

1.7.1 Net Charge Fluctuations

The fluctuations of conserved quantities in a finite phase space window, like the net charge of the system, are predicted to be one of the most sensitive signals of the QGP formation and phase transition. This may provide a complementary understanding of strong interactions [40]. The net-charge fluctuations are strongly dependent on which phase they originate from. The fluctuations in the net charge depend on the squares of the charge states. In QGP phase, $q = \pm\frac{1}{3}; \frac{2}{3}$ $(quarks)$, 0 $(gluons)$, whereas in hadron gas, $q = \pm 1$. The net-charge fluctuations in the QGP phase are significantly smaller compared to that of a hadron gas [41]. The net charge fluctuations are affected by the strong gluon domination in the QGP phase and the uncertainties from the volume fluctuations.

The net charge fluctuation is related to the D measure via the relation [39, 40, 41],

$$D \approx 4\frac{\langle \delta Q^2 \rangle}{\langle N_{\rm ch} \rangle} \approx \langle N_{\rm ch} \rangle \nu_{(+-,{\rm dyn})} + 4, \tag{1.6}$$

where, $\langle \delta Q^2 \rangle$ is the variance of the net charge $Q = N_+ - N_-$ and $N_{\rm ch} = N_+ + N_-$. This provides charge fluctuations per unit entropy. Lattice calculations including q-q interactions, D is predicted to be around 4 for uncorrelated pion gas, around 3 in HRG and much smaller, i.e, around 1 to 1.5 for a QGP. Net charge fluctuations in experiments are best studied by the observable $\nu_{(+-,{\rm dyn})}$, which is defined as [40, 42],

$$\nu_{(+-,{\rm dyn})} = \frac{\langle N_+(N_+ - 1) \rangle}{\langle N_+ \rangle^2} + \frac{\langle N_-(N_- - 1) \rangle}{\langle N_- \rangle^2} - 2\frac{\langle N_- N_+ \rangle}{\langle N_- \rangle \langle N_+ \rangle} \tag{1.7}$$

This gives the relative correlation strength of particle pairs.

In ALICE, data has been analyzed for pp as well as Pb-Pb collisions at $\sqrt{s_{\mathrm{NN}}} = 2.76$ TeV. $\nu_{(+-,\mathrm{dyn})}$ has been evaluated by counting positive and negative charged particles within $-0.5 \leq \eta \leq 0.5$ and $0.2 < p_{\mathrm{T}} \leq 5.0$ GeV/c [40]. $\nu_{(+-,\mathrm{dyn})}$ as a fucntion of the number of participants shows a saturation pattern having negative values, which indicates the domination of correlation term in Eq. 1.7. $\nu_{(+-,\mathrm{dyn})}$ has been corrected for global charge conservation and finite acceptance.

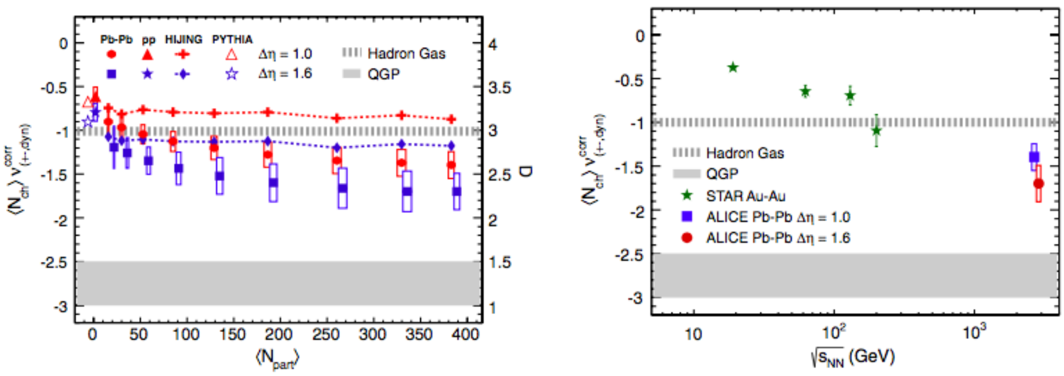

Figure 1.18: Left : $\langle N_{\mathrm{ch}} \rangle \nu^{\mathrm{corr}}_{(+-,\mathrm{dyn})}$ (left axis) and D (right axis) as a function of $\langle N_{\mathrm{part}} \rangle$ [40]. Right : Energy dependence of the net charge fluctuations, measured in terms of $\langle N_{\mathrm{ch}} \rangle \nu^{\mathrm{corr}}_{(+-,\mathrm{dyn})}$ (left axis) and D (right axis) for the top central collisions [40].

From Fig. 1.18 (left panel), a decreasing trend of D has been observed with increasing centrality, indicating more correlations between unlike sign pairs. The results are observed to be in between the Hadron Gas (HG) and QGP predictions. HIJING shows almost no centrality dependence, results being close to the HG line. The measured fluctuations may get diluted during the evolution of the system from hadronization to kinetic freeze-out because of the diffusion of charged hadrons in rapidity [40]. Energy dependence of the net charge fluctuations in Fig. 1.18 (right panel) shows a monotonic decrease with increasing beam energy. For lower energies, results are above HG values and for top RHIC energy, the results are close to HG predictions, whereas for ALICE, significantly lower fluctuations have been observed. It may be inferred from the ALICE results that the fluctuations have their origin in the QGP phase [40].

1.7.2 Balance functions

Balance function basically quantifies the degree of the separation of pairs of particles and relates that with the time of hadronization [43]. Early stage creation of $q\bar{q}$-pair leads to larger final separation and wider balance function distributions. Late stage creation results into more correlated pairs and narrower balance function distributions. To understand the mechanism of the charge creation, the correlations between the emitted particles may be used as a probe and the first results of these studies using the electric charge balance function in the relative $\Delta\eta$ and $\Delta\phi$ in Pb-Pb collisions at $\sqrt{s_{\mathrm{NN}}} = 2.76$ TeV in ALICE has been discussed in Ref. [44]. The definition of balance function for the pseudorapidity difference $\Delta\eta$ can be given as [45, 46],

$$B(\Delta\eta) = \frac{1}{2}\left[\frac{N_{+-}(\Delta\eta) - N_{--}(\Delta\eta)}{N_{-}} + \frac{N_{-+}(\Delta\eta) - N_{++}(\Delta\eta)}{N_{+}}\right], \tag{1.8}$$

where, $N_{--}(\Delta\eta)$ represents the number of $--$ particle pairs.

The widths of the balance functions, $\langle\Delta\eta\rangle$ and $\langle\Delta\phi\rangle$, are found to decrease when moving from peripheral to central collisions (shown in Fig. 1.19). Results are presented for $|\eta| < 0.8$ and $0.3 < p_{\mathrm{T}} < 1.5$ GeV/c. The results are consistent with the picture of a system exhibiting larger radial flow in central collisions but also whose charges are created at a later stage of the collision [44]. Models show mild or no centrality dependence. RHIC and LHC has minor differences in the results

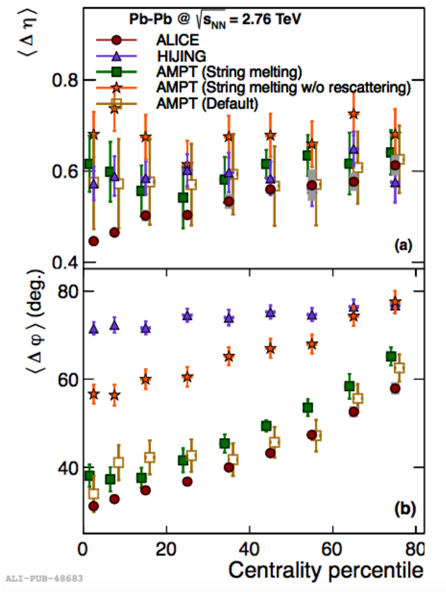

Figure 1.19: The centrality dependence of the width of the balance function $\langle \Delta\eta \rangle$ and $\langle \Delta\phi \rangle$, for the correlations studied in terms of the relative pseudorapidity and the relative azimuthal angle, respectively [44].

for the centrality dependence of the width. Recent results from ALICE have shown that the widths of the balance functions in $\langle \Delta\eta \rangle$ and $\langle \Delta\phi \rangle$ are found to decrease with increasing multiplicity for all systems, i.e, pp, p-Pb and Pb-Pb, only in the low-p_{T} region (for $p_{\mathrm{T}} < 2.0$ GeV/c). For higher values of p_{T}, the multiplicity-class dependence is significantly reduced, and the correlations of balancing partners are stronger with respect to the low transverse momentum region [47].

1.7.3 Mean p_{T} fluctuations

Event-by-event fluctuations of mean transverse momentum ($\langle p_{\mathrm{T}} \rangle$) of final-state charged particles provide information on the dynamics and correlations in heavy ion collisions [48]. Dynamical fluctuations have been observed while studying event-by-event

$\langle p_{\rm T}\rangle$ fluctuations in RHIC [49]. Similar measurement with pp accounts for the contributions of correlations due to resonance decays, jets, quantum correlations, etc. and serves as a baseline measurement.

Event-by-event $\langle p_{\rm T}\rangle$ fluctuations of charged particles in pp collisions at $\sqrt{s} = 0.9, 2.76$ and 7 TeV, and Pb-Pb collisions at $\sqrt{s_{\rm NN}} = 2.76$ TeV in ALICE have been presented in Ref. [50]. The results are presented for $|\eta| < 0.8$ and $0.15 < p_{\rm T} < 2$ GeV/c. For the analysis, two-particle transverse momentum correlator ($C_{\rm m}$) has been used, which is basically a measure of the dynamical component $\sigma^2_{\rm dyn}$ of the fluctuations. $C_{\rm m}$ is defined as [50],

$$C_{\rm m} = \langle \Delta p_{\rm T,i}, \Delta p_{\rm T,j}\rangle = \frac{1}{\sum_{k=1}^{n_{\rm ev}} N_{\rm k}^{\rm pairs}} \sum_{k=1}^{n_{\rm ev}} \sum_{i=1}^{N_{\rm k}} \sum_{j=i+1}^{N_{\rm k}} (p_{\rm T,i} - \langle p_{\rm T}\rangle_{\rm m})(p_{\rm T,j} - \langle p_{\rm T}\rangle_{\rm m}), \quad (1.9)$$

where, $n_{\rm ev}$ is the number of events in multiplicity class m, $N_{\rm k}$ is the accepted charged particles in event k, and $\langle p_{\rm T}\rangle_{\rm m}$ is $\langle p_{\rm T}\rangle$ of all tracks in all events of class m. We have $C_{\rm m} = 0$, for statistical fluctuations. The results are presented in terms of dimensionless ratio $\frac{\sqrt{C_{\rm m}}}{\langle p_{\rm T}\rangle_{\rm m}}$, indicating the strength of the dynamical fluctuations.

Results from the analysis with pp show significant non-statistical fluctuations at low multiplicity, dynamical fluctuation dilution with multiplicity and no significant collision energy dependence [50]. Peripheral Pb-Pb results are in good agreement with the pp baseline, but a reduction of the relative fluctuations has been observed towards the central collisions. From Fig. 1.20, it is evident that the significant dynamical fluctuations decrease with multiplicity for pp as well as Pb-Pb in ALICE and for Au-Au in STAR. The relative fluctuations for both energies are described well by the pp baseline fit from peripheral up to mid-central collisions [50].

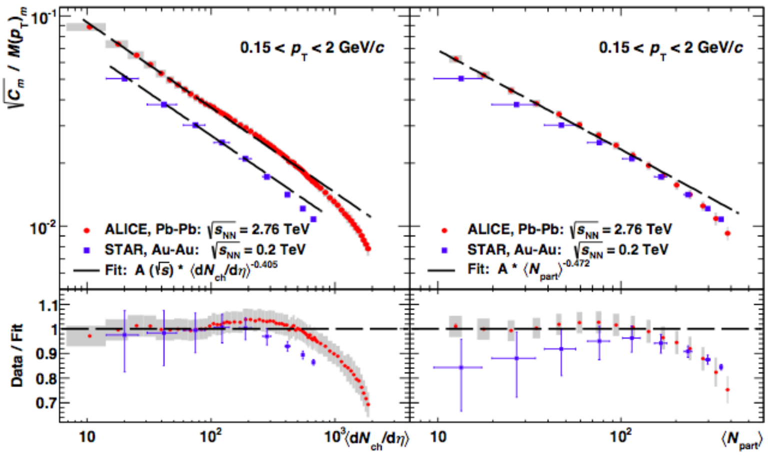

Figure 1.20: Relative dynamical fluctuations as a function of $\langle dN_{\rm ch}/d\eta \rangle$ (left) and $\langle N_{\rm part} \rangle$ (right). ALICE results for Pb-Pb collisions at $\sqrt{s_{\rm NN}} = 2.76$ TeV are compared to STAR results for Au-Au collisions at $\sqrt{s_{\rm NN}} = 200$ GeV. Ratio of data to power-law fits are also shown [50].

1.7.4 Long range correlations

Correlations that are produced across a wide range of rapidity are thought to reflect the earliest stages of the heavy-ion collisions, free from final-state effects. This has been shown using Color Glass Condensate (CGC) framework in Ref. [51]. The study of correlations among particles produced in different rapidity regions may provide an understanding of the elementary (partonic) interactions which lead to hadronization [52]. For heavy-ion collisions, it has been predicted that multiple parton interactions would produce long-range forward-backward multiplicity correlations that extend beyond one unit in rapidity, compared to hadron-hadron scattering at the same energy.

Forward-backward correlations are characterized by the correlation strength $b_{\rm corr}$, which is defined as,

$$b_{\mathrm{corr}} = \frac{\langle N_{\mathrm{f}} N_{\mathrm{b}} \rangle - \langle N_{\mathrm{f}} \rangle \langle N_{\mathrm{b}} \rangle}{\langle N_{\mathrm{f}}^2 \rangle - \langle N_{\mathrm{f}} \rangle^2} = \frac{D_{\mathrm{bf}}^2}{D_{\mathrm{ff}}^2}, \tag{1.10}$$

where, N_f and N_{b} are the multiplicities in the forward and backward rapidity hemisphere, respectively. D_{ff}^2 and D_{bf}^2 are the forward-forward and backward-forward dispersions.

Long range correlations were previously studied by the STAR experiment [53]. Recently, FB correlations have been studied extensively with different model simulations, such as, CGC model and the color string percolation model (CSPM). The FB correlation results in pp collisions at $\sqrt{s} = 0.9, 2.76$ and 7 TeV, from the ALICE experiment has been presented in Ref. [54]. Measurements are performed in $|\eta| < 0.8$ and $p_{\mathrm{T}} > 0.3$ GeV/c. A sizable increase of the correlation strength with

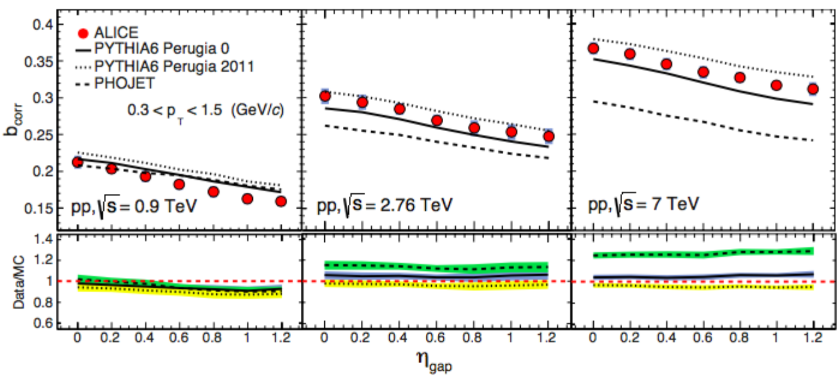

Figure 1.21: Correlation strength b_{corr} as a function of η_{gap} in pp collisions in ALICE [54].

the collision energy has been observed (Fig. 1.21), which cannot be explained exclusively by the increase of the mean multiplicity inside the windows. PYTHIA describes data reasonably well, while PHOJET fails to describe b_{corr} in azimuthal sectors [54]. Control on the centrality window is required to avoid multiplicity fluctuations within a centrality, during the similar analysis performed for the heavy ion collisions. A comparison of b_{corr} for Au-Au collisions at $\sqrt{s_{\mathrm{NN}}} = 200$ GeV and Pb-Pb collisions at $\sqrt{s_{\mathrm{NN}}} = 2.76$ TeV with HIJING in Ref. [52] shows that, the correlation strengths are higher for higher energy collisions and extend to larger rapidity windows. The correlation strengths decrease as a function of the rapidity gap. This decrease is much slower at LHC energy than at RHIC energies.

1.7.5 Particle Ratio fluctuations

Event-by-event identified particle ratio fluctuations are related to QCD phase transitions. The divergence of susceptibility is related to the increased fluctuations near the critical point. Identified particle ratio fluctuations, such as kaon-to-pion ratio (K/π), proton-to-pion ratio (p/π) and proton-to-kaon ratio (p/K) etc., are connected to strangeness fluctuations, baryon number fluctuations and baryon-strangeness correlations, respectively [55].

Particle ratio fluctuations are independent of the volume fluctuations. In experiment, the dynamical fluctuations are extracted by measuring the fluctuation observables (say, σ_{dyn}) from data and its difference from the results of the statistical fluctuations by performimg analysis with the mixed events (for mixed events, there are no correlations between the tracks). ν_{dyn} (discussed earlier) is another observable to study in this context. This is used to quantify the magnitude of the dynamical fluctuations in event-by-event measurements of particle ratios [56].

Recent results for the identified particle ratio fluctuations with the application of the identity method [57] for Pb-Pb collisions at $\sqrt{s_{\mathrm{NN}}} = 2.76$ TeV in AL-

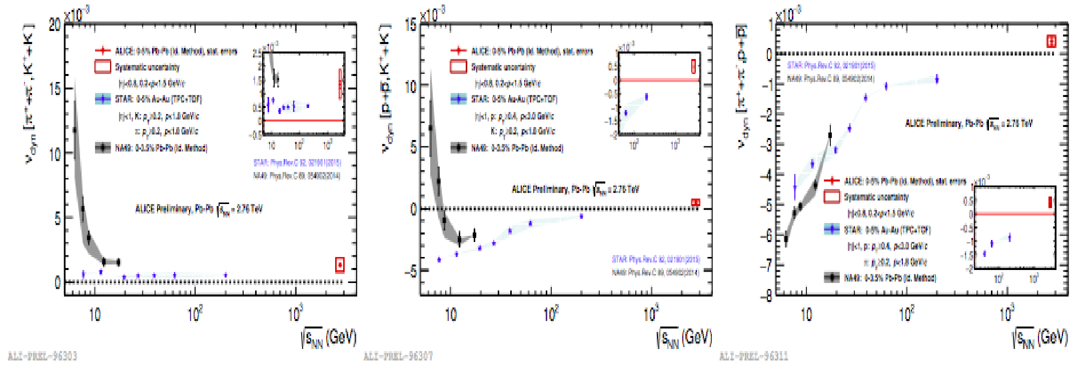

Figure 1.22: Energy dependence of ν_{dyn}. ALICE results are compared with that of central Au-Au collisions from STAR and central Pb-Pb collisions from NA49 [56].

ICE has been discussed in Ref. [56]. The results for $\nu_{\text{dyn}}[K^+ + K^-, p + \bar{p}]$ and $\nu_{\text{dyn}}[\pi^+ + \pi^-, K^+ + K^-]$ are in qualitative agreement with HIJING and AMPT models. The negative values of $\nu_{\text{dyn}}[\pi^+ + \pi^-, p + \bar{p}]$ observed in most peripheral collisions, which indicate a correlation between pions and protons, are not reproduced by the models. In all three cases, ALICE results in the most central events indicate positive results consistent with Poissonian expectation within 2σ which agree with the extrapolations based on the data at lower energies from CERN-SPS and RHIC, as shown in Fig. 1.22. More results are expected soon from the ALICE experiment.

1.7.6 Higher Moments of Net particle distributions

QCD critical point can be identified by the observation of non-monotonic behaviour of the fluctuations of globally conserved quantities, such as, net-baryon, net strangeness, net charge, etc., as a function of the beam energy. Lattice calculations suggest that the higher moments of these observables are sensitive to the phase structure of the matter produced in the high energy collisions. The moments of the net particle distributions, i.e, the mean (M), the standard deviation (σ), the skewnwss (S, representing the asymmetry of the distribution), and the kurtosis (κ, the degree to which the distribution is peaked relative to the normal distribution), which are the first, second, third and fourth order moments, respectively, are related to the corresponding higher-order thermodynamic susceptibilities and to the correlation length of the system [58, 59]. The moments of these distributions are proportional to powers of the correlation length ξ, with increasing sensitivity for higher order moments,i.e, $\langle(\Delta N)^3\rangle \propto \xi^{4.5}$, $\langle(\Delta N)^4\rangle \propto \xi^7$, etc [58, 60]. Susceptibility (χ) of a conserved system can be defined as,

$$\chi_{\mathrm{lmn}}^{\mathrm{BSQ}} = \frac{\partial^{\mathrm{l+m+n}}(p/T^4)}{\partial(\mu_{\mathrm{B}}/T)^{\mathrm{l}}\partial(\mu_{\mathrm{S}}/T)^{\mathrm{m}}\partial(\mu_{\mathrm{Q}}/T)^{\mathrm{n}}}, \tag{1.11}$$

where, l,m,n represent the derivatives and B,S,Q represent the net baryon, net strangeness and net charge, respectively. For the cancellation of the volume term while relating the susceptibilities to the moments, the products of the moments, i.e, the cumulant ratios, such as, $c_2/c_1 = \sigma^2/M$, $c_3/c_2 = S\sigma$, and $c_4/c_2 = \kappa\sigma^2$, are constructed. The freeze-out parameters can be extracted from data by measuring the ratio of the cumulants and can be compared to the predictions from lattice QCD.

Recent results from the STAR experiment on the event-by-event higher moments analysis have shown that, no significant deviation from the Poisson expectation as well as UrQMD model calculations (which does not include critical point) is there within the uncertainties for net charge (except $\kappa\sigma^2$ for the lowest beam energy) and net kaon distributions, which is observed in case of net proton distributions for $S\sigma/Skellam$ and $\kappa\sigma^2$ as shown in Fig. 1.23 [60]. A non-monotonic behaviour of the net-proton $\kappa\sigma^2$ can be seen in top $0-5\%$ central collisions, with an increase at

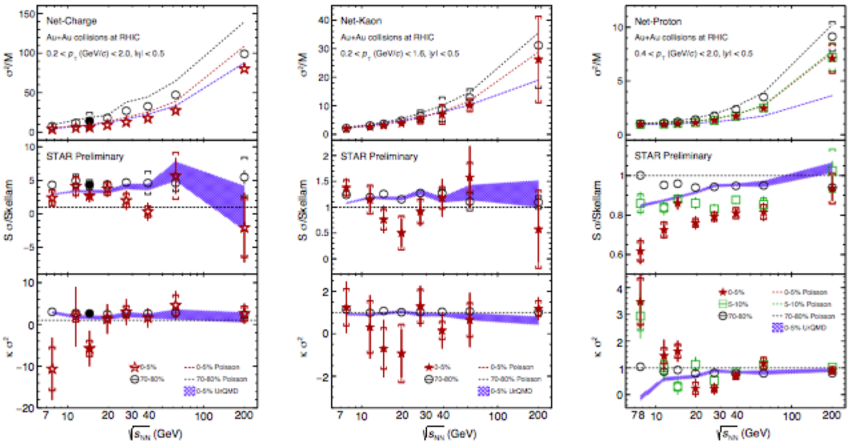

Figure 1.23: Energy dependence of the volume independent cumulant ratios of the net-charge (left figure), net-kaon (middle figure), and net-proton (right figure) distributions [59, 60] from STAR experiment.

lower energies while peripheral collisions show much smaller deviations from Poisson statistics. UrQMD calculations show suppression at lower energies due to baryon number conservation [60]. Significant deviations of moment products from the Skellam expectations, are found in the analysis of net-proton distribution [61, 62].

In ALICE, higher moments can be measured upto sixth order with Run-II data. Moreover, the lattice QCD calculations are perfomed at $\mu_{\mathrm{B}} = 0$, which is directly comparable for LHC energies. The results are expected soon from the ALICE experiment.

1.7.7 Multiplicity Fluctuations

Event-by-event fluctuations in the total charged particle multiplicities, expressed in terms of the scaled variances, are predicted to have a non-monotonic behaviour at the critical point, thus providing important informations on the QCD phase transition. It is also possible to extract the isothermal compressibility (k_{T}) of the system formed in the high energy heavy ion collisions, by the measurement of the event-by-event multiplicity fluctuations (discussed in details in Chapter 4 and Chapter 5). In this thesis work, a detailed study on the event-by-event multiplicity fluctuations has been presented using the data from the ALICE experiment as well as using different event generators.

Some important fluctuation analyses are ongoing in ALICE recently. The $\langle p_{\mathrm{T}} \rangle$ distributions in finite p_{T} ranges are being converted to distributions of effective temperatures. The dynamical fluctuations in temperature are being extracted by subtracting widths of the corresponding mixed event distributions. The specific heat (C_{v}) at the kinetic freezeout surface for the published results at RHIC energies, is presented as a function of collision energy in Ref. [63].

The charged-neutral fluctuations in the forward rapidity are being observed to search for the disoriented chiral condensate following the measurements previously done by WA98 [64] and STAR [65] experiments. The overlap area of the Photon Multiplicity Detector (PMD) and Forward Multiplicity Detector (FMD) are being used for this purpose in ALICE.

Different combinations of higher order off-diagonal susceptibilities of net charge, net baryon number and net strangeness can be estimated using different combinations of higher order central moments of conserved charges in the experiments. The measurement of these observables give information to explore the flavour carrying susceptibilities and also the nature of QCD phase transitions. Recently, this kind of analysis is ongoing in STAR experiment. A study of the second order diagonal susceptibilities and cross correlations has been presented with the results using HRG and UrQMD in Ref. [66].

1.8 Organization of the Thesis

Event-by-event multiplicity fluctuation analysis with the data from the ALICE experiment has been presented in the thesis.

In *Chapter 1*, Quantum Chromodynamics, QGP and its signatures, the fluctuation measures, etc., have been briefly introduced. *Chapter 2* contains brief description of the Large Hadron Collider (LHC), the ALICE experiment and the detectors used in ALICE. The experimentally observed results for the multiplicity distributions obtained till date from pp as well as heavy ion collisions have been discussed in *Chapter 3*. In *Chapter 4*, a discussion on the results of the multiplicity fluctuations from different ensembles has been presented. In *Chapter 5*, the earlier results for the multiplicity fluctuations in heavy ion collisions have been discussed alongwith the motivations for the study of the multiplicity fluctuations in ALICE experiment. Results from the multiplicity distributions and multiplicity fluctuations in Au-Au collisions at $\sqrt{s_{\mathrm{NN}}}$ = 7.7,19.6, 27, 62.4, 200 GeV and Pb-Pb collisions at $\sqrt{s_{\mathrm{NN}}}$ = 2.76 TeV have been shown in details using AMPT event generators, in *Chapter 6*. The description of the methods used for ALICE data analysis for the multiplicity fluctuation study, and the results from the monte carlo simulation from ALICE have been presented in *Chapter 7*. In *Chapter 8*, the results for the charged particle multiplicity distributions and fluctuations for Pb-Pb collisions at $\sqrt{s_{\mathrm{NN}}}$ = 2.76 TeV and for p-Pb collisions at $\sqrt{s_{\mathrm{NN}}}$ = 5.02 TeV have been shown and discussed. A rough estimation of the isothermal compressibility (k_{T}) of the system at the kinetic freeze-out temperatre, have been also presented in this chapter. The works presented in this thesis have been summarized in *Chapter 9*.

Bibliography

[1] E. Rutherford. The scattering of and particles by matter and the structure of the atom. Phil.Mag., 21(125):669688, 1911. http://dx.doi.org/10.1080/14786440508637080.

[2] J. Chadwick. Possible Existence of a Neutron. Nature, 129:312, 1932. http://dx.doi. org/10.1038/129312a0.

[3] G. Aad *et al.* (ATLAS Collaboration). Observation of a new particle in the search for the Standard Model Higgs boson with the ATLAS detector at the LHC. Phys.Lett. B716(1):1 29, 2012. arXiv:1207.7214.

[4] S. Chatrchyan *et al.* (CMS Collaboration). Observation of a new boson at a mass of 125 GeV with the experiment at the LHC. Phys.Lett. B716(1):3061, 2012. arXiv:1207.7235.

[5] H. Fritzsch, M. Gell-Mann, eConfC720906V2:135-165, 1972. arXiv: hep-ph/0208010v1 (2002).

[6] D. Gross and F. Wilczek, Phys. Rev. Lett. 30, 1343 (1973); H. Politzer, Phys. Rev. Lett. 30, 1346 (1973).

[7] G. S. Bali, QCD forces and heavy quark bound states, Phys. Rept., vol. 343, pp. 1136, 2001.

[8] F. Halzen and A. D. Martin, QUARKS & LEPTONS: An Introductory Course in Modern Particle Physics.

[9] Siegfried Bethke, Experimental Tests of Asymptotic Freedom, arXiv:hep-ex/0606035.

[10] http://nayak.web.cern.ch/nayak/Science_Horizon_QGP.pdf.

[11] http://home.cern/about/physics/early-universe

[12] Bennett *et al.*, "The Essential Cosmic Perspective".

[13] http://www.physicsoftheuniverse.com/topics_bigbang_timeline.html

[14] E. V. Shuryak Phys. Rep. **61**, 71 (1980).

[15] S. Ejiri, Phys. Rev. **D 78** 074507 (2008)

[16] M. A. Stephanov, Prog. Theor. Phys. Suppl. **153**, 139 (2004).

[17] Y. Aoki *et al.*, Phys. Lett. **B 643**, 46 (2006).

[18] J. D. Bjorken, Phys. Rev. **D27**, 140 (1983).

[19] Frithjof Karsch, Lecture note on Lattice QCD at High Temperature and Density, arXiv:hep-lat/0106019.

[20] B. Muller, J. Schukraft, and B. Wyslouch. First Results from Pb+Pb collisions at the LHC. Ann.Rev.Nucl.Part.Sci., 62:361386, 2012. arXiv:1202.3233.

[21] J. Adams *et al.* (for STAR Collaboration), Phys. Rev. Lett. **91**, 072304 (2003).

[22] S. S. Adler *et al.* (PHENIX Collaboration), Phys. Rev. Lett. **96**, 202301 (2006).

[23] B. Abelev *et al.* (ALICE Collaboration), Eur. Phys. J. C (2014) 74:3108.

[24] Y.-J. Lee, Nuclear modification factors from the CMS experiment. Quark Matter 2011.

[25] Cheuk-Yin Wong, Introduction to High-Energy Heavy-Ion Collisions, World Scientific (1994).

[26] T. Matsui and H. Satz, Phys. Lett. B178, 416 (1986).

[27] PHENIX Collaboration, Phys. Rev. Lett. **98**, 232301 (2007).

[28] B. Abelev *et al.* (ALICE Collaboration), Phys. Rev. Lett. **109**, 072301 (2012).

[29] B. Abelev *et al.* (ALICE Collaboration), JHEP 02 (2014) 073.

[30] B. Guerzoni, for the ALICE Collaboration, (presented in Strangeness in Quark Matter), Acta Physica Polonica B Proceedings Supplement, 2011.

[31] M. Floris, for the ALICE Collaboration, plenary talk at Quark Matter 2011, Annecy, France.

[32] J. Rafelski and B. Muller, Phys. Rev. Lett. **48** (1982) 1066.

[33] P. Koch, B. Muller, and J. Rafelski, Phys. Rep. **142**, 167 (1986).

[34] STAR Collaboration, Nucl. Phys. **A 757**, 102 (2005); PHENIX Collaboration, Nucl. Phys. **A 757**, 184 (2005); STAR Collaboration, PRL **108**, 072301 (2012).

[35] B. Abelev *et al.* (ALICE Collaboration), Physics Letters B **728** (2014) 216 227.

[36] F. Noferini (ALICE Collaboration). Anisotropic flow of identified particles in Pb-Pb collisions at $\sqrt{s_{\rm NN}} = 2.76$ TeV measured with ALICE at the LHC. Nucl.Phys., A904-905:483c486c, 2013. arXiv:1212.1292, http://dx.doi.org/10.1016/j.nuclphysa.2013.02.058.

[37] K.Aamodt *et al.* (ALICE Collaboration), Phys.Rev.Lett.105:252302,2010

[38] K.Aamodt *et al.* (ALICE Collaboration), Phys.Rev.Lett. 107:032301,2011.

[39] S. Jeon and V. Koch, in Quark-Gluon Plasma 3, edited by R. C. Hwa and X. N. Wang (World Scientific,Singapore, 2004), p. 430; arXiv:hep-ph/0304012v1.

[40] B. Abelev *et al.* (ALICE Collaboration), PRL **110**,152301 (2013).

[41] S. Jeon and V. Koch, PRL **85**, 2076 (2000).

[42] B. I. Abelev *et al.* (STAR Collaboration), Phys. Rev. **C 79**, 024906 (2009); J. Adams *et al.* (STAR Collaboration), Phys. Rev. **C 68**,044905 (2003); C. Alt *et al.* (NA49 Collaboration), Phys. Rev. **C 70**, 064903 (2004); C. Pruneau, S. Gavin, and S. Voloshin, Phys. Rev. **C 66**,044904 (2002).

[43] S. A. Bass, P. Danielewicz, and S. Pratt, PRL **85**, 2689 (2000).

[44] B. Abelev *et al.* (ALICE Collaboration), PLB **723**, 267 (2013).

[45] H. Heiselberg, Phys. Rept. **351** 161 (2001).

[46] M. Weber (ALICE Collaboration), Proceedings for Quark Matter 2012, 10.1016/j.nuclphysa.2013.02.050, arXiv:1210.5851 [nucl-ex].

[47] J. Adam *et al.* (ALICE Collaboration), Eur. Phys. J. **C 76** (2016) 86.

[48] S. A. Voloshin, V. Koch, and H. G. Ritter, Phys. Rev. **C60** 024901 (1999).

[49] J. Adams *et al.* (STAR Collaboration), Phys. Rev. **C71** (2005) 064906.

[50] B. Abelev *et al.* (ALICE Collaboration), Eur. Phys. J. **C 74** (2014) 3077.

[51] Y. V. Kovchegov, E. Levin, and L. McLerran, Phys. Rev. **C 63**, 024903 (2001).

[52] Sudipan De, T. Tarnowsky, T. K. Nayak, R. P. Scharenberg, and B. K. Srivastava, Phys. Rev. **C 88**, 044903 (2013).

[53] B. I. Abelev *et al.* (STAR Collaboration), Phys. Rev. Lett. 103, 172301 (2009).

[54] J. Adam *et al.* (ALICE Collaboration), JHEP **097** (2015).

[55] V. Koch, A. Majumder, and J. Randrup, Phys. Rev. Lett. **95**, 182301 (2005).

[56] M. Arslandok *et al.* (for the ALICE Collaboration), Proceedings of QM 2015, Nuclear Physics A 00 (2015) 14, arxiv:1512.03372 [hep-ex].

[57] Marek Gazdzicki, Phys. Rev.**C83**,054907(2011).

[58] M. A. Stephanov, Phys. Rev. Lett. **102**, 032301 (2009).

[59] L. Adamczyk *et al.* (STAR Collaboration), PRL **113**, 092301 (2014).

[60] Jochen Thader (for the STAR Collaboration), Nuclear Physics A 00 (2016) 14, arxiv:1601.00951[nucl-ex].

[61] A. Sarkar (for the STAR Collaboration), Nuclear Physics A **931** (2014) 796801.

[62] L. Adamczyk *et al.*, STAR Collaboration, Phys. Rev. Lett. **112** (2014) 032302.

[63] S. Basu*et al.*, arxiv:1601.05631 [nucl-ex].

[64] M. M. Aggarwal *et al.* (WA98 Collaboration), Phys. Rev. **C 64**, 011901 (2001).

[65] L. Adamczyk *et al.* (STAR Collaboration), Phys Rev **C91**,034905 (2015).

[66] A. Chatterjee *et al.* arxiv:1606.09573 [nucl-ex].

2

The LHC and the ALICE experiment

A brief description of the LHC and the ALICE experiment has been presented in this chapter. The detector systems involved in the ALICE experiment alongwith their physics goals have been discussed. The trigger setup for event selection, the data acquisition system, the online and offline computation for data processing and the physics analysis, etc. have been discussed too.

2.1 Large Hadron Collider

The Large Hadron Collider (LHC) at CERN, the largest particle accelerator in the world [1, 2], is installed in the 26.7 km tunnel for the CERN Large Electron-Positron (LEP) Collider, in 2001. The LHC is located under the Swiss-French border area at a depth of 50 to 175 m.

LHC has been designed to collide proton beams with a top energy of $\sqrt{s} = 14$ TeV and heavy ions (Pb-ions) with a top energy of $\sqrt{s}_{\mathrm{NN}} = 5.5$ TeV with a luminosity of $10^{34} cm^{-2} s^{-1}$ and $10^{27} cm^{-2} s^{-1}$ for proton beam and Pb-ion beam, respectively. It consists of a 26.7 km ring of superconducting magnets alongwith the accelerating structures for boosting the energy of the particles. Two beams of particles travel in opposite directions in two separate beam pipes inside the accelerator (vacuum pressure is $\sim 10^{-7}$ Pa in the beam pipe and lower than 10^{9} Pa close to the interaction point). Before the particles achieve their colliding energy, they travel many times around the accelerator ring. A combination of electric and magnetic fields helps to guide the beams inside the accelerator ring, as well as helps to squeeze the beams closer to enhance the chances for the collisions.

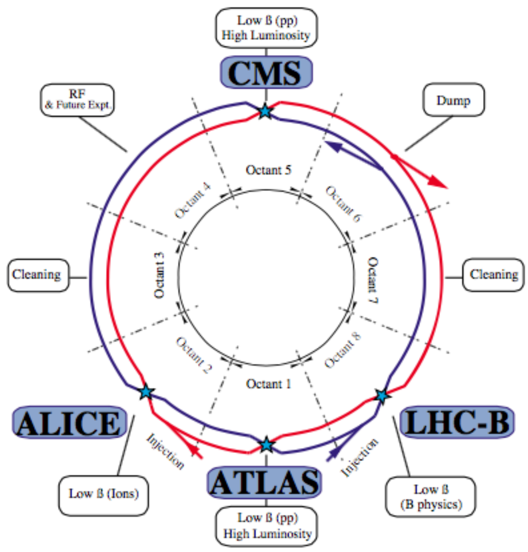

Figure 2.1: Schematic view of the Large Hadron Collider

Fig. 2.1 shows the schematic layout of the LHC. It is segmented into eight octants. Each octant has a straight section in its center, which is called point. Beam crosses at the four points, i.e, 1,2,5 and 8, among the eight points. These four pits or points contain the four major experiments. The two beams are injected into LHC into outer arcs upstream of pits 2 and 8. Collimation systems are placed at point 3 and 7 to clean the beam. The cleaning prevents particles from being lost in an uncontrolled fashion within the accelerator. Pit 4 houses the Radio-Frequency (RF) system to accelerate the beams. Pit 6 is reserved for the beam dumping system. A total of 1232 dipole magnets, each of 14.3 m length, are used to bend the beams and 392 quadrupole magnets, each 5 to 7 m long, are used to focus the beams. Just before the collision, another type of magnet is used to squeeze the particles closer together.

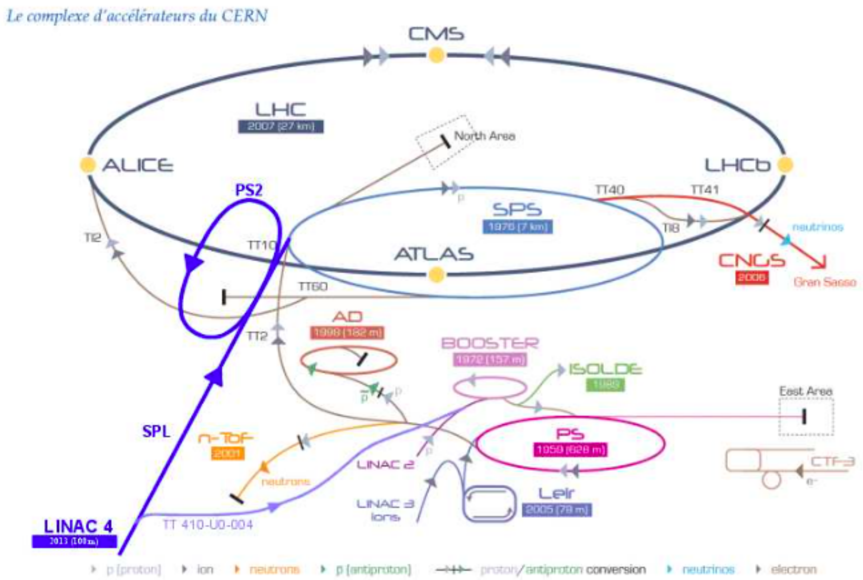

Figure 2.2: Schematic view of CERN accelerator complex

The schematic of the CERN accelerator complex is shown in Fig. 2.2. This is used to obtain the beams for the LHC. The six experiments installed at the LHC are, A Large Ion Collider Experiment (ALICE), A Toroidal LHC ApparatuS (ATLAS), the Compact Muon Solenoid (CMS), the Large Hadron Collider beauty (LHCb) experiment, the Large Hadron Collider forward (LHCf) experiment and the TOTal Elastic and diffractive cross section Measurement (TOTEM) experiment.

ALICE [3, 4] is at point 2. It is specialized for heavy-ion collisions. It explores the properties of quark-gluon plasma, a state of matter where quarks and gluons, under conditions of very high temperatures and densities, are no longer confined inside hadrons. ALICE also studies the proton proton collision as a baseline for heavy ion measurements and it is complementary to other LHC experiments.

ATLAS [5] and **CMS** [6] are diametrically opposite in Pits 1 and 5, respectively. These two detectors are general-purpose proton-proton detectors at the LHC. They investigate a wide range of physics, including the search for the Higgs boson, supersymmetry (SUSY), extra dimensions, and particles that could make up dark matter. ATLAS records sets of measurements on the particles created in collisions, i.e, their paths, energies, and their identities. Although both these experiments have the same scientific goals, however, the difference lies in the technical solutions and design of their detector magnet system to achieve these. They are also involved in heavy ion data taking.

LHCb [7] specializes in the study of the slight asymmetry between matter and antimatter present in interactions of B-particles (particles containing the b quark).

LHCf [8] shares the point 1 with ATLAS. It measures the particles produced very close to the direction of the beams in the proton-proton collisions at the LHC. The motivation is to test models used to estimate the primary energy of the ultra high-energy cosmic rays.

TOTEM [9] experiment studies forward particles to focus on physics that is not accessible to the general-purpose experiments. Among a range of studies, it measures the cross-section of the proton and also monitor accurately luminosity of the LHC. It shares intersection point Pits 5 with CMS. TOTEM includes detectors housed in specially designed vacuum chambers called Roman pots, which are connected to the beam pipes in the LHC.

By the removal of the electrons from the hydrogen atoms, protons are obtained.

Before reaching the Large Hadron Collider (LHC), they are injected from the linear accelerator (LINAC 2) into the Proton Synchrotron (PS) Booster, then the PS, followed by the Super Proton Synchrotron (SPS), where they are accelerated further to 450 GeV. From the SPS the proton beam is split into bunches travelling the LHC ring either clockwise or counter-clockwise. The bunches of protons are then accelerated to their expected reachable energy, and made to collide at the location of the four experiments ALICE, ATLAS, CMS and LHCb. Lead ions for the LHC start from a source of vaporized lead and enter LINAC 3, accelerated there to 4.2 MeV per nucleon before being collected and accelerated in the Low Energy Ion Ring (LEIR). LEIR accelerates them to 72 MeV per nucleon and sends to the PS where another acceleration is made to achieve 5.9 GeV per nucleon. The ions once again are sent through a foil to get Pb^{82+} and lead to SPS, where they are accelerated to 177 GeV per nucleon. Afterwards the ions are split into bunches and reaches into the LHC ring.

The first collisions of proton beams at $\sqrt{s} = 0.9$ TeV took place in 2009. Protons are collided at $\sqrt{s} = 2.76,\ 7,\ 8$ TeV and recently at $\sqrt{s} = 13$ TeV, after the shutdown period of LHC (for the preparation to achieve higher energies). We have data from Pb-Pb collisions at $\sqrt{s_{\mathrm{NN}}} = 2.76$ TeV and p-Pb collisions at $\sqrt{s_{\mathrm{NN}}} = 5.02$ TeV. We expect the collision of Pb-Pb beams at 5.5 A TeV in LHC in the year of 2016.

2.2 The ALICE Experiment

The ALICE is a dedicated heavy-ion detector to understand the unique physics potential of nucleus-nucleus interactions at LHC energies. The aim of the experiment is to study the physics of strongly interacting matter at extreme energy densities, where the formation of a new phase of matter, the QGP, is expected. A detailed study of the hadrons, electrons, muons and photons produced in the collision of heavy nuclei are the main observables [10, 11]. It also takes the data during proton-proton collisions to do the complementary study with the other LHC detectors as well as provides the reference to the heavy ion collisions.

2.3 The ALICE detector system

The speciality of the ALICE detector is in the tracking and identification of the particles over a large momentum range (10 MeV/c to 100 GeV/c). This allows one to study from soft to jet physics. The general layout of the ALICE detectors

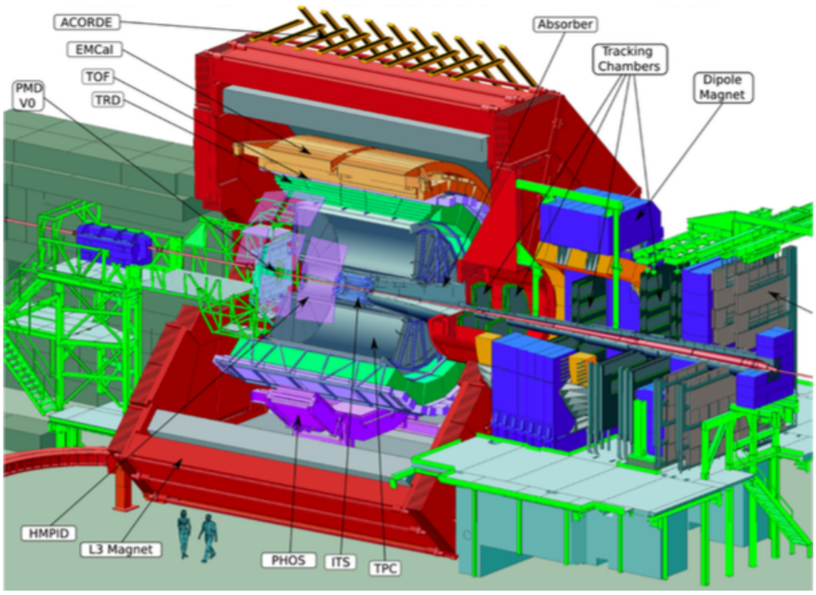

Figure 2.3: A schematic view of the ALICE detectors.

have been presented in Fig. 2.3. The ALICE is composed of 16 sub-detectors and their associated systems for power supply, cooling, gas, detector control, detector safety, trigger and data acquisition. The central part of ALICE is enclosed in the L3 solenoid, which has an internal length of 12.1 m and a radius of 5.75 m. The detectors may be classified into three main sections : central detectors, forward detectors and the Muon spectrometer [12]. The central barrel consists of the ITS, TPC, TRD, TOF, PHOS, EMCAL, HMPID and ACORDE [13, 14, 15, 16, 17, 18, 19, 20]. The forward detectors include ZDC, PMD, FMD, V0 and T0 [21, 22, 23]. Fig. 2.4

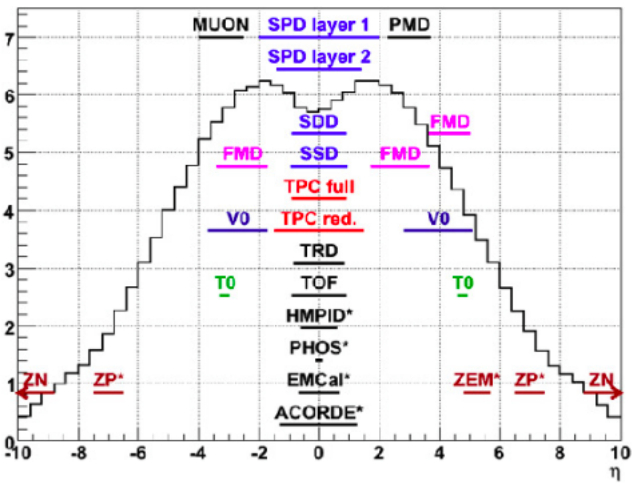

Figure 2.4: The pseudorapidity acceptance of the subdetectors in the ALICE [24].

shows the pseudorapidity acceptance of the ALICE subdetecors with a predicted $dN_{\mathrm{ch}}/d\eta$ for proton-proton collisions by PYTHIA [24]. The two detectors prepared in India are, the PMD (in the positive z direction) and the Muon spectrometer (in the negative z direction), while z-axis is along the beam direction.

2.4 Central-barrel detectors

A set of the detectors (ITS, TPC, TRD, TOF) cover the midrapidity region ($|\eta| < 0.9$) of ALICE. These are for tracking and particle identification in the very high multiplicity environment. Additional detectors like HMPID, EMCAL and PHOS are located in the central region with smaller phase space than the other central detectors.

2.4.1 The Inner Tracking System (ITS)

The ITS [13], the closest detector to the interaction point (IP), is a six layer silicon detector system with the radii from 3.9 to 43 cm. It consistes of three subsystems,

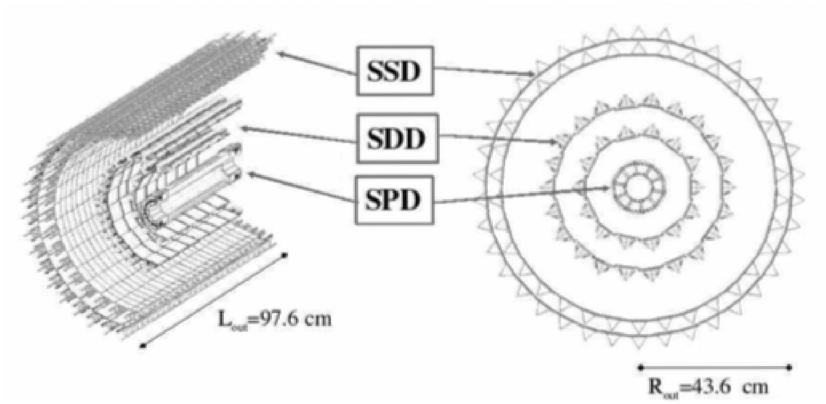

Figure 2.5: Layout of the Inner Tracking System.

i.e, Silicon Pixel Detector (SPD), Silicon Drift Detector (SDD) and Silicon Strip Detector (SSD), from the central to peripheral, as shown in Fig. 2.5.

SPD [13] constitutes the two innermost layers of the ITS. It determines the position of the primary vertex as well as for the measurement of the impact parameter of secondary tracks originating from the weak decays of strange, charm, and beauty particles. The SPD is based on hybrid silicon pixels, consisting of a two-dimensional matrix (sensor ladder) of reverse-biased silicon detector diodes. There is no energy loss information available and the readout is binary i.e. either there is a hit or there is not. The signals from this detector are used to measure the charged particle multiplicity within $|\eta| < 2.1$.

SDD constitutes the two intermediate layers of the ITS. It consists of a 300 μm thick layer of homogeneous high-resistivity silicon. It provides the dE/dx information for particle identification.

SSD is the outer most layer of the ITS and important for the matching of the tracks from the TPC to the ITS. It provides a two dimensional measurement of the track position. In addition it provides the energy-loss information to assist particle identification for low-momentum particles. The system is optimized for low mass in order to minimize multiple scattering.

ITS performs as a trigger detector. It determines the primary collision vertex and the secondary vertices, necessary for the reconstruction of charm and hyperon decays. It is also used for particle identification and tracking of the low momentum particles. It also improves the momentum and angle resolution in combination with the TPC.

2.4.2 Time Projection Chamber (TPC)

The Time-Projection Chamber (TPC) [14] is the main tracking detector of the central barrel. TPC provides, together with other central barrel detectors, charged particle momentum measurements, particle identification and the vertex determination. The TPC is cylindrical in shape, the active volume has an inner radius of about 85 cm, an outer radius of about 250 cm, and an overall length along the beam direction of 500 cm. The TPC covers a pseudo-rapidity of $|\eta| < 0.9$ for track reconstruction with full radial length and of $|\eta| < 1.5$ for tracks reconstruction with

1/3 radial length (with reduced or no matching with the other detectors). The TPC covers the full azimuth (except the dead zones). It covers a large transverse momentum range ($0.1 < p_{\mathrm{T}} < 100$ GeV/c) with good momentum resolution.

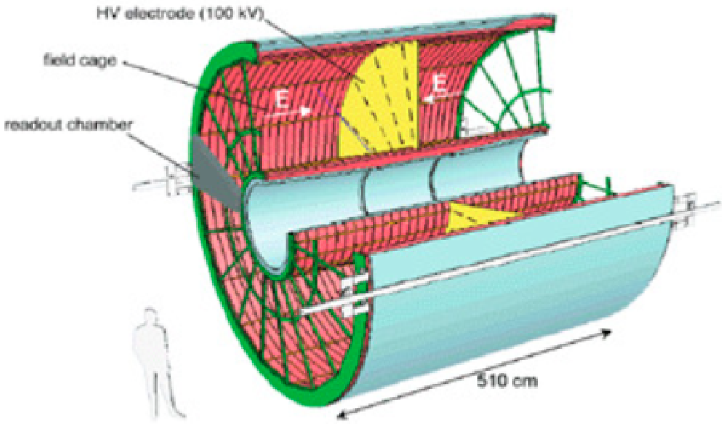

Figure 2.6: Schematic view of the Time Projection Chamber.

TPC is a gas detector with a volume of $90m^3$ filled with Ne/CO_2/N_2 gas mixture. The primary electrons are transported over a distance of 2.5 m on either side of the central electrode to the readout plates. A high voltage of 100 kV is applied between the central electrode and the readout plates giving a high voltage gradient of about 400 V/cm, which results in a maximum drift time of about 90 μs. The TPC is the slowest detector in ALICE. The TPC readout consists of multi-wire proportional chambers with cathode readout. To keep the occupancy low and to ensure the necessary specific energy-loss (dE/dx), position, and two track resolution, there are about 560000 readout pads. The schematic view of the TPC is shown in Fig. 2.6.

2.4.3 Transition-Radiation Detector (TRD)

TRD [15] provides the identification of the electrons in the central barrel for momenta above 1 GeV/c. Below this momentum, the electrons can be identified via specific energy loss measurement in the TPC. Above 1 GeV/c, transition radiation (TR) from electrons passing a radiator can be exploited in concert with the specific energy loss in a suitable gas mixture to obtain the necessary pion rejection capability. The TRD is designed to produce a fast trigger for high momentum charged particles. It is a part of level 1 trigger. In conjunction with data from the ITS and the TPC, it is possible to study the production of light and heavy vector-meson resonances and the dilepton continuum both in pp and in Pb-Pb collisions. Exploiting the excellent impact parameter resolution of the ITS it is furthermore possible to reconstruct open charm and open beauty in semi-leptonic decays.

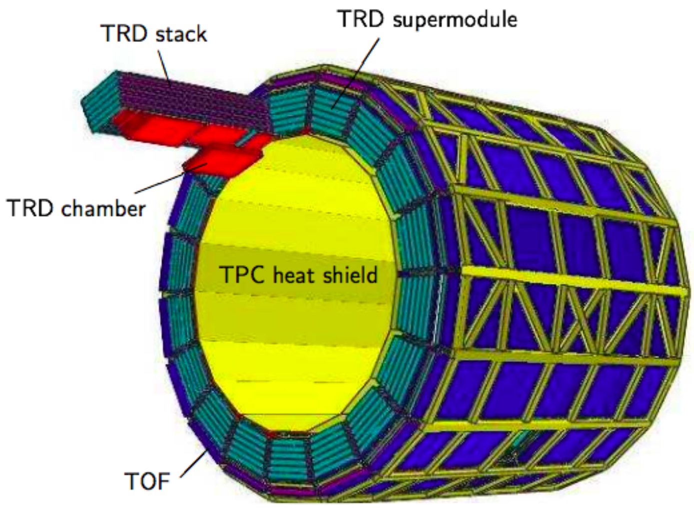

Figure 2.7: Layout of Transition-Radiation Detector (one chamber).

The TRD is located at radii of 2.9 to 3.68 m with the pseudorapidity coverage of $|\eta| < 0.84$. It consists of 540 individual read out detector modules which are arranged into 18 super modules, each of them containing 30 modules. Ionizing radiation produces electrons in the counting gas (Xe/CO2 (85 : 15)). Particles exceeding the threshold for transition radiation production ($\gamma \approx 1000$) will in addition produce about 1.45 X-ray photons in the energy range of 1 to 30 keV. X-rays in this energy regime are efficiently converted by the high-Z counting gas with the largest conversion probability at the very beginning of the drift region. All electrons from ionization energy loss and X-ray conversions will drift towards the anode wires. After gas amplification in the vicinity of the anode wires, the signal is induced on the readout pads. The layout of the TRD (one chamber) has been shown in Fig. 2.7.

2.4.4 Time-Of-Flight (TOF) detector

The Time-Of-Flight (TOF) [16] detector in ALICE provides the particle identification in the intermediate momentum range, below about 2.5 GeV/c for pions and kaons, up to 4 GeV/c for protons, with π/K and K/p separation better than 3σ, by measuring the time between the collision and the arrival of the particles in the TOF.

The TOF is a gas detector based on Multi-gap Resistive Plate Chamber (MRPC). The basic unit of the TOF system is a 10-gap double-stack MRPC strip, 122 cm long and 13 cm wide, with an active area of 120×7.4 cm^2 subdivided into two rows of 48 pads. The TOF consists of 90 modules. Every module of the TOF detector consists of a group of MRPC strips (15 in the central, 19 in the intermediate and external modules) closed inside a box that defines and seals the gas volume and supports the external front-end electronics and services. The detector covers a cylindrical surface and the modules are arranged in 18 sectors in ϕ and in 5 segments in the z-direction.

Five modules of three different lengths are needed to cover the full cylinder along the z-direction. The length of the central module is 117 cm, the intermediate ones 137 cm, and the external ones 177 cm. The overall TOF barrel length is 741 cm (active region). The TOF is located at radii from 2.70 to 3.99 m and covers a pseudo-rapidity of $|\eta| < 0.9$. The chambers have high and uniform electric field over the full sensitive gaseous volume of the detector. Any ionization produced by a traversing charged particle immediately starts a gas avalanche process which generates the observed signals on the pick-up strips. The setup achieves a very good time resolution of about 40 ps.

2.4.5 The Photon Spectrometer (PHOS)

The Photon Spectrometer [17] is a high-resolution electromagnetic spectrometer covering a limited acceptance of $|\eta| < 0.12$. The main physics objectives are the test of thermal and dynamical properties of the initial phase of the collision extracted from low p_{T} direct photon measurements and the study of jet quenching through the measurement of γ-jet correlations and high p_{T} π^0.

The PHOS is high-granularity electromagnetic spectrometer consisting of a highly segmented electromagnetic calorimeter and a Charged-Particle Veto (CPV) detector. It is positioned on the bottom of the ALICE setup at a distance of 460 cm from the interaction point. Each PHOS module is segmented into 3584 detection cells arranged in 56 rows of 64 cells. The detection cell consists of a $22{\times}22{\times}180\ mm^3$ lead-tungstate crystal, coupled to $5 \times 5\ mm^2$ Avalanche Photo-Diode (APD) followed by a low-noise preamplifier.

2.4.6 Electromagnetc Calorimeter (EMCal)

The ElectroMagnetic CALorimeter (EMCal) [18] enhances the ALICE capabilities of measuring the jet properties. It provides the L0 and L1 trigger for hard jets, photons, and electrons. The EMCal is a large layered Pb-scintillator sampling calorimeter with cylindrical geometry, located adjacent to the ALICE magnet coil at a radius of ~4.5 m from the beam axis. It covers a pseudorapidity range $|\eta| \leq 0.7$ and $\Delta\phi = 107^{o}$ and is placed almost opposite to the PHOS. It is arranged in 12 supermodule units of two types: *full size* which span $\Delta\eta = 0.7$ and $\Delta\phi = 20^{o}$, and *one-third size* which span $\Delta\eta = 0.7$ and $\Delta\phi = 7^{o}$. The lower 2 supermodules are one-third size type while the rest 10 are of full size type. These supermodules are segmented into 12288 towers. The scintillation photons produced in each tower are captured by an array of Y-11 double-clad wavelength-shifting (WLS) fibres. Each fibre terminates in an aluminized mirror at the front face of the module and is integrated into a polished, circular group of 36 at the photo-sensor end at the back of the module. The fibre bundle in a single tower terminates in a 6.8 mm diameter disk and connects to the Avalanche Photo Diode (APD) photo sensor through a short light guide. The EMCal measures the neutral energy component of jets, enabling full jet reconstruction, both in pp and Pb-Pb collisions.

2.4.7 High-Momentum Particle Identification Detector (HMPID)

The High-Momentum Particle Identification Detector [19] is measures the identified hadrons at the transverse momentum larger than 1 GeV/c. The aim is to enhance the particle identification capability of ALICE by enabling identification of charged hadrons beyond the momentum interval attainable through energy-loss (in ITS and TPC) and time-of-flight measurements (in TOF). The detector was optimised to extend the useful range for π/K and K/π discrimination, on a track-by-track basis, up to 3 GeV/c and 5 GeV/c, respectively.

The HMPID is based on proximity-focusing Ring Imaging Cherenkov (RICH) counters and consists of seven modules of about 1.5×1.5 m^2 each, mounted in an independent support cradle. The radiator, which defines the momentum range covered by the HMPID, is a 15 mm thick layer of low chromaticity C_6F_{14} (perfluoro-hexane) liquid with an index of refraction of $n = 1.2989$ at $\lambda = 175$ nm corresponding to $\beta_{\rm min} = 0.77$. Cherenkov photons, emitted by a fast charged particle traversing radiator, are detected by a photon counter which uses the novel technology of a thin layer of CsI deposited onto the pad cathode of a Multi-Wire Pad Chamber (MWPC). The HMPID, with a surface of about $11m^2$, is the largest scale application of this technique.

2.4.8 ALICE Cosmic ray Detector (ACORDE)

The ALICE COsmic Ray DEtector (ACORDE) [20] provides a fast (Level-0) trigger signal, for the commissioning, calibration and alignment procedures of some of the ALICE tracking detectors, and it also detects single atmospheric muons and multi-muon events (so-called muon bundles) in combination with the TPC, TRD, and TOF, thus allowing us to study high-energy cosmic rays in the energy region of knee in the cosmic ray spectrum.

The detector is located at the radial position of 8.5 m with the pesudorapidity coverage of $|\eta| < 1.3$. An ACORDE module consists of two scintillator counters, each with $190 \times 20\ cm^2$ effective area, placed on top of each other and read out in coincidence. The ACORDE scintillator module array, which includes 60 scintillator counter modules, is placed on top of the ALICE magnet. ACORDE provides a fast Level-0 trigger signal to the Central Trigger Processor, when atmospheric muons impinge upon the ALICE detector. The signal is used for the calibration, alignment and performance of several ALICE tracking detectors, mainly the TPC, TOF, HMPID and ITS. The operational Cosmic Ray Trigger delivers trigger signals independent of the LHC beam.

2.5 The Muon Spectrometer

The Muon spectrometer [12] provides the measurement of the complete spectrum of quarkonia ($J/\Psi, \Psi', \Upsilon, \Upsilon', \Upsilon''$), as well as ϕ-meson, via their decay in the $\mu^+\mu^-$ channel. The invariant mass resolution is of the order of 70 MeV in the J/Ψ region and about 100 MeV close to the Υ. These values are good enough to separate out all five resonance states.

The schematic diagram of the different components of the muon spectrometer is shown in Fig. 2.8. The muon spectrometer consists of a passive front absorber to absorb hadrons and photons, a high-granularity tracking systems of 10 detection planes, a large dipole magnet, a passive muon filter wall, followed by four planes of trigger chambers, and an inner beam shield to protect the chamber from primary and secondary particles produced at large rapidities. The tracking system is made of 10 cathode pad/strip chambers arranged in 5 stations of 2 chambers each. To limit the occupancy within 5%, the full set of chambers has more than 1 million channels. The trigger system is designed to select heavy quark resonance decays. The selection is

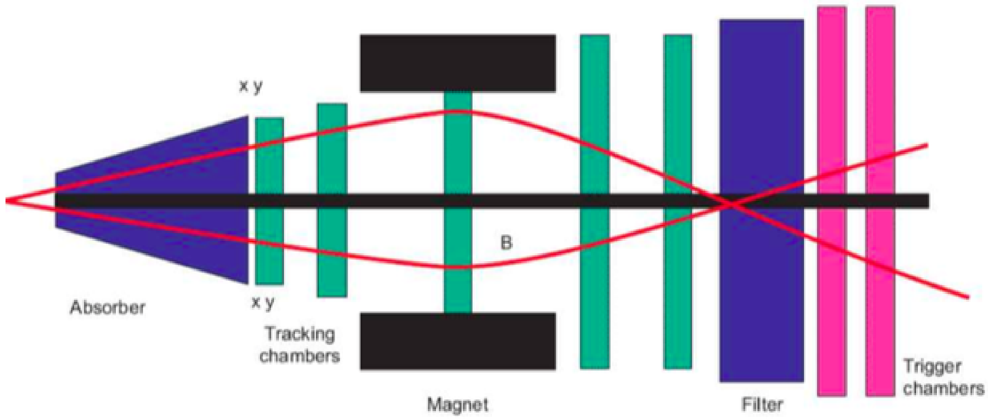

Figure 2.8: The Muon Spectrometer

made on the p_t of the two individual muons. Four planes of Resistive Plate Chambers (RPCs) arranged in 2 stations and positioned behind a passive muon filter provide the transverse momentum of each μ. The spatial resolution is better than 1 cm and the time resolution is 2 ns. The muon spectrometer covers a pseudorapidity range of $-4.0 < \eta < -2.5$ in full azimuth. The front-end electronics of muon chambers consists of MANU (MAnas NUmerique) boards and the readout system is known as Cluster Readout Concentrator Unit System (CROCUS).

2.6 The Forward Detectors

2.6.1 Zero Degree Calorimeter (ZDC)

The ZDC [21] is designed to detect the spectator nucleons by measuring the energy carried by them in the forward direction (at 0^o relative to the beam direction). The centrality information provided by the ZDC is also used for triggering at Level 1. The ZDC being also a position-sensitive detector, can give an estimate of the reaction plane in nuclear collisions.

In ALICE two sets of hadronic ZDCs are located at 116 m on either side of the Interaction Point. In addition, two small electromagnetic calorimeters (ZEM) are placed at about 7m from the IP, on both sides of the LHC beam pipe, opposite to the muon arm. Spectator protons are spatially separated from neutrons by the magnetic elements of the LHC beam line. Therefore, each ZDC set is made by two distinct detectors: one for spectator neutrons (ZN), placed between the beam pipes at 0^{o} relative to the LHC axis, and one for spectator protons (ZP), placed externally to the outgoing beam pipe on the side where positive particles are deflected.

2.6.2 Photon Multiplicity Detector (PMD)

The Photon Multiplicity Detector (PMD) [22] in ALICE provides the measurements of multiplicity and the pseudorapidity distributions of photons in the forward rapidities ($2.3 < \eta < 3.9$) with full ϕ ($0 < \phi < 2\pi$).

PMD is a preshower detector with an array of gaseous proportional counters. It consists of two identical planes with a lead converter of thickness $3X_0$ sandwiched in between them. The principle of the photon detection has been presented in Fig. 2.9. The plane towards the IP is known as the Charged Particle Veto (CPV) plane and is used for improving the photon hadron discrimination, while, the plane behind the lead plates is known as the Preshower plane. The photon, while passing through the lead plate produces a shower of positrons and electrons by the combined effect of two processes, pair production and bremsstrahlung emission. The shower particles while passing through the preshower plane produce signals which are read by the front-end electronics. The front-end electronics consists of MANAS chips. A schematic

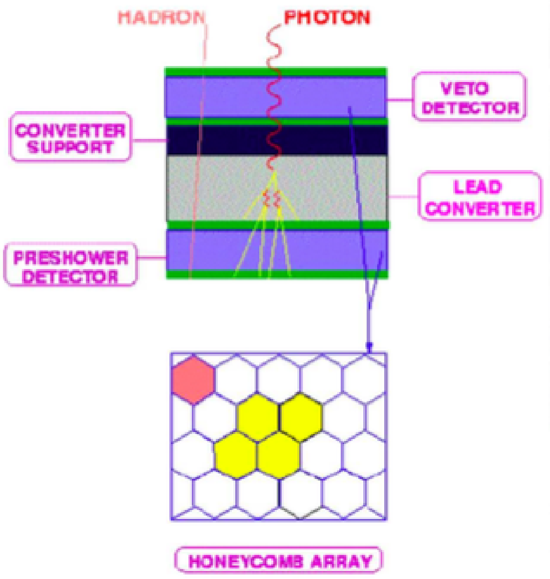

Figure 2.9: Schematic view of the photon detection by PMD.

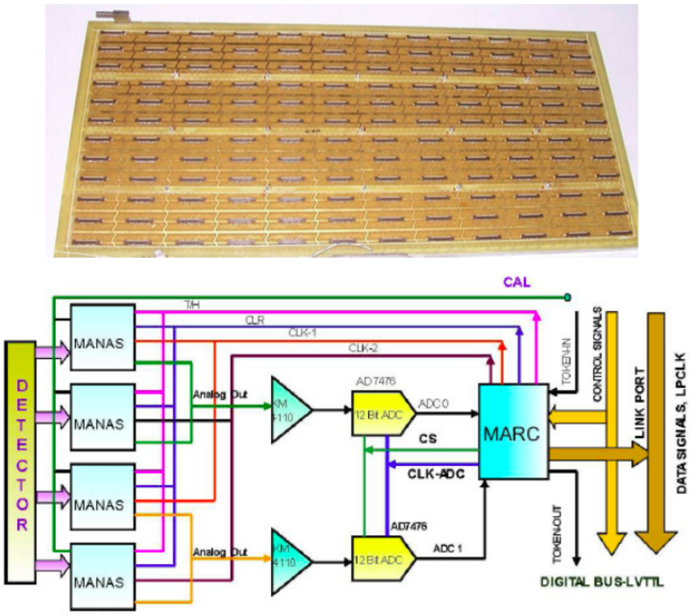

Figure 2.10: Top panel : One PMD module. Bottom panel : Schematic view of the front end electronics of PMD.

of front-end electronics (FEE) has been shown in Fig. 2.10 (bottom panel). The MANAS chip has sixteen input channels and one output channel. A group of 64 cells are connected to two 32-pin connectors by a flexible cable which connects to the FEE board at the other end. The signals are processed by the MANAS chips which provide the analog outputs. ADCs convert the analog signal coming from MANAS. The digitized output signal is sent to the MARC. MARC controls 4 MANAS chips and 2 serial 12-bit ADCs and performs zero suppression on data.

The measurement of the photon multiplicity helps to study the beam energy dependence of average photon multiplicity in forward rapidity region and limiting fragmentation behavior of photons, to determine the reaction plane for measuring the azimuthal anisotropy of the charged particles in midrapidity, to probe the thermalization by measuring the azimuthal anisotropy of the inclusive photons, to observe fluctuations in global observables like multiplicity and transverse energy, to provide signals of chiral-symmetry restoration through the measurement of $N_\gamma/N_{\rm ch}$ in a common part of phase space, etc. PMD is made by the Variable Energy Cyclotron Centre (VECC) in Kolkata, India.

2.6.3 Forward Multiplicity Detector (FMD)

The Forward Multiplicity Detector (FMD) [23] provides the measurement of charged particle multiplicity in the pseudorapidity range $-3.4 < \eta < -1.7$ and $1.7 < \eta < 5.0$ in full azimuthal angle. In addition, the information from FMD can be used to study the event-by-event multiplicity fluctuations, determination of reaction plane, and elliptic flow measurement within its pseudorapidity coverage. In conjunction with PMD, FMD can also be used to study the correlation between photons and charged-particles at forward rapidity.

The FMD consists of 5 rings of Si semiconductor detectors with a total of 51200 individual strips. The locations of the FMD rings and the basic layout of the silicon

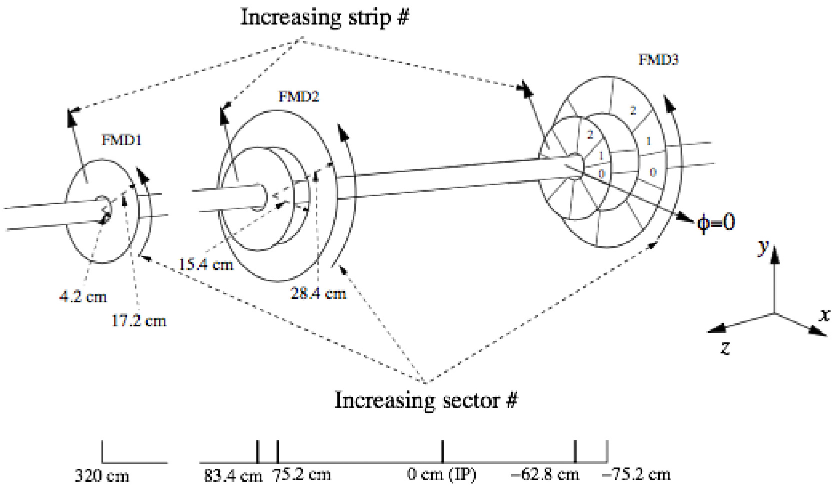

Figure 2.11: The layout of the FMD rings.

sensor within a FMD ring is shown in Fig. 2.11. The rings are of two types: the inner type consists of 10 wafers subdivided into 20 sectors with 1024 strips each. The outer type is subdivided into 40 sectors each with 512 strips. The Si wafers are 300 micrometer thick and are manufactured out of 6 diameter Si disks. The FMD consists of 3 groups of detectors called FMD1, FMD2, and FMD3. FMD2 and FMD3 each consists of a ring of inner type Si sensors and a ring of outer type Si sensors. These are located on either side of the IP. FMD1 consists of a ring of inner type Si sensors and is placed opposite to the muon spectrometer to extend the charged particle multiplicity coverage.

2.6.4 The V0 detector

The V0 detector [23] provides minimum-bias triggers for the central barrel detectors in pp and Pb-Pb collisions. It rejects the beam-gas events and provides a pre-trigger to the TRD. The V0 serves as an indicator of the centrality of the collision via the multiplicity recorded in the event. This detector also participates in the measurement of luminosity in pp collisions with a good precision of about 10%.

The V0 detector is a small angle detector consisting of two arrays of scintillator counters, called V0A and V0C, which are installed on either side of the ALICE interaction point. It is located 340 cm from the vertex on the side opposite to the muon spectrometer whereas V0C is fixed to the front face of the hadronic absorber, 90 cm from the vertex. They cover the pseudorapidity ranges $-3.7 < \eta < -1.7$ (VOC) and $2.8 < \eta < 5.1$ (V0A) and are segmented into 32 individual counters each distributed in four rings.

2.6.5 The T0 detector

The T0 [23] is the fast timing and trigger detector in ALICE. T0 detector provides several signals to the ALICE trigger, delivers an early (prior to L0 trigger) wake-up to the TRD, and gives a precise start signal for the TOF detector. In addition, it measures the approximate vertex position with a precision of $\pm 1.5\ cm$, for each interaction and generates L0 trigger when the trigger is within the reset values allowing a discrimination against the Beam-Gas interactions. The T0 can generate minimum bias and multiplicity triggers (semi-central and central).

The T0 consists of two arrays of Cherenkov Counters (called as T0-A and T0-C, which are installed on two sides of the ALICE interaction point) with 12 counters per array. The T0-A is located 375 cm from the IP covering a pseudorapidity range $4.61 < \eta < 4.92$ while the T0-C is located at 72.7 cm from the IP on the side of muon spectrometer covering a pseudorapidity range $-3.28 < \eta < -2.97$. Both T0-A and T0-C, are segmented into 12 individual counters. The T0 signal is generated online by a mean timer. The position of the T0 signal on the time axis is equal to $(T0 - C + T0 - A)/2 + T_{\text{delay}}$, where T_{delay} is the fixed delay of the analog mean timer. The position of vertex is measured as (T0-A) - (T0-C) and this value is sent to a digital discriminator with preset upper and lower limits thus providing the $T0_{\text{vertex}}$ trigger signal. The T0 has a very good time resolution of about 50 ps.

2.7 Trigger System in ALICE

The ALICE Trigger system consists of a two types of trigger : The low-level hardware trigger called Central Trigger Processor (CTP) and the High-Level Trigger (HLT) which is the software trigger.

2.7.1 Central Trigger Processor (CTP)

The CTP combines the trigger signals from the different sub-detectors to decide the acceptance of an event. It provides several levels of hardware triggers. The first level called Level-0 (L0), is delivered after 1.2 μs, the second, called Level-1 (L1), after 6.5 μs. The final trigger, which is called Level-2 (L2) trigger is delivered after 100 μs. After the Level-2 trigger the event is stored. The CTP consists of 24 Local Trigger Units (LTU) for each detector system. The output from the CTP goes to the LTUs of each detector and then to the front-end electronics to the detectors via LVDVS cables and optical fibers. The CTP forms 50 independent trigger classes combining 24 L0 inputs, 24 L1 inputs and 12 L2 inputs [25].

The information from the V0 detector and SPD detector are combined to form the *Minimum-Bias triggers* which is designed to trigger on all inelastic interactions. A set of minimum-bias triggers are available: MB1 ($V0_{\mathrm{OR}}$ or SPD_{OR} and not $V0_{\mathrm{BG}}$), MB2 ($V0_{\mathrm{OR}}$ and SPD_{OR} and not $V0_{\mathrm{BG}}$) , MB3 ($V0_{\mathrm{AND}}$ and SPD_{OR} and not $V0_{\mathrm{BG}}$). $V0_{\mathrm{OR}}$ requires a signal in either of two V0 sides, $V0_{\mathrm{AND}}$ requires signals on both sides of the V0, $V0_{\mathrm{BG}}$ indicates that a beam-gas or beam-halo collision was detected by the V0 which utilizes the timing of the collision. SPD_{OR} requires at least one chip that measured a signal in the SPD [4, 24].

2.7.2 High-Level Trigger (HLT)

In order to meet the high computing demands, the HLT [25] consists of a PC farm of up to 1000 multi-processor computers. The raw data of all ALICE detectors are received by HLT via 454 Detector Data Links (DDLs) at layer 1. The first processing layer performs basic calibration and extracts hits and clusters (layer 2). This is done in part with hardware coprocessors and therefore simultaneously with the receiving of the data. The third layer reconstructs the event for each detector individually. Layer 4 combines the processed and calibrated information of all detectors and reconstructs the whole event. Using the reconstructed physics observables layer 5 performs the selection of events or regions of interest, based on run specific physics selection criteria. The selected data is further subjected to complex data compression algorithms.

2.7.3 Data AcQuisition (DAQ) System

The main task of the ALICE DAQ system [25] is event building and export of assembled events to permanent storage. The DAQ is designed to process a data rate of up to 1.25 GB/s in heavy-ions collisions. Event building is done in two steps. Data from the sub-detectors is received by Detector Data Links (DDLs) on Local Data Concentrators (LDCs). The LDCs assemble the data into sub-events that are then shipped to Global Data Collectors (GDCs). The GDCs archive the data over the storage network as data files of a fixed size to the Transient Data Storage (TDS). During a run period, each GDC produces a sequence of such files and registers them in the ALICE Grid software (AliEn).

2.8 ALICE offline Computing

The main aim of the Offline Project is the development and operation of the framework for data processing. This includes tasks such as simulation, reconstruction, calibration, alignment, visualization and analyses. These are the final steps of the experimental activity, aimed at interpreting the data collected by the experiment and at extracting the physics content. The data production of the LHC experiment is huge. The TPC is read out by 557568 channels, delivering event sizes up to 75 MB for a central Pb-Pb collision. The computer resources required to process the ALICE data are huge and are beyond the capacity of a single institute or computing centre. Therefore data processing is distributed onto several computing centres located worldwide. There are around 80 such centres. The Grid Middleware allows treatment of this collection of distributed computing resources as an integrated computing centre. ALICE uses the ALICE Environment (AliEn) system as a user interface to connect to the Grid composed of ALICE-specific services that are part of the AliEn framework and basic services of Grid middleware.

The distributed computing infrastructure serving the LHC experimental program is coordinated by the Worldwide LHC Computing Grid (WLCG). The WLCG is highly hierarchical by nature. All real data originate from CERN, with a very large computing centre called Tier-0. Large regional computing centres, called Tier-1, share with CERN the role of a safe storage of the data. Smaller centres, called Tier-2, are logically clustered around the tier-1's. The main difference between the two is the availability of high reliability mass-storage media at Tier-1's. The major role of Tier-2's is simulation and end-user analysis. The Variable Energy Cyclotron Centre, Kolkata acts as a Tier-2 centre. Smaller centre, corresponding to departmental computing centre and sometimes called Tier-3's, contribute to the computing resources but there is no definite role or definition for them.

A dedicated framework called AliRoot (discussed later in this chapter) enables simulation and reconstruction of ALICE events and act as a basis for data analysis framework.

2.8.1 Dataflow

The strategy for data processing varies according to the type of the collision. During pp collisions the data recorded are written by the DAQ on a disk buffer at the Tier-0 (CERN) computing centre. In parallel to this, the RAW data are copied to the CASTOR tapes, exported to the Tier-1 centres to have a second distributed copy for the successive reconstruction passes that will be processed in the Tier-1, first pass processing (reconstruction, processing of alignment and calibration constants and the scheduled analysis) at the Tier-0, and fast processing of selected data on the CERN Analysis Facility (CAF). During nucleus-nucleus runs, the processing of Raw data proceeds as follows:

• Registration of RAW data in CASTOR ;

• Partial export to Tier-1 centres for remote users ;

• Partial first pass processing at the Tier-0 centre to provide rapid feedback on the offline chain ;

• Fast processing and analysis on CAF.

During the first pass reconstruction, high-precision alignment and calibration data, as well as a first set of Event Summary Data (ESD) and Analysis Object Data (AOD), are produced . The feedback derived from the first pass, including analysis, is used to tune the code for the second pass processing. One full copy of the raw data is stored at CERN, and a second one is shared among the Tier-1s outside CERN. Reconstruction is shared by the Tier-1 centres, CERN being in charge of processing the first pass. Subsequent data reduction, analysis and Monte Carlo production is a collective operation where all Tiers participate, with Tier-2s being particularly active for Monte Carlo and end-user analysis.

2.8.2 AliEn Framework

The concept of Grid is developed in ALICE to process the huge amount of ALICE data through a distributed computing resources. The top level management of the Grid resources is done through the AliEn [26] system. It is a set of middleware tools and services that implement a Grid infrastructure. AliEn has been used for both data production and end-user analysis. The AliEn system is built around Open Source components, uses Web services models and standard protocols. AliEn web services play a central role in enabling AliEn as distributed computing environment. The user interacts with them by the exchange of Simple Object Access Protocols (SOAP) messages and they constantly exchange messages between themselves behaving like a true Web of collaborating services. The AliEn has been extensively tested and used for producing the large amount of simulated data and processing the data recorded in pp and in Pb-Pb collisions. The results discussed in this thesis are obtained from the data processed by the this environment.

2.8.3 AliRoot Framework

The AliRoot [27] framework is the ALICE offline framework based on the Object-Oriented techniques for programming and, as a supporting framework, on the ROOT system, complemented by the AliEn system which gives access to the computing Grid. The framework is entirely written in C++ with some external programs still in FORTRAN. The AliRoot framework as shown in Fig. 2.12 is used for simulation, alignment, calibration, reconstruction, visualization and analysis of the experimental data.

Event simulation :

The role of the AliRoot framework is very wide and vital. It starts with the event generation; all the physics processes at the partonic level and the results of the primary particles are created by event generators. The framework provides interfaces

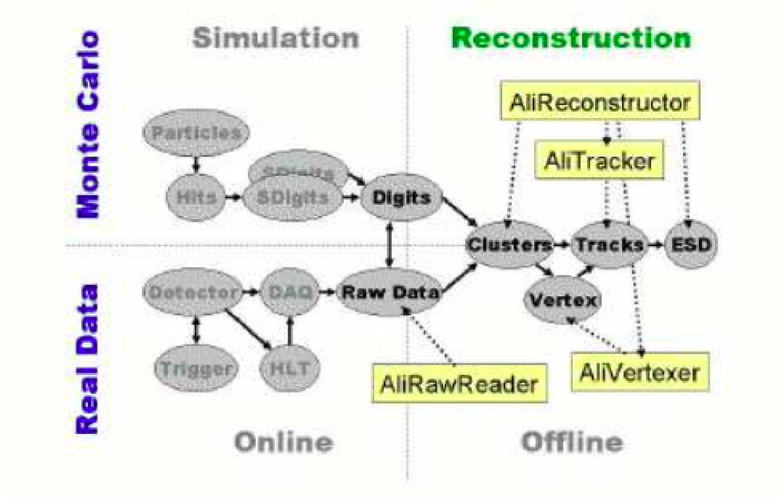

Figure 2.12: Schematic picture of AliRoot framework.

to the several event generators such as PYTHIA [28, 29], PHOJET [30, 31], HIJING [32], DPMJET [33] etc. The data produced by the event generators contain full information about the generated particles,i.e, their type, momentum, charge, and mother-daughter relationship, etc.

Detector response simulation :

The generated particles are transported through the detector geometry. The response of the each crossing particle is simulated. For the detector response simulation, different transport Monte Carlo packages are available such as GEANT3 [34], GEANT4 [35], and FLUKA [36]. The hits (energy deposited at a given point and time) are stored for each detector. The hits are converted into digits taking into account the detector and its electronics response function. The digits are stored in the specific hardware format of each detector as raw data.

Alignment framework :

The AliRoot-framework also provides the way to take care of the misalignment in positioning the part of detectors from their ideal positions. The part of detectors that are subject to relative positioning difference from the ideal one, are called *alignable volumes*. During the start of the simulation, the ideal geometry is generated by the compiled code or read from the OCDB where it was saved in previous run. Several objects are marked as alignable, that is the geometrical modeller is ready to accept modifications to their position, even if they were obtained by replication. The framework then reads the *alignment objects* which contain the *adjustments* in the position of the alignable objects. The particle transport is then performed in the modified geometry. The same procedure can be repeated during the reconstruction and, therefore, the effect of detector misalignment and the performance of alignment algorithms can be tested. During the real data reconstruction, best alignment objects are loaded from the OCDB. These are the alignment objects produced from the survey data. Survey data are automatically loaded into the Gird in a standard text format for automatic parsing and conversion to alignment objects. Alignment objects are stored in the OCDB and accessed via meta-data.

Calibration framework :

Similar to the alignment, the AliRoot-framework provides the provision for detector calibration. The calibration constants are stored in the OCDB, for first pass reconstruction, initial calibration constants come from the detector properties as measured during construction, or from online algorithms running during data-taking. Better calibration constants can be determined and stored in the OCDB for next pass reconstructions.

Reconstruction framework :

The reconstruction is performed on raw data for each detector and the final informations are stored as the Event Summary Data (ESD). The ESDs contain high level information e.g., in the case of PMD the ESD contains only the cluster properties information such as cluster ADC, cluster position, number of cells contained in the cluster, etc. The reconstruction can also be performed on the digits. Each detector has its own reconstruction code and the modular design of the AliRoot framework allows to run the reconstruction for each detector independently without interfering with the others. The reconstructed particles can be compared to the generated ones by using simulated data.

Analysis :

Analysis is the final operation performed on the data aimed at extracting and interpreting its physics content. In ALICE, analysis are performed either on the data sets which are produced after the reconstruction of real/simulated data, or on the data sets known as Analysis-Object Data (AODs) which are the reduced ESDs and contain only specific information required for a particular physics analysis. The entire analysis activities are categorized into two parts : scheduled and end-user analysis. An analysis framework is developed which can be used for both the categories. The implementation is done, using the different classes available with the ROOT software package in such a way that the user code is independent of the used computing schema. The analysis framework permits the splitting of each analysis into a tree of dependent tasks. Each task is data oriented; it registers the required input data and publishes the output. The framework is used extensively for obtaining the results presented in this thesis.

CERN Analysis Facility (CAF) :

For interactive and quick processing of the data, an analysis facility known as CERN Analysis Facility (CAF) is set up. This provides prompt analysis of pp data, pilot analysis of the Pb-Pb data, fast event reconstruction, calibration and alignment. Unlike Grid, only a part of total data recorded by the experiment and some simulated data are available on the CAF. The users can access the data and perform their analysis and tests using a parallel computing facility which is based on ROOT framework and known as Parallel ROOT Facility (PROOF) [37]. CAF is a very useful facility for quick checks on the experimental data, generating reliable parameters needed during the reconstruction such as calibration constants etc, before the second pass reconstruction.

Bibliography

[1] T. S. Pettersson (ed.), P. Lefevre (ed.), The Large Hadron Collider : conceptual design, CERN-AC-95-05 LHC (1995).

[2] LHC Design Report Volume I+II+III, CERN-2004-003-V-1, CERN-2004-003-V-2, CERN-2004-003-V-3 (2004), http://ab-div.web.cern.ch/ab-div/Publications/LHC-DesignReport.html.

[3] ALICE Collaboration, ALICE Technical Proposal for A Large Ion Collider Experiment at the CERN LHC, CERN/LHCC 95-71 (1995).

[4] The ALICE experiment at the CERN LHC, 2008 JINST 3 S08002.

[5] ATLAS Collaboration, ATLAS Technical Proposal, CERN/LHCC 94-43 (1994).

[6] CMS Collaboration, The Compact Muon Solenoid Technical Proposal, CERN/LHCC 94-38 (1994).

[7] LHCb Collaboration, LHCb Technical Proposal, CERN/LHCC 98-4 (1998).

[8] LHCf Collaboration, Technical Proposal for the CERN LHCf Experiment, CERN/LHCC 2005-032 (2005).

[9] TOTEM Collaboration, TOTEM Technical Proposal, CERN/LHCC 99-7 (1999).

[10] S.K. Prasad PhD thesis, Calcutta University, 2011.

[11] S. De PhD Thesis, Homi Bhabha National Institute, 2013.

[12] ALICE Collaboration, ALICE dimuon forward spectrometer: Technical Design Report, CERN-LHCC-99-022; http://cdsweb.cern.ch/record/401974; ALICE dimuon forward spectrometer: addendum to the Technical Design Report, CERN-LHCC-2000-046, http://cdsweb.cern.ch/record/494265.

[13] ALICE Collaboration, ALICE Inner Tracking System (ITS): Technical Design Report, CERN-LHCC-99-012, http://edms.cern.ch/file/398932/1.

[14] ALICE Collaboration, ALICE time projection chamber: Technical Design Report, CERN-LHCC-2000-001, http://cdsweb.cern.ch/record/451098.

[15] ALICE Collaboration, ALICE transition-radiation detector: Technical Design Report, CERN-LHCC-2001-021, http://cdsweb.cern.ch/record/519145.

[16] ALICE Collaboration, ALICE Time-Of-Flight system (TOF): Technical Design Report, CERN-LHCC-2000-012; http://cdsweb.cern.ch/record/430132; ALICE Time-Of-Flight system (TOF): addendum to the technical design report, CERN-LHCC-2002-016, http://cdsweb.cern.ch/record/545834.

[17] ALICE Collaboration, Technical design report of the photon spectrometer, CERN-LHCC-99-004, http://cdsweb.cern.ch/record/381432.

[18] ALICE Collaboration, ALICE electromagnetic calorimeter: addendum to the ALICE technical proposal, CERN-LHCC-2006-014, http://cdsweb.cern.ch/record/932676.

[19] ALICE Collaboration, ALICE high-momentum particle identification: Technical Design Report, CERN-LHCC-98-019, http://cdsweb.cern.ch/record/381431.

[20] A. Fernndez et al., Cosmic ray physics with the ALICE detectors, Czech. J. Phys. 55 (2005) B801; A. Fernndez et al., ACORDE a cosmic ray detector for ALICE, Nucl. Instrum. Meth. A 572 (2007) 102.

[21] ALICE Collaboration, ALICE Zero-Degree Calorimeter (ZDC): Technical Design Report, CERN-LHCC-99-005, http://cdsweb.cern.ch/record/381433.

[22] ALICE Collaboration, ALICE Photon Multiplicity Detector (PMD): Technical Design Report, CERN-LHCC-99-032; http://cdsweb.cern.ch/record/451099; ALICE Photon Multiplicity Detector (PMD): addendum to the technical design report, CERN-LHCC-2003-038, http://cdsweb.cern.ch/record/642177.

[23] ALICE Collaboration, ALICE forward detectors: FMD, TO and VO: Technical Design Report, CERN-LHCC-2004-025, http://cdsweb.cern.ch/record/781854.

[24] J. F. Grosse-Oetringhaus, PhD thesis, University of Munster, Germany, 2009.

[25] ALICE Collaboration, ALICE Technical Design Report of the Trigger, Data Acquisition, High-Level Trigger, Control System, CERN/LHCC 2003/062 (2004), https://edms.cern.ch/document/456354/2.

[26] P. Saiz et al., AliEnALICE environment on the GRID, Nucl. Instrum. Meth. A502, 437 (2003); AliEn home page, http://alien.cern.ch/.

[27] http://www.cern.ch/ALICE/Projects/offline/aliroot/Welcome.html.

[28] PYTHIA 6.4, Physics and Manual, hep-ph/0603175, FERMILAB-PUB-06-052-CD-T, March 2006.

[29] T. Sjostrand, Comput. Phys. Commun. 82, 74 (1994).

[30] R. Engel, Z. Phys. C 66, 203 (1995).

[31] R. Engel, J. Ranft, S. Roesler, Phys. Rev. D 52, 1459 (1995).

[32] M. Gyulassy, X. -N. Wang, Phys. Rev. C80, 024906 (2009).

[33] J. Ranft: New features in DPMJET version II.5, Siegen preprint, 1999.

[34] R. Brun, F. Bruyant, M. Maire, A. C. McPherson and P. Zanarini, GEANT3 user guide, CERN data handling division DD/EE/84-1 (1985), http://wwwinfo.cern.ch/asdoc/geantold/GEANTMAIN.html; M. Goossens et al., GEANT detector description and simulation tool, CERN program library long write-up W5013 (1994), http://cdsweb.cern.ch/record/1073159.

[35] S. Agostinelli et al., Geant4, a simulation toolkit, Nucl. Instrum. Meth. A506, 250 (2003), CERN-IT-2002-003, http://cdsweb.cern.ch/record/602040; http://wwwinfo.cern.ch/asd/geant4/geant4.html.

[36] A. Fasso et al., FLUKA: present status and future developments, Proceedings of the IV International Conference on Calorimeters and their Applications, World Scientific, Singapore (1994).

[37] M. Ballintijn, R. Brun, F. Rademakers and G. Roland, Distributed parallel analysis framework with PROOF, http://root.cern.ch/twiki/bin/view/ROOT/PROOF.

3
Multiplicity Distributions

In this chapter, the measurements related to the number of the produced charged particles, i.e, the multiplicity of the charged particles in high-energy collisions have been discussed. In addition, some results from the earlier and recent experiments have been presented.

3.1 Introduction

The charged-particle multiplicity produced in a collision is a basic observable measured in an experiment. The multiplicity distribution is the probability distribution to obtain the number of produced particles in the final state. This probability depends on the mechanisms of the particle production. The particles may be produced in an independent manner having no correlation among them. In this case, we observe a Poisson distribution. Therefore, wherever a deviation from Poisson distribution is observed, a correlation among the produced particles must be there. The proper understanding of the multiplicity distributions is necessary to have information on the particle-production and its mechanisms. It helps to improve the models describing the particle production. This also provides constraints on the models, or rejects the models not describing the production of the particles correctly. The models mostly are available in the form of the Monte Carlo event generators. The particle production models are briefly discussed in the next paragraph.

There are two main approaches to describe the soft-hadronic reactions. These are the quark-recombination model and the string-fragmentation model. The colliding systems generate quarks and gluons, which get detected by the detector after hadronization. In the recombination model, the lowest valence quarks are used for the recombination. The probability is described by a process independent recombination function, which basically describes the formation of the mesons (baryons) from two (three) quarks [1]. In the Cluster fragmentation models [2], the partons

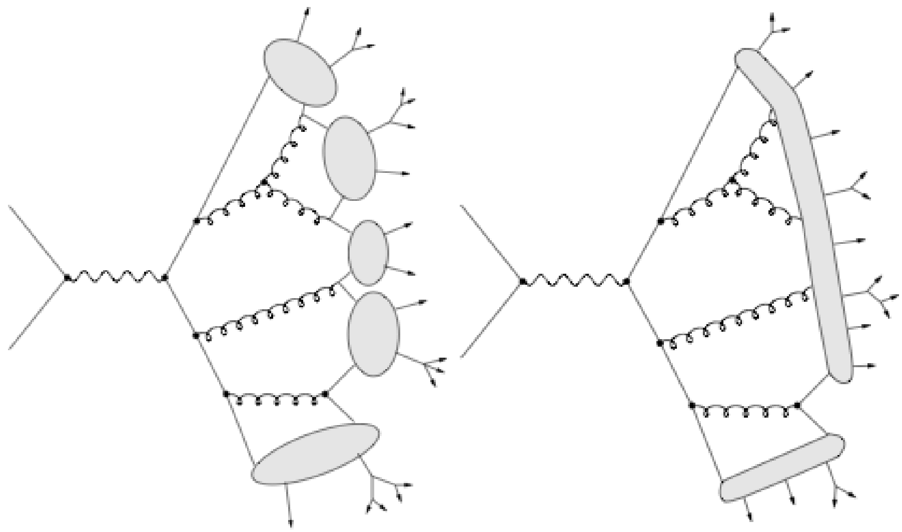

Figure 3.1: Illustration of the Cluster (left) and Lund String fragmentation (right) models for hadronization

generated in the branching process tend to be arranged in confined color-singlet clusters. After the parton-shower, quark-antiquark pairs are formed by splitting of these clusters (as shown in Fig. 3.1, on the left). These pairs undergo decay into pairs of hadrons depending on the mass of the clusters. This model faces problems to deal with the decay of the massive clusters.

The Lund String fragmentation models [3] are widely used in the event generators, such as, PYTHIA, JETSET, HIJING, etc. The basic concept of this model depends on the fact that, at long distances, the QCD field lines between the quark-antiquark pairs are compressed into a tube-like region because of the strong attraction between the two. This looks like a string (as shown in Fig. 3.1, on the right). A linear confinement potential is produced by the string. The string breaks up into two

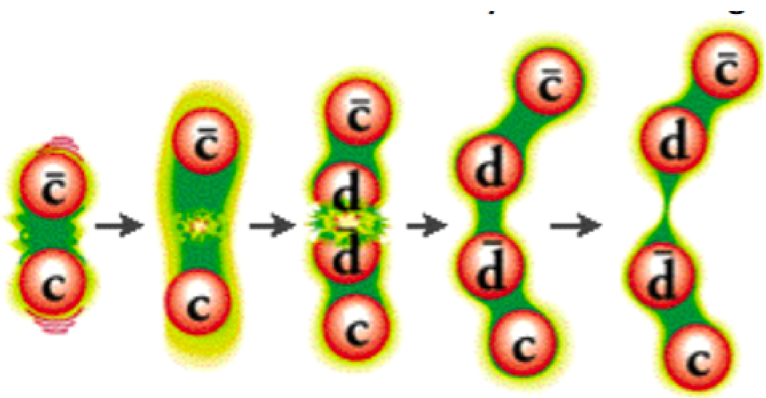

Figure 3.2: Lund String fragmentation

color-singlet strings and this process continues if the invariant mass of the string is greater than the on-shell mass of a hadron (The process is shown in Fig. 3.2). The model has extra parameters for the suppression of the heavy particles.

These particle-production models get modified depending on the information from the experiments, such as, how the particles are produced, whether they have correlations among them or not, what kind of systems are colliding, i.e, proton-proton (pp), proton-nucleus (pA) or nucleus-nucleus (AA), etc. Charged-particle multiplicity distributions help to understand these informations, which are very useful to form the proper Monte Carlo event generators.

3.2 Multiplicity distributions in pp collisions

The proper understanding of the multiplicity distributions in pp collisions is essential as a baseline to the heavy-ion results. Multiplicity distributions in pp collisions are usually presented for all inelastic collisions or non-single-diffractive (NSD) collisions. In the NSD collisions, the single diffractive events, in which one of the beam particles breaks to produce particles at higher rapidities on one side, are rejected [4].

Multiplicity distributions in pp collisions have been found to follow a universal scaling during the analysis of the Bubble chamber data below $\sqrt{s} = 24\ GeV$ [5]. This is called the KNO (Koba, Nielsen,Olesen)-scaling [6]. KNO-scaling is based on the Feynmen-scaling [7]. In this scaling, it is observed that above certain energy, the height of the rapidity distribution, i.e, $dN_{\rm ch}/dy|_{y=0}$, as well as the pseudorapidity distribution, i.e, $dN_{\rm ch}/d\eta|_{\eta=0}$ do not depend on energy. The mean multiplicity $\langle n \rangle$ at high energies is proportional to logarithm of $\sqrt{s}$, i.e, $\langle n \rangle \propto ln\sqrt{s}$. In the KNO-scaling, it is derived that a function, defined as $\psi(z) = \langle n \rangle P(n)$, where $z = n/\langle n \rangle$, remains same for all energies and thus reaches a universal scaling. It is observed that, at the CERN Intersecting Storage Rings (ISR)-energies, the KNO-scaling is satisfied [4, 8]. The charged-particle multiplicities in pp collisions for NSD events in the full phase-space were determined using the split-field-magnet (SFM)-detector. The results are shown in Fig. 3.3.

UA5 collaboration later observed the breaking of KNO-scaling in $p + \bar{p}$ collisions at $\sqrt{s} = 200\ GeV$ [4, 9]. From Fig. 3.4, it is observed that, the function plotted in the y-axis does not have a universal energy-independent form above $\sqrt{s} = 200\ GeV$.

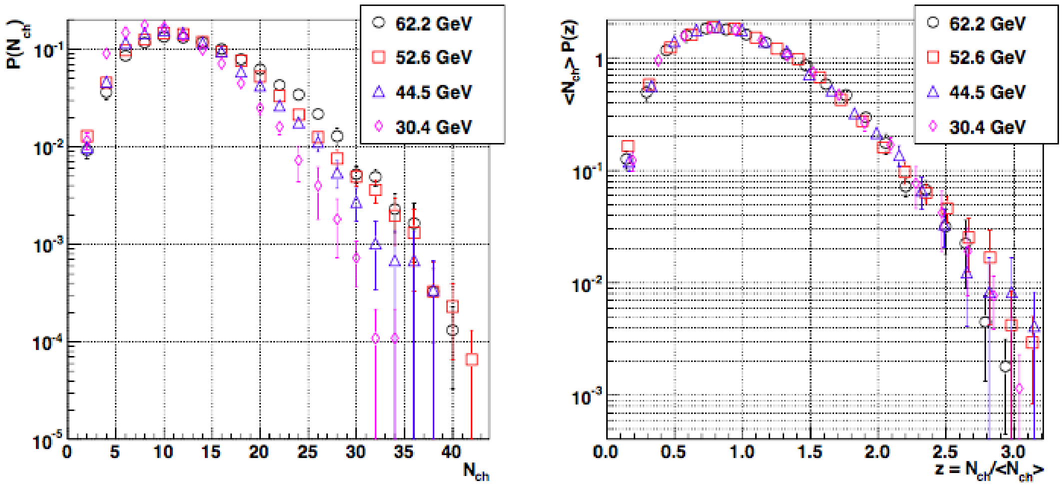

Figure 3.3: The normalized charged particle multiplicity distributions in pp collisions at ISR energies (left panel). Distributions plotted with KNO-variable and KNO-scaling satisfied (right panel)

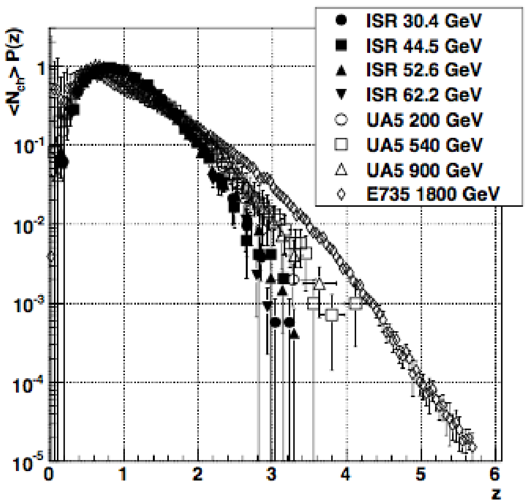

Figure 3.4: Violation of KNO-scaling at $\sqrt{s} = 200\ GeV$

It is found that above this energy, multiplicity distributions in pp collisions are well described by the Negative Binomial Distributions (NBD). NBD of an integer n is defined as,

$$P(n) = \frac{\Gamma(n + k_{\mathrm{NBD}})}{\Gamma(n+1)\Gamma(k_{\mathrm{NBD}})} \frac{(\mu/k_{\mathrm{NBD}})^n}{(1+\mu/k_{\mathrm{NBD}})^{n+k_{\mathrm{NBD}}}} \tag{3.1}$$

where, $\mu = \langle n \rangle$ is the mean multiplicity. The two parameters characterize negative binomial distributions, i.e, mean $\langle n \rangle$ and k_{NBD}, which is related to the width of the distribution. $1/k_{\mathrm{NBD}}$ is found to be increasing linearly with ln $\sqrt{s}$. We get a Poisson distribution for $k_{\mathrm{NBD}} \rightarrow \infty$. Single NBD could not describe the data very well above $\sqrt{s} = 900\ GeV$. A shoulder-like structure appears in the multiplicity distributions which later could be described well using double-NBD's. This is basically a combination of two NBD's, one soft component and another one semi-hard component. Thus, the multiplicity distributions depend on five parameters, defined as [4],

$$P(n) = \alpha_{\mathrm{soft}} \times P_{<n>_{\mathrm{soft}}, k_{\mathrm{soft}}}(n) + (1 - \alpha_{\mathrm{soft}}) \times P_{<n>_{\mathrm{semi-hard}}, k_{\mathrm{semi-hard}}}(n) \tag{3.2}$$

where, $< n >_{\mathrm{semi-hard}} \approx 2 < n >_{\mathrm{soft}}$.

Recent results for pp collisions from the CMS [10] and ALICE [11] collaboration also confirm the fact that KNO-scaling is already broken and the distributions are fitted well with the double-NBD. The results from ALICE for pp NSD events at $\sqrt{s}$ = 7 TeV and $\sqrt{s}$ = 8 TeV are shown in Fig. 3.5. The shaded areas are the combined statistical and systematic uncertainties. It is clearly observed from the ratios of the data to single and double-NBD fits, that in LHC-energies too, the multiplicity distributions are following double-NBD's, as the ratios are close to 1 for

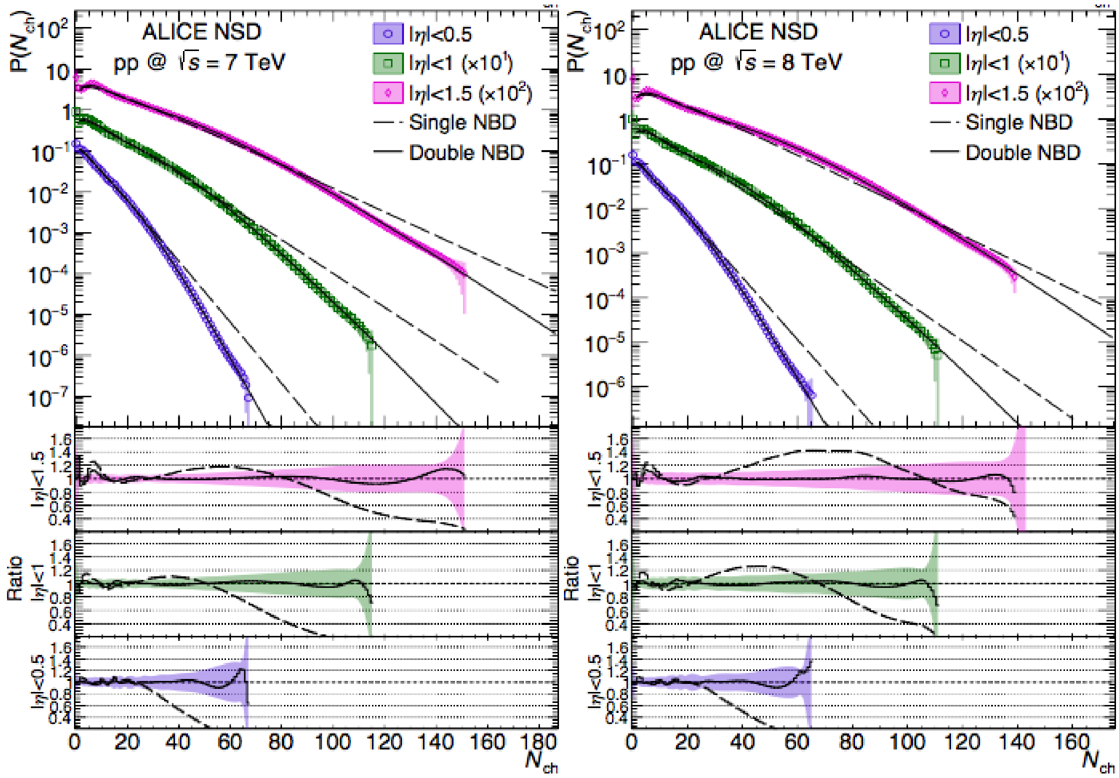

Figure 3.5: Multiplicity distributions in pp collisions for NSD events for three different η-ranges in ALICE. Ratios of the data to single and double-NBD fits are shown also

the double-NBD fits.

Multiplicity distributions in e^+e^- collisions have been found to be Poissonian earlier, at $\sqrt{s} = 29\ GeV$ [4, 12]. For Poisson distributions, the dispersion D is equal to the average multiplicity $\langle n \rangle$, i.e, $D = \sqrt{n}$. It is found that, for e^+e^- collisions, below $\sqrt{s} = 91.2\ GeV$, KNO scaling are almost satisfied. Similar to $p+\bar{p}$ collisions, a shoulder-like structure was observed in e^+e^- collisions in the Delphi experiment [13] at $\sqrt{s} = 91.2\ GeV$.

3.3 Multiplicity distributions in heavy ion collisions

Multiplicity distributions have been measured in heavy ion collisions in many experiments till now. Initially it was measured in E802-experiment at BNL-AGS in O-Cu collisions at $\sqrt{s}_{\rm NN} = 4.86\ GeV$ [4]. Then, it was measured in O-Au collisions at $\sqrt{s}_{\rm NN} = 17.3\ GeV$ in WA80-experiment in CERN. We get results also from NA35-experiment for S-S, O-Au, and S-Au collisions at $\sqrt{s}_{\rm NN} = 17.3\ GeV$ [15]. Later, multiplicity distributions were presented from WA98-experiment (CERN) [5] in Pb-Pb collisions at $\sqrt{s}_{\rm NN} = 17.3\ GeV$ and NA49-experiment (CERN) [6] in Pb-Pb collisions at 20A, 30A, 40A, 80A, and 158A GeV energies. Additionally we have results from the NA49-experiment for different systems, i.e, Pb-Pb, C-C, and Si-Si collisions at 158A GeV energy [7]. For heavy-ion collisions, depending upon the energies as well as the systems colliding, the multiplicity distributions get changed. Fig. 3.6 shows the multiplicity distribution for all charged particles for $0-1\%$ centrality in Pb-Pb collisions at 158A GeV for NA49 experiment. The dashed line here

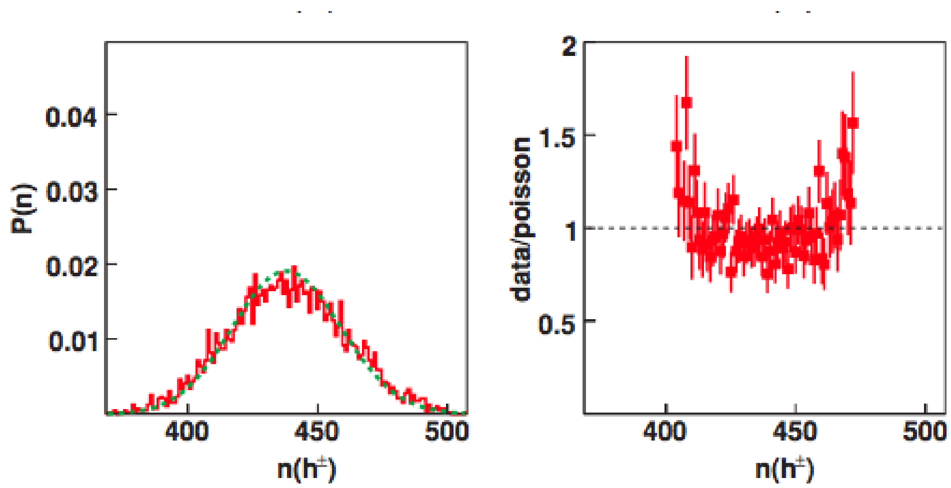

Figure 3.6: Multiplicity distribution for all charged hadrons in the most central Pb-Pb collisions at 158A GeV from NA49-experiment in the experimental acceptance

shows the Poisson distribution with the same $\langle n \rangle$ as data. In the right panel, the data to Poisson ratio has been presented [6]. Here, we see that, the distribution is not exactly Poissonian, but varies from it.

In most of the cases, the NBD's describe the multiplicity distributions in heavy-ion collisions well [4, 15]. From E802-results, it has been observed that the multiplicity distributions get fitted by the negative binomial distributions for all the pseudorapidity intervals taken, in the range $1.2 \leq \eta \leq 2.2$. From PHENIX-experiment at RHIC, results were shown for different collision-energies and different collision-systems, such as, $\sqrt{s_{\rm NN}} = 200\ GeV$ Au-Au, 62.4 GeV Au-Au, 200 GeV Cu-Cu, 62.4 GeV Cu-Cu, and 22.5 GeV Cu-Cu [11]. It is observed from Fig. 3.7 that the multiplicity distributions in Au-Au collisions are fitted with NBD very well for all centralities (The dashed lines present the fits to NBD-distributions). The data are presented as normalized to mean to see the results for all the centralities together in a convenient way. Similarly, NBD can describe well the data for Cu-Cu collisions

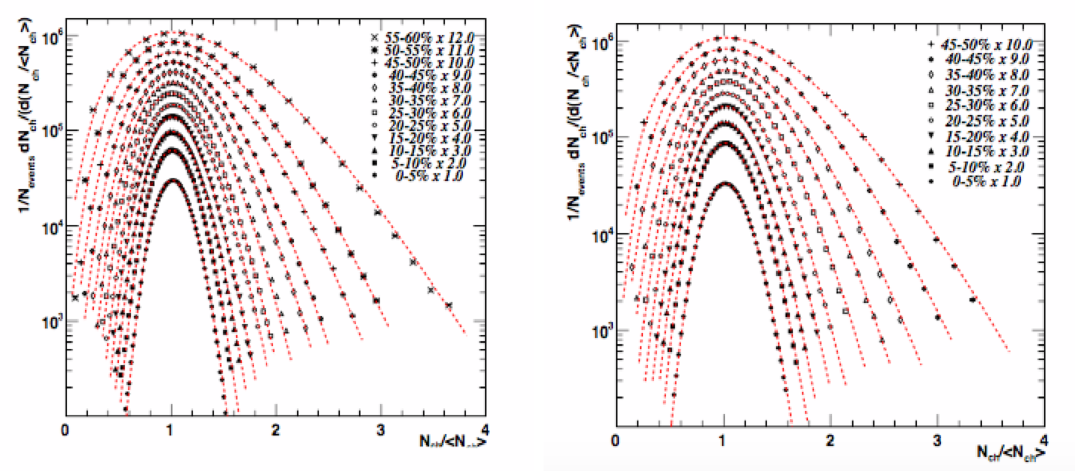

Figure 3.7: Charged-particle multiplicity distributions for Au-Au collisions at $\sqrt{s}_{\rm NN}$ = 200 GeV (left panel) and $\sqrt{s}_{\rm NN}$ = 62.4 GeV (right panel) for $0.2 < p_{\rm T} <$ 2 GeV/c in PHENIX

too at these energies [11].

An example of the multiplicity distribution in Pb-Pb collision at 2.76 TeV energy has been presented in Fig. 3.8, for a particular centrality, i.e, $40 - 41\%$. The events are generated with AMPT model with String Melting. The distribution has been fitted with NBD, which is represented by the red line. σ and mean of the multiplicity distribution has been also shown. Details of the multiplicity distributions in Pb-Pb collisions at this energy will be discussed in details later.

3.4 Multiplicity and Pseudorapidity density

Pseudorapidity density distribution of the produced particles in the high-energy collisions is a global observable which helps to understand the dynamics of the system. Pseudorapidity density, i.e, $\frac{dN}{d\eta}$ is related to the total energy of the produced

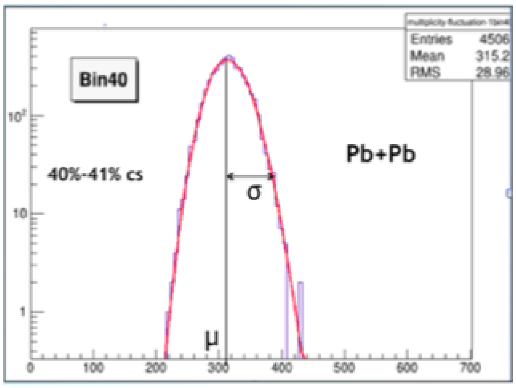

Figure 3.8: Charged-particle multiplicity distribution for $40-41\%$ centrality in Pb-Pb collisions at $\sqrt{s}_{\mathrm{NN}} = 2.76$ TeV for $0.2 < p_{\mathrm{T}} < 2$ GeV/c. Events are generated with AMPT-String Melting model

particles available at midrapidity. In [20], the total energy is expressed as,

$$E_{\mathrm{tot}} = 2E_{\mathrm{part}} \frac{dN_{\mathrm{ch}}}{d\eta}|_{\eta\leq 1} f_{\mathrm{neutral}} f_{4\pi} \tag{3.3}$$

where, E_{part} is the average energy per particle, f_{neutral} is a factor for undetected neutral particles.

The transverse energy E_{T} is the energy produced in the transverse plane with the beam direction and this is roughly related to the pseudorapidity density via [22],

$$\frac{dE_{\mathrm{T}}}{d\eta} \sim \langle p_{\mathrm{T}} \rangle \times \frac{dN}{d\eta} \tag{3.4}$$

E_{T} basically helps to understand how violent the interaction of the nuclei is. The rapidity density ($\frac{dN}{dy}$) provides information about the entropy of the system.

E_T is related to the initial energy density (ϵ_{Bj}) in the Bjorken model [23].

$$\epsilon_{Bj} = \frac{dE_T}{dy}\frac{1}{\tau_0 \pi r^2} \simeq \langle m_T \rangle \frac{3}{2}\frac{dN_{ch}}{d\eta}\frac{1}{\tau_0 \pi r^2} \tag{3.5}$$

where, τ_0 is the formation time and πr^2 is the transverse overlap area of the colliding nuclei. The initial energy-density is also very important to understand the QGP-formation.

3.4.1 Pseudorapidity density distribution of charged particles

Pseudorapidity density distribution of charged particles, i.e, $\frac{dN_{ch}}{d\eta}$ has been measured in different experiments at various energies and collision centralities. Fig. 3.9 presents

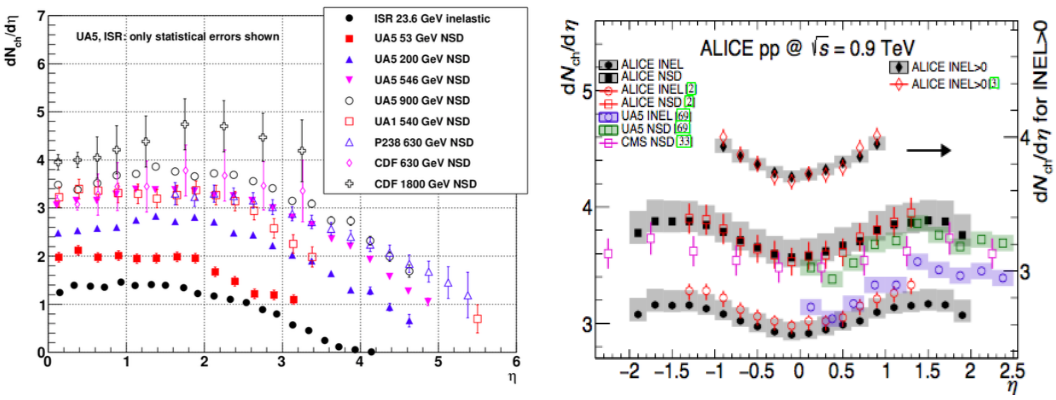

Figure 3.9: $\frac{dN_{ch}}{d\eta}$ measured in the ISR, UA5, UA1, P238 and CDF-experiments at different energies (left panel); $\frac{dN_{ch}}{d\eta}$ measured for pp collisions in ALICE [11] and CMS [21]-energies at $\sqrt{s} = 0.9$ TeV (right panel). The comparison with results from UA5-energies have been presented here

the results for $\frac{dN_{ch}}{d\eta}$ for the proton-proton collisions from the ISR to the Tevatron-energies [4]. Most of the results are shown for NSD-events except for the result obtained at the ISR-energy. The dip in the distributions around $\eta \approx 0$ comes due to the transformation of y into η. Fig. 3.10 shows the results for charged particle pseu-

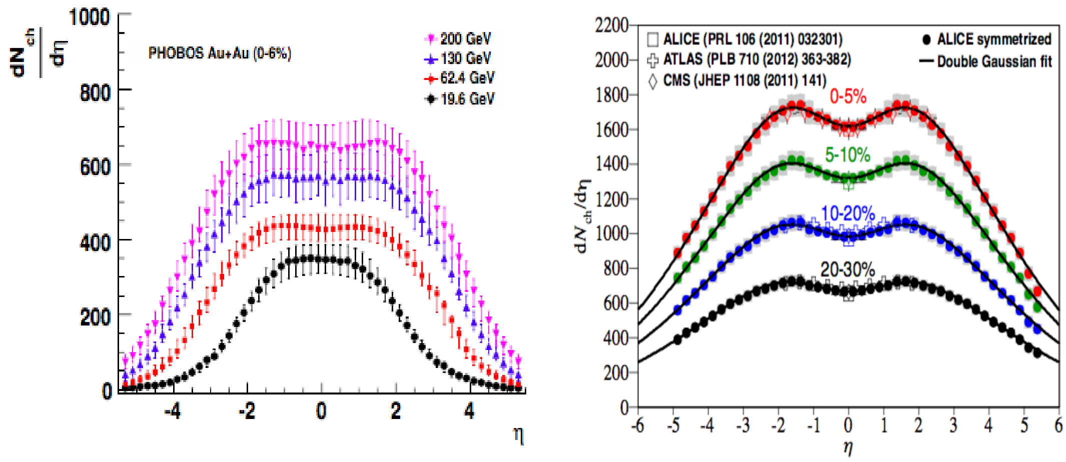

Figure 3.10: $\frac{dN_{\rm ch}}{d\eta}$ in PHOBOS-energies for Au-Au most central collisions (left panel) and in LHC-energies for Pb-Pb collisions(right panel)

dorapidity density distributions from PHOBOS and ALICE-experiments [22, 24]. The distributions in LHC-energies [24] are well fitted with double gaussian function of the form $A_1 e^{-\frac{\eta^2}{\sigma_1^2}} - A_2 e^{-\frac{\eta^2}{\sigma_2^2}}$. Here, A_1,A_2 are the amplitudes of the two gaussians and σ_1,σ_2 are the widths of the distributions.

3.4.2 Longitudinal Scaling

According to the limiting fragmentation hypothesis [25], the pseudorapidity density expressed in terms of $\eta' = \eta - y_{\rm beam}$, where $y_{\rm beam}$ is the beam rapidity ($= \sqrt{s}_{\rm NN}/m_{\rm p}$), achieves a liming value in the fragmentation region and this is independent of the collision energy. This is called the longitudinal scaling. Fig. 3.11 shows the longitunal scaling for pp collisions (left panel) and heavy ion collisions (right panel). Thus,

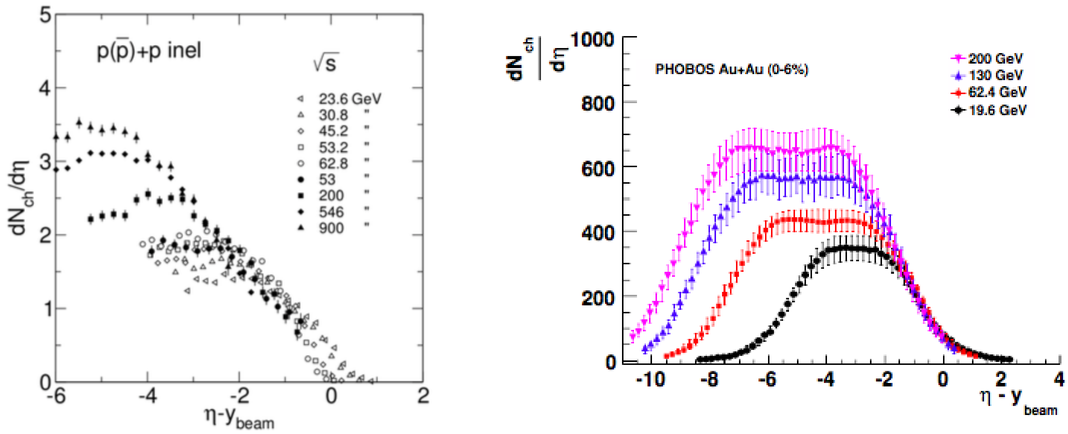

Figure 3.11: Longitudinal scaling for pp collisions for ISR, UA5, UA1 and CDF-energies [22] (left) ; Same for Au-Au collisions in PHOBOS [22]

by considering the collision process in the rest frame of the projectile, a longitudinal scaling is achieved.

3.4.3 Energy dependence of $dN_{\mathrm{ch}}/d\eta$

Charged particle pseudorapidity density per participant pair has been shown as a function of the collision energy in Fig 3.12. The power-law fits to pp-data and the most central Pb-Pb data have been also shown [27]. It is observed that the fits describe the data well.

3.4.4 Dependence of $dN_{\mathrm{ch}}/d\eta$ on N_{part}

The produced charged particles are related to the number of participants (N_{part}) and the number of binary collisions (N_{coll}). Fig. 3.13 shows the dependence of pseudorapidity density per participant pair on $\langle N_{\mathrm{part}} \rangle$ for Pb-Pb collisions at $\sqrt{s_{\mathrm{NN}}} =$ 2.76 TeV and Au-Au collisions at $\sqrt{s_{\mathrm{NN}}} = 200$ GeV [28]. The scale of 200 GeV data

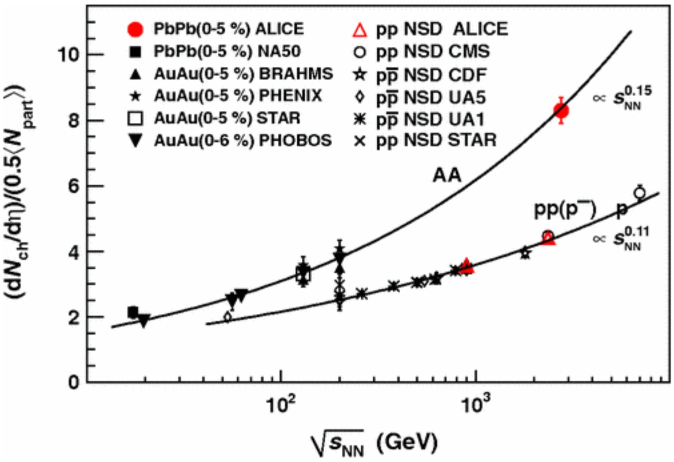

Figure 3.12: Energy dependence of $dN_{\mathrm{ch}}/d\eta$ per participant pair as a function of $\sqrt{s}_{\mathrm{NN}}$

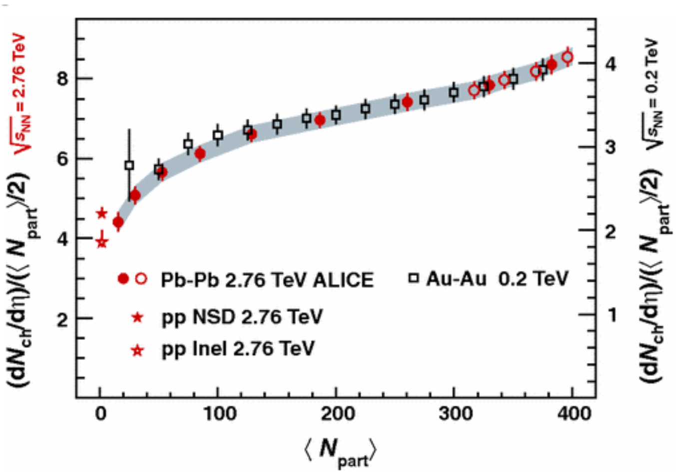

Figure 3.13: Dependence of pseudorapidity density per participant pair on $\langle N_{\mathrm{part}}\rangle$ for Pb-Pb collisions at $\sqrt{s}_{\mathrm{NN}} = 2.76$ TeV and Au-Au collisions at $\sqrt{s}_{\mathrm{NN}} = 200$ GeV [28].

is shown on the right side and the scale of the 2.76 TeV data is on the left side. In [29], a universal function with a combination of logarithmic and power-law, has been presented which can fit the results well.

3.4.5 Energy dependence of the total multiplicity

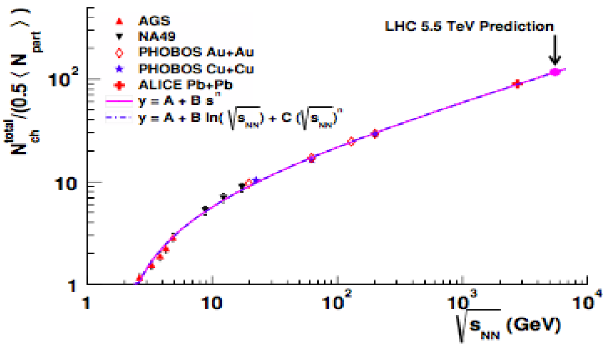

Figure 3.14: $N_{\rm ch}^{total}$ per participant pair as a function of energy. The fits with power-law and hybrid function has been shown

As soon as $dN_{\rm ch}/d\eta$ is known for a collision system at some certain energy, it is easier to get the information on the number of the total charged particles ($N_{\rm ch}^{total}$) per participant pair, by integrating the pseudorapidity distribution over the whole beam-rapidity. $N_{\rm ch}^{total}$ is related to the initial entropy. It has been shown in [29], that a hybrid function combining logarithmic and power law (shown in Fig. 3.14) can explain the results from lower energies to LHC-energies. A prediction for results at $\sqrt{s}_{\rm NN} = 5.5$ TeV has also been presented.

A detailed discussion has been presented here on the essence of the measurements related to the charged particle multiplicity distributions. The results obtained for the proton-proton and heavy-ion collisions at different energies have been reviewed.

The multiplicity distributions for Pb-Pb collisions at $\sqrt{s}_{\mathrm{NN}} = 2.76\ TeV$ will be presented and discussed in Chapter 8.

Bibliography

[1] R. C. Hwa, Phys. Rev. **D 22**,1593 (1980).

[2] G. Marchesini and B. R. Webber, Nucl. Phys. **B238**,1 (1984).

[3] B. Andersson, G. Gustafson and B. Soderberg, Z. Phys. **C20**, 317 (1983).

[4] Jan Fiete Grosse-Oetringhaus, K. Reygers, J. Phys. **G37** 083001(2010).

[5] P. Slattery. Phys. Rev. Lett. 29 1624 (1972).

[6] Z. Koba, H. B. Nielsen, and P. Olesen. Nucl. Phys. **B40** 317 (1972).

[7] R. P. Feynman. Phys. Rev. Lett. 23 1415 (1969).

[8] A. Breakstone et al. Phys. Rev. **D30** 528 (1984).

[9] R. E. Ansorge et al. Z. Phys. **C43** 357 (1989).

[10] **CMS Collaboration**, V. Khachatryan *et al.*, JHEP 1101 (2011) 079, arXiv:1011.5531 [hep-ex].

[11] **ALICE Collaboration**, J. Adam *et al.*, arXiv:1509.07541 [nucl-ex].

[12] M. Derrick *et al.* Phys. Rev. **D34** 3304 (1986).

[13] P. Abreu *et al.* Z. Phys. **C52** 271 (1991).

[14] T. Abbott *et al.* [E-802 Collaboration], Phys. Rev. **C 52**, 2663 (1995).

[15] J. Bachler *et al.* [NA35 Collaboration], Z. Phys.**C 57**, 541 (1993).

[16] M. M. Aggarwal et al. [WA98 Collaboration], Phys. Rev. **C 65**, 054912 (2002).

[17] C. Alt. *et al.* (NA49 Collaboration), Phys. Rev. **C 78**, 034914 (2008).

[18] C. Alt *et al.* [NA49 Collaboration], Phys. Rev. **C 75**, 064904 (2007).

[19] A. Adare et al. (PHENIX Collaboration) Phys. Rev. **C 78**, 044902 (2008).

[20] B. B. Back *et al.*, Nucl. Phys., vol. **A757**, pp. 28101, 2005.

[21] **CMS Collaboration**, V. Khachatryan *et al.*, Phys.Rev.Lett. 105 (2010) 022002.

[22] R. Sahoo *et al.*, Advances in High Energy Physics, Volume 2015, Article ID 612390. arxiv:1408.5773 [nucl-ex] (2014).

[23] J.D. Bjorken, Phys. Rev. **D 27**, 140 (1983).

[24] **ALICE Collaboration** E. Abbas *et al.* Phys. Lett. **B 726** (2013) 610-622.

[25] J. Benecke, T. T. Chou, C.-N. Yang and E. Yen,Phys. Rev. **188**, 2159 (1969).

[26] B. B. Back *et al.*, Nucl. Phys., vol. **A757**, pp. 28101, 2005.

[27] **ALICE Collaboration** K. Aamodt *et al.*, Phys.Rev.Lett., **vol. 105**, p. 252301, 2010.

[28] **ALICE Collaboration** K. Aamodt *et al.*, Phys. Rev. Lett. **vol. 106**, 032301, 2011.

[29] R. Sahoo and A. N. Mishra, arXiv:1304.2113 (2013).

4 Multiplicity Fluctuations : Introduction and Statistical Formalisms

The essence of the multiplicity fluctuation studies has been discussed in this chapter. The connection of the multiplicity fluctuations to the QCD-phase transition is discussed in details. The fluctuations depend on the statistical ensembles and the results for the fluctuations in different ensembles are shown here.

4.1 Introduction

The fluctuation-studies are of immense importance to study the QGP-phase. Multiplicity and its fluctuations have effects on all the other measurements. Charged particle multiplicity fluctuations have been characterised by the scaled variances of the multiplicity distributions, defined as,

$$\omega_{\mathrm{ch}} = \frac{\langle N_{\mathrm{ch}}^2 \rangle - \langle N_{\mathrm{ch}} \rangle^2}{\langle N_{\mathrm{ch}} \rangle} = \frac{\sigma^2}{\mu} \tag{4.1}$$

where, $\langle N_{\mathrm{ch}} \rangle \equiv \mu = \frac{\sum N_{\mathrm{ch}}}{n}$, N_{ch} is the multiplicity per event and n is the total number of events. σ^2 is the variance of the multiplicity distribution, as shown in Fig. 3.8.

This is an intensive quantity, i.e, independent of the volume of the system formed in the high-energy collisions.

Multiplicity fluctuations are directly related to the parameters of the multiplicity distributions. In Chapter 3, it has been discussed that the multiplicity distributions can be defined by the Negative Binomial Distibutions (Eq. 3.1). The parameters of the NBD's, i.e, the mean μ and k_{NBD} describing the charged particle multiplicity distributions, can be related to the scaled variances of the distributions by,

$$\omega_{\mathrm{ch}} = 1 + \frac{\mu}{k_{\mathrm{NBD}}} \tag{4.2}$$

Therefore, it is possible to measure the μ and σ of the charged particle multiplicity distributions to find ω_{ch}. Alternatively, it is possible to fit the multiplicity distributions, find μ and k_{NBD} as the fit parameters, use Eq. 4.2 and calculate ω_{ch}.

Multiplicity fluctuations have contributions from statistical (random) components as well as those which have dynamical (deterministic) origin. The statistical components have contributions from the choice of centrality, fluctuation in impact parameter or number of participants, finite particle multiplicity, effect of limited acceptance of the detectors, fluctuations in the number of primary collisions, effect of rescattering, etc. [1, 2, 3].The statistical components of the multiplicity fluctuations have direct impact on the fluctuations in other measured quantities. The dynamical part of the fluctuations contain interesting physics associated with the collision, which include time evolution of fluctuations at different stages of the collision, hydrodynamic expansion, hadronization and freeze-out. In order to extract the dynamical part of the fluctuations, the contribution to multiplicity from statistical components has to be well understood. We discuss the methods for controlling geometrical fluctuations so that dynamical fluctuations, if present, become more prominent.

Multiplicity fluctuations have been reported by E802 experiment [4] at AGS, WA98 [5], NA49 [6, 7], NA61 [8, 9] and CERES [10] experiments at SPS, and the PHENIX experiment [11] at RHIC.

4.2 Connection to QCD phase transition

The fluctuations of experimentally accessible quantities, such as particle multiplicity, mean transverse momentum, temperature, particle ratios, and other global observables are related to the thermodynamic properties of the system, such as the entropy, specific heat, chemical potential and matter compressibility [1, 12, 13, 14]. Fluctuations of these quantities on an event-by-event basis have been used as basic tools for understanding the particle production mechanisms, the nature of the phase transition and critical fluctuations at the QCD phase boundary.

Theoretical models, based on lattice QCD, reveal that at vanishing baryon chemical potential (μ_B), the transition from QGP to hadron gas is a smooth crossover, whereas at large μ_B, the phase transition is of first order [15]. Experimental observables at SPS and RHIC energies may point to the onset of deconfinement and a hint of first order phase transition has been indicated [14, 16, 17, 18, 19]. First order phase transitions can lead to large density fluctuations resulting in bubble or droplet formation and hot spots [2, 20, 21, 22, 23], which give rise to large multiplicity fluctuations in a given rapidity interval. The local multiplicity fluctuations have been predicted as a signature of critical hadronization at RHIC and LHC energies [24].

A non-monotonic behaviour of the fluctuations as a function of collision centrality and energy may signal the onset of deconfinement, and can be effectively used to probe the critical point in the QCD phase diagram [3]. Isothermal compressibility (k_{T}) of a system can be defined as [11],

$$k_{\mathrm{T}} = -\frac{1}{V}\left(\frac{\delta V}{\delta P}\right)_{\mathrm{T}} \tag{4.3}$$

where, V is the volume, T is the temperature, and P is the pressure of the system. The Grand Canonical Ensemble (GCE) properties may be considered to be true for experimental measurements near mid-rapidity , as energy and conserved quantum numbers here are exchanged with the rest of the system [25]. Therefore, following GCE-properties, variance is directly related to isothermal compressibility of the produced system [11, 12, 26], i.e,

$$\sigma^2 = \frac{k_{\mathrm{B}}T\mu^2}{V}k_{\mathrm{T}} \tag{4.4}$$

Therefore,

$$\omega_{\mathrm{ch}} = \frac{k_{\mathrm{B}}T\mu}{V}k_{\mathrm{T}} \tag{4.5}$$

where, μ is the mean multiplicity and k_{B} is Boltzmann's constant. So, scaled variance is directly proportional to k_{T}. The k_{T} increases almost 10-100 times at the critical point of the phase transition, where it is expected to have a power-law scaling with a critical exponent γ as,

$$k_{\mathrm{T}} \propto \left(\frac{T - T_{\mathrm{c}}}{T_{\mathrm{c}}}\right)^{-\gamma} \propto \epsilon^{-\gamma} \tag{4.6}$$

As k_{T} is proportional to the multiplicity fluctuations expressed in terms of the scaled variances of the multiplicity distributions, we expect a divergence of the scaled variance (ω_{ch}) at the critical point. This is true for liquid-gas phase transition too. In [27], by transforming Van-dar Waal's equations to GCE, it has been observed that the scaled variance has a finite value in the mixed phase, whereas diverges at the critical point. In nature, the materials are grouped into universality classes [11]. The values of the critical exponents are identical for the same universality classes. Therefore, measurement of γ basically helps to group the materials into separate universality classes.

The quark-number susceptibility (χ_{q}) is defined as the change in the quark-number density (n) for an infinitesimal change in the quark chemical potential (μ) [28],i.e,

$$\chi_{\mathrm{q}}(T,\mu) = \frac{\partial n(T,\mu)}{\partial \mu} \tag{4.7}$$

In [28], χ_{q} has been calculated with the help of two-flavour quark-meson model and using the mean-field approximation. The results are shown in Fig. 4.1. χ_{q} diverges at the critical point, i.e, at $T = T_{\mathrm{c}}$ and finite at the other temperatures. For $T < T_{\mathrm{c}}$, it is discontinuous as the system undergoes first-order phase transition. For $T > T_{\mathrm{c}}$, the discontinuity has not been observed and the quark-number density changes as a result of smooth crossover. Thus, χ_{q} is predicted to diverge at the critical point.

χ_{q} is proportional to the isothermal compressibility as,

$$k_{\mathrm{T}} = \frac{\chi_{\mathrm{q}}(T,\mu)}{n^2(T,\mu)} \tag{4.8}$$

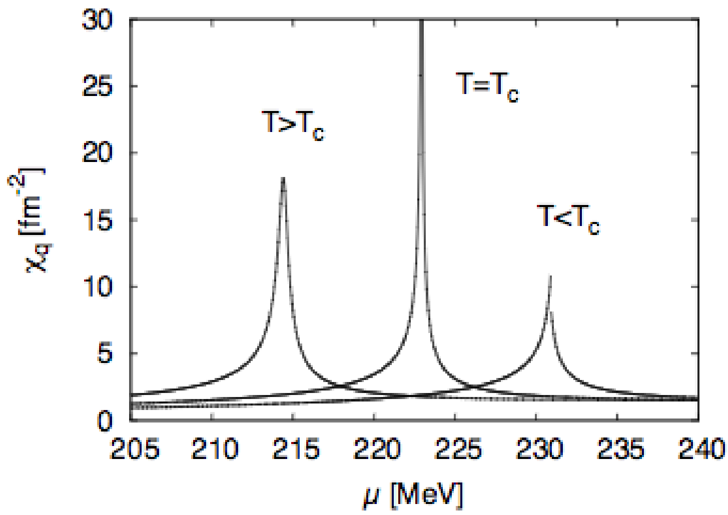

Figure 4.1: χ_{q} diverges at $T = T_{\mathrm{c}}$

Therefore, near the critical point, it is easy to compress the system [28]. In [29], with the help of lattice simulations, it has been shown that, the quark-number susceptibility diverges at the critical point and this may be because of the sudden decrease of the interaction between the quark-constituents after the chiral symmetry restoration. The scaled variance is proportional to χ_{q}. So, it will be easier to search for the critical phenomena through the measurement of the multiplicity fluctuations in the high-energy experiments.

4.3 Particle number fluctuations in statistical ensembles

In statistical physics, the micro-canonical ensemble (MCE) represents the states of an isolated system where neither energy nor particles can be exchanged with the surroundings. For the canonical ensembles (CE), the energy can be exchanged until the system reaches equilibrium, but the particles can not be exchanged. Therefore, in the non-relativistic gases, the particle number is conserved in the micro-canonical as well as the canonical ensembles. For the grand canonical ensembles (GCE), equilibrium is achieved through the exchange of both the energy and the particle numbers.

However, in the relativistic gases, the situation is different. The widths of the multiplicity distributions and the multiplicity fluctuations depend on the conservation laws obeyed by the system. In the MCE, the total charges, total energy and momentum are conserved. In the CE, the conservation of charges are observed. The particle numbers fluctuate both in MCE and CE. In general, MCE is used for systems where small numbers of particles are produced [30]. CE is applied to systems with large number of produced particles, but small number of carriers of conserved charges [31]. GCE is applied to the systems where large numbers of carriers of conserved charges are present [32].

The statistical hadron gas-model successfully described the particle multiplicities in A-A collisions for a wide range of collision energies [33]. Generally, for the high-energy heavy-ion collisions, only a part of the system (around the mid-rapidity) is considered. So, the energy and the particles may be exchanged with the rest of the system serving as heat-bath. Because of this reason, the collisions may be considered as the thermal system in the GCE, in most of the cases [25].

Thermodynamic quantities can be derived from the partition function of the system. Assuming Boltzmann ideal gas as an example, neglecting all the interactions and quantum effects, the partition function for the GCE can be written as [34],

$$Z_{\mathrm{g.c.e}}(V,T) = \sum_{\mathrm{N_+=0}}^{\infty}\sum_{\mathrm{N_-=0}}^{\infty} \frac{(\lambda_+ z)^{N_+}}{N_+!}\frac{(\lambda_- z)^{N_-}}{N_-!} = exp(2z) \tag{4.9}$$

where, z is a single particle partition function, which is a function of particle mass, V, T and modified Hankel function (K_2) [34]. λ_+ and λ_- are auxiliary parameters. For CE, charge conservation in each microstate of the system is considered and the partition function reads [34],

$$Z_{\mathrm{c.e}}(V,T) = \sum_{\mathrm{N_+=0}}^{\infty}\sum_{\mathrm{N_-=0}}^{\infty} \frac{(\lambda_+ z)^{N_+}}{N_+!}\frac{(\lambda_- z)^{N_-}}{N_-!}\delta(N_+ - N_-) = I_0 z \tag{4.10}$$

where, I_0 is the integral representation of the modified Bessel function. This leads to the calculation for the mean particle number as,

$$\langle N_{\pm}\rangle_{\mathrm{g.c.e}} = z \tag{4.11}$$

$$\langle N_{\pm}\rangle_{\mathrm{c.e}} = z\frac{I_1(2z)}{I_0(2z)} \tag{4.12}$$

Fig. 4.2 shows the result for the mean particle number [34]. Here, we clearly see thermodynamic equivalence between the two ensembles as for $V \to \infty$ (corresponds to $z \to \infty$), the mean particle numbers are same in CE and GCE.

Calculating the scaled variance (ω^{ch}) in the similar way, we have,

$$\omega^{\mathrm{ch}}_{\mathrm{g.c.e}} = 1 \tag{4.13}$$

$$\omega^{\mathrm{ch}}_{\mathrm{c.e}} = 1 + z\left(\frac{I_2(2z) + I_0(2z)}{I_1(2z)} - 2\frac{I_1(2z)}{I_0(2z)}\right) \tag{4.14}$$

Results for the scaled variances are shown in Fig. 4.3. It has been observed that,

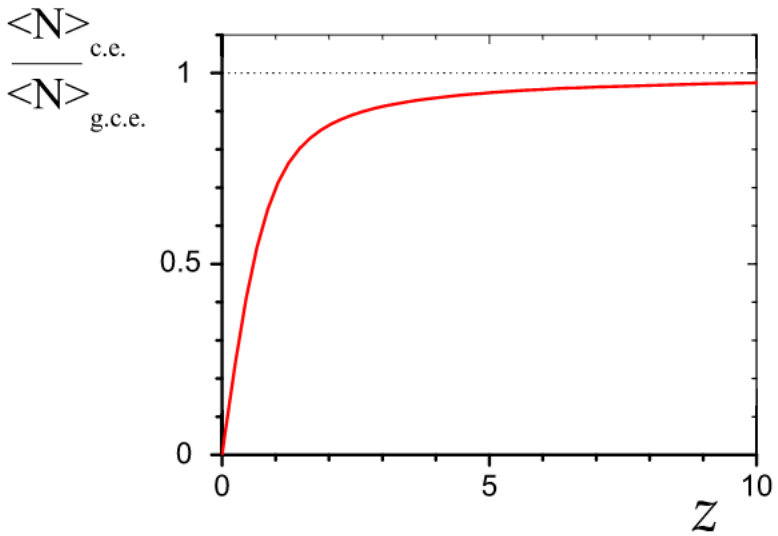

Figure 4.2: $\frac{\langle N_{\pm}\rangle_{\mathrm{c.e}}}{\langle N_{\pm}\rangle_{\mathrm{g.c.e}}}$ as a fuction of z

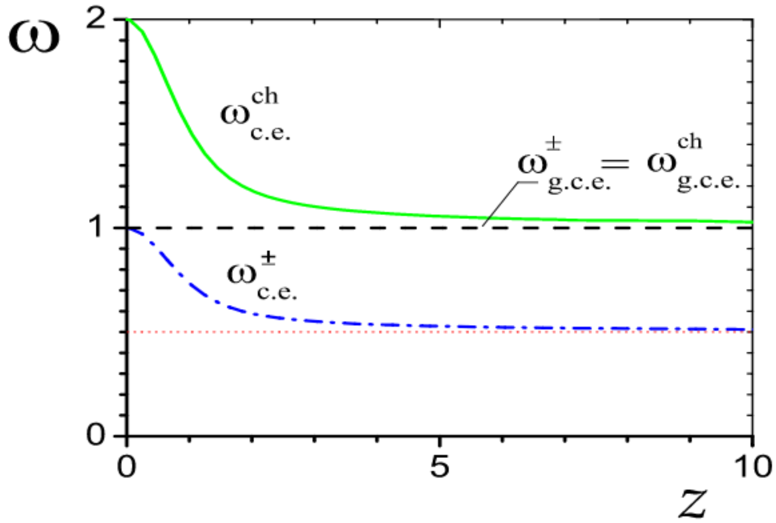

Figure 4.3: Scaled variances in CE and GCE as a fuction of z

$\omega^{\rm ch}_{\rm c.e} = 2\omega^{\pm}_{\rm c.e}$, which occurs because of the charge conservation in each microscopic state for the canonical ensemble. Therefore, in the large volume limit, the fluctuations in CE and GCE are not equal. So, the equivalence between the two ensembles are true for mean, but not for the fluctuations.

Let us discuss the similar quantities in MCE. For non-interacting massless neutral particles, neglecting the quantum effects, the microcanonical partition function (for N-particle system) can be written as [35],

$$Z_{\rm N}(E,V) = \frac{1}{E}\frac{x^{\rm N}}{(3N-1)!N!} \tag{4.15}$$

where,$x = \frac{gVE^3}{\pi^2}$. g is the degeneracy factor. It is calculated [35] that,

$$\langle N\rangle_{\rm g.c.e} \equiv \bar{N} = \left(\frac{x}{27}\right)^{\frac{1}{4}} \tag{4.16}$$

$$\langle N\rangle_{\rm m.c.e} \simeq \bar{N}\left(1 + \frac{1}{8\bar{N}} + \frac{35}{1152\bar{N}^2} + ...\right) \tag{4.17}$$

So, MCE and GCE are thermodynamically equivalent for mean as in the thermodynamic limit (i.e, $\langle N\rangle \to \infty, V \to \infty$,and $\frac{\langle N\rangle}{V} = const.$), both give same values for mean (as shown in Fig. 4.4 [35]). For GCE, the multiplicity distributions are Poissonian ($\omega^{\rm ch}_{\rm g.c.e} = 1$), but that is not the case for MCE. For MCE, the scaled variance is found to be [35],

$$\omega_{\rm m.c.e} \simeq \frac{1}{4}(1 - \frac{1}{8\bar{N}} + ...) \tag{4.18}$$

The result for the scaled variance in the MCE has been shown in Fig. 4.5. It is observed that MCE and GCE are not thermodynamically equivalent for fluctuations.

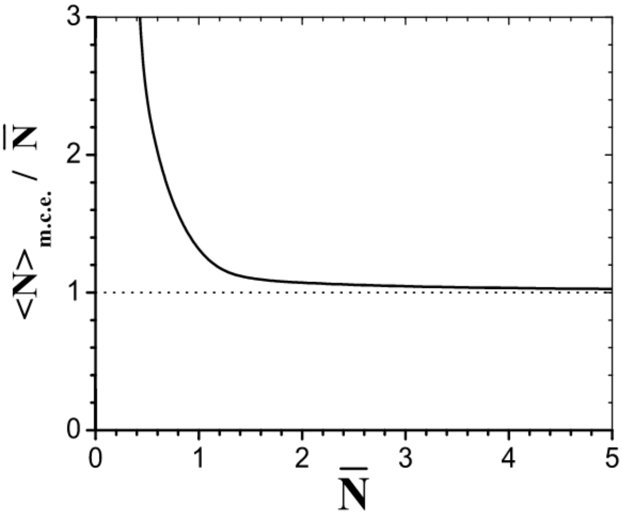

Figure 4.4: The ratio of average particles in MCE to GCE

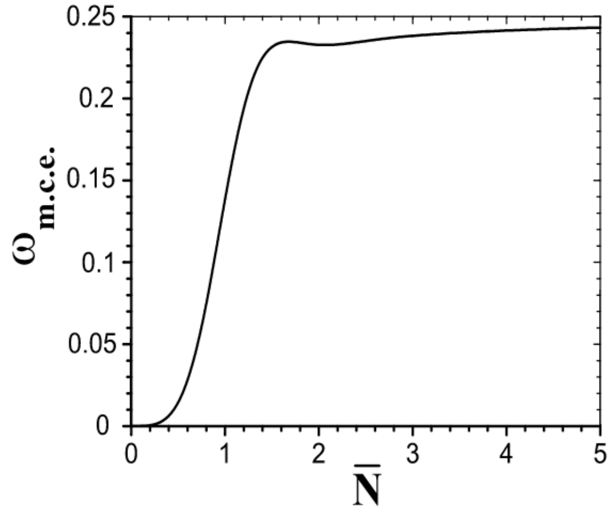

Figure 4.5: Scaled variance in the microcanonical ensemble

In the thermodynamic limit, the scaled variance in MCE is one fourth to that in GCE. An exact charge conservation makes additional suppression in the value of ω [35]. If the quantum effects are included in the calculations, then for system of massive charged particles, Bose enhancement and Fermi suppression is observed in the limit $\frac{m}{T} \to 0$. Fig. 4.6 shows the results considering quantum statistical

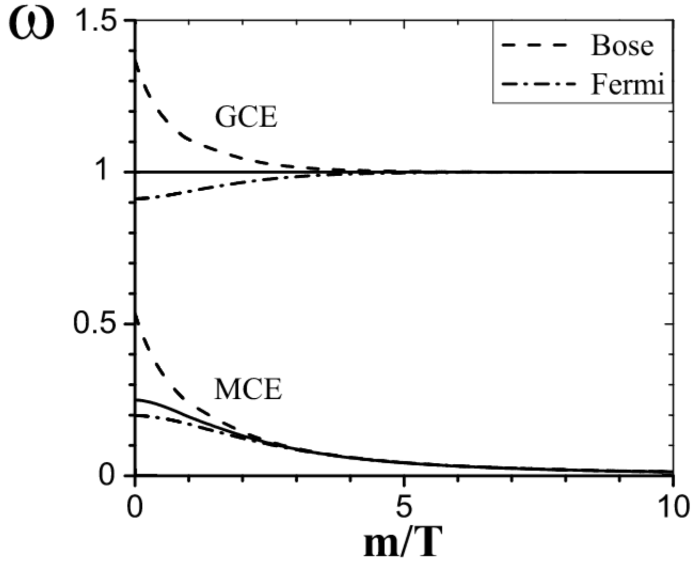

Figure 4.6: Scaled variance in MCE considering quantum effects

effects for MCE. The solid lines represent the results with Boltzmann approximation. Thus, significant changes are observed in the value of the scaled variance when massive charged particles are considered as well as the quantum statistical effects are included.

The thermodynamic limit of scaled variances are different in different ensembles. It has been discussed that the mean values are similar in different ensembles. Therefore, this difference in thermodynamic limit in ω basically arises due to the difference in the limit in the variances of the multiplicity distributions. It has been observed from the studies on ideal hadron resonance gas with the exact conservation of baryon number, strangeness, electric charge and energy, that the variance (σ^2) is an extensive quantity, but not additive [36]. As a result, the thermodynamic limits for the variances in the CE or MCE do not match with that of GCE.

Multiplicity fluctuations have been evaluated in the statistical ensembles within the hadron-resonance gas (HRG) model in the large volume limit. The microscopic correlator method ensures the conservation of baryon numbers, electric charges and strangeness for the canonical ensembles and additionally energy conservation for micro canonical ensembles [37]. The resonance decays have been included also. The scaled variances have been calculated along the chemical freeze-out line of central heavy-ion collisions from lower energies to LHC-energies. As a result, the multiplicity fluctuations in the thermodynamic limit have been observed to be suppressed due to the conservation laws. Fig. 4.7 shows the prediction for the scaled variances of the

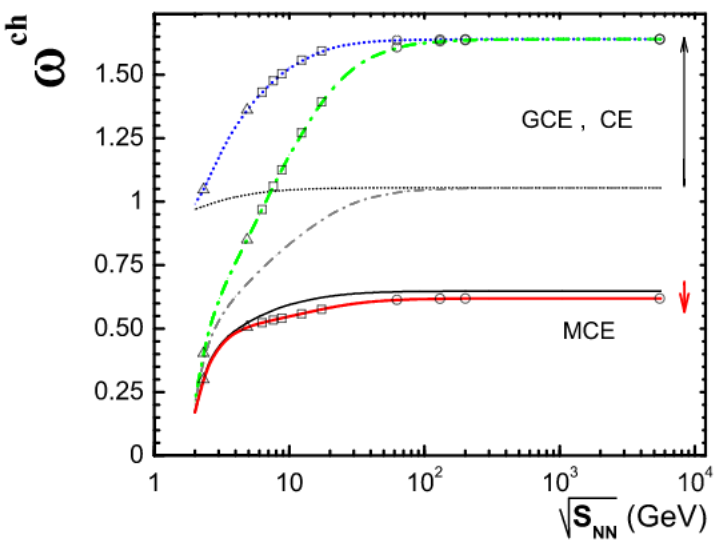

Figure 4.7: Prediction of ω_{ch} from HRG-model as a function of energy

final state (all charged) particles in the full momentum space as a function of energy. Arrows in the fig show the resonance-decay effects, which change the values of the multiplicity fluctuations observed with the Boltzmann approx. discussed earlier. In Fig. 4.7, these results are shown with black lines. At low temperatures, most of the produced charged particles are protons, so Fermi statistics dominate and at higher energies, the effect of resonance etc. becomes very important and Bose statistics dominate. Unlike GCE and CE, the value of the scaled variances decrease after resonance decays in MCE. This arises to satisfy the energy-conservation laws [37].

At 5.5 TeV, the value of ω_{ch} is predicted to be 1.640 for GCE as well as CE, and 0.619 for MCE [37]. The study of the multiplicity fluctuations in the LHC-energies will help to have more insight into the ensemble-studies.

4.4 Volume fluctuations

As discussed earlier, the multiplicity fluctuations in terms of the scaled variances are independent of the system volume. But this observable has a strong dependence on the volume fluctuations, i.e, the fluctuations in the number of participants.

In the participant model or the Wounded Nucleon model (WNM), the nucleus-nucleus collisions are assumed to be simple superposition of the nucleon-nucleon interactions. If there be no correlation present among the different wounded nucleons, the multiplicity fluctuations in the total number of particles within a particular acceptance of the detector can be written as [20],

$$\omega_{\mathrm{N}} = \omega_{\mathrm{n}} + \langle n \rangle \omega_{\mathrm{N_{part}}} \tag{4.19}$$

where, $\omega_{\rm n}$ denote fluctuations in the number of particles produced per participant and $\omega_{\rm N_{part}}$ is the fluctuation in $N_{\rm part}$. $\omega_{\rm n}$ depends on the limited acceptance of the detector. Let us assume that each participant produces m charged particles and a smaller fraction $f = \langle n\rangle/\langle m\rangle$ is accepted by the detector. For the most general case where the particles are accepted randomly, n is binomially distributed with $\sigma(n) = mf(1-f)$ for a fixed m [20]. Therefore, including the fluctuations in m charged particles, one may write,

$$\omega_{\rm n} = 1 - f + f\omega_{\rm m} \tag{4.20}$$

As an example, for NA49 experiment, $f = \langle n\rangle/\langle m\rangle = 0.77/3.7 \approx 0.21$. Using Eq. 4.20, we get. $\omega_{\rm n} \approx 1.2$. For the most central collisions, $\omega_{\rm N_{part}}$ is found to be 1.1 from theoretical calculations based on a centrality cut on the impact parameter b [20]. Therefore, the multiplicity fluctuations in the total number of particles will be, $\omega_{\rm N} \approx 1.2 + (0.77)(1.1) = 2.0$, which is in good agreement with the experimental value of 2.01.

The impact parameter and the number of participants are not measurable quantities in the experiment. In order to minimise the impact parameter fluctuations or the fluctuations in $N_{\rm part}$, narrower centrality bins should be used in the fluctuation analysis. This is discussed in case of the ALICE experiment later in details.

It has been observed that in Pb-Pb collisions even at strictly fixed value of the impact parameter, one still has a large non-poissonian fluctuation in the number of participants and the number of binary collisions with a value of $\omega > 1$, which can lead to the same fluctuation in multiplicity. The physical origin of these non-poissonian fluctuations is basically the interactions of pairs of nucleons in colliding nuclei [38].

Therefore, it is very important to minimise the fluctuations in the number of participants as maximum as possible by chosing narrower centrality bins and also it is necessary to evaluate these fluctations at least from simulation to have an estimate of how much it can affect the charged particle multiplicity fluctuations.

Bibliography

[1] M.A. Stephanov, K. Rajagopal, and E.V. Shuryak, Phys. Rev. **D 60**, 114028 (1999).

[2] G. Baym and H. Heiselberg, Phys. Lett. **B 469**, 7 (1999).

[3] Maitreyee Mukherjee *et al.* 2016 J. Phys. G: Nucl. Part. Phys. **43** 085102.

[4] T. Abbott et al. [E-802 Collaboration], Phys. Rev. **C 52**, 2663 (1995).

[5] M. M. Aggarwal et al. [WA98 Collaboration], Phys. Rev. **C 65**, 054912 (2002).

[6] C. Alt. et al. (NA49 Collaboration), Phys. Rev. **C 78**, 034914 (2008).

[7] C. Alt et al. [NA49 Collaboration], Phys. Rev. **C 75**, 064904 (2007).

[8] T. Czopowicz [NA61/SHINE Collaboration], arXiv:1503.01619 [nucl-ex].

[9] A. Aduszkiewicz et al. [NA61/SHINE Collaboration], arXiv:1510.00163 [hep-ex].

[10] H. Sako *et al.*, (CERES Collaboration), J.Phys. **G30** (2004) S1371-S1376.

[11] A. Adare et al. (PHENIX Collaboration) Phys. Rev. **C 78**, 044902 (2008).

[12] M. A. Stephanov, K. Rajagopal and E. V. Shuryak, Phys. Rev. Lett. **81**, 4816 (1998).

[13] M. A. Stephanov, Prog. Theor. Phys. Suppl. **153**, 139 (2004); Int. J. Mod. Phys. **A 20**, 4387 (2005).

[14] M. Gazdzicki, M.I. Gorenstein and S. Mrowczynski, Phys. Lett. **B 585**, 115 (2004).

[15] Y. Aoki et al., Nature **443**, 675 (2006).

[16] Marek Gazdzicki, Mark Gorenstein and Peter Seyboth, Acta Phys. Polon. **B 42** 307 (2011).

[17] M. Gazdzicki and P. Seyboth, arXiv:1506.08141v2 [nucl-ex].

[18] B. Mohanty, J. Alam, S. Sarkar, T.K. Nayak and B.K. Nandi, Phys. Rev. **C 68**, 021901 (2003).

[19] M.M. Aggarwal *et al.* (STAR Collaboration) e-Print: arXiv:1007.2613 [nucl-ex].

[20] H. Heiselberg, Phys. Rept. **351** 161 (2001).

[21] L. van Hove, Z. Phys. **C 21**, 93 (1984).

[22] J.I. Kapusta and A.P. Vischer, Phys. Rev. **C52**, 2725 (1995).

[23] A. Bialas, Phys. Lett. **B 532**, 249 (2002).

[24] R. Hwa and C.B. Yang, Phys. Rev. **C 85**, 044914 (2012).

[25] S. Jeon and V. Koch, **Hwa, R.C. (ed.) et al.: Quark gluon plasma**, 430-490 (2003), arXiv:hep-ph/0304012 (2003).

[26] F. Reif, "Fundamentals of Statistical and Thermal Physics", Indian Edition, 2010.

[27] V. Vovchenko, D.V. Anchishkin and M.I. Gorenstein, J. Phys. A: Math. Theor. 48, 305001 (2015).

[28] B. J. Schaefer and J. Wambach, Phys. Rev. **D 75**, 085015 (2007).

[29] T. Hatsuda and T. Kunihiro, Phys. Rept.247, 221(1994).

[30] F. Liu, K. Werner, J. Aichelin, Phys. Rev. **C 68** (2003) 02490.

[31] K. Redlich, L. Turko, Z. Phys. **C 5** (1980) 541; J. Rafelski, M. Danos, Phys. Lett. **B 97** (1980) 279; J. Cleymans, K Redlich, E Suhonen, Z. Phys. **C 51** (1991) 137; J. Cleymans, A. Keranen, M. Marais, E. Suhonen, Phys. Rev **C 56** (1997) 2747; F. Becattini, Z. Phys. **C 69** (1996) 485; F. Becattini, U. Heinz, Z. Phys. **C 76** (1997) 269; J. Cleymans, H. Oeschler, K. Redlich, Phys. Rev. **C 59** (1999) 1663; M.I. Gorenstein, M. Gazdzicki, W. Greiner, Phys. Lett. **B 483** (2000) 60; M.I. Gorenstein, A.P. Kostyuk, H. Stocker, W. Greiner, Phys. Lett. **B 509** (2001) 277.

[32] J. Cleymans, H. Satz, Z. Phys. **C 57** (1993) 135.

[33] P. Braun-Munzinger, K. Redlich, J. Stachel, arxiv: nucl-th/0304013, Review for Quark Gluon Plasma 3, eds. R. C. Hwa and Xin-Nian Wang, World Scientific Publishing.

[34] V.V. Begun, M. Gazdzicki, M.I. Gorenstein and O.S. Zozulya, Phys. Rev. **C70**, 034901 (2004).

[35] V.V. Begun, M.I. Gorenstein, A.P.Kostyuk and O.S. Zozulya, Phys. Rev. **C71**, 054904 (2005).

[36] F. Becattini, A. Keranen, L. Ferroni and T. Gabbriellin, Phys. Rev. **C72**, 064904 (2005).

[37] V.V.Begun *et al.*, Phys. Rev. **C76**, 024902 (2007).

[38] V. V. Vechernin and H. S. Nguyen, Phys.Rev.**C84**:054909, 2011.

5 Multiplicity Fluctuations : Earlier Measurements

Multiplicity fluctuations in terms of the scaled variances have been studied earlier in many experiments at different energies and for different collision systems. In this chapter, the results from the earlier measurements have been presented. In addition, the motivations for this analysis in LHC-energies have been discussed.

5.1 Multiplicity fluctuations in pp collisions

In order to describe the high-energy collisions, Wounded Nucleon Model (WNM) [1] was proposed, which has been discussed in the previous section. In WNM, the rescattering of the produced secondaries are not considered.

In the light of WNM, the mean number of the charged particles in high energy pp and $p\bar{p}$ collisions were parametrized as [2],

$$\langle N_{\mathrm{ch}} \rangle \simeq -4.2 + \left(\frac{s}{GeV^2} \right)^{0.155} \tag{5.1}$$

Equation 5.1 can be applied to wide range of energies, where generally KNO-scaling holds good. KNO-scaling has been discussed earlier in details, where it was observed that the multiplicity distributions remain invariant while get scaled by $\langle N_{\rm ch}\rangle$. As a result, it is obvious that the multiplicity fluctuation measures should be scaled with $\langle N_{\rm ch}\rangle$. The scaled variance of the charged particle multiplicity distribution has been parametrized as [2],

$$\omega_{\rm ch} \simeq 0.35 \frac{(\langle N_{\rm ch}\rangle - 1)^2}{\langle N_{\rm ch}\rangle} \tag{5.2}$$

In the left panel of Fig 5.1, the mean number of the charged particles have been

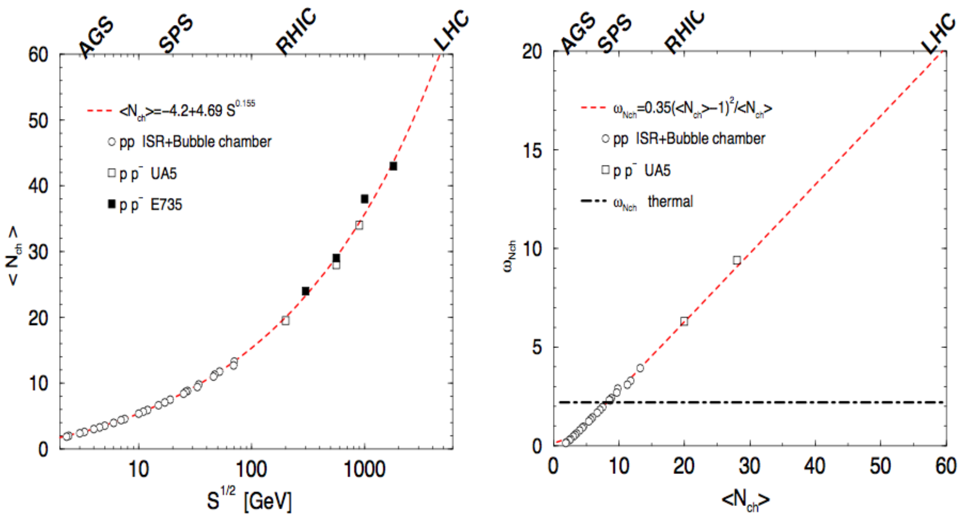

Figure 5.1: Left Panel: $\langle N_{\rm ch}\rangle$ in pp and $p\bar{p}$ collisions in a wide range of energies. Right panel: $\omega_{\rm ch}$ for the same

shown for pp or $p\bar{p}$ collisions with the help of data taken by Bubble chamber, ISR, UA5 and E735 experiments. $\langle N_{\rm ch}\rangle$ follows eq. 5.1. At SPS, RHIC and LHC energies, i.e, $\sqrt{s} \simeq 20, 200, 5000$ GeV, $\langle N_{\rm ch}\rangle$ have been found to be 7.3,20,60, respectively [2]. The right panel of Fig 5.1 shows the results for the scaled variances for pp or $p\bar{p}$ collisions in a wide range of energies as a function of $\langle N_{\rm ch}\rangle$ found in the left panel. We observe a huge difference in the values for the multiplicity fluctuations between pp collisions and the thermal fluctuations at very high energies. At these energies, the breakdown of KNO scaling makes the fluctuations larger than expected. Following Equation 5.2, at SPS, RHIC and LHC energies, scaled variances are found to be 2.0,6.2 and 20 respectively [2].

Measurements related to the multiplicity fluctuations in pp collisions have been also performed in PHENIX-experiment, which will be discussed in comparison to the results from heavy ion collisions in Section 5.5.2.

Recently, charged particle multiplicity fluctuations were measured for inelastic pp collisions at 20, 31, 40, 80 and 158A GeV energy by NA61/SHINE experiment [3] at the CERN SPS. The results for positively, negatively and all charged hadrons

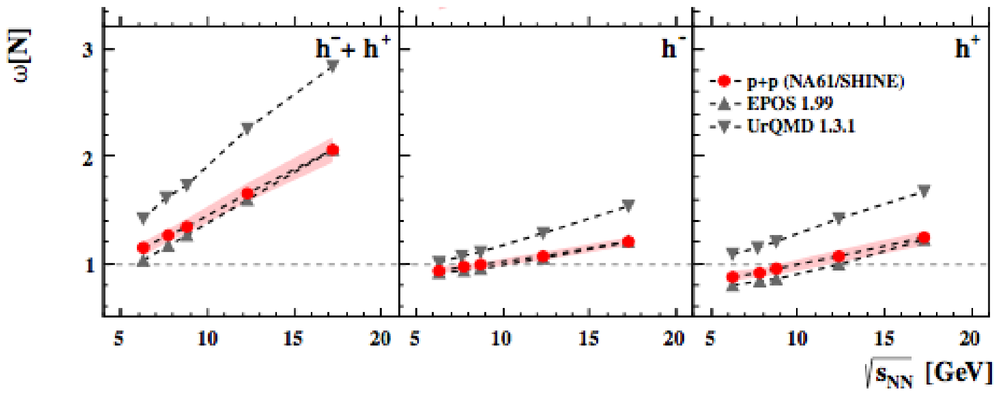

Figure 5.2: Scaled variance as a function of energy from NA61/SHINE experiment. Comparison with models EPOS 1.99 and UrQMD has been also shown

are shown in Fig. 5.2 [3]. Results are corrected for the detector inefficiencies and interaction trigger. The scaled variances are measured for the full acceptance range for NA61, where the reconstruction efficiency is greater than 90%. We observe an increase of the value of the scaled variances with increasing energy as expected. Results for the model EPOS 1.99, measured in the same acceptance as NA61, agree well with the data, but the UrQMD model does not describe the data as shown in Fig. 5.2.

5.2 Multiplicity fluctuations in heavy ion collisions

In nucleus-nucleus (AA) collisions, the fluctuations have been found to be smaller than those found in pp or $p\bar{p}$ collisions. To attain a state of the thermal equilibrium in AA-collisions, the fluctuations may become small [4]. This is also am important fact that the origin of the fluctuations in pp and AA collisions are different and as a result, the physical informations carried by them are also different. As for example, in pp collisions, it is expected to have the quantum mechanical information of the initial state from the event-by-event fluctuations in the final state. For heavy ion collisions, this is difficult. Generally, for AA collisions, the event-by-event fluctuations are related to the thermodynamic properties at the freeze-out [4].

Let us give a brief overview of the results for the multiplicity fluctuations from the earlier experiments.

WA98 Experiment: WA98 is a fixed target experiment. The data was taken with 158A GeV Pb beams from the CERN SPS in 1994, 1995, and 1996 [4]. Charged particle multiplicity was measured by Silicon Pad Multiplicity Detector (SPMD), in the pseudorapidity coverage $2.35 \leq \eta \leq 3.75$. Centrality was determined using the total transverse energy measured in the Mid-Rapidity Calorimeter (MIRAC) and the total energy deposited in the forward region, with the help of Zero Degree

Calorimeter (ZDC). Minimization of the impact parameter fluctuations were done by choosing narrower centrality bins. The charged particle multiplicity distributions were found to be gaussians mostly.

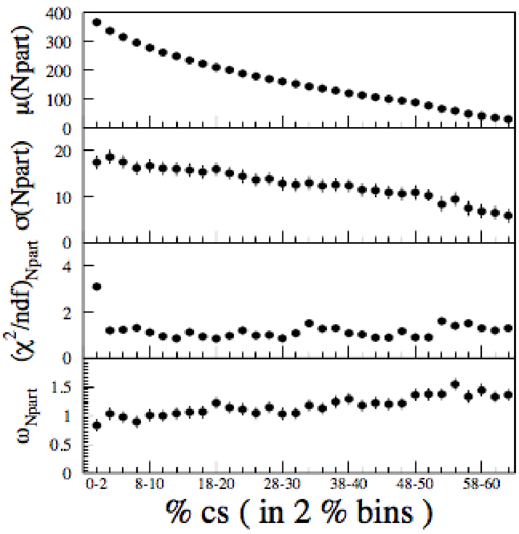

Figure 5.3: μ,σ,and $\omega_{\mathrm{N_{part}}}$ of the distributions of number of participants as a function of centrality from WA98 experiment

The fluctuations in the number of participants ($\omega_{\mathrm{N_{part}}}$) were determined using events generated by VENUS 4.12 event generator with default settings, at 158A GeV energy. $\omega_{\mathrm{N_{part}}}$ were found to vary little around 1 (Fig. 5.3) [4].

As defined earlier, the fluctuations in the number of particles produced by each source,i.e, per participant, is given by Eq. 4.20, where,$f = \frac{\langle n \rangle}{\langle m \rangle}$. $\langle n \rangle$ can be found out for each centrality as, $\langle n \rangle = \frac{\langle N_{\mathrm{ch}} \rangle}{\langle N_{\mathrm{part}} \rangle}$. The total number of particles produced per participant ($\langle m \rangle$) is found from the parametrization,

$$\langle N_{\mathrm{ch}} \rangle^{\mathrm{NN}} = -4.7(\pm 1.0) + 5.2(\pm 0.8) s^{0.145(\pm 0.01)} \tag{5.3}$$

At SPS energy, Eq. 5.3 gives a value of 7.2 [4]. Therefore, average number of charged particles per participant is 3.6. Additionally, $\omega_{\rm m}$ may be calculated using the parametrization [4],

$$\omega_{\rm m} = 0.33\frac{(\langle N_{\rm ch}\rangle - 1)^2}{\langle N_{\rm ch}\rangle} \tag{5.4}$$

At SPS energies, $\omega_{\rm m} = 1.8$. Therefore, $\omega_{\rm n}$ may be calculated for each centrality once $\langle n\rangle$ is known for each centrality from the experiment.

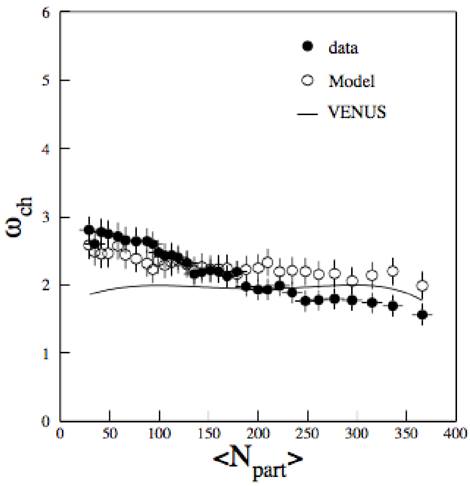

Figure 5.4: $\omega_{\rm ch}$ as a function of the number of participants from WA98 experiment. Results have been compared with the prediction from participant model and the VENUS event generator

Fig. 5.4 shows the results for charged particle multiplicity fluctuations from WA98 experiment. It is observed that the scaled variance shows a monotonic increase from central to peripheral collisions. The prediction from participant model gives similar trend, however, the increase of the scaled variances is less. The result from VENUS event generator shows almost constant value throughout.

NA49 Experiment: NA49 is a fixed target experiment, where centrality of the collision is determined by the energy of the projectile spectators in Veto Calorimeter and the particle tracking is done by TPCs. The published results for the scaled vari-

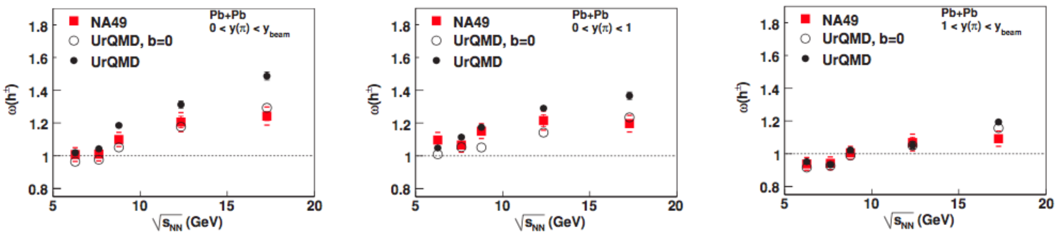

Figure 5.5: Energy dependence of the scaled variances for all charged hadrons in NA49 experiment at (i) Full experimental acceptance, (ii) midrapidity, (iii) forward rapidity

ances of the charged particle multiplicity distributions in central Pb-Pb collisions as a function of energy are shown in Fig. 5.5 [5]. We get results for the energies 20A, 30A, 40A, 80A and 158 A GeV, i.e, $\sqrt{s}_{\mathrm{NN}} = 6.27, 7.62, 8.77, 12.3$ and 17.3 GeV. Results are shown for three rapidity intervals, i.e, (i) Full experimental acceptance, (ii) midrapidity, and (iii) forward rapidity. No significant non-monotonic behaviour for the multiplicity fluctuations has been observed. Comparison to Ultra-relativistic Quantum Molecular Dynamics (UrQMD)-simulations show that UrQMD mostly overpredicts the data, both for collisions with zero impact parameter and 1% most central collisions, in the full experimental acceptance and midrapidity. In the forward rapidity, UrQMD matches with the data-results except for 158A GeV.

If q be the probability of a single particle to be accepted within the experimental acceptance and $\omega_{4\pi}$ be the scaled variance of the multiplicity distributions for all produced particles, then the scaled variance of the multiplicity distributions in the experimental acceptance can be expressed as [5],

$$\omega = 1 - q + q\omega_{4\pi} \tag{5.5}$$

Using Eq. 5.5, the scaled variances for the positive and negatively charged hadrons

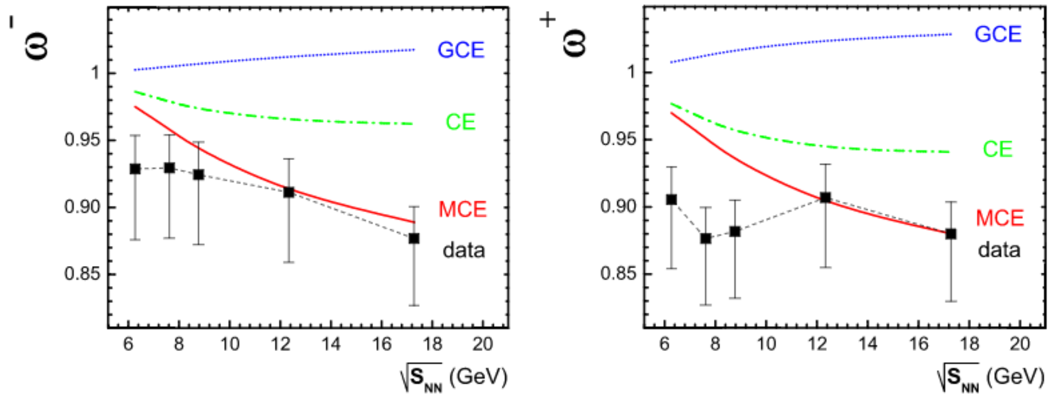

Figure 5.6: The scaled variance for the negatively (left panel) and positively (right panel) charged hadrons along the chemical freeze-out line for central Pb-Pb collisions from NA49 experiment. GCE, CE, and MCE-results calculated in the same acceptance (using Eq. 5.5) have been shown.

have been calculated for 1% most central Pb-Pb collisions. The comparison of the NA49-results with the prediction from different ensembles from hadron-resonance gas calculations have been presented in Fig. 5.6 [6] for $1 < y(\pi) < y_{\text{beam}}$. It is observed that the NA49 data is best described by the results of the hadron-resonance gas model calculated within the MCE. Rather, the data shows more suppression of the result than MCE, whereas CE and GCE overpredicts the data-results.

The centrality and system size dependence of the scaled variances in the forward rapidity region ($1.1 < y_{\text{c.m.}} < 2.6$) at 158A GeV energy has been studied in

NA49-experiment [7]. The scaled variance was observed to be close to unity and it increases towards the peripheral collisions. The multiplicity fluctuations for neg-

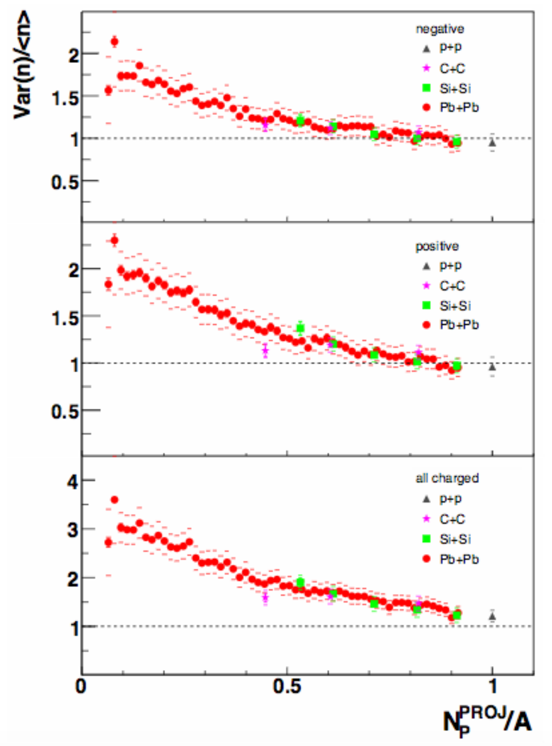

Figure 5.7: The scaled variances for negatively (upper), positively (middle) and all (bottom) charged particles in pp, semi-central C-C, semi-central Si-Si and Pb-Pb collisions as a function of the fraction of the participating nucleons for NA49 experiment

atively, positively and all charged particles in pp, semi-central C-C, semi-central Si-Si and Pb-Pb collisions as a function of the fraction of the participating nucleons, shows a scaling in $\frac{N_{\rm P}^{\rm PROJ}}{A}$, as shown in Fig. 5.7 [7]. However, the string-hadronic models could not describe the data.

PHENIX Experiment: PHENIX experiment at RHIC is a collider experiment. Large numbers of the minimum bias events were analyzed for Au-Au at $\sqrt{s_{\rm NN}}$ =

200 GeV, Au-Au at $\sqrt{s_{\mathrm{NN}}} = 62.4$ GeV, Cu-Cu at $\sqrt{s_{\mathrm{NN}}} = 200$ GeV, Cu-Cu at $\sqrt{s_{\mathrm{NN}}} = 62.4$ GeV, Cu-Cu at $\sqrt{s_{\mathrm{NN}}} = 22.5$ GeV and pp at $\sqrt{s} = 200$ GeV. The centrality of the collisions were determined by the correlation of the energy deposited in the Zero Degree Calorimeter (ZDC) with the total charge deposited in the Beam-Beam Counter (BBC) (for Au-Au at $\sqrt{s_{\mathrm{NN}}} = 200$ GeV) and total charge deposited in BBC (not using correlation with ZDC, as the resolving power of ZDC was not sufficient) for the other collisions, except for the lowest collision energy [8]. The charged particle multiplicity was measured counting the reconstructed tracks in the Drift Chamber. Minimising the background, the charged particles are counted within $|\eta| < 0.26$. The effective azimuthal acceptance were 2.1 radians for Au-Au at $\sqrt{s_{\mathrm{NN}}} = 200$ GeV and pp at $\sqrt{s} = 200$ GeV, and 2.0 radians for the other collisions.

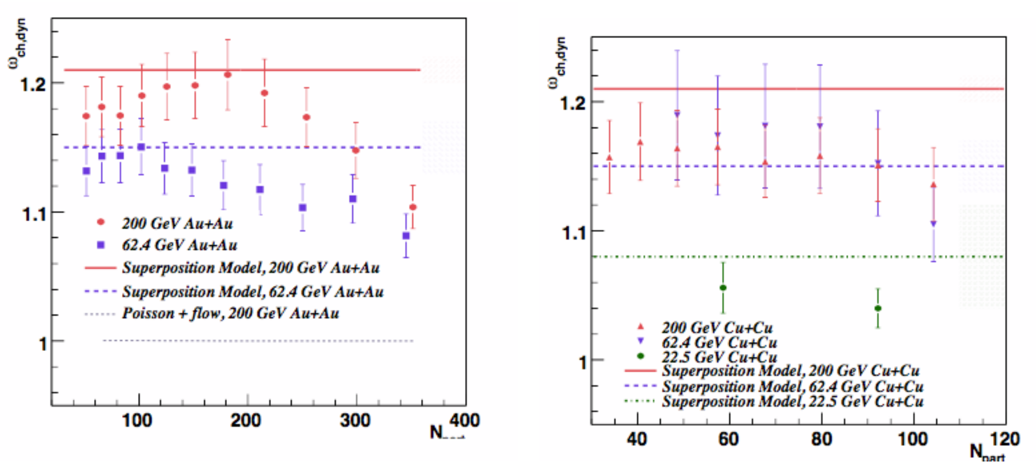

Figure 5.8: The scaled variances for Au-Au (left panel) and Cu-Cu (right panel) collisions for $0.2 < p_{\mathrm{T}} < 2.0$ GeV/c from the PHENIX experiment

The results for the scaled variances after correcting for the geometrical fluctuations, have been shown in Fig. 5.8 [8]. ω_{ch} has been observed to increase from central to peripheral collisions, and becomes almost constant after a certain $N_{\rm part}$, i.e, $N_{\rm part} < 200$ for Au-Au at $\sqrt{s}_{\rm NN} = 200$ GeV (Fig. 5.8(left panel)), which is different for different energies and different collision systems. For Cu-Cu, this increase is weaker as shown in Fig. 5.8(right panel). The results for the scaled variances are higher than the Poisson-expectation and the expectations from the superposition model have been also shown in the Fig. Data has not been observed to show the existence of the critical point, as nowhere the scaled variances have a much larger value. HIJING event generator overpredicted the data.

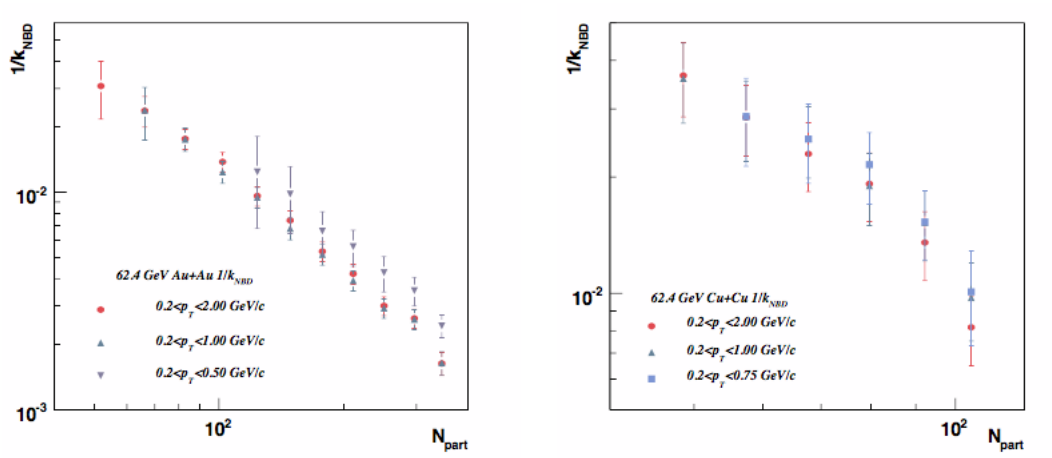

Figure 5.9: $\frac{1}{k_{\rm NBD}}$ for Au-Au at $\sqrt{s}_{\rm NN} = 62.4$ GeV (left panel) and Cu-Cu at $\sqrt{s}_{\rm NN} = 62.4$ GeV for different $p_{\rm T}$-ranges from the PHENIX experiment

No significant transverse-momentum dependence is observed from PHENIX-data. As a result, $k_{\rm NBD}$ (the parameter connected to width of the multiplicity distributions fitted with NBD), are independent of $p_{\rm T}$, as shown in Fig. 5.9.

A universal scaling was observed in the variable $\sigma^2/\mu^2 = \frac{k_{\rm B}T}{V} k_{\rm T}$ [9]. Data, as shown in Fig. 8.8, for $0.2 < p_{\rm T} < 2.0$ GeV/c (left panel) and $0.2 < p_{\rm T} < 0.75$ GeV/c

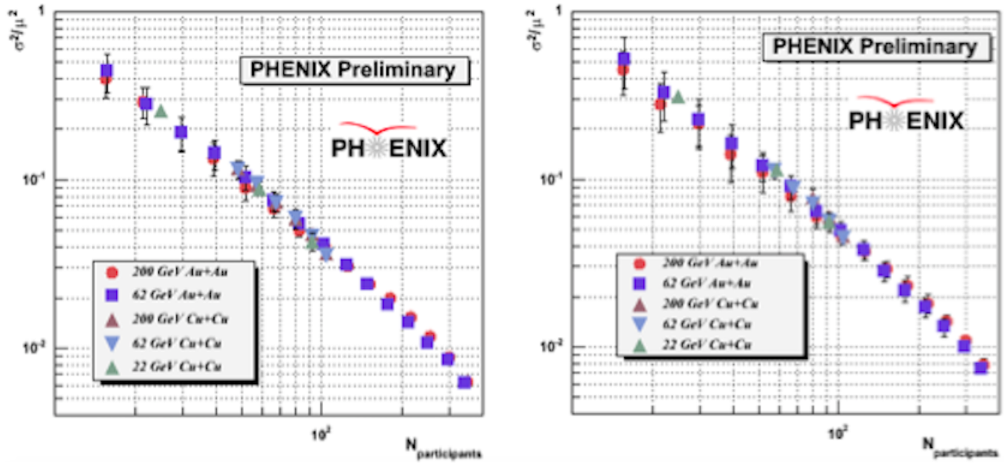

Figure 5.10: Multiplicity Fluctuation Universal Scaling from the PHENIX preliminary results for $0.2 < p_{\mathrm{T}} < 2.0$ GeV/c (left panel) and $0.2 < p_{\mathrm{T}} < 0.75$ GeV/c (right panel)

(right panel), can be described within error by a power law in N_{part} as,

$$\sigma^2/\mu^2 \propto N_{\mathrm{part}}^{-1.40\pm0.03} \tag{5.6}$$

It is predicted that in the absence of correlations in some certain acceptance range, the scaled variance decreases as the acceptance decreases and k_{NBD} is the same even for the reduced acceptance. This is followed from an important property of NBD. It is possible to decompose an original NBD into smaller subsets that follow NBD too with the same value of k_{NBD} [8]. Let's say, the original NBD has mean μ_{ch} and scaled variance ω_{ch}. Then, the scaled variance of the fractional acceptance sample will be,

$$\omega_{\mathrm{acc}} = 1 + (\mu_{\mathrm{acc}}/k_{\mathrm{NBD}}) = 1 + f_{\mathrm{acc}}(\mu_{\mathrm{ch}}/k_{\mathrm{NBD}}) \tag{5.7}$$

where, k_{NBD} is identical for the original and the subsample. Here, the fraction

$f_{\mathrm{acc}} = \mu_{\mathrm{acc}}/\mu_{\mathrm{ch}}$. Using Equation 4.2, it can be written as,

$$\omega_{\mathrm{acc}} = 1 + f_{\mathrm{acc}}(\omega_{\mathrm{ch}} - 1) \tag{5.8}$$

Thus, using Equation 5.8, it is possible to predict the value of the scaled variance in some other acceptance by knowing only the mean and the scaled variance in the experimental acceptance. The application of this useful property will be discussed in the case of the results from the event generators and the results from ALICE experiment later.

NA61/SHINE Experiment : The results of the scaled variances in inelastic pp collisions from NA61 experiment have been discussed earlier in Section 5.5.1. Phase-space acceptance for NA61 is larger than that used in NA49 experiment. Therefore, for the comparison of NA61 results to that of central Pb-Pb result from NA49, NA49 cuts were applied to NA61 data. The results are shown in Fig. 5.11. Here, the results for pp interactions were compared to 1% most central Pb-Pb collisions in NA49-M ($1.1 < y_{\pi} < y_{\mathrm{beam}}$) (top panel) and NA49-B ($0 < y_{\pi} < y_{\mathrm{beam}}$) (bottom panel) acceptances. Systematic errors are shown in bands. It is observed that the results from pp are much larger than that from central Pb-Pb for 158A GeV energy, which basically contradicts the expectations from the wounded nucleon model [3]. Within the statistical framework, the larger multiplicity fluctuations in inelastic pp interactions may be attributed to the volume fluctuations.

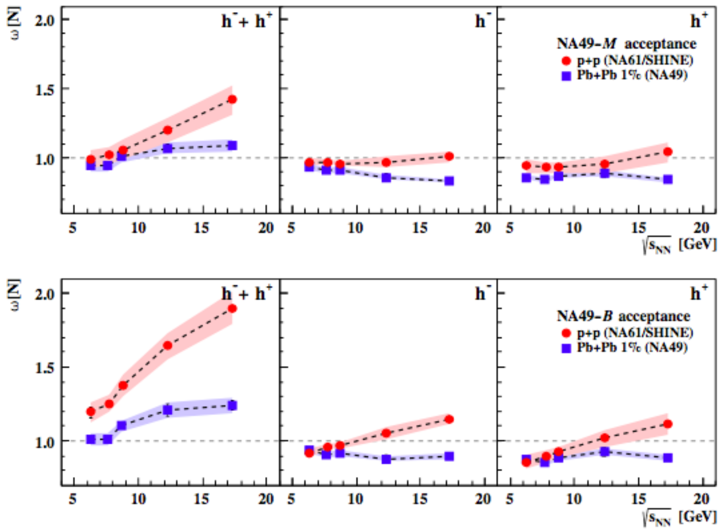

Figure 5.11: Scaled variances in inelastic pp interactions from NA61/SHINE experiment compared with central Pb-Pb collisions from NA49 experiment within the NA49-M (top panel) and NA49-B (bottom panel) acceptances

5.3 Motivation for multiplicity fluctuation analysis in ALICE

In the QCD phase-diagram, very high temperatures and low net-baryon densities, i.e, region of smooth crossover, have been achieved at the LHC-energies. Since, QCD at $\mu_{\mathrm{B}} = 0$ sets the scale of theoretical calculations, the results from LHC-energies are directly comparable. At such a high energy, large number of particles are produced per event, which makes the event-by-event studies interesting.

Since the colliding system may be considered as a thermal system in GCE, following Eq. 4.4, it is evident that,

$$\frac{\sigma^2}{\mu^2} = \frac{k_{\mathrm{B}}T}{V}k_{\mathrm{T}} \tag{5.9}$$

It is possible to estimate the value of the compressibility (k_{T}) at the thermal freeze-out (where the elastic processes cease to occur and the system breaks off into smaller parts) as a function of T and V following Eq. 5.9. The left hand side of the Eq. 5.9 can be measured from experiment per centrality class at the final-state corresponding to the thermal freeze-out. For a given centrality class it can be assumed that all the events correspond to a system with the same T and V. Earlier, at chemical freeze-out, because of the expansion of the system, the temperature of the fire ball decreases to a point where the interactions changing the number of particles are ceased. Thus, the inelastic collisions cease to occur. Therefore, chemical composition of the system is fixed. However, the hadrons produced in the final-state in a heavy ion collision are in thermal as well as chemical equilibrium [10]. It is described in [11] how these quantities may be recalculated at the higher temperature, i.e, at the chemical freeze-out. Thus, following the procedure described in [10], the compressibility of a system may be estimated at the LHC-energies.

It is predicted that in ALICE experiment, the initial state effects can be studied well [12]. Let us discuss the case when the longitudinal transverse momentum fraction x of the parton involved in a scattering process, is very small. As shown in the Fig. 5.12 (left panel), at small-x ($x < 0.01$) region, the parton distribution function is dominated by the gluons. Gluon-density increases for smaller x via BFKL equation as shown in the Fig. 5.12 (right panel). Here, one colored blob represent parton with transverse area $\sim 1/Q^2$, where Q represents the transferred momentum and longitudinal momentum $k_{\mathrm{z}} = xP$. For very high gluon-density, alongwith the gluon-bremsstrahlung process, the non-linear effects, i.e, the recombination between the gluons having similar x and occupying a same area of $\sim 1/Q^2$ takes place, followed

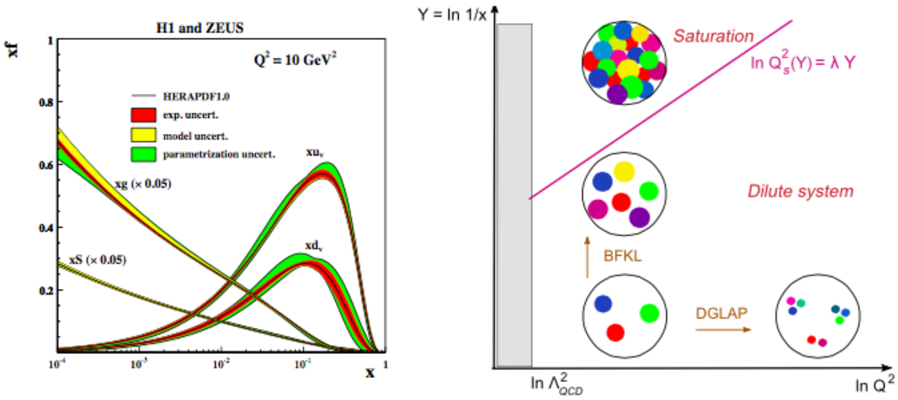

Figure 5.12: Left : Parton-distribution functions for gluon, sea-quark and valence-quark as a function of $1/x$ for $Q^2 = 10\ GeV^2$ at HERA. Right : Gluon saturation in QCD.

by the gluon-saturation.

In the experimental scenario, the small-x region can be achieved by highering the energy and for higher rapidity. Considering the energy-momentum conservation in a scattering process, x can be expressed as [12],

$$x = \frac{p_{\rm T}}{\sqrt{s}} e^{-\eta} \tag{5.10}$$

In Fig. 5.13, where the representation is as follows : $p_{\rm T} \equiv M$ and $\eta \equiv y$, it is observed that for RHIC, x can be lowered to 10^{-2} and for LHC, it can have a value of 10^{-4} with the central detectors. For LHC, with forward detectors, x can be lowered further, i.e, $x \sim 10^{-6}$. Therefore, at these high energies and small-x, it is interesting to observe the effects at the initial states.

Correlated multi-particle production from the glasma-flux tube with a correlation over length scale $\sim 1/Q_{\rm s}$ ($Q_{\rm s}$ is the saturation momentum) [12] can be studied in the framework of classical Yang-Mills dynamics. The multiplicity distributions produced

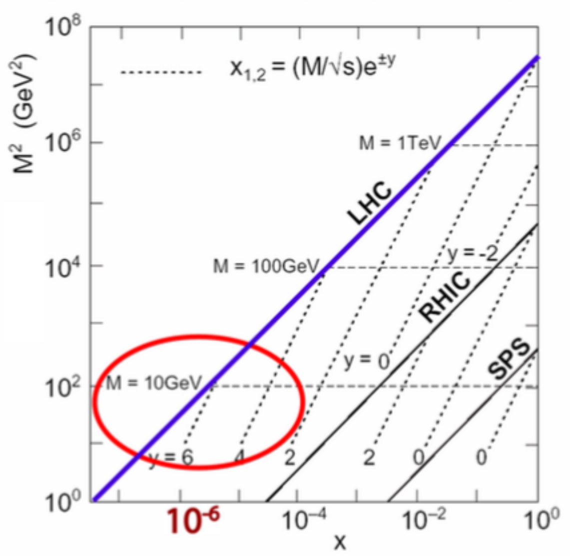

Figure 5.13: The small-x region achievable in SPS, RHIC and LHC-energies

are the negative binomial distributions and the NBD-k parameters can be extracted as [13, 14],

$$k = \kappa \frac{(N_c^2 - 1)Q_s^2 S_\perp}{2\pi} \tag{5.11}$$

where, κ represents a non-perturbative constant including infra-red divergences at the scale Q_s, $Q_s^2 S_\perp$ are the number of flux tubes in the transverse area $S_\perp$ and $(N_c^2 - 1)$ are the numbers of gluon colors from a single flux-tube. Another parameter of the distribution, i.e, the average multiplicity can be expressed as [15],

$$\mu = c \frac{C_F}{2\pi^2 \alpha_s} Q_s^2 S_\perp \tag{5.12}$$

where, $C_F = (N_c^2 - 1)/2N_c$ is the Casimir factor and α_s is the coupling constant, and c is another constant. From the equations 5.11 and 5.12, for symmetric systems at midrapidity, one can write,

$$\frac{k}{\mu} = \frac{2N_{\mathrm{c}}\pi}{c}(\kappa\alpha_{\mathrm{s}}) \tag{5.13}$$

The R.H.S of the Eq. 5.13 is basically a constant. Therefore, it is predicted that for Pb-Pb collision, k and μ should be proportional. However, for asymmetric systems, the prediction is somewhat different. Logarithmic corrections to Eq. 5.13 is needed for asymmetric (such as p-Pb) cases. Approximately the dependence can be written as [16],

$$\mu \propto k\ ln^2 \frac{Q^2_{\mathrm{s,Pb}}}{Q^2_{\mathrm{s,p}}} \tag{5.14}$$

where, it is naively expected that k will go as $Q^2_{\mathrm{s,p}}S_{\perp}$. The ratio k/μ is predicted to be of the same order in the symmetric and asymmetric collisions. Thus, the parameters characterizing the multiplicity distributions can be connected to the early stages of collision and it is important to investigate how these parameters change for different systems, i.e, Pb-Pb to p-Pb collisions.

Model calculations with Colour Glass Condensate initial energy distributions have shown that, experimental multiplicity distributions from d-Au collisions at RHIC, are better explained if multiplicity fluctuations (according to a negative binomial distribution) are included [17]. Therefore, it is also important to measure the multiplicity fluctuations in LHC-energies too in order to reproduce and explain the multiplicity distributions.

Various moments of the eccentricity of the collision zone in nucleus-nucleus collisions get affected by multiplicity fluctuations in NN collisions [17]. This is also shown in [18] for nucleus-nucleus collision in event-by-event hydrodynamics.

The source of the multiplicity fluctuations has been extensively studied in the microscopic level. Entropy, and in turn, multiplicity fluctuate from event to event due to hydrodynamic evolution of the system. Multiplicity fluctuations arising from this hydrodynamic fluctuations or noises during the hydrodynamic evolution, contribute to the final multiplicity distributions [19], even if the initial state is the same in a macroscopic sense. However, theoretical studies are ongoing to evaluate how much this affects the multiplicity distributions. The connection between these fluctuations and the multiplicity fluctuations obtained experimentally will be another interesting thing to observe.

Moreover, the fluctuations in the other measured quantities are directly affected by the statistical part of the multiplicity fluctuations. Therefore, it is necessary to determine the multiplicity fluctuations correctly to understand the effects of the these fluctuations on the other fluctuations properly.

Bibliography

[1] A. Bialas, Phys. Lett. **B 532**, 249 (2002).

[2] H. Heiselberg, Phys. Rept. **351** 161 (2001).

[3] A. Aduszkiewicz et al. [NA61/SHINE Collaboration], arXiv:1510.00163 [hep-ex].

[4] M. M. Aggarwal et al. [WA98 Collaboration], Phys. Rev. **C 65**, 054912 (2002).

[5] C. Alt. et al. (NA49 Collaboration), Phys. Rev. **C 78**, 034914 (2008).

[6] V.V.Begun *et al.*, Phys. Rev. **C76**, 024902 (2007).

[7] C. Alt et al. [NA49 Collaboration], Phys. Rev. **C 75**, 064904 (2007).

[8] A. Adare et al. (PHENIX Collaboration) Phys. Rev. **C 78**, 044902 (2008).

[9] J. T. Mitchell, Quark Matter 2006.

[10] S. Mrowczynski, Physics Letters **B 430** : 914, 1998.

[11] F. Becattini, M. Gazdzicki and J. Sollfrank, Eur.Phys.J.**C5** :143-153, 1998.

[12] E. Iancu, CERN-2014-003, pp. 197-266, arxiv:1205.0579 [hep-ph] (2012).

[13] F. Gelis, T. Lappi and L. McLerran, Nucl.Phys.**A 828**:149-160, 2009.

[14] B. Schenke, P. Tribedy, and R. Venugopalan, Phys. Rev. **C 86**, 034908 (2012).

[15] T. Lappi, Eur.Phys.J.**C 71**:1699, 2011.

[16] A. H. Rezaeian, Phys.Lett.**B 727**:218-225, 2013.

[17] A. Dumitru and Y. Nara, Phys. Rev. **C 85**, 034907 (2012).

[18] A. Chaudhuri, Phys. Rev. **C 87**, 034908 (2013).

[19] T.Hirano, QM 2014, Nuclear Physics **A 931** (2014) c831.

6 Multiplicity Fluctuations from Event Generators

In addition to simple perturbative quantum field theory description of the processes in an event in high-energy collisions, many complex things such as, non-perturbative nature of the QCD bound states, the collective behaviour observed in the heavy-ion collisions etc, occur which can not be explained by simple calculations directly. To include these complex behaviours, the full processes are factorized into individual processes which can be evaluated separately and probabilistic branching between the individul processes are performed using the Monte Carlo algorithms. Thus, depending on the existing underlying physics, the event generators randomly generate events and mimic the experimental scenario so that the results from the event generators may be compared to the experimental results.

The strategies of analyzing real data, such as corrections due to detector inefficiency etc., are decided with the use of the event generators. Comparison of the results from real data with the event generators provides information on the limitation of the known physics, as well as helps to plan for a new detector to study the new physics opportunities. In general the heavy-ion event generators help to simulate the subprocesses like, the initial-state showers, soft processes, the high multiplicity, the energy loss in the medium, resonance decay, the collective behaviour of the medium, etc.

In this chapter, the heavy-ion event generators used for the data analysis in ALICE experiment have been discussed alongwith the results of the multiplicity fluctuations from the different event generators. A comparison between the results from the event generators in different collision energies have been presented.

6.1 Event Generators used in heavy-ion collisions

6.1.1 HIJING

Heavy Ion Jet INteraction Generator (HIJING) is a Monte Carlo event generator which was first developed by M. Gyulassy and X.-N. Wang [1] in 1991. It uses a pQCD based model for multiple minijet production combined with Lund FRITIOF [2] and Dual Parton Model [3] for the description of the soft interactions. Multiple minijet production was included in the model with the initial and final state radiation. With the use of this model, jet and multi-particle production in high energy pp, p-A and A-A collisions can be well described for a wide range of energies. HIJING was designed mainly to explore the range of possible initial conditions that may occur in relativistic heavy ion collisions [1]. Binary approximation and Glauber geometry has been used in this model for the simulation of p-A and A-A collisions. Parton shadowing was taken into account by a parametrized parton distribution function inside a nucleus. The modelling of jet quenching was done by assuming an energy loss dE/dz of the partons traversing the produced dense matter.

In ALICE experiment, HIJING has been used for the simulation of Pb-Pb and p-Pb collisions.

6.1.2 DPMJET

DPMJET [4, 5, 6], the two component Dual Parton Model helps to sample pp, p-A, A-A and $\nu - A$ interactions at high energies. This is used with multiple soft chains and multiple mini-jets at each elementary interaction. Particle production is realized by the fragmentation of colorless parton-parton chains constructed from the quark content of the interacting hadrons. The model includes the cascading of secondaries within the target as well as projectile nuclei, which is suppressed by the formation time concept [5]. The excitation energy of the remaining target and projectile nuclei is calculated and using this nuclear evaporation is included into the model. It is possible to use the model upto energy 10^{21} eV/A in the laboratory frame. In a later version, DPM combines predictions of the large N_{c}, N_{f} expansion of QCD and assumptions of duality with Gribov Reggeon field theory [6]. Thus, DPM uses Reggon field theory for soft and pQCD for hard interactions.

In ALICE experiment, DPMJET has been used for the simulation of p-Pb collisions.

6.1.3 AMPT

The AMPT model [7, 8, 9] is used as a guidance for obtaining multiplicity distributions and fluctuations wherever the experimental data are not available. The model consists of four main components: the initial conditions, partonic interactions, the conversion from the partonic to the hadronic matter, and hadronic interactions. The model provides two modes: Default and String Melting (SM) [7]. In both the cases, the initial conditions are taken from HIJING [10] with two Wood-Saxon type radial density profile of the colliding nuclei. The multiple scattering among the nucleons of two heavy ion nuclei are governed by the eikonal formalism. In the default mode, energetic partons recombine and hadrons are produced via string fragmentation. The string fragmentation takes place via the Lund string fragmentation function, given by,

$$f(z) \propto \; z^{-1}(1-z)^{a} exp(-\frac{bm_T^2}{z}), \tag{6.1}$$

Interactions of the produced hadrons are described by A Relativistic Transport model (ART).

In the SM mode, the strings produced from HIJING are decomposed into partons which are fed into the parton cascade along with the minijet partons. The partonic matter coalesce to produce hadrons, and the hadronic interactions are subsequently modelled using ART. While the Default mode describes the collision evolution in terms of strings and minijets followed by string fragmentation, the SM mode includes a fully partonic QGP phase that hadronizes through quark coalescence.

For both the modes, Boltzmann equations are solved using Zhang's parton cascade (ZPC) with total parton elastic scattering cross section,

$$\sigma_{gg} = \frac{9\pi\alpha_s^2}{2\mu^2}\frac{1}{1+\mu^2/s} \approx \; \frac{9\pi\alpha_s^2}{2\mu^2}, \tag{6.2}$$

where α_s is the strong coupling constant, s and t are the Mandelstam variables and μ is the Debye screening mass. Here a, b (fragmentation parameters) α_s and μ are the key deciding factors for multiplicity yield at particular beam energy. The values are taken as 2.2, 0.5, 0.47 and 1.8 fm^{-1} respectively, corresponding to total parton elastic cross section σ_{gg}=10mb. The mean values of multiplicities are found to match to the experimental data with these tunings for a wide range of energies [11]. The AMPT model, therefore, provides a convenient way to investigate a variety of observables with the default and SM modes.

In ALICE experiment, AMPT has been used for the simulation of Pb-Pb collisions.

6.2 Determination of the Collision Centrality

Before going to the details of the results of multiplicity fluctuations from the event generators, let us first discuss on the determination of the collision centrality in high-energy collisions. Centrality determination is of immense importance for the fluctuation studies. Therefore, one need to determine the collision centrality properly before the measurement of the fluctuation observables. In this section, the collision centrality determination has been discussed with the example of the centrality determination for Pb-Pb collisions in ALICE experiment.

The particle production mechanisms are expected to be dependent on the collision energy as well as the centrality of the collision. For most of the analysis, it is important to consider proper centrality window so that fluctuations because of this selection are minimized. Centrality is characterized by the impact parameter (b) of the collision or equivalently the number of participating nucleons (N_{part}) as shown in the Fig. 6.1. In an experimental scenario it is not possible to access these two quantities, so charged particle multiplicities within a given rapidity range or energy depositions by calorimeters are used. Thus, in heavy ion collisions, the total number

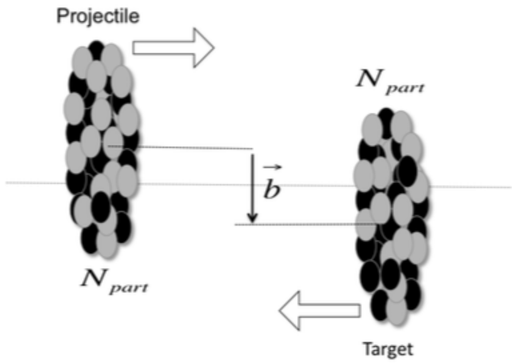

Figure 6.1: Impact parameter and the Number of Participants

of the charged particles in a given acceptance is a measure of the collision geometry. In a model dependent way, the connections of these experimental quantities to b or N_{part} are made. This is indeed needed in order to connect any measured quantity with theoretical calculations and to compare them with measurements from other experiments. The importance of centrality selection for fluctuation studies can be understood in terms of a simple participant model (discussed in Section 4.4). In this model, the number of produced particles in a collision depends on the centrality of the collision expressed in terms of N_{part} and the number of collisions suffered by each particle. Mathematically the number of produced particles can be expressed as

$$N = \sum_{i=1}^{N_{\mathrm{part}}} n_i \tag{6.3}$$

where n_i is the number of particles produced in the detector acceptance by the i^{th}-participant. On an average, the mean value of n_i is the ratio of the average multiplicity in the detector coverage to the average number of participants, i.e.,

$\langle n \rangle = \langle N \rangle / \langle N_{\text{part}} \rangle$. Thus the fluctuation in particle multiplicity is directly related to the fluctuation in N_{part}. In order to infer dynamical fluctuations arising from various physics processes one has to make sure that the fluctuations in N_{part} are minimal.

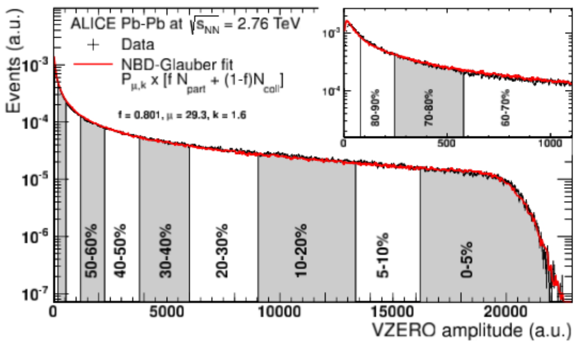

Figure 6.2: Centrality Selection using VO-Amplitude in ALICE experiment

In ALICE experiment, the centrality has been selected using V0M-detector [12, 13] as shown in the Fig. 6.2. Minimum bias distribution of the V0-multiplicity ($2.8 < \eta < 5.1$ and $-3.7 < \eta < -1.7$), (obtained after the physics selection and after applying the vertex-cut of $|V_z| < 10$ cm, removing outliers in the multiplicity correlation of TPC and V0, thus removing pile-up events, beam-gas etc.) is fitted with MC-Glauber Model, where the numbers of the particle-producing sources are given be, $f \times N_{\text{part}} + (1 - f) \times N_{\text{coll}}$. Here, N_{coll} are the number of binary collisions and f is the relative contribution of the number of participants and the number of binary collisions. In the Glauber model approach, the nuclear density profile and the nucleon-nucleon cross-section links the collision centrality to N_{part} and N_{coll}.

The number of particles produced by each source follow Negative Binomial Distribution, with the parameters μ and k_{NBD}. The values of f, μ and k_{NBD} have been measured from a fit to the minimum-bias V0-Amplitude distribution. Centrality is determined as a function of the fitted distribution. The fit is restricted to amplitudes above a value corresponding to 88% of the hadronic cross section. Centrality classes are determined by integrating the measured distribution above the cut shown in Fig. 6.2. Centrality bins are considered as $0-5\%$,$5-10\%$,$10-20\%$,.....,$70-80\%$, etc.

In Section 6.3, a study of charged particle multiplicity fluctuations as a function of centrality and beam-energy for Au-Au collisions for the Beam Energy Scan (BES) energies at RHIC (from $\sqrt{s}_{\mathrm{NN}} = 7.7$ GeV to 200 GeV) and Pb-Pb collisions at LHC-energy ($\sqrt{s}_{\mathrm{NN}} = 2.76$ TeV) from the available experimental data as well as using different modes of the AMPT model has been presented. Additionally, the method of centrality selection for fluctuation studies from the AMPT event generator and the centrality bin width corrections have been discussed. Multiplicity distributions for a wide range of the collision energies are presented too.

The results of the multiplicity fluctuations from the HIJING and DPMJET model in case of Pb-Pb collisions and p-Pb collisions in ALICE experiment will be discussed in details later in Chapter 7.

6.3 Results from AMPT

The parameters of AMPT-model have been described in Section 6.1.3. For the following analysis, the fragmentation parameters, a and b, are taken as 2.2 and 0.5 respectively, α_{s} and μ are taken as 0.47 and 1.8 fm^{-1}, corresponding to a cross-section σ_{gg}=10mb. The values of $a, b, \alpha_{\mathrm{s}}$, and μ are tuned, and the cross-sections are found to be 1.5 mb, 3 mb, 6 mb and 10 mb. The mean values of multiplicities

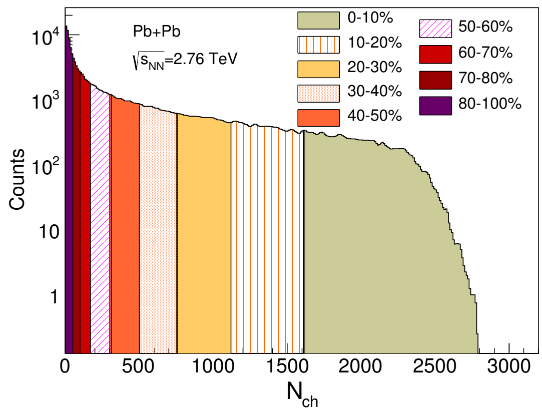

Figure 6.3: An example of centrality selection from minimum-bias distribution of charged particles generated with SM mode of AMPT for Pb-Pb collisions at $\sqrt{s}_{\rm NN}$ = 2.76 TeV for $2.0 < |\eta| < 3.0$ and $0.2 < p_{\rm T} < 2.0$ GeV/c.

are found to match to the experimental data with the tunings of a, b, $\alpha_{\rm s}$ and μ as 2.2, 0.5, 0.47 and 1.8 fm^{-1}, respectively.

6.3.1 Centrality selection and centrality bin width correction

The particle production mechanisms are expected to be dependent on the collision energy as well as the centrality of the collision. As stated earlier, for most of the analysis, it is important to consider proper centrality window so that fluctuations because of the selection are minimised.

In the present study, centrality is selected using the minimum bias distribution of charged particles in the forward pseudorapidity (η) range of $2.0 < |\eta| < 3.0$, and the multiplicity fluctuations are calculated in the central η-range ($|\eta| < 0.5$) [11]. Thus the two η-ranges are very distinct and the fluctuation results are unbiased. As an example of centrality selection procedure, in Fig. 6.3 we present the minimum bias charged particle multiplicity distribution within $2.0 < |\eta| < 3.0$ and transverse momentum (p_{T}) range of $0.2 < p_{\mathrm{T}} < 2.0$ GeV/c in Pb-Pb collisions at $\sqrt{s}_{\mathrm{NN}} = 2.76$ TeV obtained from AMPT model. Depending on the centrality selection requirement, the area under the curve is divided into centrality percentiles. The shaded regions in the figure show selections in 10% centrality cross-section bins (20% bin is shown for most peripheral collisions). For experimental data, centralities are selected by Glauber model fits to the minimum-bias distributions of charged particles as discussed earlier [12, 13].

Finer bin in centrality needs to be selected for fluctuation studies. This will avoid inherent fluctuations in N_{part} and number of charged particles within a centrality class.

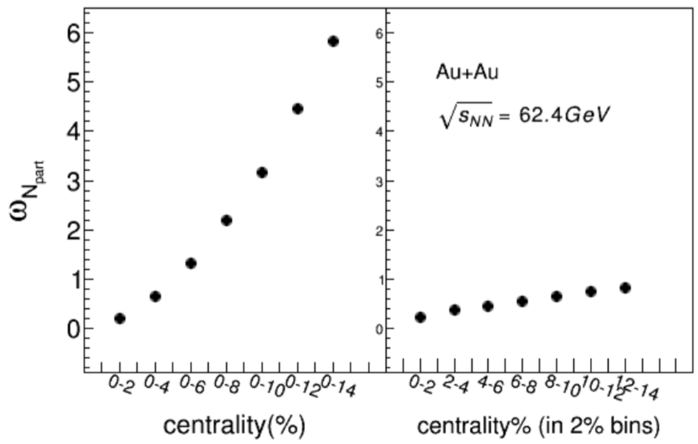

Figure 6.4: Fluctuations in N_{part} as a function of different centrality bins for Au-Au collisions at $\sqrt{s_{NN}} = 62.4$ GeV using the default mode of AMPT. The left panel shows the fluctuations for continuous increase of centrality and the right panel shows the results for narrow centrality bins.

As discussed earlier, fluctuations in $\langle N_{\mathrm{part}} \rangle$ need to be minimized while selecting the centrality. This is studied by calculating the fluctuations of $\langle N_{\mathrm{part}} \rangle$ for two sets

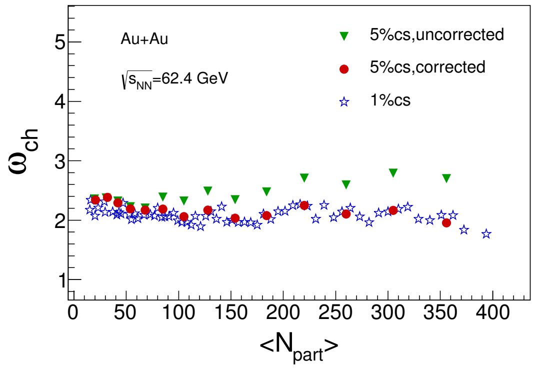

Figure 6.5: Effect of centrality bin width correction on scaled variances (ω_{ch}) is shown for choosing 5% centrality bins with the results for Au-Au collisions at $\sqrt{s_{NN}} = 62.4$ GeV using the default mode of AMPT as a function of $\langle N_{\rm part}\rangle$.

of results. In the left panel, the fluctuations of $\langle N_{\rm part}\rangle$ are estimated for progressively increasing centrality selection according to cross section, such as, $0-2\%$, $0-4\%$, $0-6\%$, $0-8\%$, $0-10\%$, etc. This is shown in the left panel of Fig. 6.4. It is observed that the fluctuations increase monotonically with the increasing width of the centrality window. This certainly affects the results of multiplicity fluctuations. In the right panel, the fluctuations of $\langle N_{\rm part}\rangle$ are estimated for narrow and uniform centrality bins in terms of cross sections, such as, $0-2\%$, $2-4\%$, $4-6\%$, $6-8\%$, $8-10\%$, etc. The results, shown in the right panel of Fig. 6.4, vary slowly as a function of centrality. It is obviously desirable to select finer bins in centrality for fluctuation analysis.

Selection of narrow centrality bins helps to get rid of inherent fluctuations within a centrality bin. The inherent fluctuations are intrinsic fluctuations arising from the difference in geometry even within the centrality bin. A centrality bin scans a range of charged particle multiplicity with different cross sections. This introduces geometrical fluctuations which need to be controlled. Choosing very narrow centrality window minimises the geometrical fluctuations. But it may not be always possible to present the results in such narrow bins, mainly because of lack of statistics and also because of centrality resolution of detectors used. It is desirable to choose somewhat wider centrality bins, such as 5% or 10% of the total cross sections. But these choices introduce inherent fluctuations which need to be corrected. This is done by taking the weighted average of the observables, such as,

$$X = \frac{\sum_i n_{\rm i} X_{\rm i}}{\sum_i n_{\rm i}}, \tag{6.4}$$

where the index i runs over each multiplicity bin, $X_{\rm i}$ represents various moments for the i-th bin, and $n_{\rm i}$ is the number of events in the i-th multiplicity bin. $\sum_i n_{\rm i} = N$ is the total number of events in the centrality bin.

This is demonstrated in Fig. 6.5 in terms of centrality dependence of scaled variance of the multiplicity distributions for Au-Au collisions at $\sqrt{s_{NN}} = 62.4$ GeV with the generated events from the default version of AMPT. Three sets of $\omega_{\rm ch}$ values are presented. The values of $\omega_{\rm ch}$ obtained with 5% centrality bins are much larger compared to the ones with 1% centrality bins. This variation comes because of wide 5% bins. After making the correction of the bin width effect, the fluctuations for the 5% cross section bins reduce by close to $\sim 23\%$ and $\sim 8\%$, respectively for central and peripheral collisions, and almost coincide with that of the 1% cross section bin. No centrality bin width dependence is observed after employing the correction. Thus by choosing narrow bins in centrality and making centrality bin width correction within each centrality window, the volume fluctuations are minimised.

6.3.2 Multiplicity distributions from event generators

Particle multiplicity distributions for different beam energies and collision centralities help to understand the mechanisms of particle production and constrain various models. Figure 6.6 shows minimum bias charged particle multiplicity distributions for $|\eta| < 0.5$ and $0.2 < p_{\rm T} < 2.0$ GeV/c in Au-Au collisions at $\sqrt{s_{NN}}$ =19.6 GeV, 27 GeV, 62.4 GeV and 200 GeV, using the default mode of AMPT, and Pb-Pb collisions at $\sqrt{s}_{\rm NN} = 2.76$ TeV using the SM mode of AMPT. As seen from the figure, each distribution gives the maximum extent of the multiplicity for a given collision energy for a given number of events. The maximum extent is larger for larger collision energy.

The minimum bias multiplicity distribution is a convolution of multiplicity distributions with different centrality bins. This is illustrated in Fig. 6.7 for charged particle multiplicity distributions in case of Pb+Pb collisions at $\sqrt{s}_{\rm NN} = 2.76$ TeV from the SM mode of AMPT model. Minimum bias distribution as well as distributions at different centrality bins are presented.

Width of the multiplicity distribution for a given centrality gives the extent of the fluctuation. Thus the physics origin of the fluctuations are inherent in the width of the multiplicity distributions. One of the ways to understand this to plot the multiplicity distributions within a centrality bin by scaling it to the mean value of multiplicity ($\langle N_{\rm ch}\rangle$). This is presented in Fig. 6.8 for Au-Au collisions at $\sqrt{s}_{\rm NN} = 62.4$ and 200 GeV using default AMPT and Pb-Pb collisions at $\sqrt{s}_{\rm NN}$ =2.76 TeV using the SM mode of AMPT. The vertical axes are multiplied by different factors for better visibility. In this representation, it is observed that the widths of the distributions are inversely proportional to volume, that is to $\langle N_{\rm ch}\rangle$. Thus the distributions become

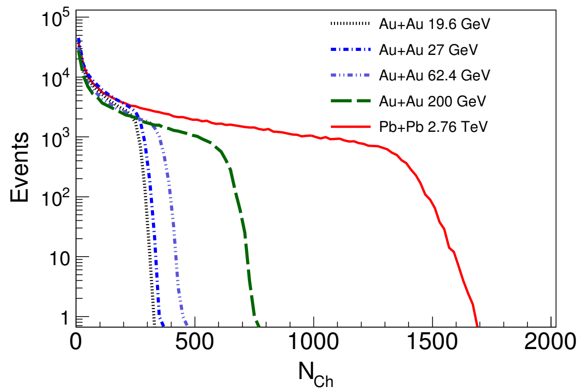

Figure 6.6: Minimum-bias distributions for charged particles for Au-Au collisions at 19.6, 27, 62.4 and 200 GeV using default AMPT model and for Pb-Pb collisions at $\sqrt{s_{\rm NN}}$ = 2.76 TeV, obtained using SM version of AMPT within $|\eta| < 0.5$ and $0.2 < p_{\rm T} < 2.0$ GeV/c.

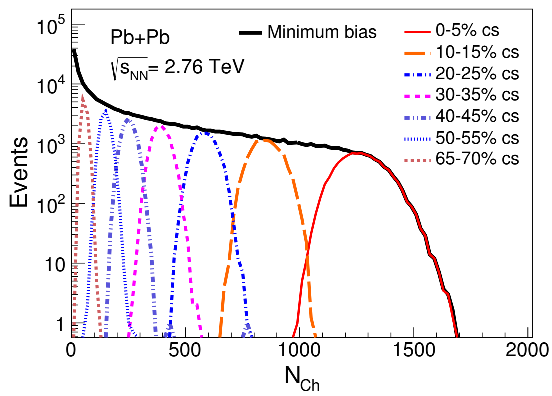

Figure 6.7: Charged particle multiplicity distributions for different centralities for Pb-Pb collisions at $\sqrt{s_{\rm NN}}$ = 2.76 TeV using SM mode of AMPT model within $|\eta| < 0.5$ and $0.2 < p_{\rm T} < 2.0$ GeV/c.

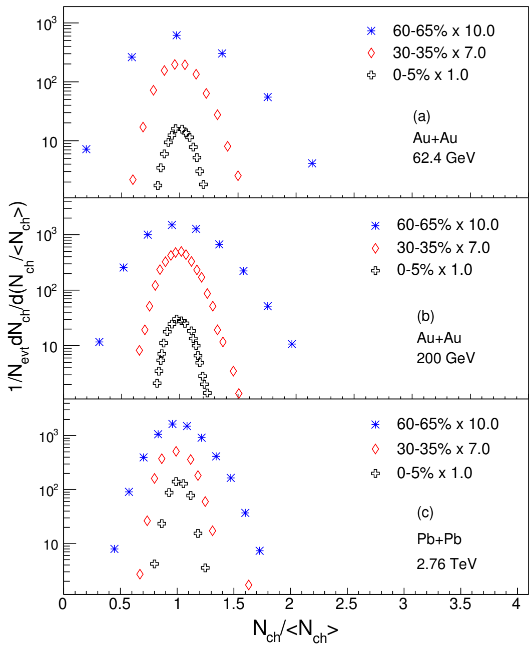

Figure 6.8: Scaled multiplicity distributions of charged particles for centralities corresponding to 0-5%, 30-35% and 60-65% cross sections for within $|\eta| < 0.5$ and $0.2 < p_{\mathrm{T}} < 2.0$ GeV/c using default AMPT for Au-Au collisions at $\sqrt{s_{\mathrm{NN}}}$ = (a) 62.4 GeV, (b) 200 GeV, and using SM mode of AMPT for Pb-Pb collisions at $\sqrt{s_{\mathrm{NN}}}$ = (c) 2.76 TeV. The scaling of the charged particle distributions are made to the mean values of the distributions.

narrower in going from peripheral to central collisions for all energies. This extensive nature of the representation is avoided by calculating the scaled variance.

6.3.3 Multiplicity Fluctuations

Multiplicity fluctuations are studied as a function of collision centrality for Au-Au collisions at $\sqrt{s}_{\rm NN}$ = 7.7 GeV,19.6 GeV, 27 GeV, 62.4 GeV, 200 GeV and Pb-Pb collisions for $\sqrt{s}_{\rm NN}$ = 2.76 TeV for 5% centrality bins from peripheral to central collisions. For each centrality bin, the multiplicity distributions are corrected using centrality bin width correction method. The AMPT model gives the number of participating nucleons for each centrality bin and so the results are presented as a function of $\langle N_{\rm part}\rangle$. The statistical errors of the μ and σ are calculated using the Delta theorem [14] method. Errors for $\omega_{\rm ch}$ are obtained by propagating the errors on μ and σ. In most cases, statistical errors are observed to be small.

Figure 6.9 shows the results for μ, σ and $\omega_{\rm ch}$ as a function of $\langle N_{\rm part}\rangle$ for five collision energies. The left panels show the results for events generated using the default mode of AMPT and the right panels give the results obtained using SM mode of AMPT. For $\sqrt{s}_{\rm NN}$ = 2.76 TeV, only the results from the SM mode are presented. It is observed that for all collision energies, μ and σ increase smoothly in going from peripheral to central collisions for all energies. The centrality evolution of the moments can be understood by the Central Limit Theorem (CLT) according to which,

$$\mu \propto \langle N_{\rm part}\rangle \tag{6.5}$$

$$\sigma \propto \sqrt{\langle N_{\rm part}\rangle}. \tag{6.6}$$

It is to be noted that $\langle N_{\text{part}} \rangle$ is proportional to the volume of the system, and so ω_{ch} is a volume independent term. In Figure 6.9, μ and σ are fitted with respective CLT-form as in the above expressions with the constant of proportionality as free parameter. The CLT curves are superimposed on the AMPT points. The centrality evolution of the moments follow the trend of the CLT at all energies. Deviations to CLT fits are seen for central collisions at the highest energy considered.

The bottom panels of Fig. 6.9 show the scaled variances (ω_{ch}) as a function of centrality for different collision energies. The results are similar for both default and SM modes of AMPT. At low collision energies, ω_{ch} show a drop in going from most peripheral collisions after which the values remain unchanged. At higher energies, ω_{ch} remain rather constant as a function of centrality.

Beam-energy dependences of the multiplicity fluctuations have been studied by combining results from available experimental data with AMPT model calculations. Experimental results for heavy-ion collisions are available for WA98 [15] and NA49 [16, 17] experiments at CERN SPS and PHENIX [18] experiment at RHIC. Since these experimental results are presented for different detector acceptances, these have to be scaled to a common acceptance in order to present in the same figure. The available results are scaled for $\Delta\eta < 1$ using the prescription given Ref. [18]. If ω_{acc1} represents the measured scaled variance and ω_{acc2} is the scaled variance within $\Delta\eta < 1$, then we have [18],

$$\omega_{\text{acc2}} = 1 + f_{\text{acc}}(\omega_{\text{acc1}} - 1) \tag{6.7}$$

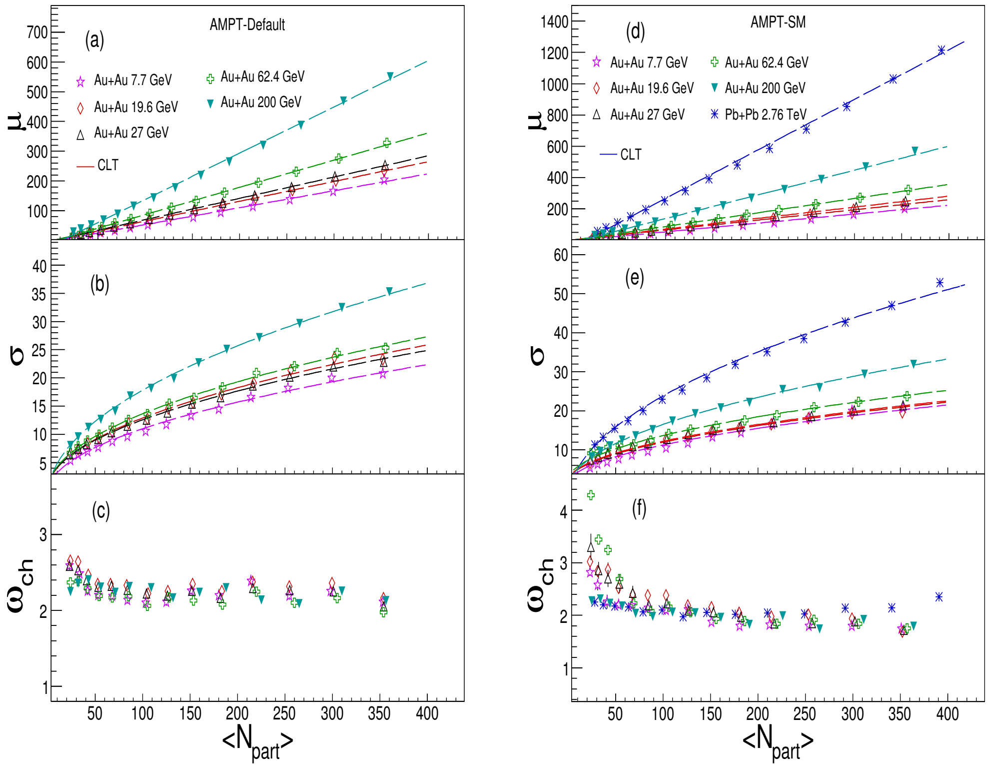

Figure 6.9: μ, σ and ω_{ch} of charged particles within $|\eta| < 0.5$ and $0.2 < p_{\mathrm{T}} < 2.0$ GeV/c as a function of centrality for a wide range of collision energies. The left panels show the results from the default mode of AMPT and the right panels show the corresponding results from the SM mode of AMPT. Dashed lines represent fits using the central limit theorem.

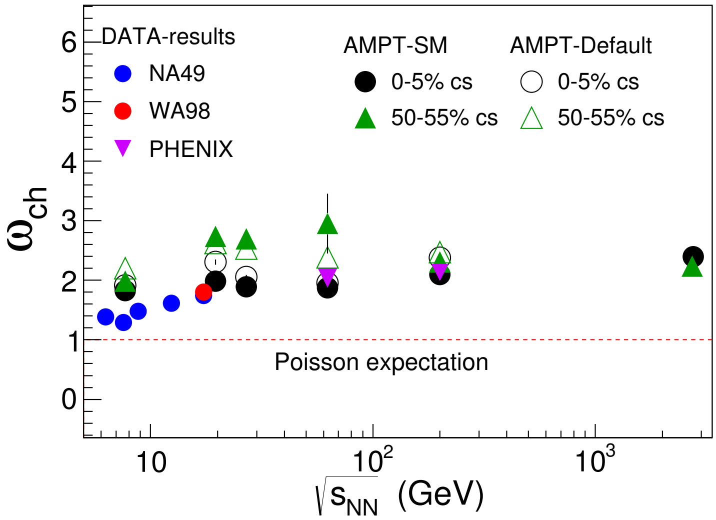

Figure 6.10: Beam-energy dependence of scaled variance ($\omega_{\rm ch}$) as a function of collision energy for available experimental data and for events generated using two modes of AMPT model.

where,

$$f_{\rm acc} = \frac{\mu_{\rm acc2}}{\mu_{\rm acc1}}. \tag{6.8}$$

The values of $\omega_{\rm acc2}$ have been calculated from the data provided by the experiments. Fig. 6.10 shows the values of $\omega_{\rm ch}$ for central collisions for WA98, NA49 and PHENIX experiments. The results for $\omega_{\rm ch}$ are also presented for two different centralities ($0-5\%$ and $50-55\%$ of total cross section) using the default and SM modes of AMPT. A slow rise in $\omega_{\rm ch}$ has been observed from low to high collision energies and then remaining constant at higher energies. The AMPT results overestimate those of NA49 experimental data, but are close to those of WA98 and PHENIX data. These values are larger compared to the Poisson expectations. Generally,

ω_{ch} is constructed in such a way that statistical fluctuations give the same result at any multiplicity. Thus, it has negligible dependence on centrality and beam energy. $\omega_{\rm ch}$ at higher energies and central collisions are found to be ~2 within the limits of statistical precision.

6.4 Estimation of $\omega_{\rm ch}$ from the participant model

An estimation for the multiplicity fluctuation can be made in the light of the participant model, where the nucleus-nucleus collisions are assumed to be superposition of nucleon-nucleon interactions (as described in Ref. [13]). Here, the total multiplicity

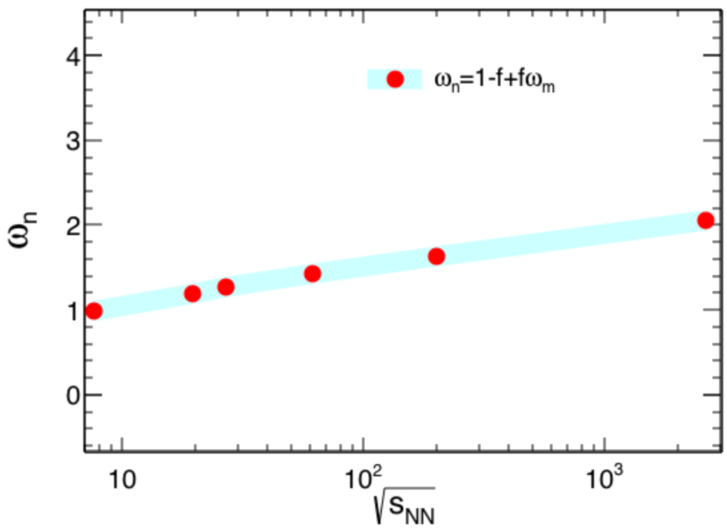

Figure 6.11: Beam-energy dependence of $\omega_{\rm n}$ as a function of collision energy

fluctuation has contributions due to fluctuations in $N_{\rm part}$ and also due to the fluctuation in the number of particles produced per participant. As discussed in Section

4.4, ω_{ch} can be expressed as,

$$\omega_{\text{ch}} = \omega_{\text{n}} + \langle n \rangle \omega_{N_{\text{part}}} \tag{6.9}$$

where, n is the number of charged particles produced per participant, ω_{n} denotes fluctuations in n, and $\omega_{N_{\text{part}}}$ is the fluctuation in N_{part}. The value of ω_{n} has a strong dependence on acceptance. The fluctuations in the number of accepted particles (n) out of the total number of produced particles (m) can be calculated by assuming that the distribution of n follows a binomial distribution. This is given as [13, 15],

$$\omega_{\text{n}} = 1 - f + f\omega_{\text{m}}, \tag{6.10}$$

where f is the fraction of particles accepted (as discussed in Section 4.4). The values of f are obtained from the published proton-proton collision data for total number of charged particles and number of charged particles in mid-rapidity over the energy range considered [22, 23, 24]. ω_{m} is calculated from the total number of charged particles using the formulation given in Ref. [15]. Using these, we obtain the values of ω_{n} as a function of collision energy. The values of ω_{n} vary within 0.98 to 2.0 corresponding to $\sqrt{s_{\text{NN}}}$ =7.7 GeV to 2.76 TeV. These values match with those reported for SPS collisions [15, 20]. The values of ω_{n} for different energies have been presented in Fig. 6.11. The values are determined within a precision of ± 0.1, which has been shown by the shaded region in Fig. 6.11. By using the values of ω_{n} in Eqn. 6.9, we find that ω_{ch} from the statistical model calculations are close to those of the AMPT results presented in Fig. 6.10. It has been observed from the Fig. 6.12. In this fig, the red-shaded region represents the estimation from the

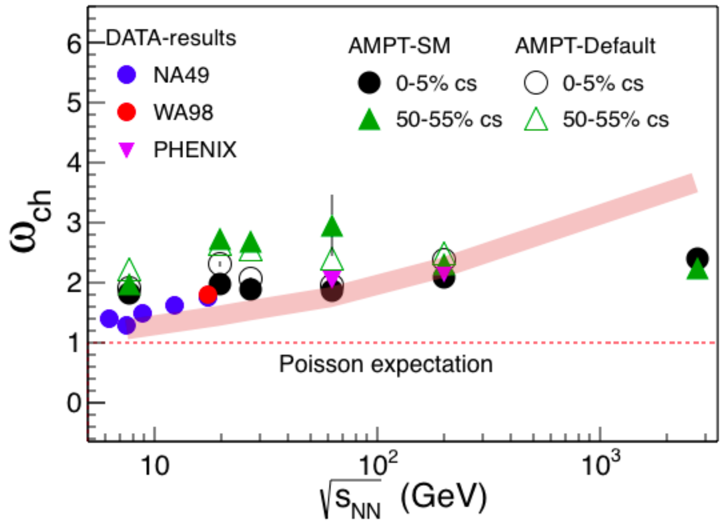

Figure 6.12: Estimation of $\omega_{\rm ch}$ within the participant model (shown by the shaded region)

participant model. It is evident that, at the LHC energy, the AMPT results are somewhat smaller. We observe that the values of $\omega_{\rm n}$ has a major contribution to $\omega_{\rm ch}$.

6.5 Discussions

Collision energy dependence of fluctuations of charged particle multiplicity, presented in Fig. 6.10 does not show any non-monotonic behaviour for the AMPT results as well as for experimental data. The experimental data and AMPT results are rather close to each other. Non-monotonic behaviour is not expected from the AMPT event generator as it does not contain any physics specific to phase transition and critical behaviour. The absence of non-monotonic behaviour in the experimental data point to the absence of critical phenomenon for the systems studied at SPS and

RHIC. In addition, the observed fluctuations in charged particles may be affected by the evolution of fluctuation during the early collision time to freeze-out. More data for Beam Energy Scan (BES) energies at RHIC are needed to make any definitive conclusion on the critical behaviour. The results presented using the AMPT event generator provide baselines for these studies at BES energies and for collisions at the Large Hadron Collider (LHC).

Multiplicity fluctuations arise from several known sources such as, fluctuations in the number of sources producing multiplicity, fluctuations in the number of particles produced in each source, detector-acceptance, resonance decays, etc. If particles are produced independently, one gets $\omega_{ch} = 1$. But as we move to higher energies, the non-statistical fluctuations increase and automatically contribute to the increased value of the fluctuation as discussed in Ref. [20]. Various studies have been reported in the literature in order to explain the values for multiplicity fluctuations expressed in terms of the scaled variances [18, 19, 13, 25, 26]. As discussed in Chapter 4, Ref. [19] gives a prediction for the values of scaled variance in GCE, CE and MCE using the hadron resonance gas model at chemical freeze-out for the central heavy-ion collisions for a wide collision energy range. According to these calculations, we get a value for ω_{ch} between 1.4 to 1.64 for GCE, 1.06 to 1.64 for CE, and 0.534 to 0.619 for MCE. At higher energies, the scaled variance is predicted to be similar for CE and GCE. Results presented in Fig. 6.10 are close to the GCE description for higher collision energies [11].

Event generators, by including dynamical phenomenon and critical behavior, are absent at present. This study offers a baseline for the future endeavour to pursue research on particle multiplicity fluctuations at Facility for Antiproton and Ion Research (FAIR), RHIC and LHC energies.

Bibliography

[1] M. Gyulassy, X. -N. Wang, Phys. Rev. **C80**, 024906 (2009).

[2] B. Andersson, G. Gustafson and B. Nilsson-Almquist, Nucl. Phys.**B281**, 289 (1987).

[3] A. Capella, U. Sukhatme and J. Tran Thanh Van, Z. Phys. **C 3**, 329 (1980); J. Ranft, Phys. Rev. **D37**, 1842 (1988); Phys. Lett.**188B**, 379 (1987).

[4] J. Ranft: New features in DPMJET version II.5, Siegen pre print, 1999.

[5] J. Ranft, DPMJET version II.5, arXiv:hep-ph/9911232v1, (1999).

[6] Stefan Roesler et. al., arXiv:hep-ph/0012252v1 (2000).

[7] Z.-W. Lin, C.M. Ko, B.-A. Li, B. Zhang, S. Pal, Phys. Rev. **C 72**, 064901 (2005).

[8] Z.W. Lin *et al.*, Phys. Rev. **C 64**, 011902 (2001).

[9] B. Zhang *et al.*, Phys. Rev. **C 61**, 067901 (2000).

[10] X.-N. Wang, M. Gyulassy, Phys. Rev. **D 44**, 3501 (1991).

[11] Maitreyee Mukherjee *et al.* 2016 J. Phys. G: Nucl. Part. Phys. **43** 085102.

[12] B. Abelev *et al.* (ALICE Collaboration), Phys. Rev. **C 88**, 044909 (2013).

[13] K. Aamodt *et al.* (ALICE Collaboration), Phys.Rev.Lett.**106**:032301, 2011.

[14] X. Luo, J. Phys. G : Nucl. Part. Phys. **39** 025008 (2012), arXiv:1109.0593v1 (2012).

[15] M. M. Aggarwal *et al.* (WA98 Collaboration) Phys. Rev. **C 65**, 054912 (2002).

[16] C. Alt. *et al.* (NA49 Collaboration), Phys. Rev. **C 78**, 034914 (2008).

[17] M. Rybczynskil *et al.* (NA49 Collaboration), Jour. of Phys.: Conference Series **5**, 74 (2005).

[18] A. Adare *et al.* (PHENIX Collaboration) Phys. Rev. C 78, 044902 (2008), arXiv: 0805.1521[nucl-ex] (2008).

[19] V. Begun, M. Gazdzicki, M.Gorenstein, M.Hauer, V.Konchakovski, and B.Lungwitz , arxiv:nucl-th/0611075 (2007).

[20] G.V.Danilov and E.V.Shuryak, arxiv:nucl-th/9908027 (1999).

[21] H. Heiselberg, Phys. Rept. **351** 161 (2001).

[22] B.B. Back *et al.* (PHOBOS Collaboration), arXiv:nucl-ex/0301017.

[23] K. Aamodt *et al.* (ALICE Collaboration), Phys. Rev. Lett. **106** 032301 (2011).

[24] S. Chatrchyan *et al.* (CMS Collaboration) and G. Antchev *et al.* (TOTEM Collaboration), Eur. Phy. Jour. **C74** 2053 (2014).

[25] M. Gazdzicki and P. Seyboth, arXiv:1506.08141v2 [nucl-ex].

[26] G. Baym and H. Heiselberg, Phys. Lett. **B 469**, 7 (1999).

7 Analysis Details in ALICE

In this chapter, the analysis tools used for the multiplicity fluctuation studies in Pb-Pb and p-Pb collisions at the ALICE energies have been discussed in details. Alongwith the data-sets and track-cuts used for the analysis, the centrality selection, centrality binwidth correction, detector effect, efficiency correction, statistical error estimation, and data clean-up have been discussed in the following sections. The technical challenges encountered in course of the analysis and the techniques developed to deal with them, have been described also.

7.1 Selection of data-sets and track-cuts

The data taken by ALICE in 2010 has been analyzed for Pb-Pb collisions at $\sqrt{s_{\mathrm{NN}}}$ = 2.76 TeV and for p-Pb collisions at $\sqrt{s_{\mathrm{NN}}}$ = 5.02 TeV, data taken in 2013 has been analyzed. 14 million and 12 million events have been analyzed for Pb-Pb and p-Pb collisions respectively. In Table 7.1, the colliding systems, collision energy, vertex cuts, data-sets used, number of events analyzed, triggers used and the event generators used in the analysis have been listed.

Colliding systems	Pb-Pb	p-Pb
Collision energy	$\sqrt{s}_{\mathrm{NN}} = 2.76$ TeV	$\sqrt{s}_{\mathrm{NN}} = 5.02$ TeV
Vertex-cuts	$-10 < V_{\mathrm{z}} < 10$ cm, $-0.3 < V_{\mathrm{x}}, V_{\mathrm{y}} < 0.3$ cm	$-10 < V_{\mathrm{z}} < 10$ cm
Data sets used	LHC 10h pass 2 AOD 086	LHC 13b pass 3 AOD
Simulation data sets	LHC 11a10a bis AOD 090, anchored to LHC 10h pass 2 AOD 086	LHC 13b2_efix_p1 AOD, anchored to LHC 13b pass 3 AOD
Number of events analyzed	14 million (data), 2 million (Simulation)	12 million (data), 30 million (Simulation)
Triggers used	kMB	kINT7
Event generators used	HIJING	DPMJET

Table 7.1: Data sets used for the analysis

7.1.1 Data Sample used for analysis

For Pb-Pb analysis :

Period/Production/pass : LHC 10h pass 2 AOD 086; Statistics : $\sim$ 14M events (all events), and $\sim$ 400K events (cleaned events); Run numbers used (all events) : 90 run numbers;

Run numbers used (after data cleanup) : 13 run numbers

For p-Pb analysis :

Period/Production/pass : LHC 13b pass 3 AOD; Statistics : $\sim$ 12M events (cleaned events);

Run numbers used (cleaned events) : 12 run numbers

7.2 Analysis Flow-Chart

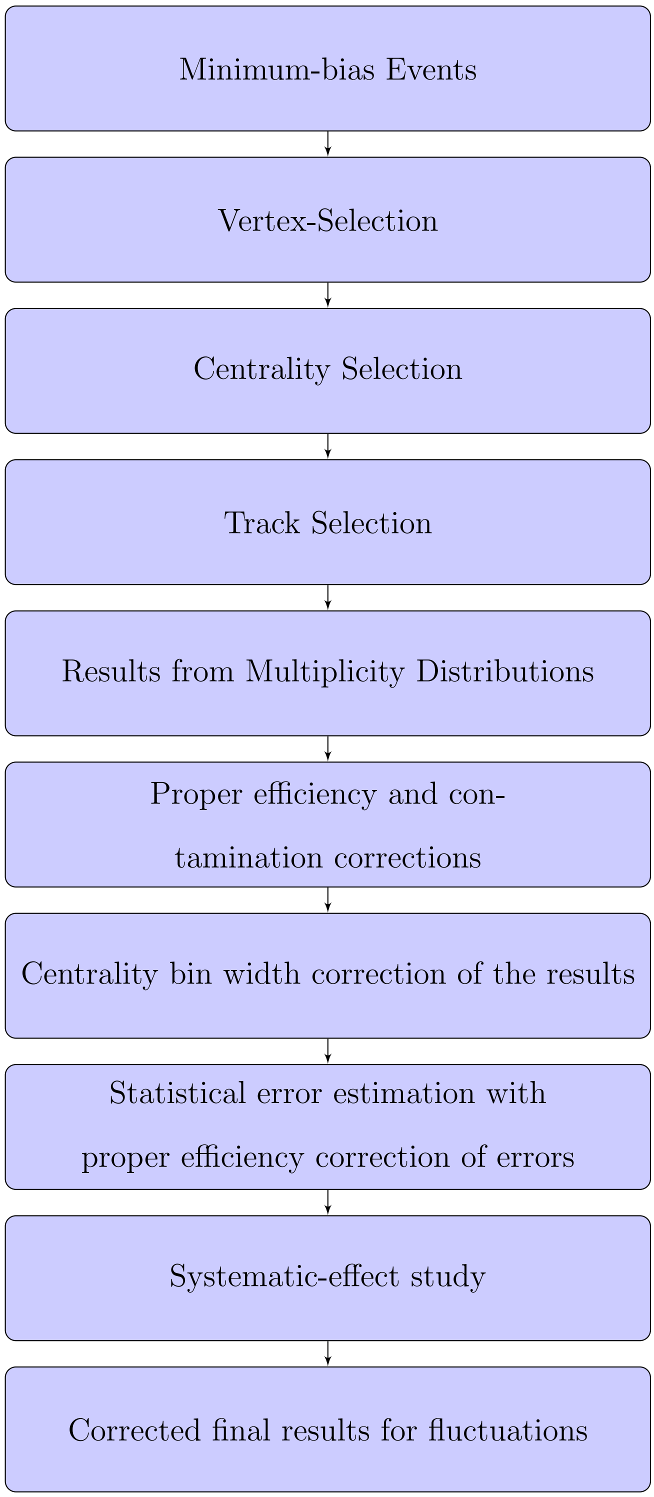

7.2.1 Detectors used for the analysis

In the analysis, ITS (mainly SPD) [1] detectors have been used for the selection of the vertex and tracking. TPC [2] has been also used for tracking. V0-detectors [3] have been used for the selection of centrality.

7.2.2 Selection of Trigger

The minimum-bias triggers (described earlier in Section 2.7.1), denoted by kMB for Pb-Pb and kINT7 for p-Pb. have been used for this analysis.

7.2.3 Vertex-cuts

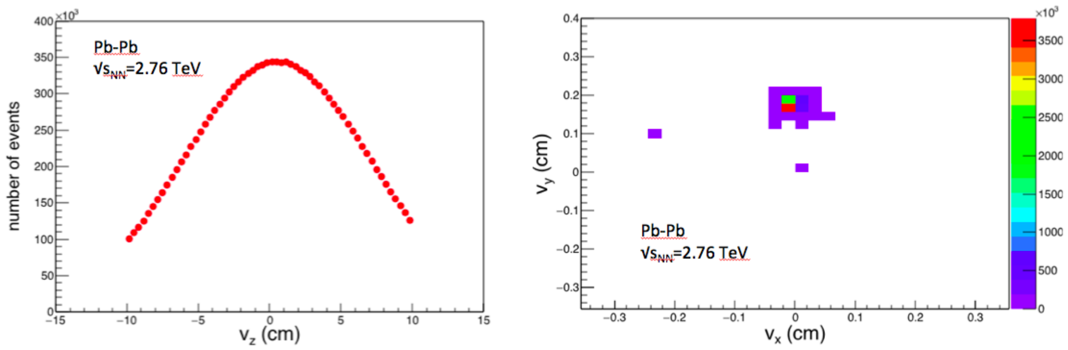

Figure 7.1: Vertex-cuts used for Pb-Pb data analysis at $\sqrt{s_{NN}}$ = 2.76 TeV. Left panel : $V_{\rm z}$-cut. Right panel : $V_{\rm x}, V_{\rm y}$-cut

The vertex-cuts used for Pb-Pb data analysis at $\sqrt{s_{NN}}$ = 2.76 TeV for the cleaned events, after trigger selection, have been shown in Fig. 7.1 as an example. Additional vertex-cut used for Pb-Pb :($|V_{\rm z_{track}}| - |V_{\rm z_{SPD}}| < 5\ mm$), to ensure that only those tracks are selected that are coming from the primary vertex.

For p-Pb analysis at $\sqrt{s_{NN}} = 5.02$ TeV, $-10 < V_z < 10$ cm has been used as listed in Table 7.1.

7.2.4 Track-cuts

Hybrid tracks are used for the multiplicity fluctuation analysis. In 2010, some of the SPD channels were off during data taking which was the main cause behind the holes in the phi-distribution. Acceptance plays an important role in fluctuation studies. Therefore, the track-cut should be chosen in such a way so that the huge phi-holes can be taken care of.

Hybrid track-cuts are global tracks which are basically a combination of three tracks and the resultant distribution has no phi-holes within it. Fig. 7.2 shows how

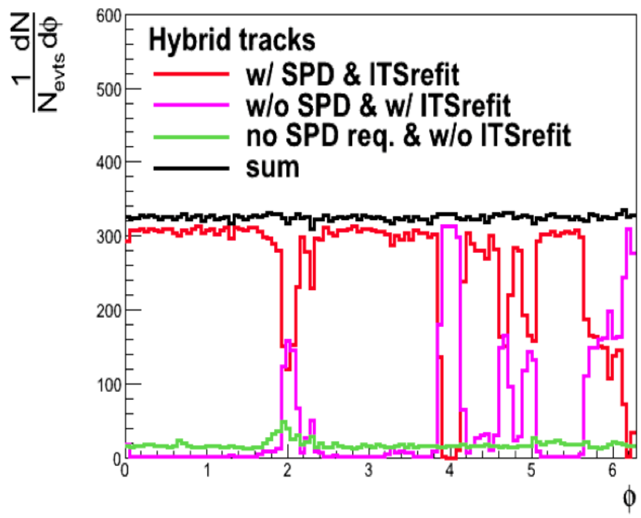

Figure 7.2: Hybrid Track-cuts

the phi-holes have been taken care of using the hybrid-track cuts. These are basically sum of three kind of tracks : these are the global tracks with SPD hit(s) and an

ITS refit, global tracks without SPD hit(s) and with an ITS refit constrained to the primary vertex, and global tracks without ITS refit constrained to primary vertex.

Another track-cut has been used for the analysis, which is the TPC-only track-cut. These are global tracks, possessing cuts for only Time Projection Chamber (such as TPC cuts for particle identifications etc).

Transverse momentum range	$0.2 < p_{\mathrm{T}} < 2.0$ GeV/c
Pseudorapidity range	$-0.8 < \eta < 0.8$
Distance of Closest Approach (DCA-cuts)	$DCA_{\mathrm{xy}} < 2.4\ cm, DCA_{\mathrm{z}} < 3.2\ cm.$
Number of TPC-clusters	80 (minimum)
χ^2 per number of clusters	4.0 (maximum)

Table 7.2: Kinematic cuts used for the analysis

The kinematic cuts used for Pb-Pb as well as p-Pb data analysis have been listed in Table 7.2. Transverse momentum range has been taken as $0.2 < p_{\mathrm{T}} < 2.0$ GeV/c, to ensure that in this analysis, mainly soft particles are to be dealt with. Below this range of p_{T}, the detector-efficiency is low. The parameters have been varied to study the systematic uncertainties, which will be discussed in details in Chapter 8.

7.2.5 Monte-Carlo Simulation

For MC simulation, the following data sets have been used :

For Pb-Pb analysis :

Period/Production/pass : LHC 11a10a bis AOD 090; Statistics : $\sim$ 2M events; Run numbers used : 133 run numbers.

For p-Pb analysis :

Period/Production/pass : LHC 13b2_efix_p1 AOD; Statistics : $\sim$ 30M events; Run numbers used : <u>26 run numbers.</u>

7.3 Centrality determination in ALICE

Collision centrality is the measure of initial overlap region of the colliding nuclei and it is an important quantity to be measured correctly to study the properties of QCD matter at very high energies. Centrality determination helps in the comparison of ALICE measurements with those of other experiments as well as with theoretical calculations [4]. In general, centrality percentile can be obtained by integrating the impact parameter distribution. In ALICE, the centrality is defined as the percentile of hadronic cross-section corresponding to multiplicity above a threshold value ($N_{\text{ch}}^{\text{THR}}$) or energy deposited in ZDC below some given value ($E_{\text{ZDC}}^{\text{THR}}$),i.e., as defined in [4],

$$c \approx \frac{1}{\sigma_{\text{AA}}} \int_{N_{\text{ch}}^{THR}}^{\infty} \frac{d\sigma}{dN'_{\text{ch}}} dN'_{\text{ch}} \approx \frac{1}{\sigma_{\text{AA}}} \int_{0}^{E_{\text{ZDC}}^{\text{THR}}} \frac{d\sigma}{dE'_{\text{ZDC}}} dE'_{\text{ZDC}} \tag{7.1}$$

where, σ_{AA} is the total nuclear interaction cross-section. Cross-section may be replaced by the number of observed events after the correction for trigger efficiency. In heavy ion collision, the strong electromagnetic field generated contaminate the hadronic cross-section in the most peripheral collisions. Centrality determination is thus restricted upto which this contamination effect is negligible.

In the Ref. [4], the methods used for the centrality determination for the analysis of Pb-Pb data taken in 2010 and 2011 have been described in details. Glauber model has been implemented. The hadronic cross-section is determined mainly by using VZERO amplitude distribution fitted with the Glauber model as described in

Section 6.2. In Table 1 in [4], the mean values of $N_{\rm part}$ and $N_{\rm coll}$, RMS (the measure of dispersion) and systematic uncertainties obtained with Glauber MC calculation for each centrality class defined by the sharp-cuts in the impact parameter have been listed for Pb-Pb collisions. In Fig. 7.3 taken from Ref. [4], the geometric properties

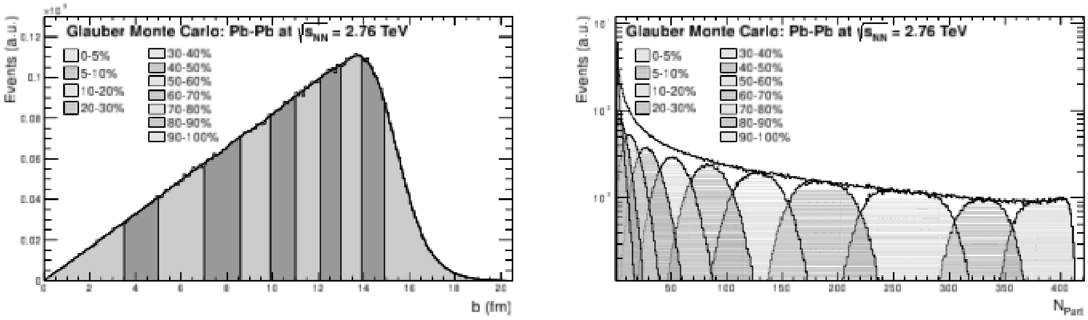

Figure 7.3: Geometric properties from Glauber MC calculation for Pb-Pb collisions at $\sqrt{s_{NN}} = 2.76$ TeV.

from Glauber MC calculation has been shown. In the left panel, impact patameter distribution for hadronic cross-section percentiles has been presented and in the right panel, $N_{\rm part}$ distributions for corresponding centrality classes have been shown. These centrality classes have been used in the multiplicity fluctuation analysis of Pb-Pb data at $\sqrt{s_{NN}} = 2.76$ TeV.

Centrality can be determined using ZDC also. In this case, centrality classes are defined by cuts on the two-dimensional distribution of the ZDC energy as a function of the ZEM amplitude [4]. The centrality selection uses the anti-correlation ZDC vs ZEM valid until the fragmentation breaks it. Thus, the centrality classes are defined within 0 *to* 35% centrality.

7.3.1 Resolution of the centrality determination

In ALICE, the centrality determination procedure uses different methods and we have different centrality estimators. Centrality can be determined using sum of amplitudes in the V0-detectors, or the number of clusters in the outer layer of SPD, or from ZDC. The resolution of the centrality classes is measured on an event-by-event basis. This is basically the RMS of the distribution of the differences between the centrality determined by different estimators and the average value of the centrality for each event [4]. Fig. 7.4 shows the centrality resolution for different

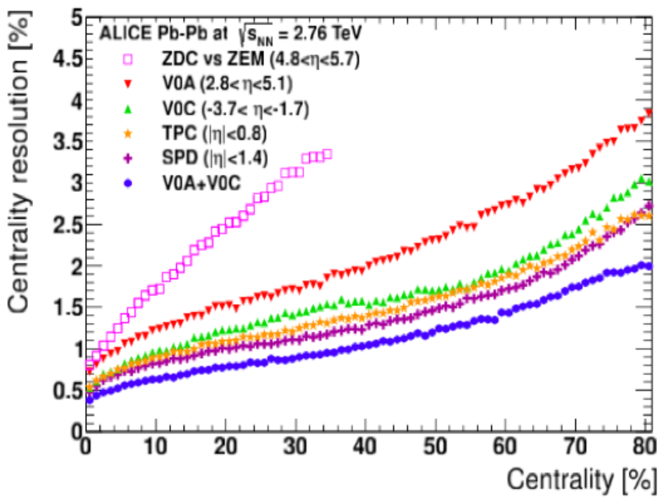

Figure 7.4: Centrality Resolution for different centrality estimators in ALICE

centrality estimators. It is evident that the resolution depends on the rapidity range of the detector. The centrality estimator combining V0A and V0C provides the best centrality resolution as shown in Fig. 7.4. Therefore, for Pb-Pb data analysis, V0M has been used as the centrality estimator.

7.3.2 Centrality in Monte Carlo

Centrality classes are defined in Monte Carlo, where the particle densities are kept same as in real data. HIJING MC already was tuned to have reduced multiplicity in the mid-rapidity region for the first physics analyses. Because of this reason, SPD and TPC produces classes with similar multiplicity as in data, but V0 multiplicity is very much different in MC and data. Therefore, for centrality selection in MC from V0-multiplicity, it has been scaled in MC to match the particle densities in the same centrality classes as in real data.

7.3.3 Centrality selection in p-Pb analysis

For p-Pb analysis, centrality is selected using V0A detector in ALICE [6]. The V0A-multiplicity has been fitted with NBD-Glauber function. The centrality classes are defined exactly as discussed previously. In Fig. 7.5, the centrality selection from

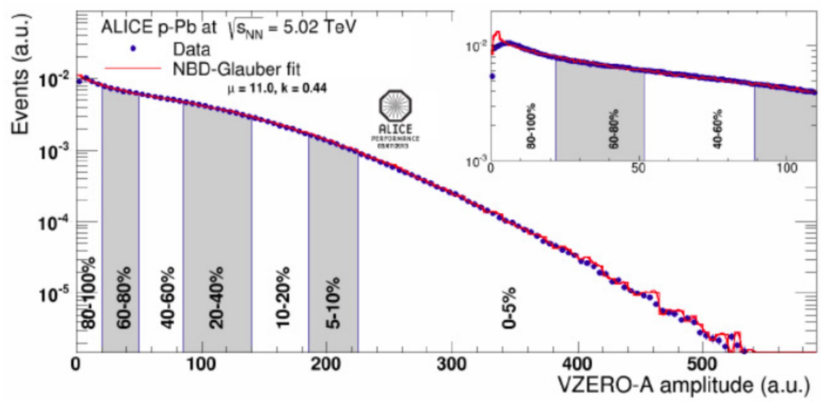

Figure 7.5: Centrality selection from V0A for p-Pb analysis

V0A-multiplicity for p-Pb analysis is shown. For the multiplicity fluctuation analysis in p-Pb, the centrality classes used are thus defined using V0A.

7.3.4 Centrality Bin Width Correction in ALICE

The essence of Centrality Bin Width (CBW) Correction [7] has been discussed in details in context of the results from AMPT event generator in Section 6.3.1.

Doing analysis using narrower centrality bins(i.e, 1% cs) or, analysis with 5% cs, with centrality binwidth correction applied, is justified. It is obvious to get rid of the geometry fluctuations. While selecting centrality using V0-multiplicity, it has been observed that one can further reduce the volume fluctuation by selecting 0.5% cs, instead of 1% cs. Figure 7.6 shows that the scaled variance is increasing

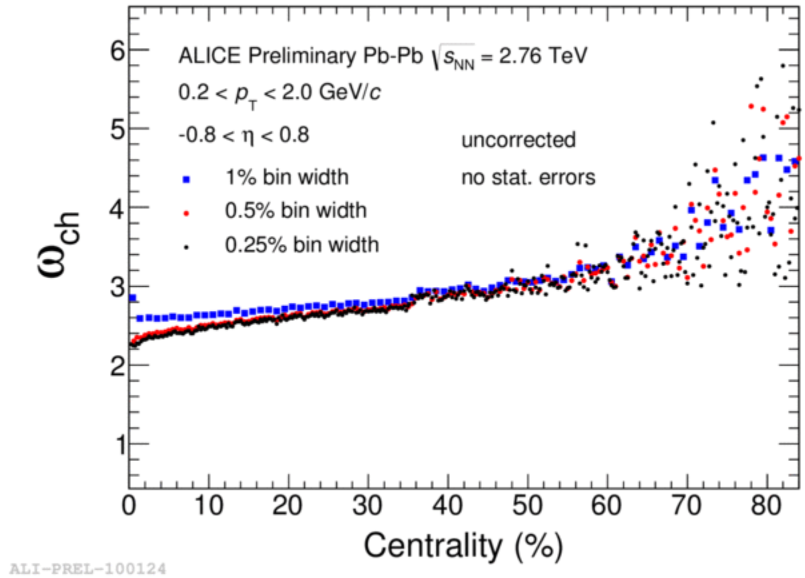

Figure 7.6: Centrality Bin Width Effect using Pb-Pb data at $\sqrt{s_{NN}} = 2.76$ TeV for $0.2 < p_T < 2.0$ GeV/c and $-0.8 \leq \eta \leq 0.8$

from central to peripheral collisions (results are not corrected for detector-effect here). It is observed that, from central collisions upto $\sim$ 40% cs, there is little difference between the results for scaled variance for 0.5% cs and 1% cs. This is quite obvious as resolution for VZERO is less than 1.0 beyond 40% centrality. Here, we discuss how this affects the multiplicity fluctuation results. There is no difference between 0.5% cs and 0.25% cs results. Therefore, it is decided to correct the results for bin width effect using 0.5% centrality bins upto 40% cs, and then using 1% cs from 40% to the peripheral collisions. It is evident from Fig. 7.4 that the centrality resolution of V0A+V0C is greater than 1 in the most peripheral collisions (i.e, peripheral to 60% centrality). Therefore, using 1% cs bins or 1% cs to 1.5% cs bins for the binwidth correction give similar results from 60% to the most peripheral collisions. The final results will be presented in 5% centrality bins after applying the binwidth correction.

7.4 Data clean-up

The charged particles are measured within $|\eta| < 0.8$ and centrality is selected from the minimum bias distribution of the V0-multiplicity, in the region $2.8 < \eta < 5.1$ and $-3.7 < \eta < -1.7$. We expect these two multiplicities to be correlated nicely, but we have observed some uncorrelated events while analysing the data. Figure 7.7 shows the correlation plot. We observe that there are some uncorrelated events. The percentage of these events are very small, only $\sim 0.014\%$ of the total events. For fluctuation studies, it is desirable to get rid of the uncorrelated events. First, we try the cleanup of the data using mean-multiplicity from V0 for different run numbers for the most central collisions. Figure 7.8 shows the cleanup using $\langle V0 - Multiplicity \rangle$. We get two separate distributions for $\langle V0 - Multiplicity \rangle$, while plotting it with respect to the run numbers. Correlation-plot drawn for once excluding the right-side run numbers of the red-line, and again excluding the left-side run numbers of the red-line. We are left with reduced number of events, but still we have uncorrelated

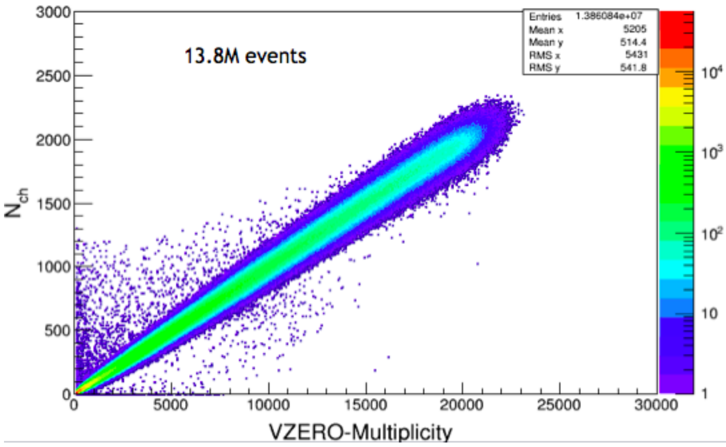

Figure 7.7: Correlation between N_{ch} and V0-Multiplicity considering all events for Pb-Pb collisions at $\sqrt{s_{\text{NN}}} = 2.76$ TeV

events.

Next, we have tried the cleanup using $\langle N_{\text{ch}} \rangle$ from the most central collisions. Figure 7.9 shows cleanup with $\langle N_{\text{ch}} \rangle$. From the distribution of $\langle N_{\text{ch}} \rangle$ from all the run numbers, we excluded run numbers for which $\langle N_{\text{ch}} \rangle > \mu \pm \sigma$. We are left with 12 million events, but still failed to remove the uncorrelated events. Figure 7.10 shows that V0M has a very good correlation with SPD-clusters. Therefore, it is not possible to cleanup the above said uncorrelated events using SPD-clusters. In reality, almost all run numbers have a few uncorrelated events. So it is very difficult to cleanup the data. It is then obviously wise to do run number-by-run number analysis and remove all the run numbers that are responsible for the uncorrelated events. Thus, we take only 13 runs ($\sim 400K$ events) which have no outliers. This has been taken to verify whether there be any effect on the final results if only cleaned-up sample is used. Figure 7.11 shows the nice correlation using only 13 run numbers having no uncorrelated events.

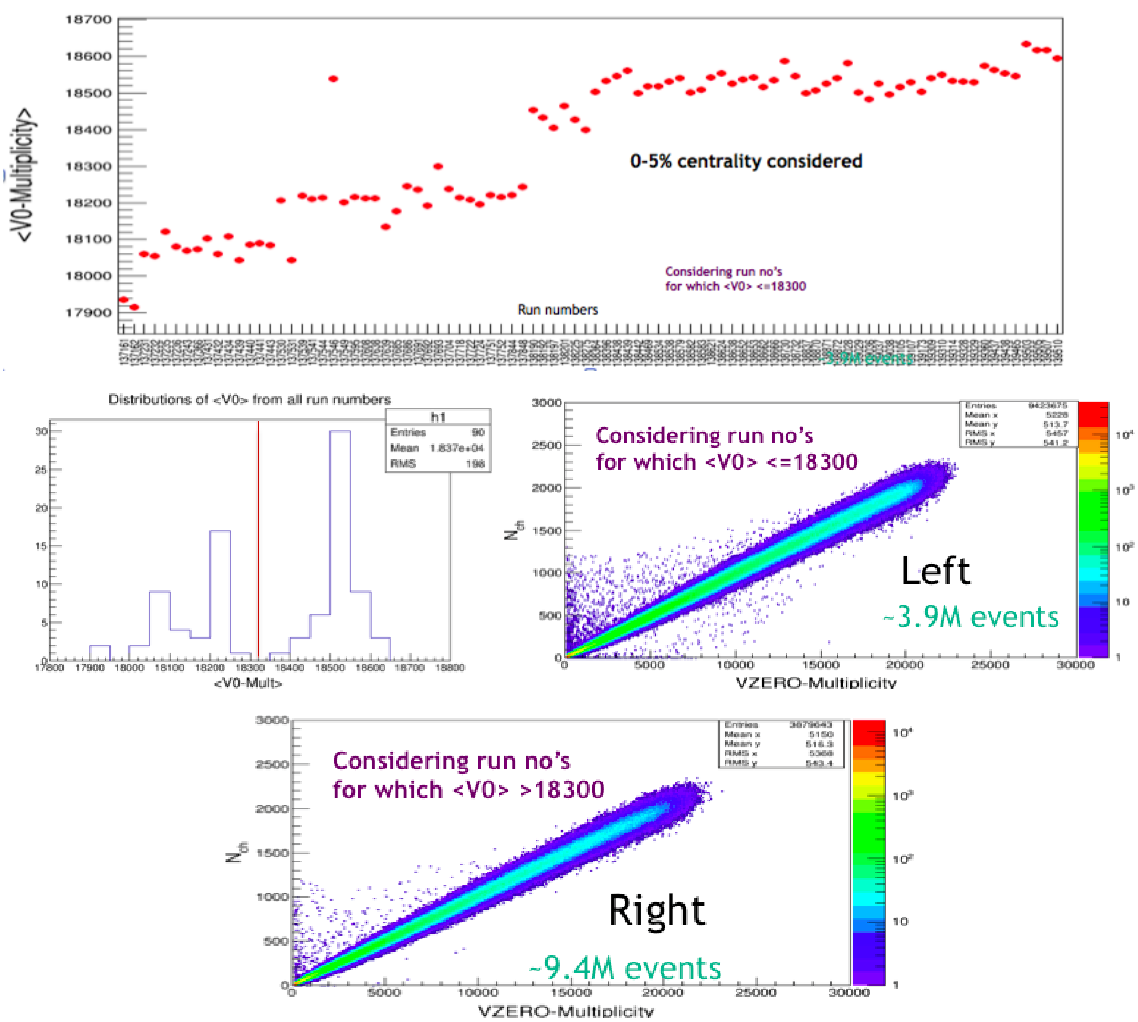

Figure 7.8: Cleanup using $\langle V0-Multiplicity\rangle$ Top panel : $\langle V0-Multiplicity\rangle$ with respect to run numbers, Middle left : Distributions of $\langle V0 - Multiplicity\rangle$ from all run numbers, Middle right : Correlation plot considering the left-side distribution of the Middle left panel plot, Bottom panel : Correlation plot considering the right-side distribution of the Middle left panel plot.

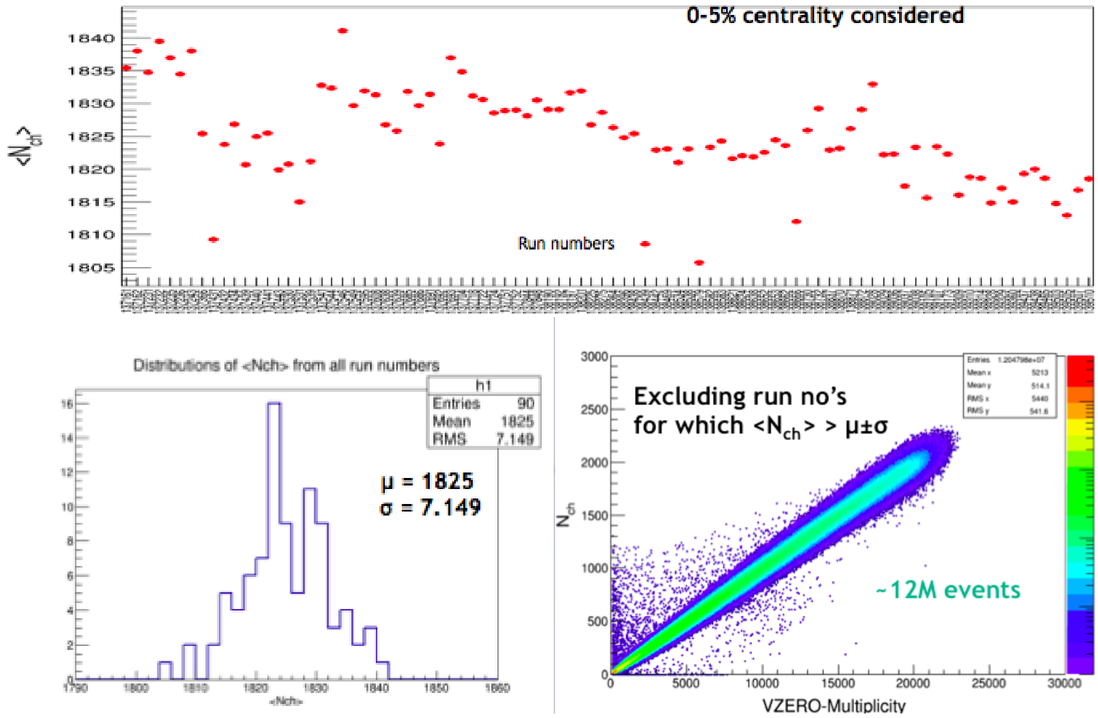

Figure 7.9: Cleanup of the uncorrelated events using $\langle N_{\mathrm{ch}} \rangle$

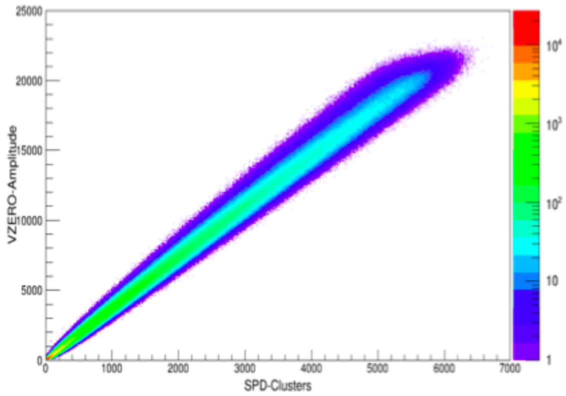

Figure 7.10: Cleanup of the uncorrelated events using SPD-cluster

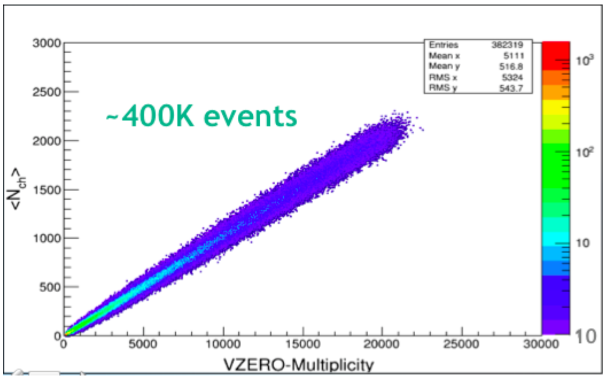

Figure 7.11: Nice correlation obtained using only 13 run numbers having no uncorrelated events for Pb-Pb collisions at $\sqrt{s_{\mathrm{NN}}} = 2.76$ TeV.

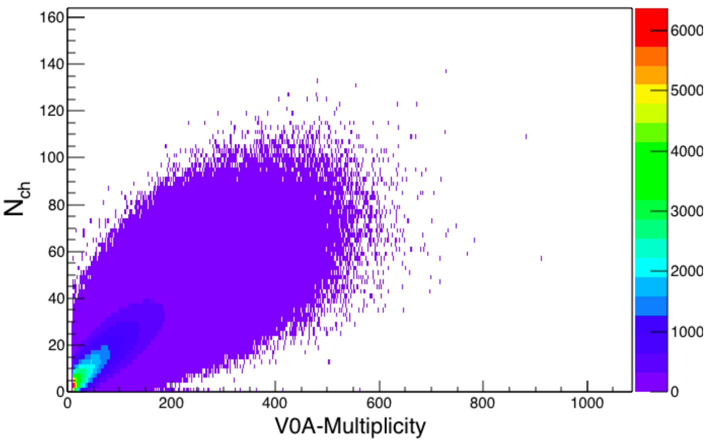

Figure 7.12: Correlation between N_{ch} and V0A-Multiplicity for p-Pb collisions at $\sqrt{s_{\mathrm{NN}}} = 5.02$ TeV

For p-Pb analysis, The correlation between N_{ch} and V0A-multiplicity for p-Pb collisions at $\sqrt{s_{\mathrm{NN}}} = 5.02$ TeV with ∼12 million events has been presented in Fig. 7.12.

7.5 Detector-Effect Study

Detectors are observed to have efficiencies less than 100% while detecting particles after a collision. The inefficiency of a detector arises because of tracking, limited acceptance, momentum resolution, vertex reconstruction, etc. In event-by-event analyses, corrections for these inefficiencies are not straightforward and it need special treatments.

7.5.1 Efficiency and Contamination corrections to Higher Order Moments

The study of the higher order cumulants got immense importance as a sensitive probe to phase transition and to search for the critical point on the QCD phase diagram. Moments of conserved quantities such as net-charge, net-baryon, net-strangeness as well as total charge particle-fluctuations are expected to show a deviation of an order of magnitude of its normal value near the critical point. Results from higher moments of conserved quantities have recently been reported in STAR and PHENIX experiments at RHIC (BNL). To extract the dynamical part of the fluctuations properly, it is needed to minimise the sources of statistical fluctuations (as discussed earlier) as well as to understand and correct for the inefficiency of the detector-systems involved in the experiment. The efficiency may be a constant, or may change depending on phase-space (i.e, transverse momentum, rapidity, azimuthal angle, etc). It is also necessary to calculate the statistical errors properly to have an estimate about how much we are limited by the statistics in the given condition of the experiment.

Let us discuss the procedures used to estimate the efficiency corrections. If it is assumed that N are the number of particles in every event, we can write,

$$\langle n \rangle = \epsilon N \tag{7.2}$$

where $\langle n \rangle$ is the mean observed particles and ϵ is the detector efficiency (illustrated later in details). But this fact does not indicate that in each event j, the number of observed particles be ϵN, as in that case variance will be zero. In reality, observed particle distribution has a finite width, which appears because of the observed particle fluctuations in each event around $\langle n \rangle$ [8].

A simplified way for the local efficiency corrections to higher order moments has been presented here. Additionally, the statistical error estimation by delta theorem, and the correction for the error due to inefficiency of the detector, even when the detector efficiency depends on the phase-space, has been discussed in details in the following sections. The problems in the computational part have been discussed too.

Earlier discussions on the efficiency corrections to higher order moments mostly assume the efficiency factor ϵ as a constant. In a recent study by Xiofeng Luo, the detector efficiency has been assumed as a variable quantity depending upon phase-space [9]. Here, we have tried to express the efficiency corrections to higher order moments and the related observables as a function of factorial moments and to calculate those in a simpler way, so that it can make the life of an experimentalist easier.

Generally, in these kind of approaches, the incident (produced) particles are assumed to be distributed according to P(N) and the observed particles are distributed according to

$$p(n) = \sum_{N} w(n|N)P(N) \tag{7.3}$$

where, $w(n|N)$ denotes the probability to observe n particles from N incident particles. Generally, $w(n|N)$ is modelled by a binomial distribution. So

$$w(n|N;\epsilon) = \frac{N!}{n!(N-n)!}\epsilon^{\mathrm{n}}(1-\epsilon)^{\mathrm{N-n}} \tag{7.4}$$

where, ϵ is the efficiency factor, which may be defined as,

$$\epsilon = \frac{\langle n\rangle_{reconstructed-primary}}{\langle N\rangle_{truth-primary}} \tag{7.5}$$

Therefore, we have,

$$\begin{aligned}
\langle n\rangle &= \int nP(n)dn \\
&= \int ndn \int w(n|N)P(N)dN \\
&= \int P(N)dN \int w(n|N)ndn \\
&= \epsilon \int P(N)NdN \\
&= \epsilon\langle N\rangle
\end{aligned} \tag{7.6}$$

A recent analysis on the energy-dependence of the higher moments of net-proton by the STAR collaboration used this approach [10]. Thus, the correction for mean reads,

$$\langle n \rangle = \epsilon \langle N \rangle \tag{7.7}$$

Using the factorial moments for the calculation of the efficiency factor, where, factorial moments are defined by,

$$F_{\mathrm{i}} = \langle \frac{N!}{(N-i)!} \rangle \tag{7.8}$$

We get,

$$\langle N \rangle = F_1 \tag{7.9}$$

and,

$$\sigma_{\mathrm{n}}^2 = \epsilon^2 \sigma_{\mathrm{N}}^2 + \epsilon \langle N \rangle - \epsilon^2 \langle N \rangle \tag{7.10}$$

Equation 7.10 represents the correction for sigma. Therefore, for the scaled variance, we have,

$$\omega_{\mathrm{ch_n}} = \epsilon(\omega_{\mathrm{ch_N}} - 1) + 1 \tag{7.11}$$

where, $\omega_{\mathrm{ch_n}}$ is the measured one and $\omega_{\mathrm{ch_N}}$ is the corrected one.

To include contamination corrections to the analysis, i.e, to correct the results for the secondary particles mostly, the efficiency-factor can be expressed as,

$$\epsilon = \frac{\langle n \rangle_{reconstructed-all}}{\langle N \rangle_{truth-primary}}, \tag{7.12}$$

instead of Equation 7.5. In Equation 7.12, $\langle n \rangle_{reconstructed-all}$ represents all the particles detected by the detector, instead of considering only primary particles. Naturally, the efficiency-factors evaluated this way are greater than the factor calculated in the previous way considering only observed primary particles.

7.5.2 Local efficiency corrections to higher order moments

In reality, efficiency factor depends on the phase-space, (i.e, transverse momentum, rapidity, acceptance, etc.), We have to correct for these local efficiency effects.

Taking care of these local efficiency effects [8], let us assume, N(x) be the number of produced particles in phase-space bin at x and n(x) be the number of observed particles at x. The event-averaged number of produced and observed particles at x are given by $\langle N(x) \rangle$ and $\langle n(x) \rangle$. To obtain the event average over all the particles, we need sum over all bins, i.e,

$$\langle N \rangle = \sum_{x} \langle N(x) \rangle \tag{7.13}$$

The probability $w(n(x)|N(x);\epsilon(x))$ is introduced to observe n(x) particles in phase-space-bin at x for given N(x) incident particles and variable detection efficiency $\epsilon(x)$. w is modelled as a binomial distribution as was done previously.

$$w(n(x)|N(x);\epsilon(x)) = \frac{N(x)!}{n(x)!(N(x)-n(x))!}\epsilon(x)^{\mathrm{n(x)}}(1-\epsilon(x))^{\mathrm{N(x)-n(x)}} \tag{7.14}$$

Therefore, we can write here,

$$p(n((x_1),..,n(x_{\rm n}))) = \sum_{N(x)} w(n(x_1)|N(x_1);\epsilon(x_1))..w(n(x_{\rm n})|N(x_{\rm n});\epsilon(x_{\rm n}))P(N((x_1),..,N(x_{\rm n}))) \tag{7.15}$$

Since, binomial distributions for various phase-space bins are independent (only particles are considered here, not anti-particles as the situation is illustrated for total charged particles), we get, for any phase-space bin, $\langle n(x)\rangle = \epsilon(x)\langle N(x)\rangle$.

Therefore, for the correction of mean, we get,

$$F_1 = \langle N\rangle = \sum_{i=1}^{m}\langle N(x_{\rm i})\rangle = \sum_{i=1}^{m}\frac{n(x_{\rm i})}{\epsilon(x_{\rm i})}, \tag{7.16}$$

where, m denotes the number of phase-space bins.

After adding up all the terms, correctly taking all the cross-terms in the calculation, we have the expression for the second factorial moment as,

$$F_2 = \sum_{i=1}^{m}\sum_{j=i}^{m}\frac{\langle n(x_{\rm i})(n(x_{\rm j}) - \delta_{x_{\rm i}x_{\rm j}})\rangle}{\epsilon(x_{\rm i})\epsilon(x_{\rm j})} \tag{7.17}$$

and, we get variance as,

$$\sigma_{\rm N}^2 = F_2 + F_1 - F_1^2 \tag{7.18}$$

Using the Equations (7.16), (7.17) and (7.18), phase-space dependent efficiency-corrected moments (upto second order) can be evaluated.

7.5.3 Statistical Error Estimation

Event-by-event multiplicity fluctuation analysis is limited in statistics. It is very important to estimate the statistical errors properly. Statistical error is estimated with the help of delta theorem [11]. Statistical errors calculated here are phase-space dependent efficiency-corrected, as the errors are expressed in terms of the efficiency-corrected factorial moments discussed in the previous section.

For this analysis, first, we express all the quantities in terms of the raw moments, where, the moment (μ_{n}) of a probability function P(N) taken about 0 is,

$$\begin{aligned} \mu_{\mathrm{n}} &= \langle N^{\mathrm{n}} \rangle \\ &= \int N^{\mathrm{n}} P(N) dN \end{aligned} \tag{7.19}$$

Raw moments can be expressed in terms of the central moments using the inverse binomial transform. However, for this analysis, it is easier to express the things in terms of the raw moments as the total number of charged particles are to be dealt with, instead of the net-number.

According to the general, if $F = F(\mu_{\mathrm{i}}, \mu_{\mathrm{j}})$, then,

$$Var(F) = \left(\frac{\partial F}{\partial \mu_{\mathrm{i}}}\right)^2 Var(\mu_{\mathrm{i}}) + \left(\frac{\partial F}{\partial \mu_{\mathrm{j}}}\right)^2 Var(\mu_{\mathrm{j}}) + 2\left(\frac{\partial F}{\partial \mu_{\mathrm{i}}}\right)\left(\frac{\partial F}{\partial \mu_{\mathrm{j}}}\right) cov(\mu_{\mathrm{i}}, \mu_{\mathrm{j}}) \tag{7.20}$$

where,

$$cov(\mu_{\mathrm{i}}, \mu_{\mathrm{j}}) = \mu_{\mathrm{i+j}} - \mu_{\mathrm{i}}\mu_{\mathrm{j}} \tag{7.21}$$

Equation 7.21 represents the covariance-term, which should be included in this analysis, as μ and σ are evaluated from the same distribution. It is observed that addition of the covariance-term basically reduces the statistical errors.

Expressing in terms of the raw moments, it can be written as,

$$\mu_1 = \langle N \rangle \tag{7.22}$$

So,

$$\begin{aligned}\triangle\mu_1 &= \left(\frac{Var(\mu_1)}{n_{\text{event}}}\right)^{\frac{1}{2}} \\ &= \left(\frac{\mu_{1+1} - \mu_1^2}{n_{\text{event}}}\right)^{\frac{1}{2}} \\ &= \left(\frac{F_2 + F_1 - F_1^2}{n_{\text{event}}}\right)^{\frac{1}{2}} \\ &= \frac{\sigma}{\sqrt{n_{\text{event}}}}\end{aligned} \tag{7.23}$$

Here, the factorial moments are defined as, $F_{\text{m}} = \langle\frac{N!}{(N-m)!}\rangle$. The variance can be written as ,

$$\sigma = \sqrt{(\mu_2 - \mu_1^2)} \tag{7.24}$$

Then,

$$\triangle\sigma = \left(\frac{Var(\sigma)}{n_{\text{event}}}\right)^{\frac{1}{2}} \tag{7.25}$$

where, after calculation using the above formula for $Var(F)$,

$$Var(\sigma) = \frac{\mu_4 - \mu_2^2}{4(\mu_2 - \mu_1^2)} + \mu_1^2 - \frac{\mu_1(\mu_3 - \mu_1\mu_2)}{\mu_2 - \mu_1^2} \tag{7.26}$$

Again, the expression for scaled variance can be written as,

$$\omega_{\mathrm{ch}} = \frac{\mu_2}{\mu_1} - \mu_1 \tag{7.27}$$

$$\triangle\omega_{\mathrm{ch}} = \left(\frac{Var(\omega_{\mathrm{ch}})}{n_{\mathrm{event}}}\right)^{\frac{1}{2}} \tag{7.28}$$

After all the calculations, we have,

$$Var(\omega_{\mathrm{ch}}) = \left(1 + \frac{\mu_2}{\mu_1^2}\right)^2 (\mu_2 - \mu_1^2) + \frac{\mu_4 - \mu_2^2}{\mu_1^2} - 2\left(1 + \frac{\mu_2}{\mu_1^2}\right)\frac{(\mu_3 - \mu_1\mu_2)}{\mu_1}, \tag{7.29}$$

where, all the moments can be expressed in terms of the phase-space dependent efficiency corrected factorial moments as,

$$\mu_1 = F_1 \tag{7.30}$$

$$\mu_2 = F_2 + F_1 \tag{7.31}$$

$$\mu_3 = F_1 + F_3 + 3F_2 \tag{7.32}$$

$$\mu_4 = F_4 + F_1 + 7F_2 + 6F_3 \tag{7.33}$$

Using all the above equations, statistical errors for mean, sigma and scaled variance have been evaluated. The errors have to be binwidth-corrected while expressing it in 5% centrality bins. For bin width correction, errors from each bin (say, i) are always added in quadrature, such as,

$$error = \sqrt{(\sum_{i}^{n} \omega_{\mathrm{i}}^2 Err_{\mathrm{i}}^2)} \tag{7.34}$$

where,

$$\omega_{\rm i} = \frac{n_{\rm i}}{\sum_i^n n_{\rm i}} \tag{7.35}$$

where, $n_{\rm i}$ denotes the number of events in i-th bin.

Due to the truncation issues, it is difficult to evaluate the moments involving large numbers properly. The code for evaluating the factorial moments will be found in [12]. The problem of the truncation issues have been taken care of in this code. With the help of the code, it is possible to correctly calculate upto 9th-moment.

The systematic errors occur mainly due to the variation in the several cuts used in the analysis. The sources and the percentages of the systematic errors will be discussed in details in Chapter 8.

7.6 Simulation framework

To understand the effect of the detector-system, a simulation framework needs to be developed. During the transport of the generated particles through the detector geometry, the detector-response to each particle crossing the detector is simulated. For this, different transport Monte Carlo packages are available. The response of the detectors to the charged particles in the full ALICE experimental setup has been estimated by the Aliroot simulation package where all the detector systems have been described in GEANT3 framework.

For evaluation of the detector response for Pb-Pb collisions, event generator used is HIJING 1.36.

For evaluation of the detector response for p-Pb collisions, event generator used is

DPMJET.

7.7 Results from MC-Simulation for Pb-Pb collisions at $\sqrt{s_{\mathrm{NN}}} = 2.76$ TeV

In this section, the results regarding the detector-response to the charged particles produced in Pb-Pb collisions at $\sqrt{s_{\mathrm{NN}}} = 2.76$ TeV have been presented.

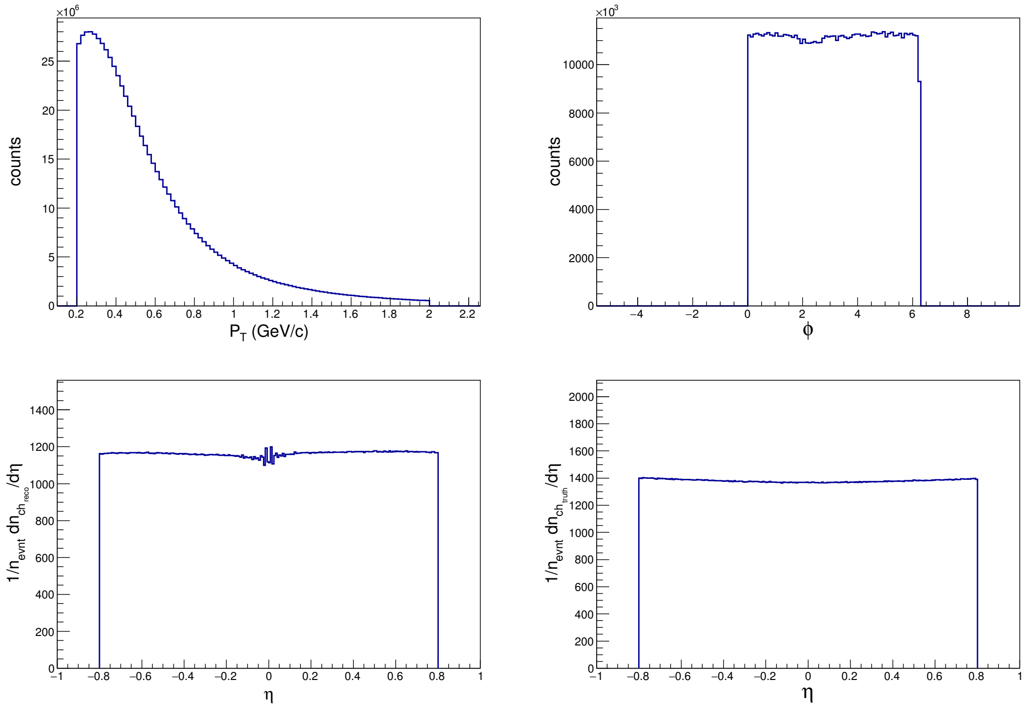

Figure 7.13: Quality Assurance (QA) plots from MC-HIJING for hybrid track-cuts. Top left : p_{T} distribution from the reconstructed track. Top right : ϕ-distribution Bottom left : Normalised η-distribution from the reconstructed track. Bottom right : Normalised η-distribution from the MC-Truth

Figure 7.13 shows the QA plots from MC-analysis. The vertex-cuts are taken as discussed in Section 6.1.4. The p_T and η distributions in Figure 7.13 show the kinematic cuts to be $0.2 < p_{\mathrm{T}} < 2$ GeV/c and $|\eta| < 0.8$. No ϕ-holes are observed in the ϕ-distribution as hybrid tracks (discussed in Section 6.1.5) have been considered for the analysis.

7.7.1 Efficiency factors

A non-flat transverse-momentum dependence of the efficiency is observed in the analysis-region, i.e, $0.2 < p_{\mathrm{T}} < 2$ GeV/c in ALICE. Therefore, it is necessary to take care of this local efficiency effect using the method described earlier. A flat

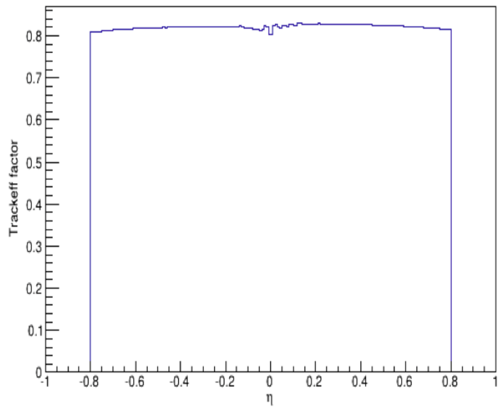

Figure 7.14: η-dependence of the efficiency factors for hybrid track-cut

η-dependence of the tracking efficiency-factors in the analysis-region is observed as shown in the Figure 7.14.

It is evident that to correct for the detector inefficiency, non-flat transverse-momentum dependence of the efficiency factor has to be corrected properly. Variable transverse-momentum bins are implemented in the analysis so that, we have larger number of p_{T}-bins in the region $0.2 < p_{\mathrm{T}} < 0.6$ GeV/c, where the non-flatness is much more than the rest of the momentum-range. The transverse-momentum range is divided into nine bins as (0.2,0.3,0.4,0.5,0.6,0.8,1.0,1.2,1.6,2.0). For each bin, the efficiency factors are evaluated and the number of charged particles have been counted. Dividing p_{T} vs centrality dependence for MC+GEANT (Considering ALL particles instead of taking only primary, so that effect of the secondaries can be included in the Monte Carlo analysis) by MC-Truth, the efficiency factors for each centrality have been evaluated. The left panel of the Figure 7.15 shows the efficiency

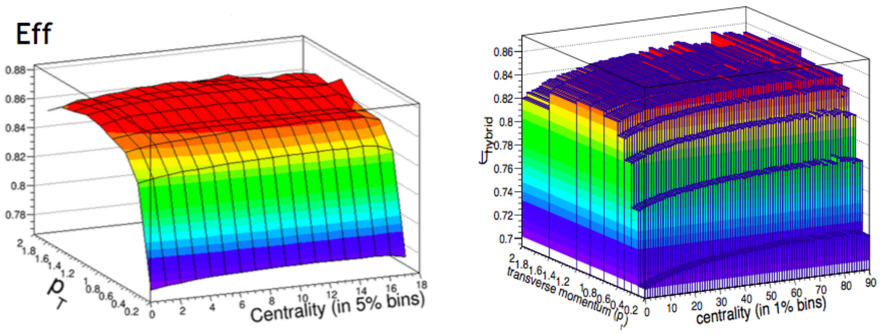

Figure 7.15: p_{T}-dependence of the efficiency factors. Left panel : From TPC-only track-cut taking equal p_{T}-bin. Right Panel : From hybrid track-cut taking variable p_{T}-bin. Effect of secondaries are included in the efficiency factors.

factors for equal transverse-momentum bin for TPC-only track cuts. The right panel of the Figure 7.15 shows the efficiency factors for variable transverse-momentum bin for hybrid track cuts.

It can be observed from the plot that the detector efficiency (including the effect from the contamination) is roughly around 82% while evaluated considering the hybrid track-cuts. The variations of the efficiency factors are much more in the region $0.2 < p_{\mathrm{T}} < 0.6$ GeV/c compared to the region $0.6 < p_{\mathrm{T}} < 2.0$ GeV/c. Therefore, to correct for the inefficiencies properly, it is wise to take the variable p_{T}-bins. Thus, the bincontents from the plot in the right panel of Figure 7.15 give efficiency factors per p_{T}-bin ($\epsilon(x_{\mathrm{i}})$), where i denotes each bin. The efficiency-correction factors are observed to be flat for the p_{T}-bin under correction. No large fluctuation in the efficiency-factors have been observed, at least upto $\sim 65\%$ centrality bins.

7.7.2 Local Efficiency Corrected Results

The results for the mean, variance and the scaled variance have been corrected using the efficiency factors discussed in the previous section.

From the p_{T}-distributions, for MC+GEANT (considering ALL particles) and MC-Truth, one can count $n(x_{\mathrm{i}})$, i.e, the number of all observed charged particles within a p_{T}-bin, and $N(x_{\mathrm{i}})$, i.e, the number of the produced particles within that particular p_{T}-bin, respectively. Thus, for $i = 9$, we have total 9 terms to add up for each centrality to get corrected mean for that centrality. And, total 99terms $(9(N_{\mathrm{i}}(N_{\mathrm{i}} - 1)$ terms, alongwith 90 $N_{\mathrm{i}}N_{\mathrm{j}}$ terms to add up to get corrected σ for that perticular centrality.

As discussed earlier, using Equations (7.16), (7.17) and (7.18), it is possible to calculate the correct values of the moments for each centrality. The results have been shown in Figure 7.16. Considering the ratios of the efficiency-corrected results to the truth-results, which basically give the outcomes of the Monte Carlo closure test to check the validity of the efficiency correction method, μ exactly matches, σ matches within 1% and the scaled variance matches within $\sim 1.5\%$. Therefore, from the ratios, it can be inferred that the efficiency correction method illustrated here is validated and working quite well.

The results are bin width corrected using 0.5% centrality bins upto 40% centrality from the most central collisions, and using 1% centrality bins from $40 - 90\%$ centralities. Thus, the geometrical fluctuations have been minimised with the help

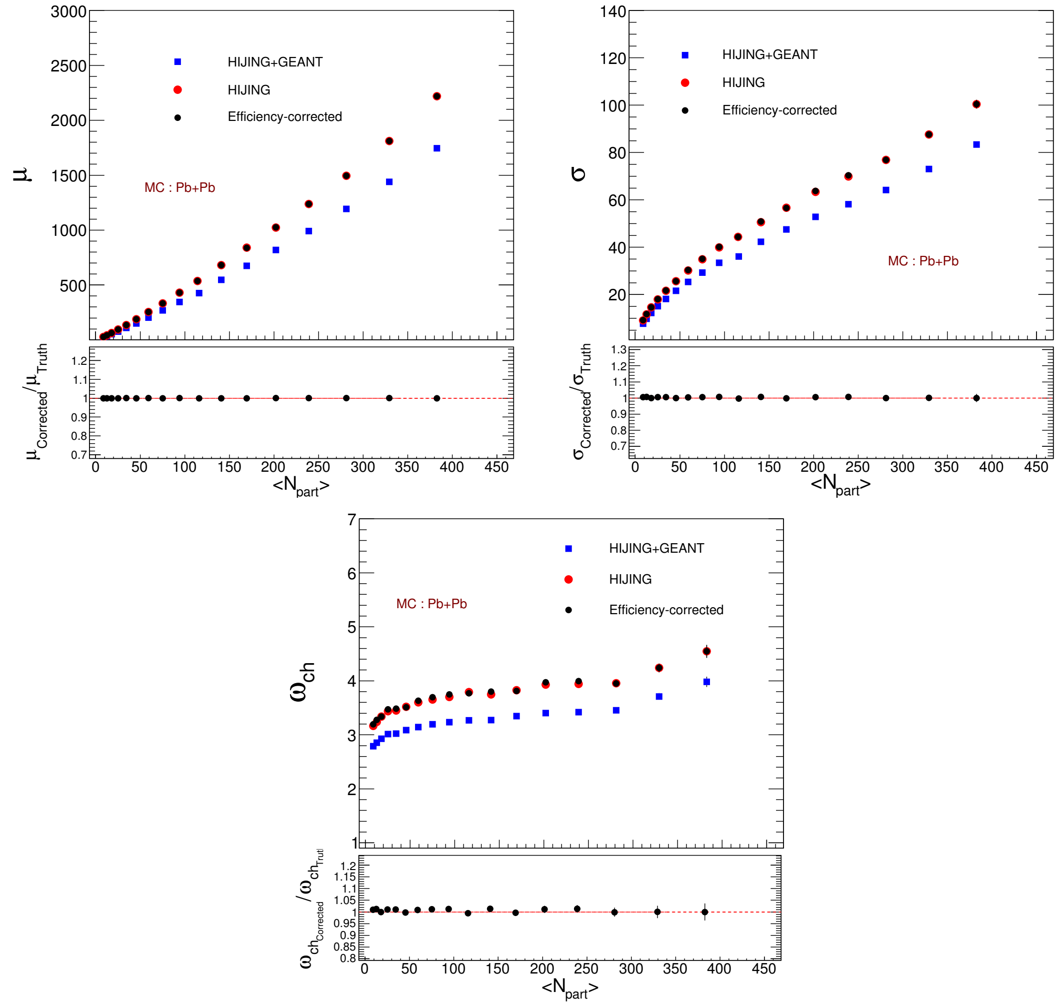

Figure 7.16: HIJING, HIJING+GEANT and Efficiency-corrected (with variable transverse-momentum bins). Top left : μ, Top right : σ, and Bottom panel : $\omega_{\rm ch}$ for hybrid track-cuts. The ratios of the efficiency-corrected results to the truth-results have also been shown for the three cases.

of the binwidth corrections.

The statistical errors have been evaluated with the help of the delta theorem as discussed in Section 6.4.3. Errors are shown in the figures. Addition of the covariance term reduces the error. Figure 7.17 shows that the statistical errors reduce by a large

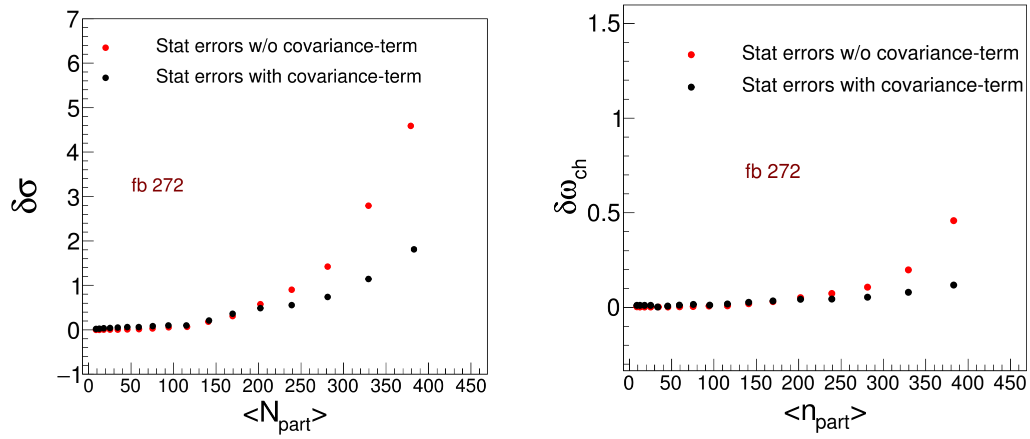

Figure 7.17: Effect of applying the covariance-term to the statistical errors for : Left panel : σ, Right panel : ω_{ch}. Results are shown for the hybrid track-cuts (fb 272).

factor for the central collisions, both for σ and ω_{ch}), after applying the covariance-term to the statistical errors. Results are shown for the hybrid track-cuts (fb 272).

It has been investigated how much is the change in the values of the observables while changing the type of track-cuts, using efficiency-corrected results from MC. It is observed from Fig. 7.18, that the tracking efficiencies affect the results for mean by $\sim$ 1%, for sigma by $\sim$ 2.5% and for scaled variance by $\sim$ 4%. These effects of changing the track-cuts have been again evaluated with real data and added to systematic errors to the final results which will be discussed in Chapter 8.

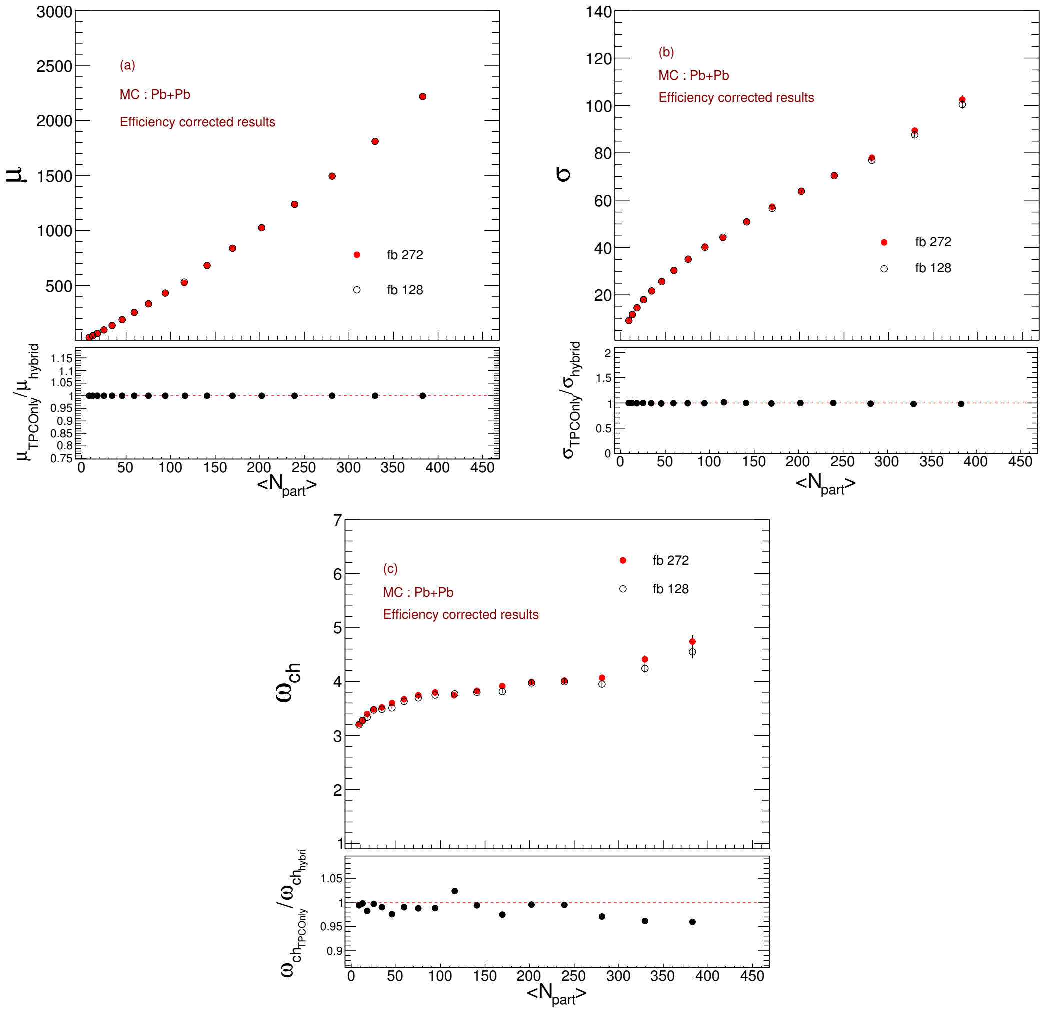

Figure 7.18: Efficiency-corrected results from MC (with variable transverse-momentum bins). Top left : μ, Top right : σ, and Bottom panel : $\omega_{\rm ch}$ for hybrid (fb 272) and TPC-only (fb 128) track-cuts. The ratio between the efficiency-corrected results have also been shown for the three cases.

7.7.3 Essence of the p_{T}-dependent efficiency corrections

It is useful to observe how much is the difference of the results while taking constant efficiency factors for the efficiency correction and taking the effects of the phase-space (p_{T} in this case) on the efficiency factors. Figure 7.19 shows such a ratio for the scaled

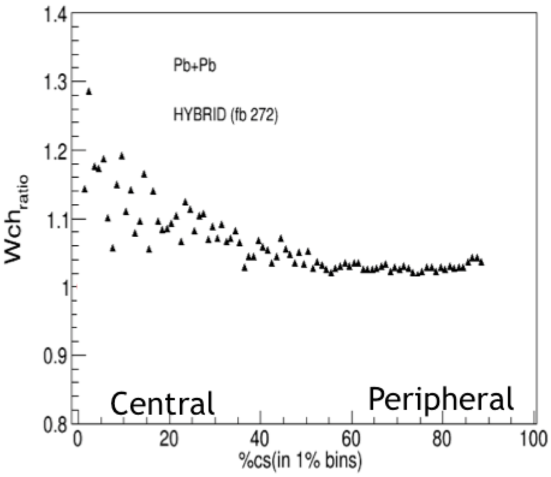

Figure 7.19: Result for $\omega_{\mathrm{ch}_{\mathrm{ratio}}}$ of efficiency-corrected result to HIJING-results without applying p_{T}-dependent efficiency correction

variance with respect to 1% centrality bins. It is observed that the ratio between the efficiency-corrected results and HIJING-results for the observables are much higher if the p_{T}-dependent efficiency correction is not implemented. The ratio becomes $\sim 20-30\%$ for the efficiency-corrected results with constant efficiency factors, whereas it comes down to $\sim 1.5\%$ when the p_{T}-dependence has been considered (results shown earlier). This implies the essence of the p_{T}-dependent efficiency corrections. Thus, the local efficiency corrections have been implemented for the first time in ALICE.

7.7.4 Estimation of the fluctuations from N_{part}

As discussed earlier, the charged particle multiplicity fluctuations are directly affected by the volume fluctuations or the fluctuations in the number of participants [13, 14, 15]. N_{part} can not be measured experimentally from real data. However, it is possible to have an estimation of N_{part} from the Monte Calo simulation.

Fluctuation in N_{part} (i.e, ω_{Npart}) has been estimated using the information of the number of participants from the collision geometry from HIJING, while the centrality is selected from the minimum bias primary charged particle distribution at the kinematic level (before passing through the detectors) within the pseudorapidity range $2.8 < |\eta| < 5.1$ and $-3.7 < |\eta| < -1.7$, i.e, exactly similar range for the V0-detectors. N_{part}-distributions are plotted for the particular centralities defined in the said procedure and from the distributions, it is possible to find out the mean ($\langle N_{\text{part}} \rangle$), variance and the scaled variance (ω_{Npart}). From the Figure 7.20, the

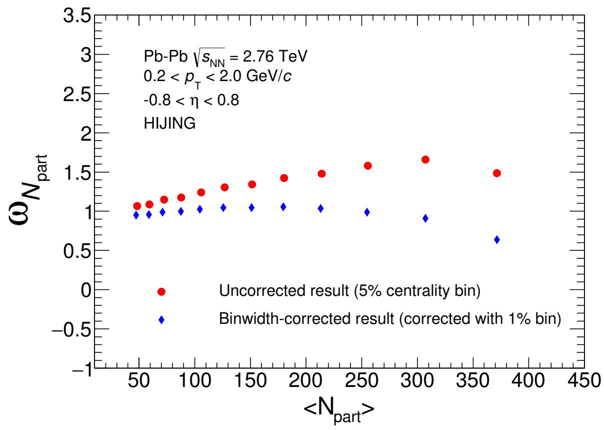

Figure 7.20: Fluctuations in N_{part} from HIJING in ALICE

binwidth-corrected values of ω_{Npart} is observed to be close to unity, except for the most central collisions. Therefore, it can be concluded that, by choosing narrow bins in centrality, fluctuations in N_{part} can be minimised.

7.7.5 Discussion on the possible biases

The centrality selection fixing V0-Multiplicity instead of N_{part} may bias the result of multiplicity distributions and constrain the possible fluctuations. Prescription is to select centrality using the Zero Degree Calorimeter (ZDC), so that one can get centrality, in turn, by fixing N_{part}. Centrality selection from ZDC is generally done using ZDC-ZEM anti-correlation upto the break-up point of ZDC, i.e, upto 40% centrality. Also, MC-production is not available for ZDC-centrality selection till now. Volume fluctuation is observed to be very high in this case. So, it has been

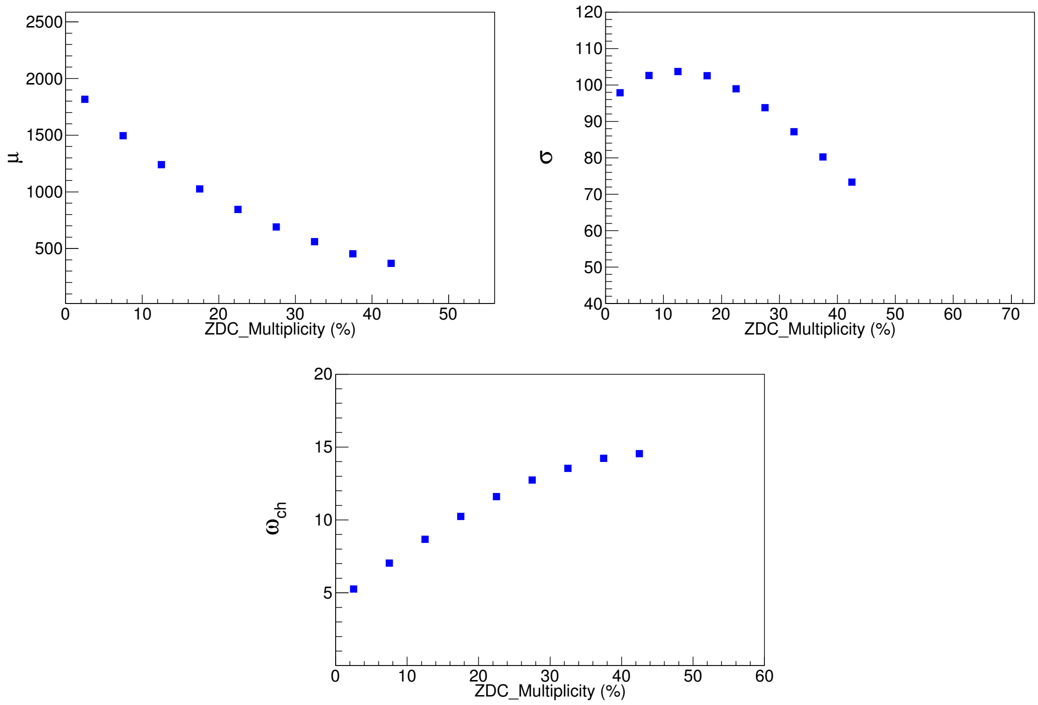

Figure 7.21: Results of the moments using centrality definition from ZDC. Top left : μ, Top right : σ, and Bottom panel : ω_{ch} for hybrid track-cuts.

decided not to use ZDC for this analysis.

Basically, the centrality is selected from V0M, i.e, from a particular η-window, and the multiplicity distributions are measured in a different η-window. Whether this kind of selection of centrality is biasing the results or not, is the point of concern. To test whether the above statement is correct, we use 200K Pb-Pb events gener-

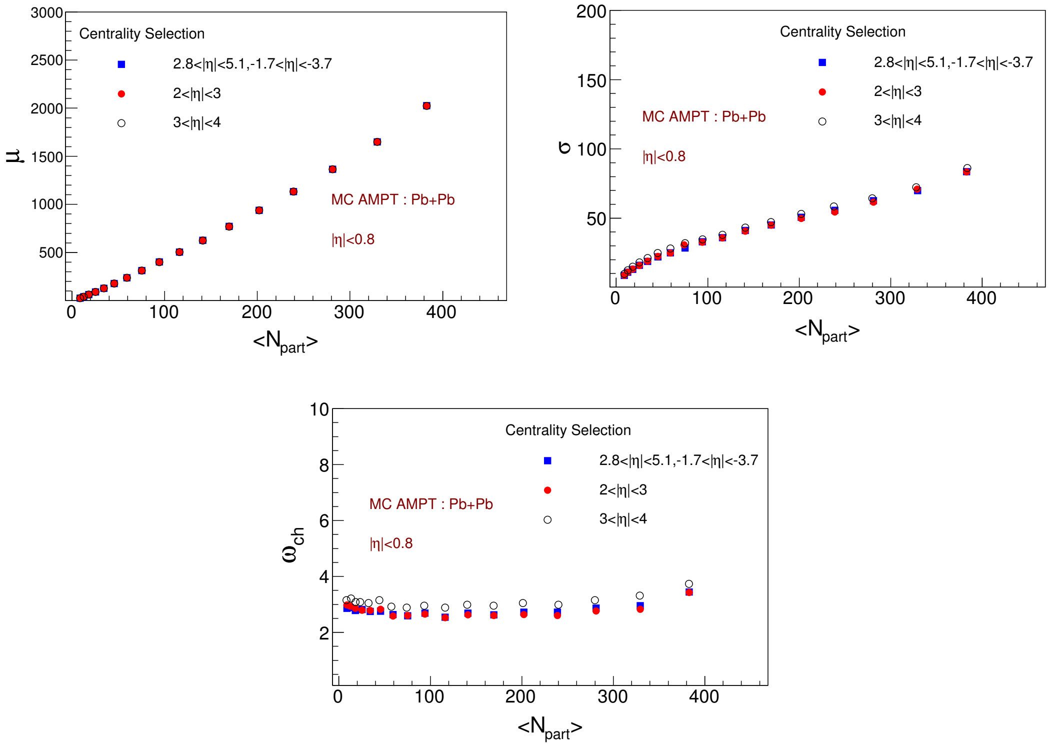

Figure 7.22: Results from AMPT-String Melting models using centrality selection from three different η-windows, for (a) μ, (b) σ, and (c) ω_{ch} measured from the multiplicity distributions within $|\eta| < 0.8$.

ated by AMPT-String melting model at $\sqrt{s_{\mathrm{NN}}} = 2.76\ TeV$. We use the charged particle multiplicities from three different η-windows, as shown in the Figure 7.22 as centrality estimators. Mean (μ), sigma (σ) and scaled variances (ω_{ch}) are estimated from the multiplicity distributions in $|\eta| < 0.8$. It is observed that μ, σ and ω_{ch}

match well, even if we use different η-window for centrality selection. Therefore, it can be concluded that the centrality selection using multiplicity from a different η-window does not bias the final results to a great extent, unless the centralities are selected from a pseudorapidity range having a hump within it.

7.8 Results from MC-Simulation for p-Pb collisions at $\sqrt{s_{\mathrm{NN}}} = 5.02$ TeV

DPMJET event generator is used in ALICE for the studies with MC-simulation for p-Pb collisions at $\sqrt{s_{\mathrm{NN}}} = 5.02$ TeV. For these studies, vertex-cuts are taken exactly similar to the analysis for Pb-Pb collisions. Thus, the events considered for the analysis are within $|V_{\mathrm{z}}| < 10$ cm. No vertex-cut has been applied in the XY-plane for the p-Pb analysis. In Fig. 7.23, the quality assurance plots for the analysis with p-Pb have been presented. No phi-holes are observed as hybrid track-cuts (fb 768) have been used for the analysis. The p_{T} distribution from the reconstructed track shows the p_{T}-range taken clearly, which is also similar to the analysis with Pb-Pb. The normalised η-distributions from the reconstructed as well as from the original tracks have been shown in the figure.

7.8.1 Efficiency factors

Figure 7.24 shows the efficiency factors for variable transverse-momentum bin for hybrid track cuts for p-Pb collisions at $\sqrt{s_{\mathrm{NN}}} = 5.02$ TeV.

It can be observed from the plot that the detector efficiency (including the effect from the contamination) is roughly around 83% while evaluated considering the

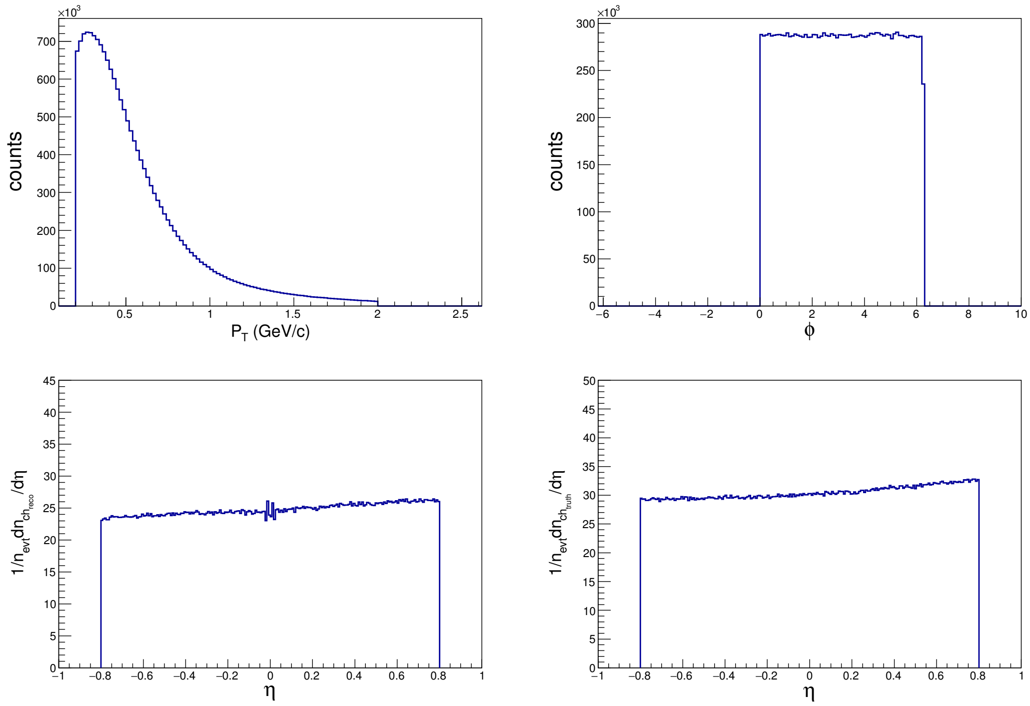

Figure 7.23: Quality Assurance (QA) plots from MC-DPMJET for p-Pb collisions at $\sqrt{s_{\rm NN}}$ = 5.02 TeV for hybrid (fb 768) track-cuts, considering ∼900K events. Top left : $p_{\rm T}$ distribution from the reconstructed track. Top right : ϕ-distribution. Bottom left : Normalised η-distribution from the reconstructed track. Bottom right : Normalised η-distribution from the MC-Truth

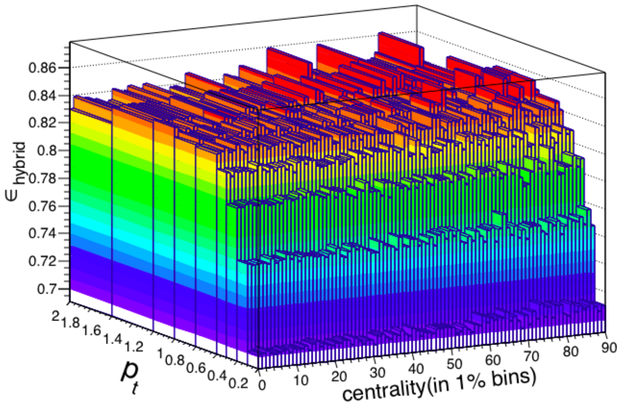

Figure 7.24: p_{T}-dependence of the efficiency factors (including effect of the contaminations) evaluated with the hybrid track cuts for p-Pb collisions at $\sqrt{s_{\mathrm{NN}}} = 5.02$ TeV

hybrid track-cuts. Similar to the case for Pb-Pb analysis, the variations of the efficiency factors are much more in the region $0.2 < p_{\mathrm{T}} < 0.6$ GeV/c compared to the region $0.6 < p_{\mathrm{T}} < 2.0$ GeV/c. Therefore, to correct for the inefficiencies properly, it is wise to take the more number of p_{T}-bins within $0.2 < p_{\mathrm{T}} < 0.6$ GeV/c. The efficiency-correction factors are flat for the bin under correction. No large fluctuations in the efficiency-factors have been observed, at least upto $\sim 60\%$ centrality bins.

7.8.2 Local Efficiency Corrected Results

With the above mentioned cuts, the charged particle multiplicity distributions are observed for p-Pb collisions for different centralities defined by V0A-multiplicity as described in Section 7.3.3. The distributions are corrected for the detector inefficiency in the similar way followed for the Pb-Pb analysis.

The efficiency-corrected results for μ, σ, and ω_{ch} have been shown in the Fig. 7.25,

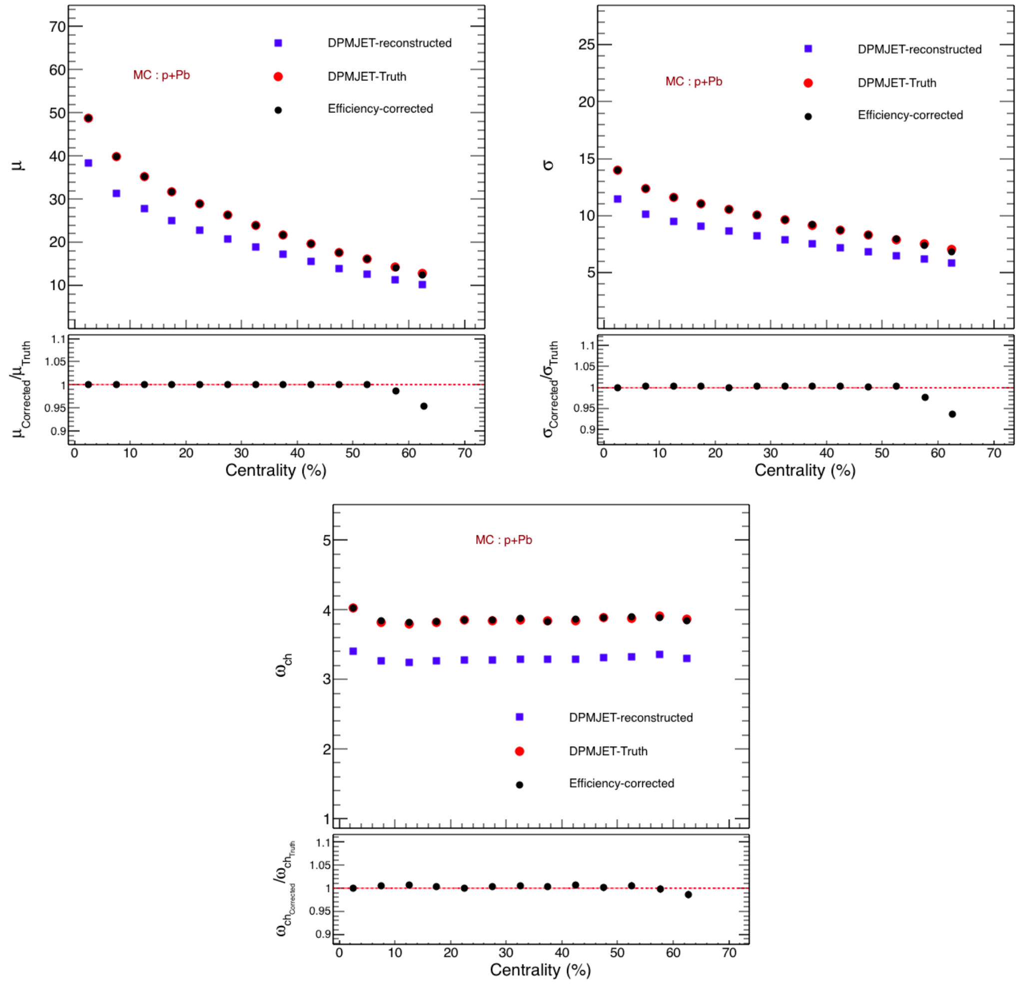

Figure 7.25: DPMJET-truth, DPMJET-reconstructed and Efficiency-corrected results with variable transverse-momentum bins, for p-Pb analysis. Top left : μ, Top right : σ, and Bottom panel : $\omega_{\rm ch}$ for hybrid track-cuts. The ratios of the efficiency-corrected results to the truth-results have also been presented for the three cases.

alongwith the results from the reconstructed as well as the original (DPMJET-Truth) tracks. All the results are binwidth corrected. It has been observed that within 60% centrality, the efficiency corrected and the truth results match well within $\sim 2\%$ for μ, $\sim 3\%$ for σ and $\sim 1\%$ for ω_{ch}. Thus, efficiency correction is validated for this analysis after checking with the monte carlo closure test. The slight differences in the values of the original results and the efficiency-corrected results will be added as the systematic errors in the final results for p-Pb collisions at $\sqrt{s_{\text{NN}}} = 5.02$ TeV. The final results have been presented in Chapter 8.

Bibliography

[1] ALICE Collaboration, ALICE Inner Tracking System (ITS): Technical Design Report, CERN-LHCC-99-012, http://edms.cern.ch/file/398932/1.

[2] ALICE Collaboration, ALICE time projection chamber: Technical Design Report, CERN-LHCC-2000-001, http://cdsweb.cern.ch/record/451098.

[3] ALICE Collaboration, ALICE forward detectors: FMD, TO and VO: Technical Design Report, CERN-LHCC-2004-025, http://cdsweb.cern.ch/record/781854.

[4] B. Abelev *et al.* (ALICE Collaboration), Phys. Rev. **C 88**, 044909 (2013), arXiv:1301.4361 [nucl-ex] (2013).

[5] K. Aamodt *et al.* (ALICE Collaboration), Phys.Rev.Lett.**106**:032301, 2011.

[6] https://twiki.cern.ch/twiki/bin/viewauth/ALICE/PACentStudies.

[7] Nihar R. Sahoo, S. De, T. K. Nayak, Phys. Rev. **C 87**, 044906 (2013), arXiv:1210.7206 [nucl-ex] (2013).

[8] A. Bzdak and V. Koch, Phys. Rev. **C 91**, 027901 (2015).

[9] Xiofeng Luo, Phys. Rev. **C 91**,034907 (2015).

[10] L. Adamczyk *et al.* (STAR Collaboration) ,Phys. Rev. Lett. 112, 032302 (2014).

[11] X. Luo, J. Phys. G : Nucl. Part. Phys. **39** 025008 (2012), arXiv:1109.0593v1 (2012).

[12] https://github.com/ptribedy/moment_efficiency_v2.0.

[13] H. Heiselberg, Phys. Rept. **351** 161 (2001).

[14] M. M. Aggarwal *et al.* (WA98 Collaboration) Phys. Rev. **C 65**, 054912 (2002).

[15] G.V.Danilov and E.V.Shuryak, arXiv:nucl-th/9908027 (1999).

8

Results of Charged particle Multiplicity Fluctuations in ALICE

In this chapter, the final results of the multiplicity distributions and the multiplicity fluctuations for Pb-Pb collisions at $\sqrt{s_{\mathrm{NN}}} = 2.76$ TeV as well as for p-Pb collisions at $\sqrt{s_{\mathrm{NN}}} = 5.02$ TeV have been presented from the ALICE experiment. The sources and percentages of the systematic errors have been discussed. An estimation of the isothermal compressibility (k_{T}) has been presented here for the first time. Additionally, the results from pp collisions have been shown as a baseline.

8.1 Results from ALICE data : Pb-Pb collisions at $\sqrt{s_{\mathrm{NN}}} = 2.76$ TeV

8.1.1 Quality Assurance

Let us first have a quick look on the quality assurance (QA) plots from the ALICE data for Pb-Pb collisions at $\sqrt{s_{\mathrm{NN}}} = 2.76$ TeV. The data-sets, track-cuts and the other cuts have been discussed already in details in Section 6.1. Here, only the event counter and the pseudorapidity density distribution have been shown. The rest of the cuts (i.e, p_{T} and ϕ-cuts) are exactly similar to those discussed for the Monte Carlo analysis in Section 6.7. In Fig. 8.1, the QA plots are shown for 14M

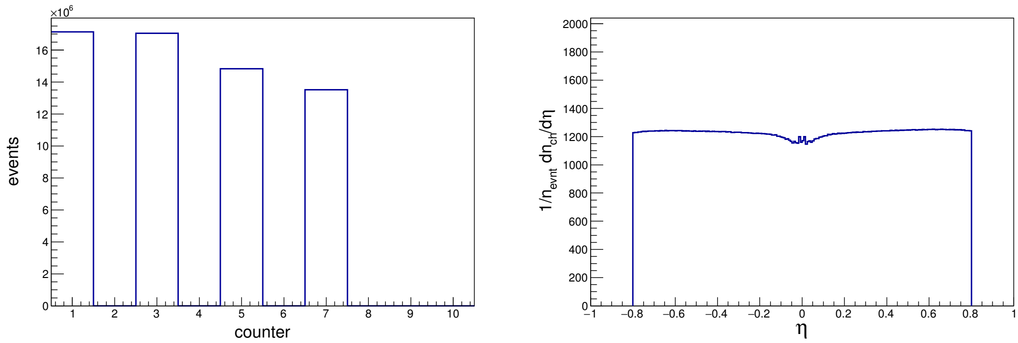

Figure 8.1: QA plots for ALL events for Pb-Pb collisions at $\sqrt{s_{\mathrm{NN}}} = 2.76$ TeV. Left panel : EventCounter, Right panel : Normalised η-distribution for $0-5\%$ centrality.

events. In the left panel, an eventcounter has been shown to have an estimation of the number of events. The counter counts *1* for all events, it counts *3*, for the events which pass through the minimum bias triggers. These two give similar results as shown in Fig. 8.1. The counter counts *5* for the events one gets after the vertex selection and it counts *7* after the proper centrality selection. In the right panel, the normalised η-distribution has been shown for all events for $0-5\%$ centrality. The cut in pseudorapidity is taken as $|\eta| < 0.8$, as discussed earier. Figure 8.2 shows the QA plots for the cleaned events (∼400 K events, as discussed in Section 7.4).

8.1.2 Total charge multiplicity distributions

With the use of the above said cuts, the results of the total charge multiplicity distributions from ALL events for Pb-Pb collisions at $\sqrt{s_{\mathrm{NN}}} = 2.76$ TeV are shown in Fig. 8.3. The distributions are shown for $0-60\%$ centralities, in 5%-centrality bins.

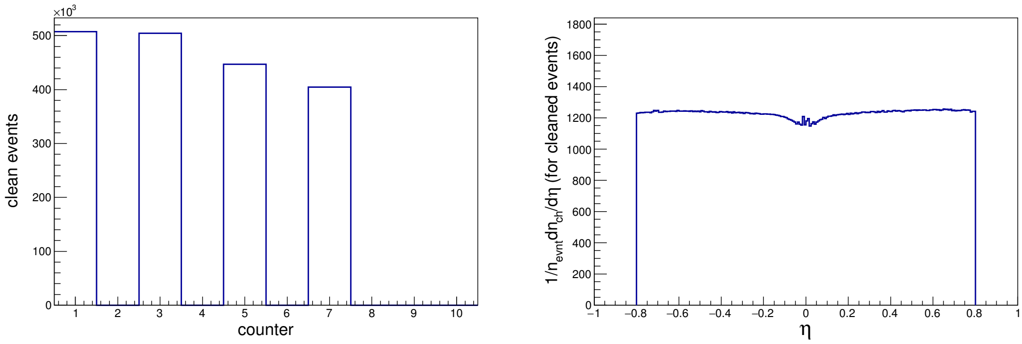

Figure 8.2: QA plots for cleaned events. Left panel : EventCounter, (b) Right panel : Normalised η-distribution for $0 - 5\%$ centrality.

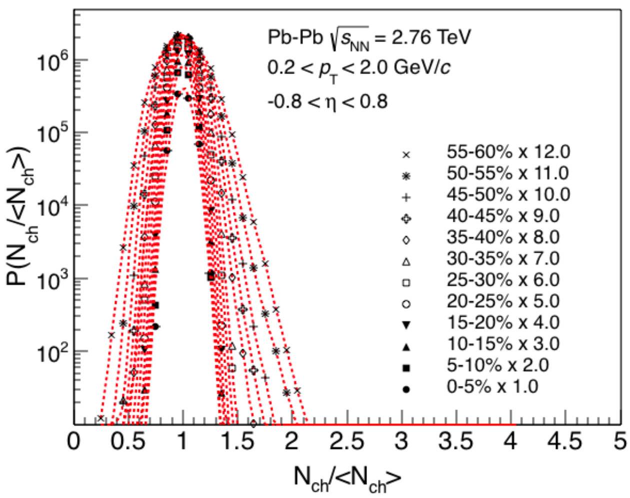

Figure 8.3: Total charge multiplicity distributions for Pb-Pb collisions at $\sqrt{s_{\rm NN}}$ = 2.76 TeV for different centralities. The red dashed lines are the fits to the multiplicity distributions (see text)

These are the results from data, without applying any corrections. The multiplicity distributions are scaled to the mean ($\langle N_{\rm ch} \rangle$). The vertical axes are multiplied by different factors for better visibility as discussed in Section 6.3.2. The dashed lines are the fits to the multiplicity distributions. It has been observed that, starting from extreme peripheral collisions upto 35% centrality, the multiplicity distributions are fitted quite well with the NBD's with χ^2 per degrees of freedom less than 1, whereas from 35% centrality to the most central collisions, the distributions become narrower and they are fitted better with the Gaussians.

8.1.3 Results from the multiplicity distributions

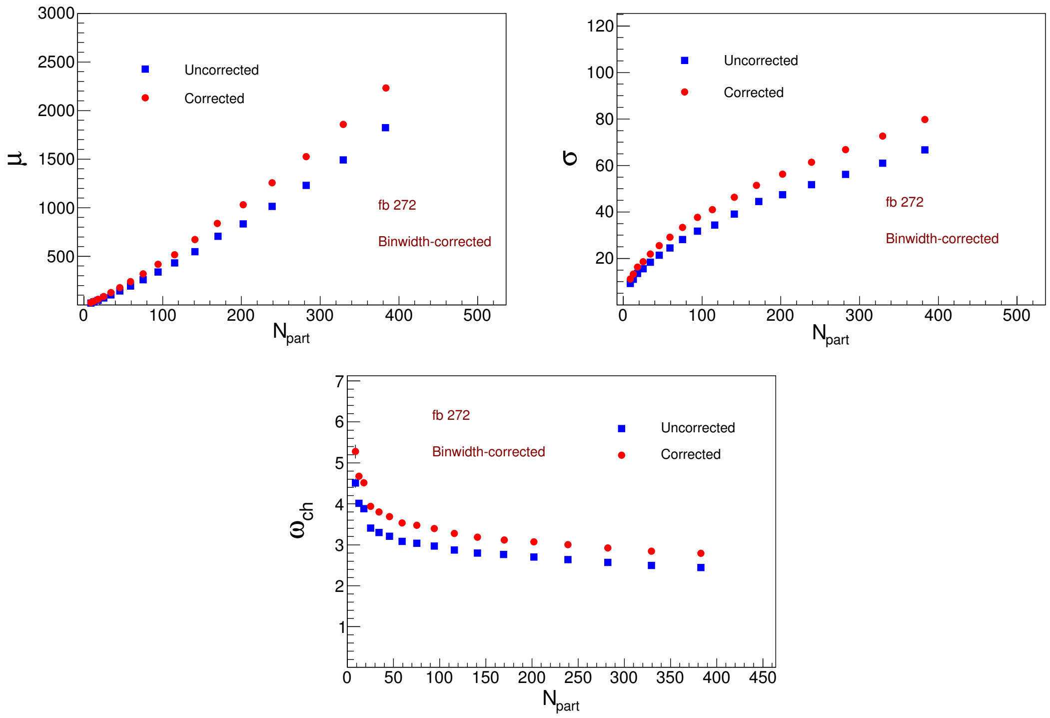

Figure 8.4: Efficiency-uncorrected and corrected results for ALL events, using hybrid-track cuts (fb 272). Top left : μ. Top right : σ. Bottom panel : $\omega_{\rm ch}$

Figure 8.4 shows the uncorrected and the efficiency-corrected results (the efficiency corrections have been performed using the procedure described earlier in Section 7.5.2) for μ, σ and ω_{ch}, using the hybrid track-cuts. These results are for 14M events. The results are binwidth corrected. We observe that, μ and σ are increasing from peripheral to central collisions, as expected. Scaled variance increases slowly from central to peripheral collisions. Statistical errors are evaluated with the delta theorem with the proper efficiency corrections and are within the data-points for most of the cases. At extreme peripheral, the scaled variance suddenly increases much and we have larger statistical errors in the extreme peripheral. Figure 8.5

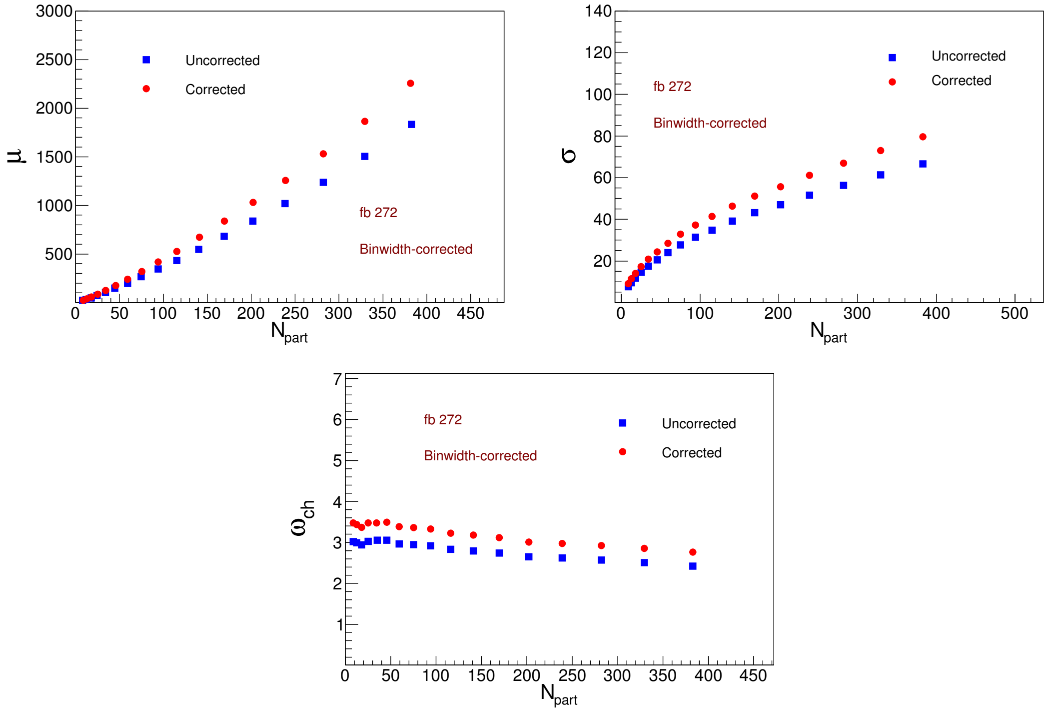

Figure 8.5: Efficiency-uncorrected and corrected results for cleaned events, using hybrid-track cuts. Top left : μ, Top right : σ, and Bottom panel : ω_{ch}

shows the similar results for the cleaned events. At extreme peripheral, the sudden increase of the value for the scaled variance and its statistical error has not been observed. From Figure 8.6, it is evident that starting from the most central collisions

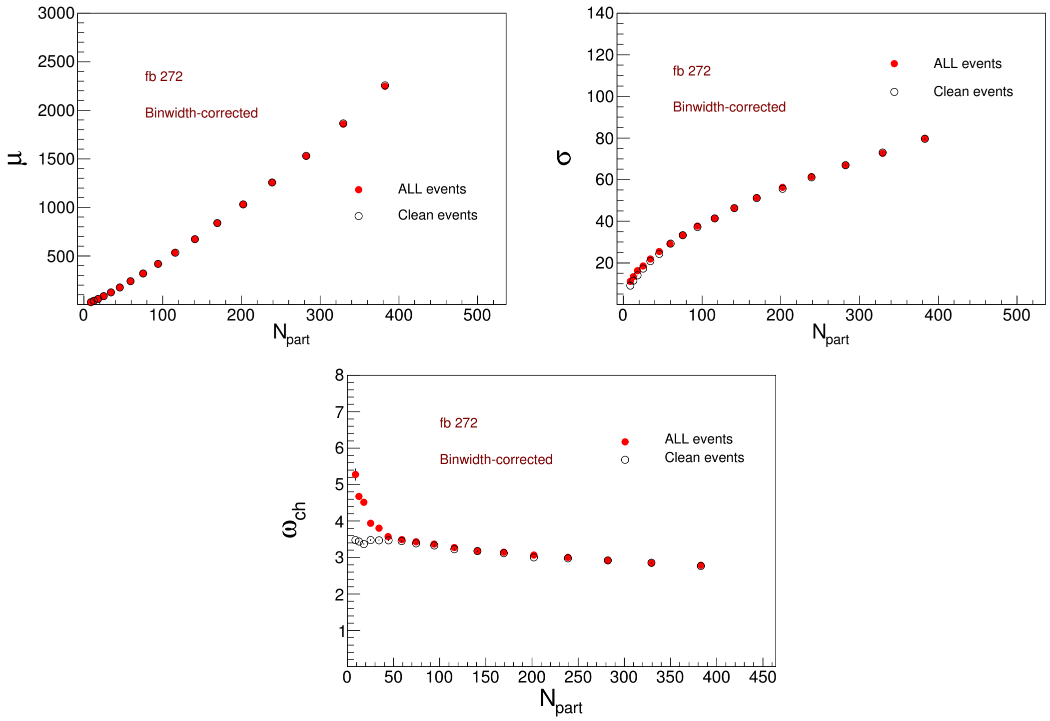

Figure 8.6: Comparison between the efficiency-corrected results for ALL and cleaned events for (a) μ, (b) σ, and (c) ω_{ch}. Results are shown using the hybrid-track cuts.

down to $N_{\mathrm{part}} \sim 50$, all events and the cleaned events give similar results. Therefore, the results will be presented for ALL events, without losing the statistics and will be shown down to $N_{\mathrm{part}} \sim 50$.

8.1.4 Estimation of the systematic errors

For each and every experiment, the experimental setup has some limitations and slight mismatch between the results obtained with different track-cuts, different vertex-cuts, etc. It is important to estimate this mismatch, which is the source of the systematic error.

The main source of the systematic error in this analysis is the effect of changing the track-cuts.

Effect of changing track − quality cuts :

Systematic study has been performed using another global track-cut, i.e, the TPC-Only track-cuts (filterbit 128) in addition to the hybrid-track cuts (filterbit 272). In the Figure 8.7, the results have been shown down to $N_{\rm part} \sim 50$. It has been observed that for the scaled variances, the ratios of the results obtained using the hybrid track-cuts and the TPC-only track-cuts, vary between $4\% - 7\%$. This much of difference is added as systematic error.

Effect of changing vertex cuts :

Systematic study has been done with the hybrid track-cut, changing the vertex-z position to $\pm 5\ cm$, in addition to the results from the hybrid-track cut, where the vertex-z position is considered as $\pm 10\ cm$. Figure 8.8 shows that the ratios between the values of the observables using different vertex-cuts vary very little. The ratio is almost equal to 1, for all the centralities.

Effect of removing $\mathbf{Vx}, \mathbf{Vy}$ − cuts :

Figure 8.9 shows that the effect of the removal of the $V_{\rm x}, V_{\rm y}$ cuts affects the final results by $\sim 1\%$.

Effect of changing the magnetic polarity :

Figure 8.10 shows that for scaled variance, positive polarity affects the final result by maximum $\sim 1\%$ and negative polarity affects by maximum $\sim 1.5\%$. These have been added to the systematics too.

Another effect of the systematics has been considered to be from the Monte Carlo closure test, i.e, from the difference between the efficiency-corrected and the truth-

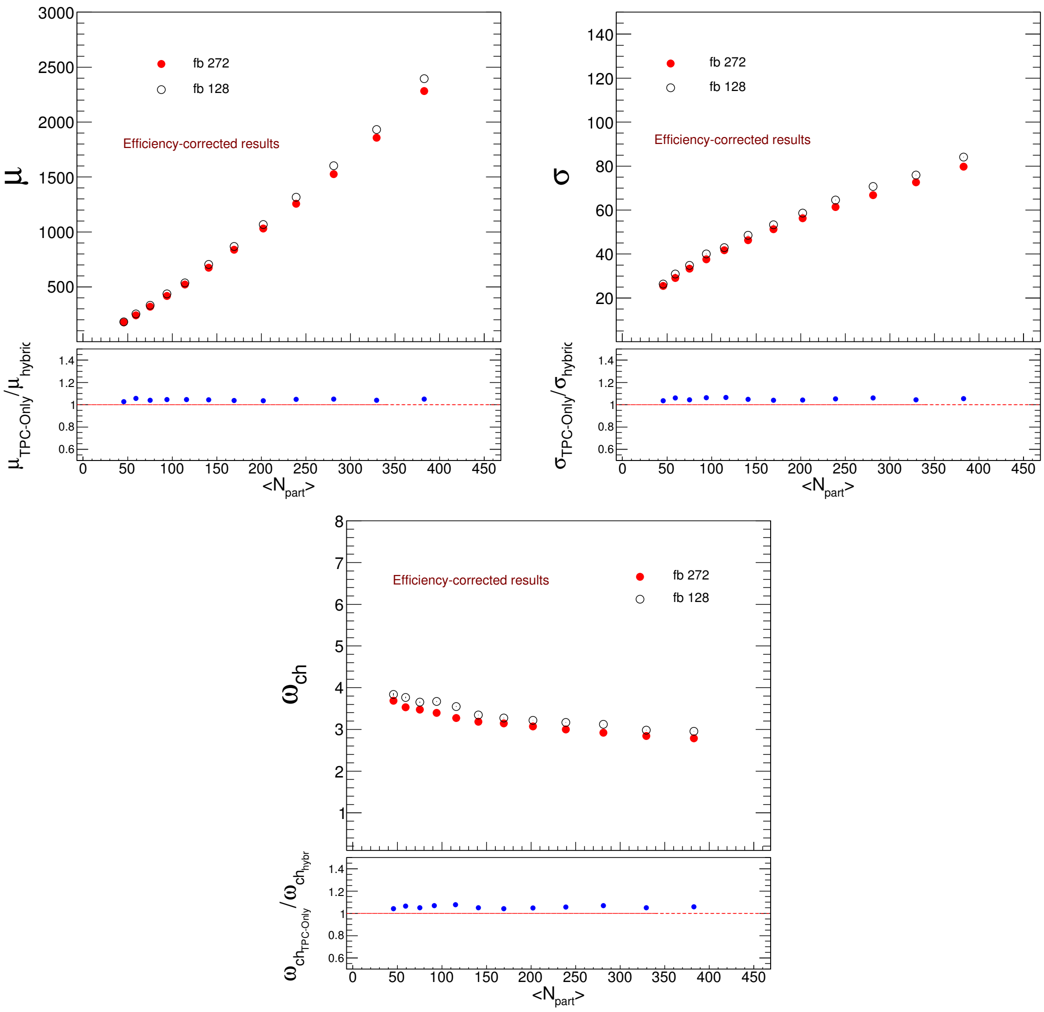

Figure 8.7: Systematic-study using TPC-Only track-cuts. Results for μ (Top left),σ (Top right), and ω_{ch} (Bottom panel) have been shown. The ratios of the values between the two-track cuts have also been presented.

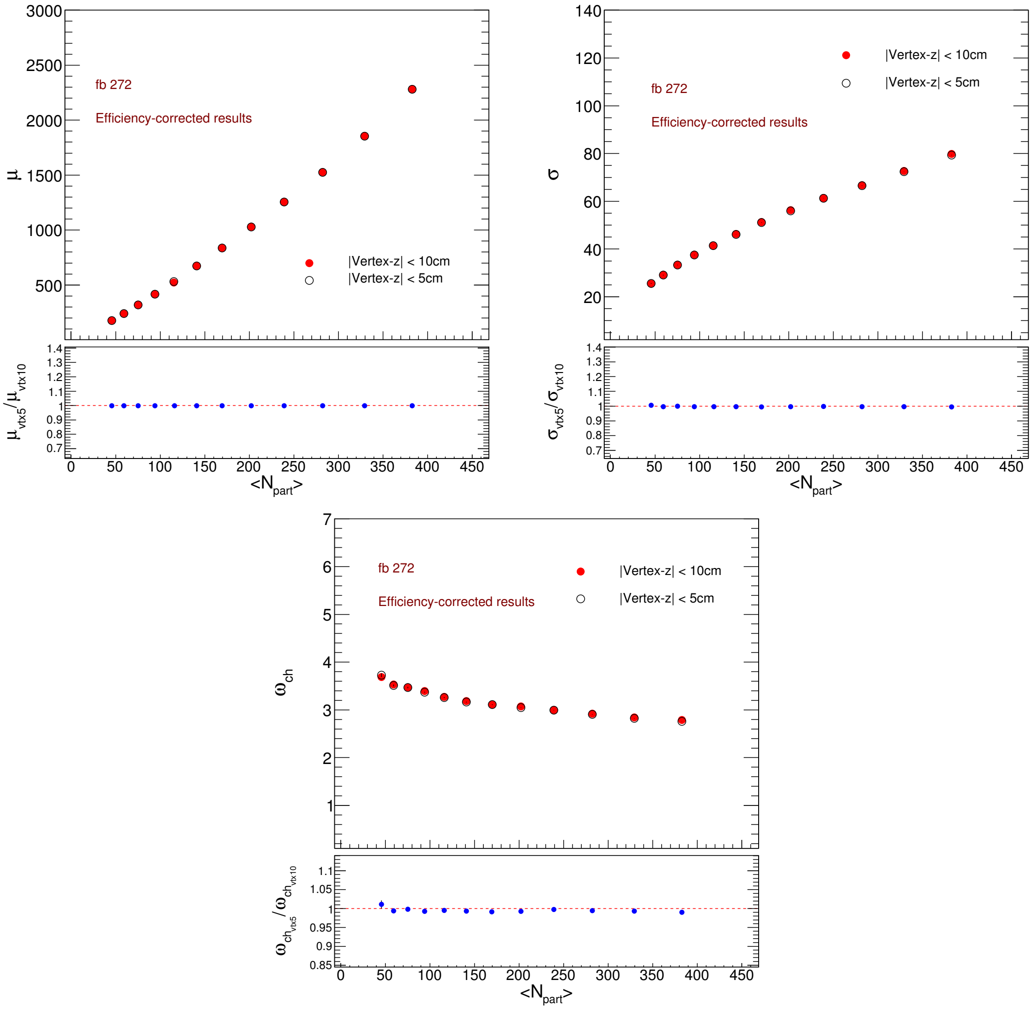

Figure 8.8: Systematic-study using $|z_{\text{vertex}} < \pm 5\, cm|$. Results for μ (Top left), σ (Top right), and ω_{ch} (Bottom panel) have been shown. The ratios of the values between the two vertex-cuts, for the same hybrid track-cuts have also been presented here.

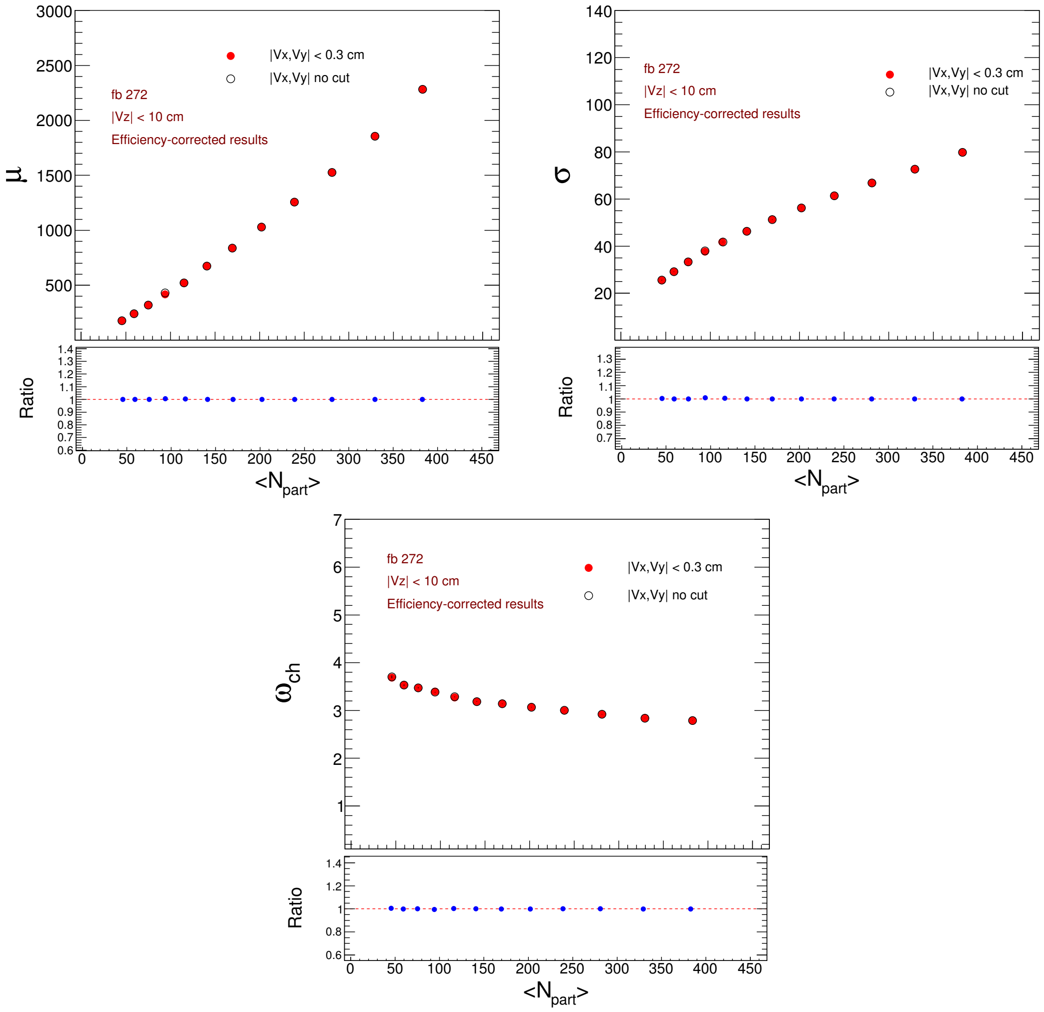

Figure 8.9: Systematic-study using removal of $|V_{\text{x}}, V_{\text{y}}| < 0.3\ cm|$. Results for μ (Top left),σ (Top right), and ω_{ch} (Bottom panel) have been shown. The ratios of the values while using the cuts and removing the cuts, for the same hybrid track-cuts have also been presented.

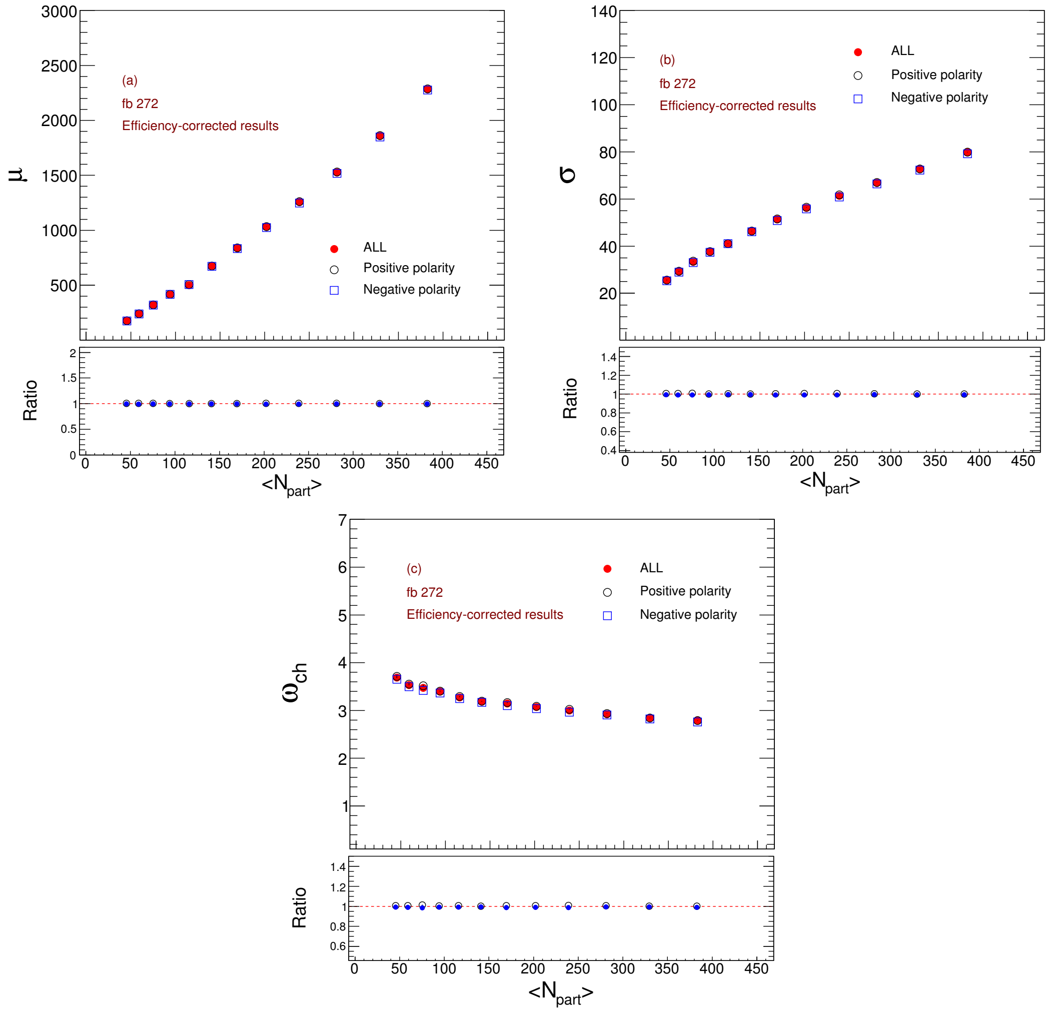

Figure 8.10: Systematic-study using ALL events, taking the events with positive magnetic polarity and events with negative magnetic polarity. Results for (a) μ, (b) σ, and (c) $\omega_{\rm ch}$ has been shown. The ratios of the positive and negative polarity events to ALL events have also been presented.

results. This has been discussed earlier in Section 7.7. Also, the tracking-efficiency effects on the monte carlo results have been evaluated earlier, which should be added to the systematic errors as well.

Sources of the Systematic errors	Mean (μ)	Sigma (σ)	Scaled Variance (ω_{ch})
Different Track-cuts	$3.5 - 4.8\%$	$3.8 - 6\%$	$4 - 7.5\%$
MC closure test	$\sim$0.01%	$\sim$0.7%	$\sim$1.4%
Different vertex-cuts	$0.1 - 0.5\%$	$\sim$0.5%	$0.1 - 0.8\%$
Removal of $V_{\text{x}}, V_{\text{y}}$-cuts	$\sim$0.10%	$\sim$0.20%	$\sim$0.5%
Magnetic polarity (positive)	$0.1 - 0.5\%$	$0.1 - 0.7\%$	$0.1 - 0.8\%$
Magnetic polarity (negative)	$0.1 - 0.7\%$	$0.5 - 1\%$	$0.8 - 1.5\%$
Effect of data cleanup	$0.1 - 0.5\%$	$0.3 - 0.8\%$	$0.9 - 1.5\%$
Changing DCA_{xy} by $\pm 25\%$	$0.5 - 0.9\%$	$0.8 - 1.2\%$	$1.3 - 1.6\%$
Changing DCA_{z} by $\pm 25\%$	$0.4 - 0.9\%$	$0.7 - 1\%$	$1.2 - 1.7\%$
Total (adding in quadrature)	$\sim 3.5 - 5\%$	$\sim 4 - 6\%$	$\sim 6 - 8\%$

Table 8.1: Sources of the systematic errors and their contributions in percentages

The main sources of the systematic errors and their contributions in percentages have been presented in Table 8.1. The total systematic errors have been calculated by adding all the contributions in quadrature. Systematic errors of $\sim 5\%, \sim 7\%, \sim 8\%$ have been applied to the corrected final results for $\mu, \sigma, \omega_{\text{ch}}$ respectively.

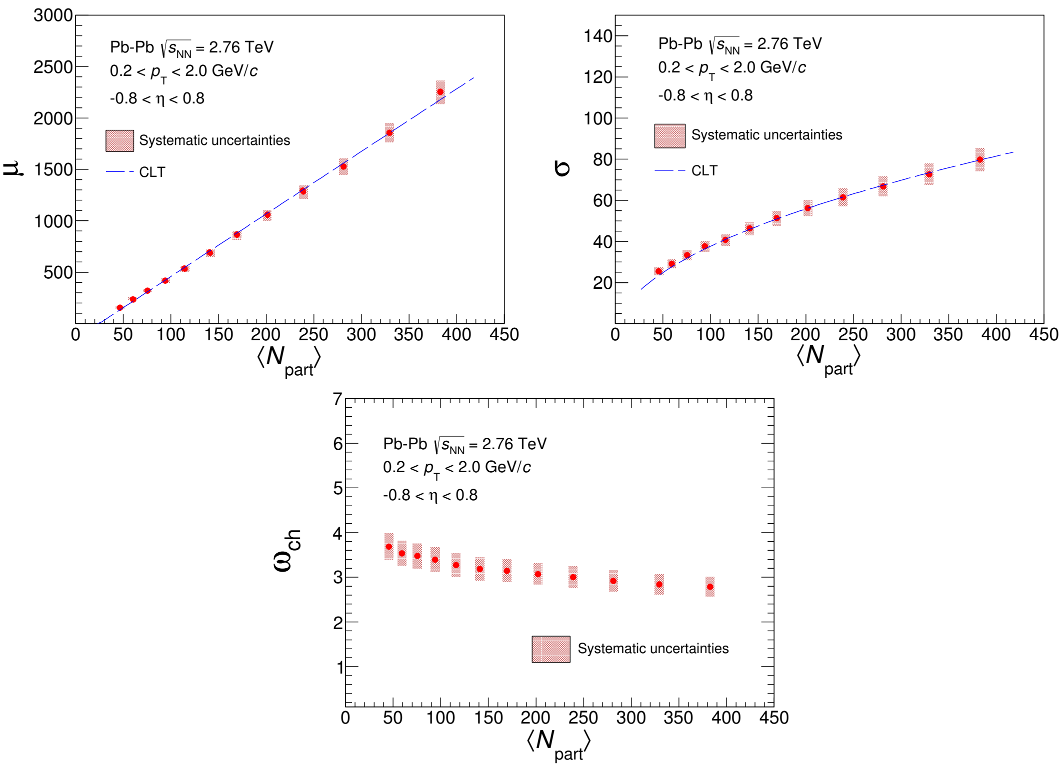

Figure 8.11: Corrected results for μ (Top left), σ (Top right), and $\omega_{\rm ch}$ (Bottom panel). Statistical errors are within the data-points. Systematic errors are $\sim 5\%, \sim 7\%, \sim 8\%$ for $\mu, \sigma, \omega_{\rm ch}$ respectively. The results for μ and σ follow the trend of the Central Limit Theorem.

8.1.5 Corrected final results

In Figure 8.11, the efficiency-corrected final results for μ, σ, and ω_{ch} have been shown. The results are binwidth corrected. The systematic uncertainties have been applied to the final results. A slowly decreasing trend has been observed for the scaled variances from the peripheral to the central collisions.

The results for μ, and σ have been fitted by the predictions from the Central Limit Theorem (CLT), as discussed earlier in Section 7.3.3 and in Ref. [1]. Considering the constant of proportionality as free parameter, it has been observed that the centrality evolution of μ, and σ follow the trend of CLT, within the systematics.

The value of μ has been compared with the published results from spectra [2], integrating over the experimental p_{T}-range and it is found to match within the systematics.

These results have been presented in Quark Matter 2015. The preliminary results from ALICE presented in QM 2015 have been presented in **Appendix A**.

8.1.6 Comparison with Models

The corrected results from data has been compared with the results from HIJING and AMPT-String Melting Models. Centrality selection in data and monte carlo is not exactly similar. The centrality from data has been selected using the AliCentrality class as described in [3]. In Figure 8.12, the centrality selection for the HIJING and AMPT-results have been done from the minimum-bias charged particle distribution in the range $2.8 < |\eta| < 5.1$ and $-3.7 < |\eta| < -1.7$. N_{part}-information is taken from the geometry of the collision. It is observed in Figure 8.12 that the trend for the scaled variance predicted from the models are opposite to the corrected

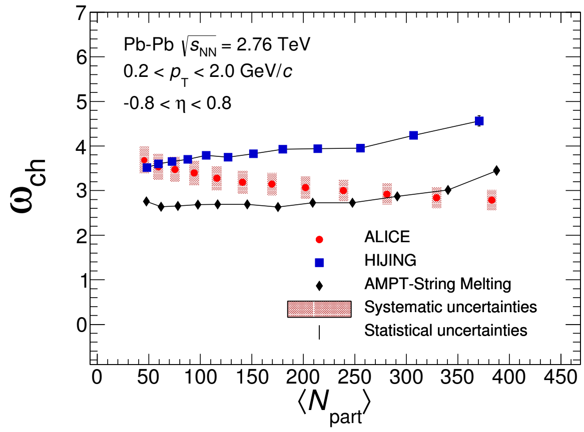

Figure 8.12: Comparison between data and model-results. HIJING and AMPT-String Melting (with 200K generated events) models are used for comparison.

results from data, though the results from the models are of comparable values as from data. The increased values for the scaled variances in HIJING may be because of the contribution from jets, especially, for the central collisions.

8.1.7 Acceptance-effect study

In the full phase-space, the total charge is conserved. But for a finite acceptance range, the total charge varies event to event. The number of accessible charged particles increase as the η-window increases. To study the effect of the acceptance on the observable, the same study has been repeated for three different η-windows, i.e, $|\eta| < 0.8$, $|\eta| < 0.5$, and $|\eta| < 0.3$.

Figure 8.13 shows the study of the observable varying the η-ranges, keeping the p_{T}-range same always. From the figure, it has been observed that as the acceptance-range is decreasing, the value of the scaled variance decreases. If it is assumed that there is no significant correlations present over the acceptance-range considered, the

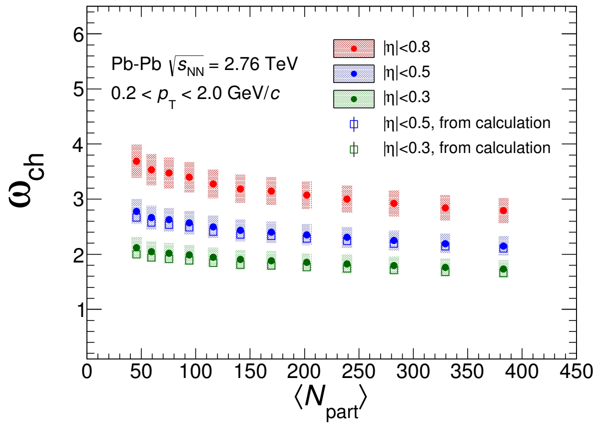

Figure 8.13: Study of scaled variance varying η-ranges, keeping the p_T-range unaltered.

scaled variance (ω_{acc}) at any other acceptance-range can be written as,

$$\omega_{acc} = 1 + f_{acc}(\omega_{ch} - 1) \tag{8.1}$$

where,

$$f_{acc} = \frac{\mu_{acc}}{\mu_{ch}} \tag{8.2}$$

Here, μ_{acc} is the mean at the other acceptance-range [4]. Estimation using the formula above has been superimposed on the results in Fig 8.13. It has been observed that the estimation matches the results within systematics. This is a very useful finding as one gets an opportunity to know the corrected value of the scaled variance, at any acceptance, just by knowing μ_{acc}, without performing extensive calculations to get efficiency-corrected σ.

The change in ω_{ch} for the most central collisions with the change in the pseudorapidity window size ($\triangle\eta$) has been presented in Fig. 8.14. In the left panel, the

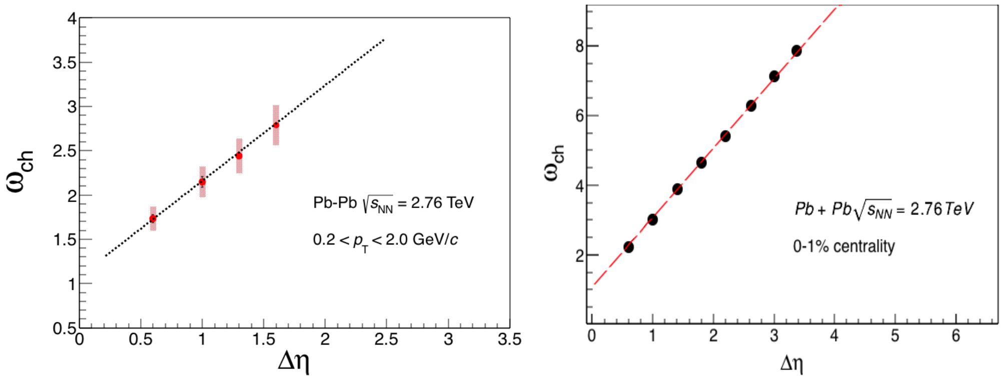

Figure 8.14: $\triangle\eta$-dependence of ω_{ch} for the most central collisions. Left panel : Results from ALICE data for $0-5\%$ centrality. Right panel : Results from AMPT-String Melting Model for $0-1\%$ centrality.

results are presented for ALICE data and for $\triangle\eta < 1.6$, $\triangle\eta < 1.3$, $\triangle\eta < 1.0$ and $\triangle\eta < 0.6$. A linear dependence has been observed. Results are fitted well within the systematics with the function $f = 1.08(1+x)$. In the right panel, the results are presented from simulation using AMPT-String melting model for a wide ranges of $\triangle\eta$. For simulation also, a linear dependence is observed and the scaled variances go on increase as a function of the pseudorapidity window size.

8.1.8 Estimation from the Monte Carlo Glauber model

Previously, an estimation of $\omega_{\rm ch}$ for the most central Pb-Pb collisions from the superposition model have been presented in Section 7.4. In this section, a rough estimation of $\omega_{\rm ch}$ has been presented from the monte carlo Glauber model. In ALICE, for CL1, we have, $\mu = 8.74$ and $k_{\rm NBD} = 0.76$. Therefore, for CL1, we have,

$$\frac{\sigma^2}{\mu} = 1 + \frac{\mu}{k_{\rm NBD}} = 1 + \frac{8.74}{0.76} = 12.5, \tag{8.3}$$

which is a constant in the Glauber analysis.

CL1 is basically the cluster in the second pixel layers and we have $\triangle\eta < 4.0$. Using the acceptance-dependence discussed in the previous section, we have roughly,

$$12.5 = c(1 + x), \tag{8.4}$$

where, c is a constant. It is evaluated as 2.5. Therefore, for this analysis, i.e, $\triangle\eta < 1.6$, we have,

$$\omega_{\rm ch} \simeq 2.5(1 + 1.6) = 6.5 \tag{8.5}$$

It is clearly evident from Fig. 8.15, that Glauber model overpredicts the results for

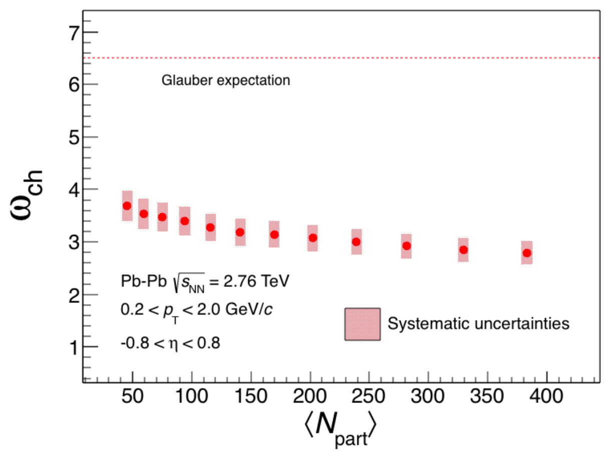

Figure 8.15: Estimation of $\omega_{\rm ch}$ from Glauber model

$\omega_{\rm ch}$ from data.

8.1.9 Study with different p_{T} ranges

To study the effect of different p_{T}-ranges on the observables, the maximum p_{T}-range is taken as $0.2 < p_{\mathrm{T}} < 2.0$ GeV/c, to avoid the contributions from the jet particles. For the study, the p_{T}-ranges are taken as $0.2 < p_{\mathrm{T}} < 2.0$ GeV/c, $0.2 < p_{\mathrm{T}} < 1.5$ GeV/c, and $0.2 < p_{\mathrm{T}} < 1.0$ GeV/c, keeping $|\eta| < 0.8$ same for all the three cases. Results have been presented in Fig. 8.16. A decrease of the values of ω_{ch} has

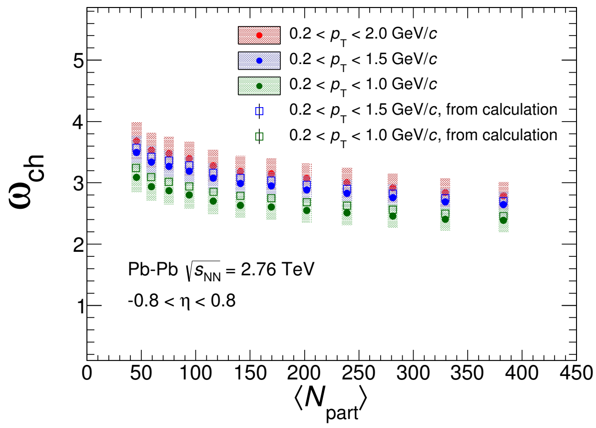

Figure 8.16: Study of scaled variance varying p_{T}-ranges, keeping the η-range unaltered.

been observed when p_{T} range is decreasing. No significant p_{T}-dependent dynamical fluctuations or sudden increase in the values of the observables have been observed.

Likewise the case for η-dependence, the scaled variance (ω_{pT}) at some other transverse-momentum range can be described by,

$$\omega_{\mathrm{pT}} = 1 + f_{\mathrm{pt}}(\omega_{\mathrm{ch}} - 1) \tag{8.6}$$

where,

$$f_{\mathrm{pt}} = \frac{\mu_{\mathrm{pT}}}{\mu_{\mathrm{ch}}} \tag{8.7}$$

where, μ_{pT} is the mean at the other p_{T}-range [4]. The theoretical estimations match with the experimental results within systematics. Therefore, the value of scaled variance at any p_{T} can be estimated, by knowing only μ_{pT}.

8.1.10 Comparison of the results with lower energies

Studies are performed in the acceptance range used in the PHENIX experiment earlier. Therefore, the kinematic cuts taken are, $|\eta| < 0.26$, $\phi <= 2.1$ radians for Au-Au collisions at $\sqrt{s_{\mathrm{NN}}} = 200$ GeV, $\phi <= 2.0$ radians for Au-Au collisions at $\sqrt{s_{\mathrm{NN}}} = 62.4$ GeV and $0.2 < p_{\mathrm{T}} < 2.0$ GeV/c.

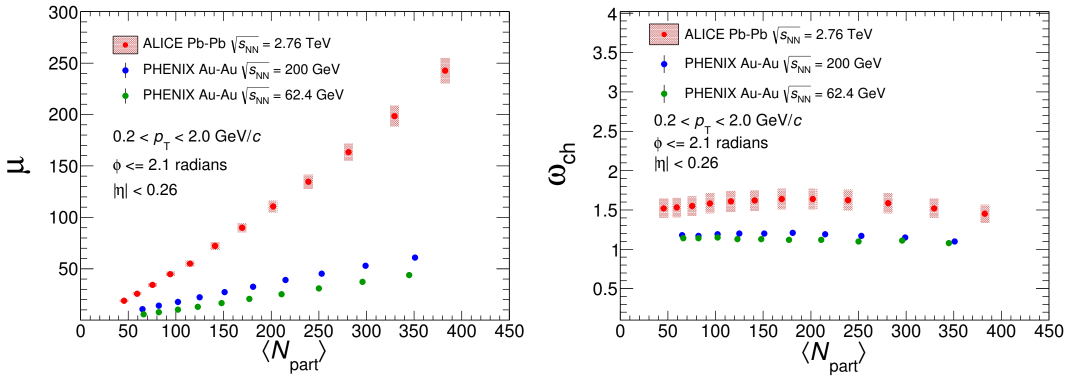

Figure 8.17: Comparison of the results with that of PHENIX-experiment. Left panel : Results for μ, Right panel : Results for ω_{ch}.

In PHENIX, the centrality is determined by the total charge deposited in Beam-Beam Counter (BBC) positioned in the range $3.0 < |\eta| < 3.9$. As expected, much higher value for μ is observed in ALICE, as shown in the left panel of Fig. 8.17. ω_{ch}

is higher in ALICE, following almost similar trend as that of PHENIX.

The correlations coming from the final-state interactions, i.e, resonance decays etc, may affect the results at the higher energies more. As for reference, the value of the scaled variance obtained in NA49 experiment for $0-5\%$ centrality bin, was explained previously combining the initial state fluctuations (calculated within the framework of the participant model) with the effect from resonance-decays [6]. For higher energies, these effects increase and as a result, an increase of $\omega_{\rm ch}$ can be predicted.

8.1.11 Universal Scaling of Multiplicity Fluctuations

A universal scaling is observed during the multiplicity fluctuation studies. In the Grand Canonical Ensemble, following Equation (4.4), one may write,

$$\frac{\sigma^2}{\mu^2} = \frac{k_{\rm B}T}{V} k_{\rm T}, \tag{8.8}$$

where, μ is the mean multiplicity, σ^2 is the variance, $k_{\rm B}$ is Boltzmann's constant, $k_{\rm T}$ is the isothermal compressibility of the produced system.

In Fig. 8.18, experimental values of $\frac{\sigma^2}{\mu^2}$ are plotted as a function of $N_{\rm part}$. Same observable has been evaluated using different cuts, i.e, the red points represent the results from ALICE experiment for Pb-Pb collisions at $\sqrt{s_{\rm NN}} = 2.76$ TeV for $|\eta| < 0.8$, the magenta points represent the results from ALICE experiment when the study is performed for PHENIX-acceptance (mentioned earlier), the blue and green points represent the results from PHENIX experiment for Au-Au collisions at $\sqrt{s_{\rm NN}} = 200$ GeV and $\sqrt{s_{\rm NN}} = 62.4$ GeV, respectively. $p_{\rm T}$-cut is same for all the studies, i.e, $0.2 < p_{\rm T} < 2.0$ GeV/c. The blue dashed lines represent the fits to the

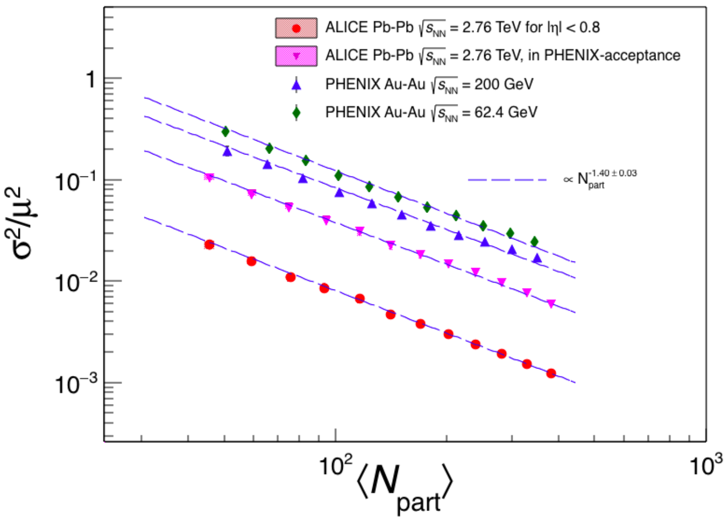

Figure 8.18: Multiplicity Fluctuation Universal Scaling

results.

From Fig. 8.18, it is evident that the data can be described by power law in N_{part} as,

$$\frac{\sigma^2}{\mu^2} \propto N_{\text{part}}^{-1.40\pm0.03}, \tag{8.9}$$

The constant of proportionality being 5.1, 20.8, 45.8, and 77.5, for the four cases described above, respectively. To observe the results clearly, x and y-axes have been taken in log-scale. ALICE results are within the systematic error of $\sim 10\%$.

This kind of universal scaling was first described by J.T.Mitchell [7] for PHENIX experiment. Here, similar scaling has been found for ALICE experiment too.

8.1.12 Extraction of Isothermal Compressibility

From the multiplicity fluctuation analysis for Pb-Pb collisions in ALICE, the value of the mean, variance and the scaled variance of the multiplicity distributions as a function of the number of participants have been presented. All the systematic sources and their percentages have been described in details. A universal scaling is found in $\frac{\sigma^2}{\mu^2}$.

Additionally, a rough estimation of the isothermal compressibility is presented here. $k_{\rm T}$ has been calculated using the Eq. 8.8. Thus, $k_{\rm T}$ can be estimated at the kinetic freeze-out, with the help of the data from ALICE experiment. For the most central Pb-Pb collisions in ALICE, we have,

$$\frac{\sigma^2}{\mu^2} \simeq 0.00122. \tag{8.10}$$

Taking the HBT-radius as 7 fm [8], T as 95 MeV (T represents the kinetic freeze-out temperature here) [9], and $k_{\rm B} = 1$, in natural units, $k_{\rm T}$ is found to be about 0.018 $fm^3 MeV^{-1}$. This is very small value, indicating that the system is not easy to compress. Isothermal compressibility represents the fractional change in the volume of the system with the unit change of the pressure, at constant temperature. Therefore, its unit should be in inverse of pressure, which is $fm^3 MeV^{-1}$, in natural units. Compressibility is a very important thermodynamic quantity which is related to the speed of the sound. Bulk modulus is the inverse of the compressibility, which basically measures material's resistance to uniform compression.

The ratios of the compressibilities measured in different energies will be a very good extension of this study, as that will provide an estimation of how much $k_{\rm T}$ changes with the energy for the collisions. Following Eq. 8.8, for two different systems at, say energy **1** and energy **2** can be described as,

$$k_{\mathrm{T_{ratio}}} = \frac{k_{\mathrm{T_1}}}{k_{\mathrm{T_2}}} = \frac{\omega_{\mathrm{ch_1}}\mu_2}{\omega_{\mathrm{ch_2}}\mu_1}, \tag{8.11}$$

where, at the kinetic freeze-out, (T/V) is assumed to be roughly same for a wide energy range of WA98 (Pb-Pb collisions at $\sqrt{s_{\mathrm{NN}}} = 17.3$ GeV), PHENIX (Au-Au collisions at $\sqrt{s_{\mathrm{NN}}} = 200$ GeV, Au-Au collisions at $\sqrt{s_{\mathrm{NN}}} = 62.4$ GeV), to ALICE experiments (Pb-Pb collisions at $\sqrt{s_{\mathrm{NN}}} = 2.76$ TeV). The results for WA98 and PHENIX have been corrected to obtain the results in the similar acceptance as in ALICE. The result is presented in Fig. 8.19. The ratios are 1.3, 1.16, 1.0, and

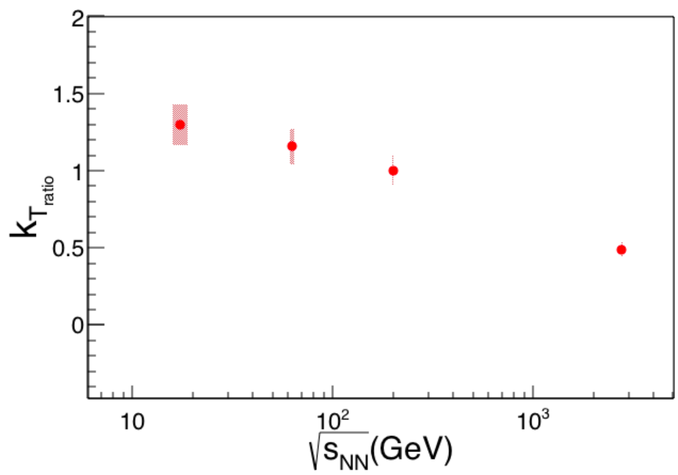

Figure 8.19: Estimation of k_{T}-ratios (see text) as a function of energy

0.49, respectively, putting the result for Au-Au collisions at $\sqrt{s_{\mathrm{NN}}} = 200$ GeV as a baseline. The results are within a systematic error of $\sim 10\%$. From these results, it is indicated that the systems are easier to compress in lower energies, than in higher energies. At the critical point, k_{T} as well as the susceptibility is expected to diverge. As a result, the systems are easiest to compress near the critical point.

This procedure followed for the calculation of hadronic matter compressibility with the help of the multiplicity distribution parameters from the experiments and performing an event-by-event analysis, was described very nicely in Ref. [10]. For a given centrality class, it is assumed that all events correspond to a system with the same T and V. To evaluate the isothermal compressibility at the chemical freeze-out, the temperature at the chemical freeze out can be found from the thermal model predictions done by Cleymans [11]. But, for the final state particles, a sizable fraction comes from hadron resonance decays [10]. Therefore, we need the exact multiplicities of the charged particles at the chemical freeze-out, which is a difficult task, at least from experiments. However, it may be estimated within the thermodynamical model considering the hadron resonances [12].

8.2 Results for p-Pb collisions at $\sqrt{s_{\rm NN}} = 5.02$ TeV

For the analysis of ALICE data for p-Pb collisions at $\sqrt{s_{\rm NN}} = 5.02$ TeV, the data taken in 2013 ($\sim 12M$ events) has been used as discussed in Section 7.1. To describe the cuts used for the analysis, the normalised η-distribution has been presented in Fig 8.20. All the cuts used for the analysis are exactly similar to those used in Pb-Pb collisions as described in Table 7.1 and Table 7.2. Centrality selection has been done using V0A-detector (described in Section 7.3.3). The uncorrected multiplicity distributions for different centralities have been shown in Fig. 8.21. The distributions are scaled over the mean multiplicity. The multiplicity distributions for all the centralities are fitted very well with the negative binomial distributions, having the χ^2 per degrees of freedom less than unity.

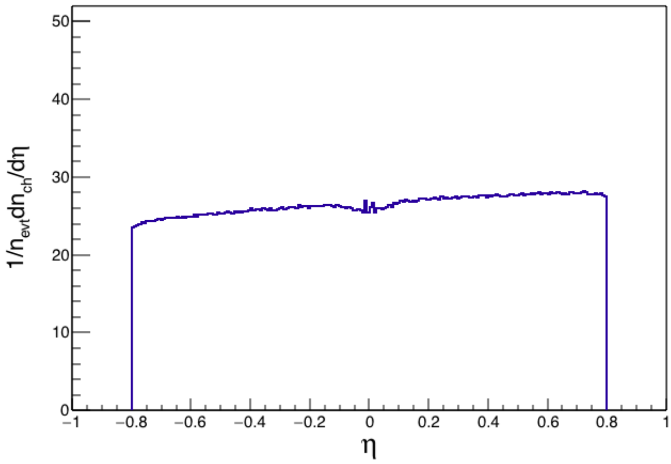

Figure 8.20: Normalised η-distribution for p-Pb collisions at $\sqrt{s_{\mathrm{NN}}} = 5.02$ TeV for $0 - 5\%$ centrality.

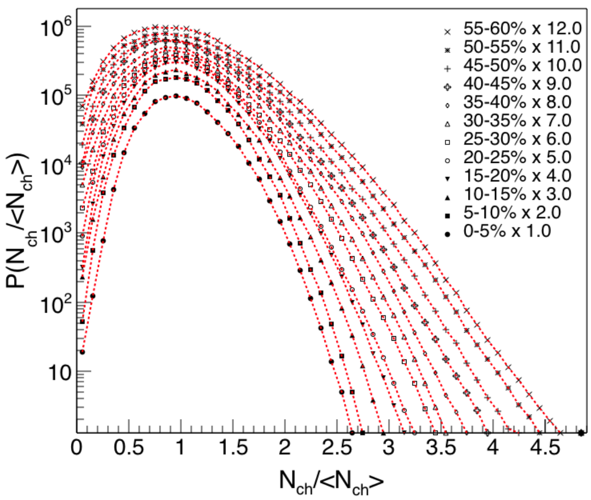

Figure 8.21: Total charge multiplicity distributions for p-Pb collisions at $\sqrt{s_{\mathrm{NN}}} =$ 5.02 TeV for different centralities. The red dashed lines are the NBD-fits to the multiplicity distributions.

8.2.1 Results from the multiplicity distributions

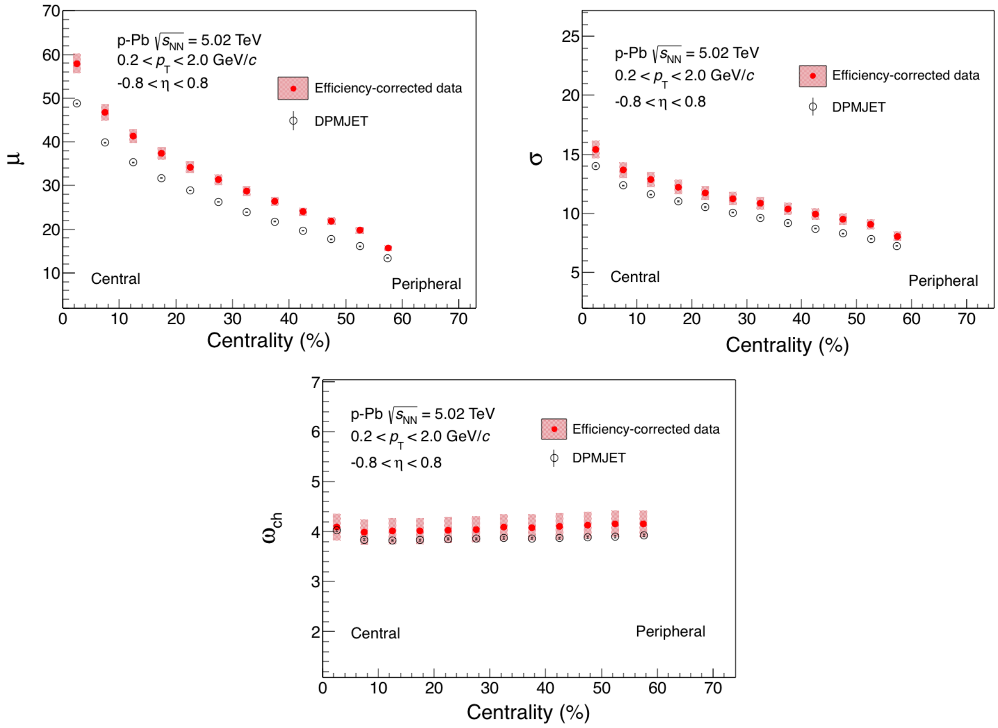

Figure 8.22: Efficiency corrected results for p-Pb collisions at $\sqrt{s_{NN}} = 5.02$ TeV as a function of centrality. Top left : μ. Top right : σ. Bottom panel : ω_{ch}. The results are compared with the simulation results using DPMJET event generator.

The results from the multiplicity distributions are shown in Fig. 8.22. The results are efficiency corrected and the binwidth corrections have been applied to the results. The sources for the systematic errors are similar as described for the analysis with Pb-Pb collisions. The studies have been done using different centrality estimators too. A schematic view of p-Pb collisions alongwith the different centrality estimators used have been shown in Fig. 8.23. The centrality estimators used for p-Pb collisions in ALICE are CL1, V0A, V0M (i.e, V0A+V0C), and ZNA. For CL1, strong bias is observed due to full overlap with the tracking region. For the energy detected

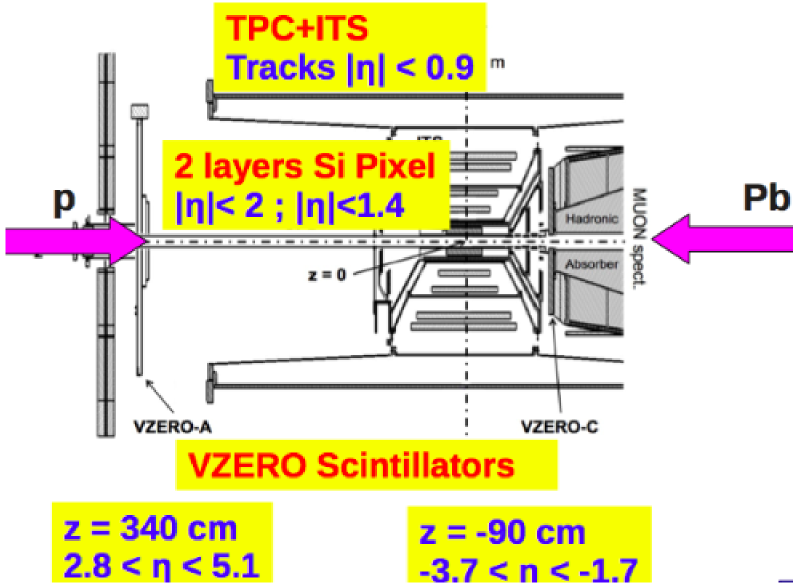

Figure 8.23: Different centrality estimators used in p-Pb collisions. Additionally the TPC-tracking region has been shown.

by the neutron calorimeter on the Pb-remnant side (ZNA), we have small bias due to slow nucleon production independent of the hard processes. For V0M, reduced bias is expected as V0A and V0C are outside the tracking region. For V0A, reduced bias is expected because of the enhanced contribution from the Pb fragmentation region. These are described in details in Ref. [13]. For this analysis, V0M and V0A are used for centrality estimation and the difference between the results are added as systematic errors. ZDC has not been used for the problem with the resolution and for this analysis, it is very important to have a agood centrality resolution for the estimator. However, the total percentage of the overall systematic errors for μ, σ and $\omega_{\rm ch}$ are $\sim 4\%,\ 5\%,\ 6.5\%$ respectively.

In Fig. 8.22, the results are presented as a function of centrality. Results are shown down to 60% centrality, in the region where the efficiency correction shows very good match in the monte carlo closure test. The results have been compared with the results from DPMJET event generator. The statistical and the systematic errors are shown in the plots. It is observed that the results from data for the scaled variances increase monotonically from central to peripheral collisions. Simulation results give similar trend as that of data for μ and σ, but the values are lower. For $\omega_{\rm ch}$, the results from DPMJET as a function of centrality remains almost constant, however, it match with the data results almost within the systematics.

Another thing can be observed from the results that the values of $\omega_{\rm ch}$ are higher than the values observed for the scaled variances for Pb-Pb collisions at $\sqrt{s_{\rm NN}}$ = 2.76 TeV.

8.2.2 Results from the multiplicity distribution parameters

The parameters characterizing the multiplicity distributions may be connected to the early stages of collisions as discussed in Section 4.6. In this section, the results of the parameters from the multiplicity distributions, i.e, the mean (μ) and $k_{\rm NBD}$ have been presented for p-Pb as well as Pb-Pb collisions. The results presented here are efficiency corrected and binwidth corrected.

In the left panel of Fig. 8.24, the results from p-Pb collisions have been shown. Results are shown for all the centralities (down to $\sim$ 60% centrality), as the distributions are fitted well with the NBD's. The dependence of the parameters, within the systematic error of $\sim$ 4% for μ and $\sim$ 7.5% for $k_{\rm NBD}$, is observed to follow the polynomial of 2nd order as,

$$f_1(x) = -0.48 + 0.35x - 0.00014x^2 \quad (8.12)$$

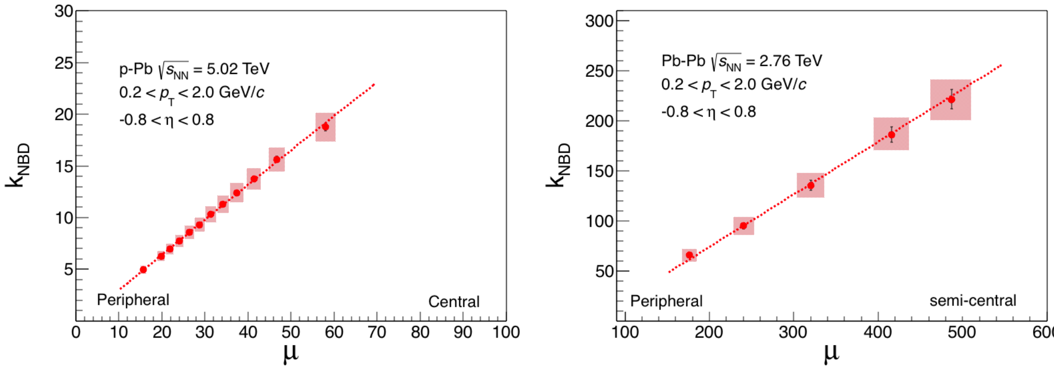

Figure 8.24: Relation between the multiplicity distribution parameters μ and k_{NBD}. Left panel : for p-Pb collisions at $\sqrt{s_{\mathrm{NN}}}$ = 5.02 TeV. Right panel : for Pb-Pb collisions at $\sqrt{s_{\mathrm{NN}}}$ = 2.76 TeV. The red dashed lines represent the fits.

and, the ratio of the parameters, i.e, $\frac{k_{\mathrm{NBD}}}{\mu}$ is found to be 0.31 to 0.33. Therefore, it can be inferred that the dependence is not exacly linear and k_{NBD} and μ are not exactly proportional to each other.

In the right panel of Fig. 8.24, the same results are shown for Pb-Pb collisions upto 35% centrality, where the distributions can be fitted by NBD's. For more central collisions, the distributions follow gaussians. The systematic errors are $\sim$ 5% for μ and $\sim$ 9.5% for k_{NBD}. A dependence between the parameters observed here is of the form,

$$f_2(x) = -31.2 + 0.53x \tag{8.13}$$

and, $\frac{k_{\mathrm{NBD}}}{\mu}$ is found to be around 0.43. Therefore, a linear dependence between the parameters has been observed in case of symmetric collisions, i.e, Pb-Pb collisions. These are important results which may be connected to the initial stages of the collisions. However, these results will be more interesting to study in the forward region where $x \sim 10^{-6}$ can be achieved.

8.3 Results for pp collisions at $\sqrt{s} = 0.9, 2.76, 7$ and 8 TeV

In this section, the results from ALICE data are presented for pp collisions at $\sqrt{s} = 0.9, 2.76, 7$ *and* 8 TeV. The results for pp collisions work as a baseline study and an estimation can be made how much the fluctuation is different for different collision systems, i.e, for pp, p-Pb and Pb-Pb collisions. Fig. 8.25 shows an estimation of

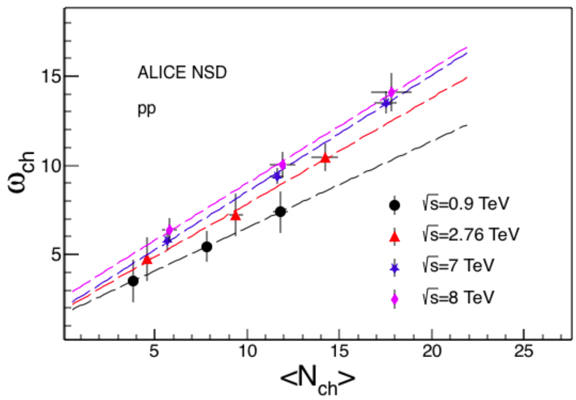

Figure 8.25: Scaled variance as a function of $\langle N_{\text{ch}} \rangle$ for pp collisions in ALICE for $\sqrt{s} = 0.9, 2.76, 7$ and 8 TeV respectively. The dashed lines represent the fits.

the scaled variance as a function of $\langle N_{\text{ch}} \rangle$ for pp collisions in ALICE experiment for $\sqrt{s} = 0.9, 2.76, 7$ and 8 TeV respectively. The left most points represent results for $|\eta| < 0.5$, middle points for $|\eta| < 1.0$ and right most points for $|\eta| < 1.5$. $\langle N_{\text{ch}} \rangle$ goes upto ~ 20 for $\sqrt{s} = 8$ TeV, as shown in the fig. From the results of the multiplicity distributions for pp collisions in ALICE for non-single diffractive (NSD) events [14],

μ and σ are evaluated as,

$$\mu = \frac{\sum N_{\rm ch} P(N_{\rm ch})}{\sum P(N_{\rm ch})} \tag{8.14}$$

$$\sigma^2 = \frac{\sum N_{\rm ch}^2 P(N_{\rm ch})}{\sum P(N_{\rm ch})} - \mu^2 \tag{8.15}$$

where, $N_{\rm ch}$ and $P(N_{\rm ch})$ can be found out from the distributions. Using Equation 8.15, the scaled variances have been calculated. It has been observed that the dependence of $\omega_{\rm ch}$ on $\langle N_{\rm ch}\rangle$ is linear. For the four energies, $\sqrt{s} = 0.9, 2.76, 7$ and 8 TeV respectively, the fit functions are,

$$f_1 = 0.50x + 1.5 \tag{8.16}$$

$$f_2 = 0.603x + 1.83 \tag{8.17}$$

$$f_3 = 0.648x + 2.027 \tag{8.18}$$

$$f_4 = 0.632x + 2.675 \tag{8.19}$$

The χ^2 per degrees of freedom for the fits are less than unity. An increase in the values of the scaled variances has been observed for pp collisions in comparison with p-Pb and Pb-Pb collisions.

8.4 Discussions

The results for the multiplicity fluctuations for all charged particles in terms of the scaled variances have been presented for p-Pb as well as pp collisions, in addition to the results from Pb-Pb collisions. For p-Pb collisions, it is shown that the scaled variances slowly increase from the central to the peripheral collisions. For pp collisions, the scaled variances increase for a particular acceptance as the energy increases.

It has been observed that the values for ω_{ch} for similar energies are highest for pp collisions, lower for p-Pb collisions and the lowest for Pb-Pb collisions. This indicates a falsification of the Wounded Nucleon Model (WNM), as the multiplicity fluctuations in heavy ion collisions can not be less than the fluctuations in pp collisions within WNM. This has been discussed in case of the results of the multiplicity fluctuation analysis from NA61 experiments [15]. The increased values of the multiplicity fluctuations for p-Pb and pp collisions may be attributed to the volume fluctuations. However, to evaluate the fluctuations neglecting the effect of the volume as well as the volume fluctuations, strongly intensive quantities, i.e, Δ and Σ can be used as an extension to this study.

Bibliography

[1] Maitreyee Mukherjee *et al.* 2016 J. Phys. G: Nucl. Part. Phys. **43** 085102.

[2] https://aliceinfo.cern.ch/ArtSubmission/node/112.

[3] B. Abelev *et al.* (ALICE Collaboration), Phys. Rev. **C 88**, 044909 (2013), arXiv:1301.4361 [nucl-ex] (2013).

[4] A. Adare *et al.*, Phys. Rev. **C 78**, 044902 (2008), arXiv: 0805.1521[nucl-ex] (2008).

[5] M. L. Miller, K. Reygers, S. J. Sanders, and P. Steinberg, Glauber modeling in high energy nuclear collisions, Ann.Rev.Nucl.Part.Sci., vol. 57, pp. 205243, 2007.

[6] G.V.Danilov and E.V.Shuryak, arXiv:nucl-th/9908027.

[7] J.T.Mitchell, "Scaling Properties of Fluctuation and Correlation Results from PHENIX", Quark Matter 2006.

[8] L. Graczykowski et al., (ALICE Collaboration), EPJ Web of Conferences 71, 00051 (2014).

[9] B. Abelev et al. (ALICE Collaboration), Phys. Rev. C 88, 044910 (2013).

[10] Stanislaw Mrowczynski, Physics Letters **B 430** 1998 (914).

[11] J. Cleymans, H. Oeschler, K. Redlich and S. Wheaton, Phys. Rev. **C 73**, 034905 (2006).

[12] F. Becattini, M. Gazdzicki, J. Sollfrank, Eur.Phys.J.**C5** :143-153,1998.

[13] J.Adam et al. (ALICE Collaboration), Phys. Rev. **C 91**, 064905 (2015).

[14] J.Adam et al. (ALICE Collaboration), arxiv: 1509.07541 [nucl-ex].

[15] K. Grebieszkow, "Event-by-event fluctuations-the future of ion physics", X Polish Workshop on Relativistic Heavy-Ion Collisions, 2013.

9 Summary & Outlook

In this thesis, a study of the charged particle multiplicity fluctuation has been presented with the analysis of data from the ALICE experiment.

Multiplicity of the produced particles is a very simple observable to study. A hint of the particle production mechanism is provided with the help of the multiplicity distribution study. As for example, one expects a Poisson distribution when the particles are produced independently, and deviation from the Poisson distribution gives a hint of the presence of correlation in the system.

The multiplicity fluctuation (ω_{ch}) is defined as the variance of the multiplicity distribution, scaled over the mean of the multiplicity distribution. The multiplicity fluctuations are independent of the volume of the system produced in the high energy collisions, but depend on the volume fluctuations. Multiplicity fluctuations have both statistical and dynamical sources. The statistical components such as, impact parameter fluctuations in the finite centrality bin width, effect of limited acceptance of the detector, the fluctuations in the number of participants, etc., are to be minimised in order to extract the dynamical fluctuations. The statistical fluctuations affect the other measurements. The scaled variance, being proportional to the isothermal compressibility as well as the quark-number susceptibility (χ_q) of the system, is expected to increase about an order of magnitude near the QCD critical point.

The multiplicity fluctuation analysis is possible due to the production of large number of particles in each event at these ultra-relativistic energies. In ALICE experiment, Bjorken-x below 10^{-4} is achievable with the central detectors, providing a good opportunity to study the initial state effects. The multiplicity distribution parameters (when the distributions are fitted well with the negative binomial distributions) may be connected to the early stages of collision and an interesting observation has been made how these parameters change for different collision systems, i.e, from Pb-Pb to p-Pb collisions.

Detectors used for the analysis are ITS (for vertex selection and tracking), V0 (for centrality selection), TPC (for tracking), etc. Detailed studies are performed for the centrality selection, track selection, etc. Non-uniformity in the charged particle multiplicity distribution is the cause behind the impact parameter fluctuation within a finite centrality bin, which is called *centrality bin width effect*. The correction to this effect has been discussed in details. The final results are presented for 5% centrality bins, after applying the centrality bin width correction. The estimation of the efficiency factors, including the phase-space dependence (transverse momentum dependence in case of ALICE) as well as the effect of the contamination and the correction for the detector inefficiency, is the main challenge of this study. The efficiency corrections to the higher order moments (upto second order) and the related observables are expressed as a function of factorial moments, to make the complex calculations easier. The truncation issues occuring for very large numbers have been taken care of in the analysis code. Statistical error estimation has been done using Delta Theorem and the errors are phase space dependent efficiency corrected properly. The efficiency correction method shows a very good match in the monte carlo closure test. The final results are efficiency corrected. The volume fluctuations are estimated within the monte carlo framework and it is close to unity. The effect of the possible biases on the analysis have been discussed too. The sources of the systematic errors to the final results have been discussed in details. Main sources of the errors are, the effect coming from different track cuts, different vertex cuts, different magnetic field, effect of data cleanup, etc.

The results are analyzed for Pb-Pb collisions at $\sqrt{s_{\rm NN}} = 2.76$ TeV (data taken in 2010) and for p-Pb collisions at $\sqrt{s_{\rm NN}} = 5.02$ TeV (data taken in 2013). Systematic errors for $\omega_{\rm ch}$ is around 8% for Pb-Pb collisions and around 6.5% for p-Pb collisions. A monotonically decreasing trend for $\omega_{\rm ch}$ has been observed from peripheral to the central collisions. The results have been compared with the results from event generators, i.e, HIJING and AMPT String Melting for Pb-Pb analysis and DPMJET for p-Pb analysis. HIJING, AMPT show a mismatch between the results from the data and the simulation. The results from DPMJET match with the data results from p-Pb within the systematics. Study of the effect of detector acceptance on the observable has been performed using three different acceptance (η) ranges, keeping $p_{\rm T}$-range always same. The multiplicity fluctuations are observed to be decreased with reduced acceptance. The same study has been performed with three different transverse momentum ranges, keeping η always same. With the decrease of $p_{\rm T}$-range, the multiplicity fluctuations have been found to be decreased. Glauber model overpredicts the result from data. The ALICE results studied within the acceptance same as that of PHENIX experiment, show a much higher μ and $\omega_{\rm ch}$ in ALICE, probably due to the correlations coming from the final state interactions, i.e, resonance decays etc, which should affect the results in the higher energies more. A universal scaling in σ^2/μ^2 as a function of the number of participants has been observed in the multiplicity fluctuation analysis with the heavy ion collisions. A rough estimation of k_{T} of the system has been presented at the kinetic freeze-out temperature, which is $\sim 0.018\ fm^3MeV^{-1}$, for the most central Pb-Pb collisions. Results from the multiplicity distribution parameters alongwith the relation between the parameters, i.e, k_{NBD} and μ have been also presented and discussed.

Additionally, the results for the charged particle multiplicity distributions and fluctuations have been studied uding the AMPT default and string melting event generators for Au-Au collisions at $\sqrt{s_{\mathrm{NN}}} = 7.7$ to 200 GeV and for Pb-Pb collisions at $\sqrt{s_{\mathrm{NN}}} = 2.76$ TeV. Results are presented for $0.2 < p_{\mathrm{T}} < 2$ GeV/c, and $|\eta| < 0.5$. The results are compared with the earlier results from NA49, WA98 and PHENIX experiments also. The experimantal results are scaled to have the results in the similar acceptance. Collision energy dependence of the charged particle multiplicity fluctuations does not show any non-monotonic behaviour for AMPT as well as data results. A slow rise in ω_{ch} has been observed from low to high collision energies and remains constant at higher energies. Event generators, by including dynamical phenomenon and critical behavior, are absent at present. Therefore, this study basically provides a baseline for the future multiplicity fluctuation studies.

It will be interesting to study the same observables for even higher energies, i.e, for the collision of Pb-Pb beams at 5.5 A TeV. At higher energies, the number of particles produced per event will be even more and it will be interesting to notice how much will be the change in the values of the observables. We expect the collision of Pb-Pb beams at 5.5 A TeV in LHC in the year of 2016. With more particles per event and with the same analysis performed in the forward rapidities for p-Pb as well as Pb-Pb collisions, one can get more insight into the initial state effects, because in the forward rapidities in LHC, Bjorken-x value of 10^{-6} can be achieved. In these cases, the relation between the multiplicity distribution parameters can be studied as well. The scaled variance has no volume term, as discussed earlier, but it has a dependence on the volume fluctuation. It is important to get rid of the volume fluctuation term in order to correctly compare the fluctuations in different collision systems, i.e, pp, p-Pb and Pb-Pb collisions. For this, strongly intensive quantities, i.e, Δ, Σ can be used. These strongly intensive quantities are formed in such a way so that it does not have the effect from the volume fluctuation term. The fluctuation studies with the strongly intensive quantities are interesting extension to this study with the scaled variances.

Appendix A

Results from Quark Matter 2015

The preliminary results from ALICE on the multiplicity fluctuation analysis in Pb-Pb collisions at $\sqrt{s_{\rm NN}}$ = 2.76 TeV have been presented here. The results were presented in Quark Matter 2015.

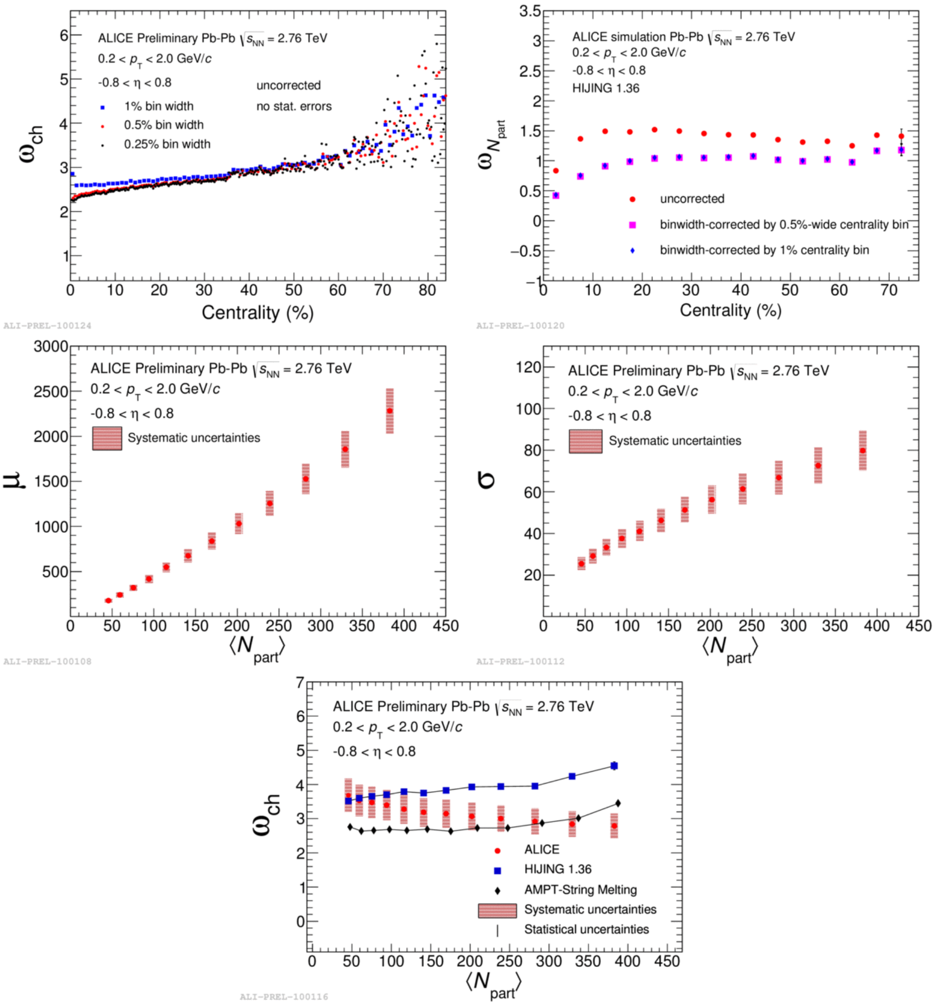

Figure 9.1: Preliminary results from ALICE : Binwidth effect (Top Left); Fluctuations in $N_{\rm part}$ (Top Right); μ (Middle Left), σ (Middle Right) from the multiplicity distributions; Results for $\omega_{\rm ch}$ from data compared to models (Bottom panel).